SHEAR AND SHEAR FRICTION OF ULTRA-HIGH PERFORMANCE CONCRETE BRIDGE GIRDERS

A Dissertation
Presented to
The Academic Faculty

By

Charles Kennan Crane

In Partial Fulfillment
Of the Requirements for the Degree
Doctor of Philosophy in Civil Engineering

Georgia Institute of Technology

August, 2010

Shear and Shear Friction of Ultra-high Performance Concrete Bridge Girders

Approved by:

Dr. Lawrence F. Kahn, Advisor
School of Civil and Environmental Engineering
Georgia Institute of Technology

Dr. Kimberly E. Kurtis
School of Civil and Environmental Engineering
Georgia Institute of Technology

Dr. Roberto T. Leon
School of Civil and Environmental Engineering
Georgia Institute of Technology

Dr. Russell Gentry
College of Architecture
Georgia Institute of Technology

Dr. Benjamin Graybeal
Turner-Fairbank Highway Research Center
Federal Highway Administration

Date Approved: July 2, 2010

For Chandra and Annabel:

who are both my support and my inspiration

ACKNOWLEDGEMENTS

I cannot say that this Ph.D. is wholly mine. There are so many people to whom I owe so much. My advisor Dr. Lawrence Kahn has been a great mentor to me as well as an example of what a great academic/practitioner should be. I am proud to have studied under him. I also could not have made it without the guidance and input of my committee: Dr. Kimberly Kurtis, Dr. Roberto Leon, Dr. Russell Gentry, and Dr. Benjamin Graybeal. Thank you all for all of the time and effort you have invested in me and my research.

This research was funded by the Georgia Department of Transportation (GDOT) research project No. 2043 Task Order No. 02-08 and project No. 07-05, Task Order No. 02-37. Mr. Kevin Kirkley and Tindall Corporation as well as Mr. Peter Calcetas and LaFarge Corporation provided invaluable help in casting the UHPC girders. Their support is gratefully acknowledged. The opinions, conclusions, and recommendations presented herein are those of the author and do not necessarily represent the opinions and recommendations of the cooperating organizations.

I would also like to thank all of my fellow graduate students who have helped through commiseration and back-breaking work: Victor Garas, Mauricio Lopez, John Bunyasaranand, Jonathan Hurff, Brett Holland, Robert Moser, Amal Jayapalan, Curtis O'Malley, and Ben Deaton. I also could not have finished without the help of some great research assistants: Luis Fajardo, Chris Noyer, Andrea Penno, Danielle Simpson, John Bennett, Kate Howard, Roshanak Gharaat, and Kinzie Rieckmann. Mr. Andy Udell and Jeremy Mitchell also worked tirelessly to keep research going in the lab.

I have been fortunate to have wonderful support outside of school as well. Thank you to all of my brothers and sisters at ChristChurch Presbyterian. The Fellowship of Christian Graduate Students at Georgia Tech has been a wonderful place of community and encouragement. Thanks also to my wonderful friends at Octane for keeping me caffeinated and entertained during long hours of writing.

My parents, Charlie and Martha Crane and Roger and Victoria Garrett, have supported me and believed in me through everything. My sister and brother-in-law, Christy and Gordon Hwang, have also given me their encouragement and wisdom. I thank my entire family most of all for their love.

All of the thanks and love it my heart to my wonderful wife, Chandra. She has been my friend and supporter through more years of school than anyone should have to endure. Her name belongs on this Ph.D. more than does mine.

Lastly, it was a desire to serve my Lord, Jesus Christ, that took me to grad school to begin with. He is both the Builder and the Architect, and I am humbled to have spent this time learning about His world. He has shown Himself to be faithful, even when I am faithless. His alone is the glory.

TABLE OF CONTENTS

ACKNOWLEDGEMENTS iv

LIST OF TABLES ix

LIST OF FIGURES xi

NOTATION xxv

SUMMARY xxix

CHAPTER 1: INTRODUCTION 1
1.1 Purpose and Objectives 1
1.2 Motivation 2
1.2.1 Shear Friction 2
1.2.2 Diagonal Tension Shear 3
1.3 Research Methodology 4
1.4 Thesis Organization 7
1.5 References 9

CHAPTER 2: BACKGROUND 10
2.1 Material Characterization of Ultra-High Performance Concrete 10
2.2 Shear Friction 11
2.2.1 Push-off Tests 12
2.2.2 Composite Beams 35
2.3 Diagonal Tension Shear 42
2.4 References 44

CHAPTER 3: SHEAR FRICTION PUSH-OFF TESTS WITH ULTRA HIGH PERFORMANCE CONCRETE 48
3.1 Introduction 48
3.2 Research Significance 51
3.3 Experimental Procedure 51
3.4 Experimental Results and Discussion 60
3.4.1 Monolithic UHPC Results 60
3.4.2 UHPC/HPC Cold Joint Results 64
3.4.3 Comparison with Code Equations 68
3.4.4 Proposed Shear Friction Constants for Monolithic UHPC 73
3.4.5 Effect of Interface on Performance of All-UHPC Specimens 75
3.4.6 Effect of Reinforcement Ratio on Performance of All-UHPC Specimens 75
3.4.7 Effect of Surface Preparation on Performance of Cold Joint UHPC/HPC Specimens 76

3.4.8 Effect of Reinforcement Ratio on Performance of UHPC/HPC Specimens 76
3.5 Conclusions 77
3.6 References 77

CHAPTER 4: INTERFACE SHEAR CAPACITY OF SMALL COMPOSITE T-BEAMS 79
4.1 Introduction 79
4.2 Research Significance 79
4.3 Background 80
4.4 Test Setup 84
4.5 Experimental Results and Discussion 88
4.6 Comparison to Push-off Tests 100
4.7 Conclusions and Recommendations 103
4.8 References 104

CHAPTER 5: INTERFACE SHEAR PERFORMANCE OF FULL-SCALE UHPC BRIDGE GIRDERS WITH CAST-IN-PLACE HPC DECKS 105
5.1 Introduction 105
5.2 Previous Research 105
5.3 Specimen Design 106
5.4 Beam Testing 117
5.5 Results and Analysis 130
5.5.1 Comparison to Code Equations 130
5.5.2 Comparison to Push-off and Small Composite Beam Results 134
5.6 Conclusions 140
5.7 References 141

CHAPTER 6: DIAGONAL TENSION SHEAR CAPACITY OF PRECAST PRESTRESSED ULTRA-HIGH PERFORMANCE CONCRETE BRIDGE GIRDERS 143
6.1 Background 143
6.1.1 Previous Research 143
6.1.2 Current UHPC Codes 144
6.2 Experimental Program 152
6.2.1 Shear Test 1-1a (non-composite girder with 2-#4 [M13] bars at 24-in. [0.61m] spacing) 155
6.2.2 Shear Test 1-2 (fluted interface with no reinforcement) 163
6.2.3 Shear Test 2-1 (smooth interface with no reinforcement) 169
6.2.4 Shear Test 2-2 (fluted interface with 2-#4 [M13] bars at 24-in. [0.61m] spacing) 176
6.2.5 Shear Shear Test 3-1 (reduced flange width fluted interface with no reinforcement) 181
6.2.6 Shear Test 3-2 (reduced flange width, smooth interface with 2-#4 [M13] bars at 12-in [0.31m] spacing) 186
6.3 Analysis of Results 190
6.3.1 Shear Capacity Based on Direct Tension Capacity 191

6.3.2 Shear Capacity Based on Simplified Modified Compression Field Theory 193
6.3.3 Comparison of Experimental and Theoretical Shear Capacities 197
6.4 Conclusions 200
6.5 References 200

CHAPTER 7: FIBER ALIGNMENT IN UHPC GIRDERS 202
7.1 Introduction 202
7.2 Background 202
7.3 Experimental Methods 204
7.3.1 Image Analysis 206
7.3.2 Compression Testing of Cores 214
7.4 Comparison of Results 225
7.5 Conclusions 231
7.6 Further Research 232
7.7 References 233

CHAPTER 8: CONCLUSIONS, RECOMMENDATIONS, AND FUTURE RESEARCH 236
8.1 Conclusions 236
8.2 Recommendations 238
8.3 Future Research 238
8.4 References 239

APPENDIX A: PUSH-OFF TEST LOAD-SLIP CURVES AND FAILURE PICTURES 240

APPENDIX B: SHEAR ROSETTE STRAINS 283

APPENDIX C: SMALL COMPOSITE BEAM DATA 291

APPENDIX D: FULL-SCALE COMPOSITE PRESTRESSED UHPC GIRDER DATA 297
D.1 Instrumentation of Full-Scale Composite UHPC Bridge Girders 297
D.1.1 Embedded Gauges 297
D.1.2 Longitudinal Strain Measurement 300
D.1.3 Deck Slip Measurement 302
D.1.4 Shear Strain Measurement 302
D.1.5 Deflection Measurement 303
D.1.6 Force Measurement 304
D.2 Thermal Curing Data for UHPC Girders 306
D.3 Losses at Strand Release 307
D.4 Transfer Length of Strands in UHPC Girders 309
D.5 Longitudinal Strain Gauge Test Data 310
D.6 References 318

LIST OF TABLES

Table 2-1 Effect of Surface Preparation on Max Load and Slip at Failure 35

Table 3-1 Specimen Specification 58

Table 3-2 Monolithic push-off specimen ultimate shear experimental and predicted values, 1kN=0.225 kip 61

Table 3-3 Experimental and predicted shear capacities of UHPC/HPC push-off specimens, 1kN=0.225 kip 65

Table 4-1 Summary of Experimental Results 87

Table 4-2 Initial stiffnesses of composite t-beams 90

Table 4-3 Experimental and predicted interface shear stresses, psi (MPa) 93

Table 4-4 Ratio of $v_{exp\ max}$, experimental interface shear stress at maximum load to predicted interface shear stress 99

Table 4-5 Ratio of $v_{exp\ slip}$, experimental interface shear stress at slip load to predicted interface shear stress 100

Table 5-1 Comparison of interface steel and surface preparation for shear tests 109

Table 5-2 Experimental interface shear stresses compared to ACI and AASHTO code predictions. 133

Table 5-3 Ratio of experimental shear interface shear stresses to code predictions. 134

Table 6-1 AASHTO Type II UHPC girder shear test results (Graybeal, 2005). 147

Table 6-2 Test parameters for shear tests performed by Hegger and Bertram (2008) 148

Table 6-3 Shear test properties. 152

Table 6-4 Calculation of shear capacity by direct tension strength 192

Table 6-5 Calculation of shear capacity by simplified modified compression field theory. 196

Table 6-6 Comparison of experimental shear capacities to prediction equations 198

Table 7-1 Compression Core Details 216

Table 7-2 Compression Test Results.....220
Table 7-3 Summary of Compression Test Results.....221
Table 7-4 Tukey-Kramer HSD Analysis of Compression Test Results.....221
Table D-1 VWSG readings before and after strand release. 308

LIST OF FIGURES

Figure 1-1 Schematic overview of research approach. 5

Figure 1-2 Overview of specimens used in multi-scale interface shear tests. 6

Figure 1-3 Overview of specimens used in multi-scale diagonal tension shear tests. .7

Figure 2-1 The push-off specimens used by Hanson (1960) varied the interface area between 48 and 192 in^2. The reinforcement ratios varied between 0.002 and 0.008. 13

Figure 2-2 Typical stress-slip curves for push-off tests by Hanson (1960). Note that the effect of stirrups has been removed from these curves. 14

Figure 2-3 The push-off specimen used by Anderson (1960) had a 100 in^2 interface area and varied the reinforcing ratio between 0.002 and 0.0248. 16

Figure 2-4 Push-off results from Anderson (1960) compare steel ratio to the ultimate interface shear stress in the concrete. Two different concrete strengths were used for the cast-in-place portion of specimens. 17

Figure 2-5 Shear friction hypothesis (Birkeland and Birkeland, 1966). 18

Figure 2-6 Shear friction equation compared to experimental data for push-off tests and girder tests from Birkeland and Birkeland (1966). 19

Figure 2-7 Results of precracked push-off shear tests compared to shear friction equation from Hofbeck et. al. (1969). 22

Figure 2-8 Push-off specimen for cyclic loading of interface. The dashed line represents the interface between precast and cast-in-place concretes (Paulay, Park et al., 1974). 25

Figure 2-9 The push-off specimens used by Kahn and Mitchell (2002) had interface areas of 60 in and reinforcement ratios varying from 0.0037 and 0.0147. 31

Figure 2-10 Shear stress versus slip of high performance concrete with varying amounts of steel fiber. C70/00 contains no steel, C70/20 contains 33.7 lb of steel fibers per cubic yard, and C70/40 contains 67.4 lb of steel fibers per cubic yard. Point A denotes first peak. (Barragán, Gettu et al., 2006). 33

Figure 2-11 Setup for interface shear tests conducted by Banta (2005). The normal force (w_n) mimics the dead load on the structure and the P forces create shear across the interface between the two materials. 34

Figure 2-12 Design for composite girder casting and testing performed by Hanson (1960). In the elevation view, the X's indicate slip dial locations and the triangles indicate deflection measurement locations. 37

Figure 2-13 Comparison of push-off and T-beam results by Hanson (1960). 38

Figure 2-14 Typical load deflection curve for a composite beam with smooth interface compared to ACI predicted behavior (Patnaik, 2001). 41

Figure 3-1 Design of monolithically cast specimens using only UHPC. The dot-dashed line indicates the shear plane and where a crack was created on pre-cracked specimens. 1 in.=25.4mm. 53

Figure 3-2 Design of composite push-off specimen. The dot-dashed line indicates the shear plane and the cold joint location. 1 in.=25.4mm. 54

Figure 3-3 Specimen formwork for (a) monolithic pour (b) composite pour. 55

Figure 3-4 Section cut showing loading and position of monolithic specimen during pre-cracking. 57

Figure 3-5 Typical loading and push-off test of a composite specimen. 59

Figure 3-6 Typical load-slip curves for all-UHPC push-off specimens. 62

Figure 3-7 (a) Overall specimen setup, (b) initial cracking of a typical specimen, (c) & (d) crack initiating at an angle of 0° to 30° to shear plane. 63

Figure 3-8 Typical load-slip curves for UHPC/HPC push-off specimens. The curves for the unreinforced specimens had approximately the same slope as that shown for U-H-S-0 with maximum values listed in Table 3-2. 66

Figure 3-9 (a) Specimen after testing, (b) slip at joint visible at reinforcement markings, (c) failed fluted interface. 67

Figure 3-10 Comparison of all-UHPC push-off specimens to ACI shear friction equation, Equation (3-1). 69

Figure 3-11 Comparison of UHPC-HPC push-off specimens to ACI shear friction equation, Equation (3-1). 70

Figure 3-12 Comparison of all-UHPC push-off specimens to AASHTO shear friction equation, Equation (3-2). (1 MPa=145 psi). 71

Figure 3-13 Comparison of all-UHPC push-off specimens to AASHTO shear friction equation, Equation (3-2). (1 MPa=145 psi). 72

Figure 3-14 Linear regression analysis of uncracked monolithic push-off capacities with 90% confidence interval for an individual predicted value. 74

Figure 3-15 Linear regression analysis of precracked monolithic push-off capacities with 90% confidence interval for an individual predicted value. 74

Figure 4-1 Typical T-beam cross section. Note: 1 in = 25.4 mm; No. 3 bar = 10 M; No. 9 bar = 29 M. 85

Figure 4-2 Typical reinforcement for all beams. Note: 1 in = 25.4 mm; No. 3 bar = 10 M; No. 9 bar = 29 M. 85

Figure 4-3 Typical loading test set-up and instrumentation. 88

Figure 4-4 Load-deflection plots for beams with slip and max load denoted. Note: 1 in = 25.4 mm; 1 lb = 4.45 N. 90

Figure 4-5 Moment-curvature plots for beams with theoretical moment-curvature curves plotted. Note: 1 in = 25.4 mm; 1 lb = 4.45 N. 91

Figure 4-6 Comparison of interface shear stress results to predictions using AASHTO LRFD Eq. (4-1). Note: 1 psi = 0.0069 MPa. 95

Figure 4-7 Comparison of interface shear stress results to predictions using ACI Eq. (4-2). Note: 1 psi = 0.0069 MPa. 96

Figure 4-8 Comparison of interface shear results with ACI Shear Friction Eq. (3). Note: 1 psi = 0.0069 MPa. 97

Figure 4-9 Comparison of interface shear stress results to predictions using Loov and Patnaik Eq. (4). Note: 1 psi = 0.0069 MPa. 98

Figure 4-10 Comparison of interface shear results with Kahn and Mitchell Eq. (5). Note: 1 psi = 0.0069 MPa. 99

Figure 4-11 Comparison of interface shear push-off tests and composite small beam tests with ACI interface shear equation (4-2). 101

Figure 4-12 Comparison of interface shear push-off tests and composite small beam tests with AASHTO interface shear equation (4-1). 102

Figure 5-1 Design cross section for Girder 1 and Girder 2. As-built sections shown in Chapter 6. 108

Figure 5-2 Design cross section for Girder 3 (reduced top flange). As-built sections shown in Chapter 6. 109

Figure 5-3 Dimensioned drawing of formliner used in creating fluted UHPC surface. 110

Figure 5-4 Fluted surface of UHPC girder after removal of formliner. 110

Figure 5-5 Girder 1 elevation. 111

Figure 5-6 Girder 2 elevation. 112

Figure 5-7 Girder 3 Elevation. 113

Figure 5-8 Girder 1 and 2 with composite HPC deck. Notice 3/4-in. haunch. 115

Figure 5-9 Girder 3 with composite HPC deck. Notice 3/4-in. haunch. 116

Figure 5-10 Temperature and shrinkage reinforcement for HPC deck on Girder 1. .. 116

Figure 5-11 Elevation view of external instrumentation for flexure testing of Girder 1. (All instrumentation except string potentiometers is mirrored on other side of beam.). 120

Figure 5-12 Beam 1 prior to flexural testing. 121

Figure 5-13 Shear-slip curve for east end of beam. Note the initiation of slip at approximately 35 kips. 121

Figure 5-14 Load-deflection curve for flexural test with linear curve fits before and after deck slip. 122

Figure 5-15 Instrumentation and setup for shear test 1-2. 123

Figure 5-16 Setup for shear test 1-2. 123

Figure 5-17 Load – deflection curve for shear test 2-1. Note the change in slope at a load of 391 kips. 124

Figure 5-18 Shear – slip curve for test 1-2. 124

Figure 5-19 Instrumentation and setup for tests 2-1, 2-2, 3-1, and 3-2. 126

Figure 5-20 Shear – slip curve for shear test 2-1. Note that slip initiated immediately from the time of loading. 127

Figure 5-21 Shear – slip curve for shear test 2-2. Note the initiation of slip at 421 kips of shear force. 127

Figure 5-22 Load- deflection curve for shear test 2-2. Note that slip initiation coincided with a load drop and slope change at a load of 632 kips. 128

Figure 5-23 Shear – slip curve for shear test 3-2, east end of the beam. Slip was determined to initiate at a shear force of 143 kips. 128

Figure 5-24 Shear – slip curve for shear test 3-2, west end of the beam. Slip was determined to initiate at a shear force of 153 kips. 129

Figure 5-25 Load deflection curve for shear test 3-2. 129

Figure 5-26 Comparison of full-scale composite beam shear tests to AASHTO LRFD shear friction provisions. 133

Figure 5-27 Comparison of full-scale composite beam shear tests to ACI shear friction Equation 5-3. 134

Figure 5-28 Results of push-off, small beam, and full-scale beam interface shear tests compared to Equation 5-2. 137

Figure 5-29 Results of push-off, small beam, and full-scale beam interface shear tests compared to Equation 5-3. 138

Figure 5-30 Results of push-off, small beam, and full-scale beam interface shear tests compared to Equations 5-6 and 5-7 proposed by Kahn and Mitchell (2002) and Loov and Patnaik (1994), respectively. 139

Figure 6-1 Cross-section of UHPC beam tested by Hegger et. al. (2004). All units in mm. Note: 1 in = 25.4mm. 145

Figure 6-2 Cross-section of UHPC beam tested by Hegger and Bertram (2008). All prestressing strands were 0.5-in (13 mm) diameter 7-wire strands prestressed to 125kN (556 kips) each. All units in mm. Note: 1 in = 25.4mm. 148

Figure 6-3 Comparison of previous research with current AASHTO (2010) code equations. 149

Figure 6-4 As built cross-section of precast prestressed UHPC girders 1 and 2. See Chapter 5 for design dimensions. 153

Figure 6-5 As built cross-section of precast prestressed UHPC girder 3 (reduced top flange). See Chapter 5 for design dimensions. 154

Figure 6-6 Cross-section of girder 3 with cast-in-place deck. 155

Figure 6-7 Elevation view of experimental setup and instrumentation for shear test 1-1a. 156

Figure 6-8 Shear test 1-1a during testing. 156

Figure 6-9 Load deflection curve for shear test 1-1a. 157

Figure 6-10 Initial shear cracks were first visible at a load of 325 kips (1,450 kN), which corresponded to a shear force of approximately 200 kips (890 kN). 159

Figure 6-11 Principal strains for shear test 1-1a. 159

Figure 6-12 Principal compressive strain angle for shear test 1-1a. 160

Figure 6-13 Stress-strain curve for No. 4 reinforcing bar used in girder stirrups. 161

Figure 6-14 Force in shear stirrup. 161

Figure 6-15 Flexural compression failure resulted in loss of a large piece of the top flange. 162

Figure 6-16 Shear cracks in test 1-1a. 163

Figure 6-17 Elevation view of experimental setup and instrumentation for shear test 1-2. 1-in = 25.4 mm. 164

Figure 6-18 Instrumentation for shear test 1-2. 165

Figure 6-19 Load deflection curve for shear test 1-2. 167

Figure 6-20 Principal strains for shear test 1-2. 167

Figure 6-21 Principal compressive strain angle for shear test 1-2. 168

Figure 6-22 Diagonal tension shear failure of shear test 1-2. 168

Figure 6-23 Experimental setup and instrumentation for shear test 2-1. 170

Figure 6-24 Load-deflection curve for shear test 2-1. 171

Figure 6-25 Principal strains for shear test 2-1. 171

Figure 6-26 Principal compressive strain angle for shear test 2-1. 172

Figure 6-27 Adjusted principal strains for shear test 2-1. 172

Figure 6-28 Adjusted principal compressive strain angle for shear test 2-1. 173

Figure 6-29 Flexural compression failure of shear test 2-1. Note the plate-like morphology of the UHPC failure surface. 174

Figure 6-30 Top flange of girder 2 after shear test 2-1. 174

Figure 6-31 Shear cracks from shear test 2-1. 175

Figure 6-32 Experimental setup and instrumentation for shear test 2-2 and 3-2. East end is to the right of the figure. 177

Figure 6-33 Shear test 2-2 prior to loading. 178

Figure 6-34 Load-deflection curve for shear test 2-2. 178

Figure 6-35 Principal strains for shear test 2-2. The gauges detached at a shear force of 420 kips, but shear failure did not occur until a shear force of 480 kips. 179

Figure 6-36 Principal compressive strain angle for shear test 2-2. The gauges detached at a shear force of 420 kips, but shear failure did not occur until a shear force of 480 kips. 180

Figure 6-37 Diagonal tension shear failure of girder 2 during shear test 2-2. 181

Figure 6-38 Load deflection curve for shear test 3-1. 182

Figure 6-39 Principal strains for shear test 3-1. 183

Figure 6-40 Principal compressive strain angle for shear test 3-1. 183

Figure 6-41 Adjusted principal strains for shear test 3-1. 184

Figure 6-42 Adjusted principal compressive strain angle for shear test 3-1. 184

Figure 6-43 Flexural compression failure of shear test 3-1. 185

Figure 6-44 Shear cracking in test 3-1. 186

Figure 6-45 Load deflection curve for shear test 3-2. Initiation of slip on each end of the beam is marked with a circle. 187

Figure 6-46 Principal strains for shear test 3-2. 188

Figure 6-47 Principal compressive strain angle for shear test 3-2. 189

Figure 6-48 Shear cracking in test 3-2. 189

Figure 6-49 Flexural compression failure of shear test 3-2. 190

Figure 6-50 Observed shear stresses compared to Equation 6-10. 199

Figure 7-1 Girder 2 during shear testing. The undamaged portion at right was cut out for use in fiber alignment study. 205

Figure 7-2 Cutting diagram and specimen numbering for fiber alignment study. ... 206

Figure 7-3 Grinder preparation of UHPC specimens for fiber alignment image analysis. 207

Figure 7-4 Image capture setup for fiber alignment analysis. 207

Figure 7-5 Steps of image analysis in ImageJ software. a) Image capture, b) application of threshold, c) fiber count, and d) analysis of uncounted fibers and combined fibers. 209

Figure 7-6 Variation of orientation coefficient with depth in the z-direction. For 0.25 in through 1 in depths, n=3; for 1.25 in, n=7; and for 1.5 and 1.75 in, n=6. 211

Figure 7-7 Statistical analysis of orientation number versus depth. No significant statistical difference exists based on available data. 211

Figure 7-8 Orientation coefficients of fibers in UHPC beam web in three orthogonal axes. The X, Y, and Z direction averages and standard deviations are based on 16, 15, and 29 observations, respectively. 213

Figure 7-9 Statistical analysis of fiber orientation coefficient. Green diamonds represent 95% confidence intervals, that is, there is a 95% chance that the population mean lies in this range. 213

Figure 7-10 Cylinder end grinding for compression cylinders. 215

Figure 7-11 Compression and modulus of elasticity test setup. 218

Figure 7-12 ANOVA and Tukey test for peak stress compared to direction. 222

Figure 7-13 ANOVA and Tukey test for maximum strain compared to direction. ... 223

Figure 7-14 ANOVA and Tukey test for strain at peak stress compared to direction. 223

Figure 7-15 ANOVA and Tukey test for modulus of elasticity up to 40% of max stress [E40] compared to direction. 224

Figure 7-16 ANOVA and Tukey test for modulus of elasticity up to 90% of max stress [E90] compared to direction. 224

Figure 7-17 ANOVA and Tukey test for modulus of elasticity change [E40-E90] compared to direction. 225

Figure 7-18 Average orientation coefficient versus average compressive strength (load cell) for X, Y, and Z directions. 227

Figure 7-19 Average orientation coefficient versus average maximum strain for X, Y, and Z directions. 227

Figure 7-20 Average orientation coefficient versus average strain at maximum stress for X, Y, and Z directions. 228

Figure 7-21 Average orientation coefficient versus average modulus of elasticity up to 40% of peak stress [E40] for X, Y, and Z directions. 228

Figure 7-22 Average orientation coefficient versus average modulus of elasticity up to 90% of peak stress [E90] for X, Y, and Z directions. 229

Figure 7-23 Average orientation coefficient versus average change in modulus of elasticity [E40-E90] for X, Y, and Z directions. 229

Figure A-1 Load-slip curves for U-H-F-0 specimens 240

Figure A-2 U-H-F-0-A after failure. 241

Figure A-3 UHPC side of failure interface for specimen U-H-F-0-A. Note shear failure through HPC "shear keys" created by fluted interface. 241

Figure A-4 Close-up of interface failure of specimen U-H-F-0-A. 242

Figure A-5 U-H-F-0-B after failure. 242

Figure A-6 HPC side of interface failure surface of specimen U-H-F-0-B. Notice the failure occurred almost totally through the HPC rather than the UHPC. 243

Figure A-7 Load-slip curves for U-H-F-2 specimens 243

Figure A-8 U-H-F-2-A after failure. 244

Figure A-9 Interface crack in specimen U-H-F-2-A. Notice differential slip between halves at rebar indicator line. 244

Figure A-10 U-H-F-2-B after failure. This specimen was taken past maximum load to emphasize the crack and to show the post-peak behavior. 245

Figure A-11 Reverse side of specimen U-H-F-2-B. Spalling was observed in the HPC above the stirrup locations. 245

Figure A-12 Close-up of spalling cracks in specimen U-H-F-2-B. 246

Figure A-13 U-H-F-2-C after failure. 246

Figure A-14 Close-up of interface crack in specimen U-H-F-2-C. 247

Figure A-15 Load-slip curves for U-H-S-0 specimens 247

Figure A-16 U-H-S-0-A after failure. 248

Figure A-17 Smooth UHPC surface of specimen U-H-S-0-A after interface failure. . 248
Figure A-18 U-H-S-0-B after failure. 249
Figure A-19 Interface surfaces of specimen U-H-S-0-B. 249
Figure A-20 U-H-S-0-C after failure. 250
Figure A-21 UHPC failure surface of specimen U-H-S-0-C. Minor cracking of the surface UHPC can be seen at the left. 250
Figure A-22 Load-slip curves for U-H-S-1 specimens 251
Figure A-23 U-H-S-1-A after failure. 251
Figure A-24 Close-up of interface crack in specimen U-H-S-1-A. 252
Figure A-25 U-H-S-1-B after failure. 252
Figure A-26 Interface crack in specimen U-H-S-1-B. 253
Figure A-27 U-H-S-1-C after failure. 253
Figure A-28 Load-slip curves for U-H-S-2 specimens 254
Figure A-29 U-H-S-2-A after failure. 254
Figure A-30 Interface crack in specimen U-H-S-2-A. 255
Figure A-31 Spalling of HPC over rebar locations in specimen U-H-S-2-A. 255
Figure A-32 U-H-S-2-B after failure. 256
Figure A-33 Spalling of HPC over rebar locations in specimen U-H-S-2-B. 256
Figure A-34 Interface surfaces of specimen U-H-S-2-B after failure. 257
Figure A-35 U-H-S-2-C after failure. 257
Figure A-36 Interface crack in specimen U-H-S-2-C. 258
Figure A-37 Spalling of HPC over stirrup in specimen U-H-S-2-C. 258
Figure A-38 Load-slip curves for U-H-S-3 specimens 259
Figure A-39 U-H-S-3-A after failure. 259
Figure A-40 Interface crack in specimen U-H-S-3-A. 260
Figure A-41 U-H-S-3-B after failure. 260

Figure A-42 Interface crack in specimen U-H-S-3-B. 261
Figure A-43 U-H-S-3-C after failure. 261
Figure A-44 Interface crack in specimen U-H-S-3-C. 262
Figure A-45 Load-slip curves for U-H-B-0 specimens 262
Figure A-46 U-H-B-0-A after failure. 263
Figure A-47 Interface surfaces of specimen U-H-B-0-A. 263
Figure A-48 U-H-B-0-B after failure. 264
Figure A-49 Interface surfaces of specimen U-H-B-0-B. 264
Figure A-50 U-H-B-0-C after failure. 265
Figure A-51 Interface surfaces of specimen U-H-B-0-C. 265
Figure A-52 Load-slip curves for U-U-S-0 specimens 266
Figure A-53 Load-slip curves for U-U-S-2 specimens 266
Figure A-54 Load-slip curves for U-U-MC-0 specimens 267
Figure A-55 U-U-MC-0-A after failure. 267
Figure A-56 Failure crack in specimen U-U-MC-0-A. 268
Figure A-57 U-U-MC-0-B after failure. 268
Figure A-58 Failure crack in specimen U-U-MC-0-B. 269
Figure A-59 U-U-MC-0-C after failure. 269
Figure A-60 Failure crack in specimen U-U-MC-0-C. 270
Figure A-61 Load-slip curves for U-U-MC-2 specimens 270
Figure A-62 U-U-MC-2-A after failure. 271
Figure A-63 Interface crack slip in specimen U-U-MC-2-A 271
Figure A-64 U-U-MC-2-B after failure. 272
Figure A-65 Slip along pre-induced crack in specimen U-U-MC-2-B 272
Figure A-66 U-U-MC-2-C after failure. 273

Figure A-67 Separation across pre-existing interface crack in specimen U-U-MC-2-C. 273

Figure A-68 Load-slip curves for U-U-UC-0 specimens. Specimen C had to be loaded twice. 274

Figure A-69 U-U-UC-0-A after failure. 274

Figure A-70 Reverse side of U-U-UC-0-A after failure. 275

Figure A-71 Halves of specimen U-U-UC-0-A. 275

Figure A-72 Close-up of failure surface of specimen U-U-UC-0-A. 276

Figure A-73 U-U-UC-0-B after failure. 276

Figure A-74 Reverse side of specimen U-U-UC-0-B after failure. 277

Figure A-75 Halves of specimen U-U-UC-0-B. Note failure along rebar interface. 277

Figure A-76 U-U-UC-0-C after failure. 278

Figure A-77 Reverse side of specimen U-U-UC-0-C after failure. Note two failure cracks. 278

Figure A-78 Load-slip curves for U-U-UC-2 specimens. 279

Figure A-79 U-U-UC-2-A after failure. 279

Figure A-80 Reverse side of specimen U-U-UC-2-A after failure. 280

Figure A-81 Close-up of failure surface of specimen U-U-UC-2-A. 280

Figure A-82 U-U-UC-2-B after failure. 281

Figure A-83 Failure surfaces of specimen U-U-UC-2-B 281

Figure A-84 U-U-UC-2-C after failure. 282

Figure A-85 Separation of steel wide flange from specimen U-U-UC-2-C. Note weld failures. 282

Figure B-1 Shear test 1-1a rosette strains. 283

Figure B-2 Shear test 1-2 rosette strains. 284

Figure B-3 Shear test 2-1 rosette strains. 285

Figure B-4 Shear test 2-1 adjusted rosette strains. 286

Figure B-5 Shear test 2-2 rosette strains. 287

Figure B-6 Shear test 3-1 rosette strains. 288

Figure B-7 Shear test 3-1 adjusted rosette strains. 289

Figure B-8 Shear test 3-2 rosette strains. 290

Figure C-1 Load-slip curves for left and right sides of beam 0-B 291

Figure C-2 Linear curve fit of initial portion of load-deflection curve for beam 0-B. 292

Figure C-3 Load-slip curves for left and right sides of beam 4-S. Right slip gauge experienced very high amounts of noise. 292

Figure C-4 Linear curve fit of initial portion of load-deflection curve for beam 4-S. 293

Figure C-5 Load-slip curves for left side of beam 7-S. Right slip gauge data was not useable. 293

Figure C-6 Linear curve fit of initial portion of load-deflection curve for beam 7-S. 294

Figure C-7 Load-slip curves for left and right sides of beam 0-FL 294

Figure C-8 Linear curve fit of initial portion of load-deflection curve for beam 0-FL. 295

Figure C-9 Load-slip curves for left and right sides of beam 7-FL. 295

Figure C-10 Linear curve fit of initial portion of load-deflection curve for beam 7-FL. 296

Figure C-11 Linear curve fit of initial portion of load-deflection curve for plain beam. 296

Figure D-1 Internal gauge locations in UHPC girders. 298

Figure D-2 Placement of internal gauges in UHPC girders. 298

Figure D-3 Thermocouple placement prior to casting of UHPC girders. 299

Figure D-4 Close-up of VWSG placement at bottom of UHPC girder. 299

Figure D-5 DEMEC gauge and gauge points in bottom flange of UHPC girder. 300

Figure D-6 Longitudinal LVDTs used for measuring strain profiles in full-scale girders during flexural and shear testing. 301

Figure D-7 Slip LVDT during full-scale girder testing. 302

Figure D-8 String potentiometer for measuring deflection during full-scale girder testing. 304

Figure D-9 Figure D-9: Load cell setup for tests 1-1 and 1-1a. 305

Figure D-10 Load cell setup for tests 1-2, 2-1, 2-2, 3-1, and 3-2. 305

Figure D-11 Temperature variations during thermal curing of UHPC girders. 306

Figure D-12 UHPC compressive strength gain. 307

Figure D-13 Creep and Shrinkage Strain of UHPC Beams (extrapolated linearly to time=0 from time=0.32) 309

Figure D-14 Typical transfer length plot. Transfer length was determined to be the point at which the smoothed data line crossed 95% of the plateau value. 310

Figure D-15 Longitudinal strains at center span in test 1-1. All gauge locations are measured from the bottom of the girder. 311

Figure D-16 Longitudinal strains at load location in test 1-1a. All gauge locations are measured from the bottom of the girder. 312

Figure D-17 Longitudinal strains at load location in test 1-2. All gauge locations are measured from the bottom of the girder. 313

Figure D-18 Longitudinal strains at load location in test 2-1. All gauge locations are measured from the bottom of the girder. 314

Figure D-19 Longitudinal strains at load location in test 2-2. All gauge locations are measured from the bottom of the girder. 315

Figure D-20 Longitudinal strains at load location in test 3-1. All gauge locations are measured from the bottom of the girder. 316

Figure D-21 Longitudinal strains at load location in test 3-2. All gauge locations are measured from the bottom of the girder. 317

NOTATION

A = surface roughness constant from Hanson (1960) (300 psi for smooth, 500 psi for rough)

A_c = area of concrete contact across interface

A_{cv} = area of concrete considered to be engaged in interface shear transfer ($b_{vi}d_v$)

A_i = interface area

A_s = area of steel across the interface

A_v = area of interface shear reinforcement crossing the shear plane within the area A_{cv}

A_v = area of transverse reinforcement within distance s

A_{vf} = area of steel across the interface

b = width of cross section parallel to axis of bending at point of interest for shear stress calculation

b_0 = minimum width of web carrying shear (b_v) from French code

b_v = interface width considered to be engaged in shear transfer

b_v = width of web adjusted for the presence of ducts (not to be confused with interface width which is also denoted by b_v in AASHTO)

b_{vi} = interface width considered to be engaged in shear transfer

c = cohesion factor

d = distance from top of slab to centroid of bottom tensile reinforcement, in. (ACI 2008).

d_e = distance from centroid of steel to extreme compression fiber.

d_v = the distance between the centroid of the tension steel and the mid-thickness of the slab to compute a factored interface shear stress (AASHTO 2010)

d_v = effective shear depth, not to be taken as less than the greater of *0.72h* or *0.9*d_e

f'_c = specified compressive strength of concrete

f_{cj} = concrete compressive strength (f'_c) from French code

f_{ct} = tensile cracking strength

f_{pc} = the compressive stress of the concrete at the centroid of the cross-section resisting external loads or at the junction of web and flange when the centroid lies within the flange.

f_{rr} = the rupture residual stress, taken as the average tensile stress carried between first cracking and a strain of 0.003 in tension.

f_t = the tensile strength of concrete

f_y = yield strength of steel

h = depth of girder and deck (when present)

I = moment of inertia

k = constant for interface shear calculation (Loov and Patnaik1994)

K_1 = concrete cohesion term that is related to strength (Mattock 2001, AASHTO 2010)

K_2 = portion of concrete strength available to resist shear (Mattock 2001, AASHTO 2010)

K_3 = maximum interface shear capacity (Mattock 2001)

P = interface reinforcement ratio (Saemann and Washa 1964)

P_c = permanent net compressive force normal to the shear plane

Q = first moment of the area above the point of interest for shear stress calculation

s = spacing of transverse reinforcement

S = the effective shear area ($b_v d_v$) from French code

T = tension force in steel

v = shear stress

V = shear force

V_c = portion of shear resistance provided by concrete

V_n = nominal shear resistance

V_{ni} = nominal interface shear resistance

V_p = portion of the prestressing force resisting shear.

V_{Rb} = concrete contribution to shear capacity in French code

V_s = portion of shear resistance provided by steel reinforcement

V_u = ultimate shear capacity

X = shear span to depth ratio (Saemann and Washa 1964)

Y = shear stress, psi (Saemann and Washa 1964)

z = shear depth (d_v) from French code

μ = coefficient of friction

β = factor indicating ability of diagonally cracked concrete to transmit tension and shear

β_u = angle of maximum compressive stress measured from longitudinal axis from French code

γ = engineering shear strain

ε_s = the net longitudinal tensile strain in the section at the centroid of the tension reinforcement

θ = angle of inclination of diagonal compressive stresses.

λ = adjustment factor for lightweight concrete

λ = correction factor related to concrete density (Loov and Patnaik 1994)

ρ = reinforcement ratio

ρ_v = interface shear reinforcement ratio

ρ_{vf} = interface shear reinforcement ratio

σ_{Nx} = concrete cohesion term suggested by Mattock and Hawkins (1972)

σ_p = average tensile stress carried by fibers after cracking until a limiting strain of 0.003 from French code

σ_x = stress in the x direction

τ = engineering shear stress

φ = angle of roughness in shear friction theory

φ = resistance factor

SUMMARY

Ultra-High Performance Concrete (UHPC) is a new class of concrete characterized by no coarse aggregate, steel fiber reinforcement, low w/c, low permeability, compressive strength exceeding 29,000 psi (200 MPa), tensile strength ranging from 1,200 to 2,500 psi (8 to 17 MPa), and very high toughness. These properties make prestressed precast UHPC bridge girders a very attractive replacement material for steel bridge girders, particularly when site demands require a comparable beam depth to steel and a 100+ year life span is desired.

In order to efficiently utilize UHPC in bridge construction, it is necessary to create new design recommendations for its use. The interface between precast UHPC girder and cast-in-place concrete decks must be characterized in order to safely use composite design methods with this new material.

Due to the lack of reinforcing bars, all shear forces in UHPC girders have to be carried by the concrete and steel fibers. Current U.S. codes do not consider fiber reinforcement in calculating shear capacity. Fiber contribution must be accurately accounted for in shear equations in order to use UHPC.

Casting of UHPC may cause fibers to orient in the direction of casting. If fibers are preferentially oriented, physical properties of the concrete may also become anisotropic, which must be considered in design.

The current research provides new understanding of shear and shear friction phenomena in UHPC including:

- Current AASHTO codes provide a non-conservative estimate of interface shear performance of smooth UHPC interfaces with and without interface steel.
- Fluted interfaces can be created by impressing formliners into the surface of plastic UHPC. AASHTO and ACI codes for roughened interfaces are conservative for design of fluted UHPC interfaces.
- A new equation for the calculation of shear capacity of UHPC girders is presented which takes into account the contribution of steel fiber reinforcement.
- Fibers are shown to preferentially align in the direction of casting, which significantly affects compressive behavior of the UHPC.

CHAPTER 1
INTRODUCTION

1.1 Purpose and Objectives

The overall purpose of this research was to determine if UHPC can effectively be used for precast, prestressed bridge girders. Specifically, the main objectives of this research were:

1. To use shear-friction push-off specimens to quantify the shear capacity of monolithic UHPC as well as UHPC with cold-joints and pre-existing cracks. The contribution of steel fibers and shear stirrups to shear capacity were studied.
2. To quantify the diagonal tension shear capacity of UHPC bridge girders and how it was affected by varying amounts of shear reinforcement. These results were compared to the monolithic UHPC push-off tests to see how fibers and reinforcing steel contribute to carrying shear across diagonal shear cracks in UHPC.
3. To use shear friction push-off specimens made from HPC cast against UHPC in order to simulate the connection between girder and deck. The effects of varying surface preparations and amounts of steel on interface shear capacity were studied.
4. To compare the interface shear capacity of the UHPC-HPC push-off specimens with composite T-beams. These T-beams were much easier to construct, analyze, and test than full-scale girders, so they provided a convenient middle scale between push-off tests and full-scale prestressed girders.

5. To quantify the shear capacity of the interface between a precast UHPC bridge girder and a cast-in-place HPC bridge deck. Specifically, the effects of the amount of steel crossing the interface and the surface preparation of the UHPC were studied.
6. To determine the extent of preferential alignment of fibers in precast UHPC beams. This fiber orientation was then correlated to maximum compressive stress, maximum compressive strain, and modulus of elasticity.

1.2 Motivation

The Federal Highway Administration along with many state Departments of Transportation are looking to create bridges with 100-year lifespans and minimal need for maintenance. Existing steel bridges are expensive to maintain, so many are being replaced by prestressed concrete. When looking to replace steel bridge girders with girders of approximately equivalent capacity, depth, and weight, UHPC is one of the only options currently available. Highly optimized beam cross-sections have been created for use of this material, but their construction requires sophisticated formwork that is both expensive to manufacture and more difficult to use than formwork for traditional I-shaped girders.

1.2.1 Shear Friction

Currently, bridges constructed from precast prestressed I-girders usually rely on composite action with a cast-in-place concrete deck for carrying live loads. This connection has been created by two means: 1) roughening of the girder surface to 1/4

inch amplitude by raking, and 2) extending shear reinforcement from the girder into the deck. The self-consolidating nature of UHPC prevents the surface from being roughened by raking. Also, based on previous research, UHPC does not require shear stirrups to resist shear forces because of the steel fibers in the concrete (Graybeal, 2006; Garas, 2009). In light of these differences, the effects of varying surface preparations and transverse reinforcement on interface shear capacity of UHPC must be evaluated. Current codes based on shear friction must be validated for use with this new material.

1.2.2 Diagonal Tension Shear

Diagonal tension shear capacity of UHPC girders must also be evaluated in order to safely design with UHPC. Due to the lack of passive steel reinforcement, all shear forces in the UHPC girder have to be carried by the concrete and steel fibers. Current U.S. codes do not consider fiber reinforcement in calculating shear capacity. The diagonal tension shear performance will validate the manufacturer's claim that no shear reinforcement is necessary in UHPC bridge girders. Few tests have been performed on the shear performance of UHPC bridge girders and none on interface shear across the bonded connection between a precast UHPC section and poured-in-place high performance or ultra high performance concrete. In order to make a comprehensive design code for the use of UHPC in shear, more tests must be performed to better characterize and quantify the mechanics of failure. Specifically, it is important to determine how concrete strength, fiber reinforcement, and conventional stirrups interact in carrying shear stresses in UHPC.

1.3 Research Methodology

A multi-scale research approach is used to experimentally investigate interface shear and diagonal tension shear in composite UHPC bridge girders. The goal of this approach is to provide a thorough understanding of shear in composite UHPC bridge girders and to correlate the results of full-scale tests to results of smaller tests. Once this is accomplished, smaller tests can be accurately used to predict structural behavior of full-scale designs. The full-scale composite girders used for these tests had interface lengths over 28 feet. The medium scale T-beams had interfaces that were approximately 10 feet in length. The push-off specimens had interfaces that were 1 foot in length. Figure 1-1 shows a graphical representation of this multiscale approach.

Push-off tests were used to compare shear friction results of UHPC with those for normal and high-strength concrete. They were also used to better understand the shear transferred across a pre-existing crack in monolithic UHPC. No push-off shear testing has been done to date examining the interface shear capacity of monolithic UHPC with or without a pre-existing crack. These tests seek to test the effect of aggregate interlock and steel fiber reinforcement on shear friction behavior.

Composite beam tests were used to examine the interface shear friction capacity of HPC cast against UHPC under bending, similar to what would be experienced in the field. To date, no composite tests have been performed with UHPC, so little is known about the interface shear performance of these beams.

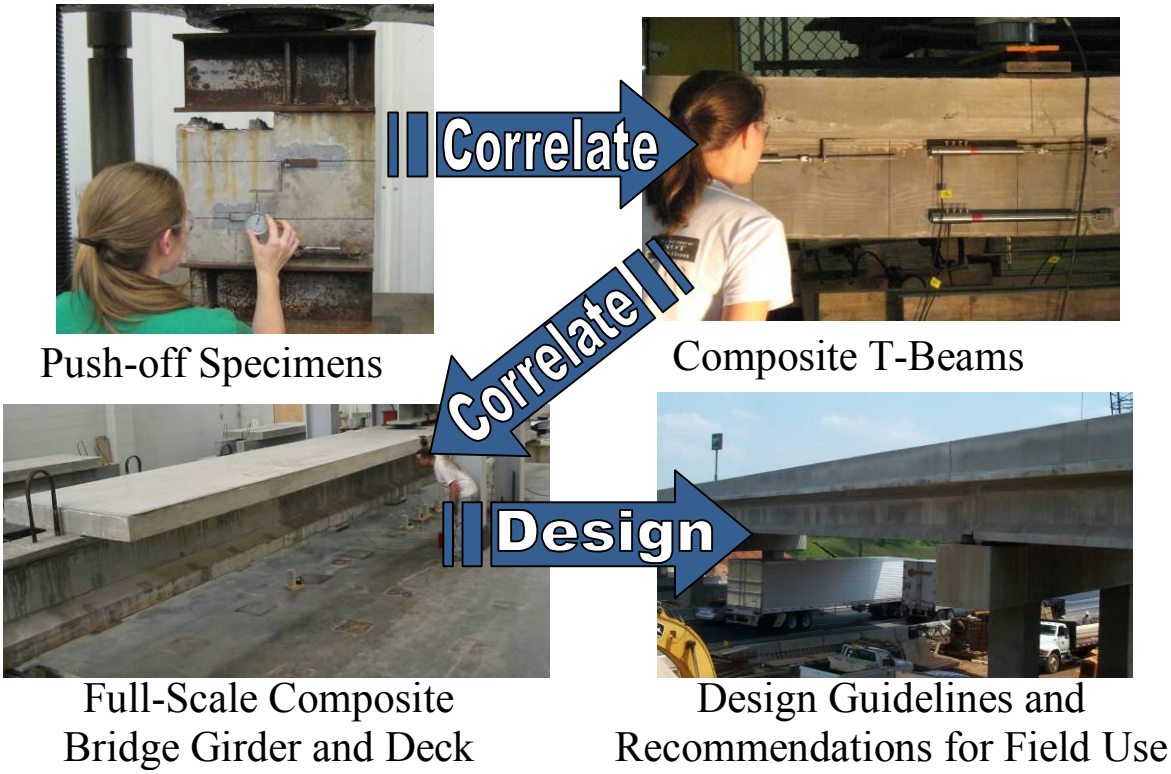

Figure 1-1: Schematic overview of research approach.

At each of these scales, the effects of interface preparation or shear plane condition and reinforcement ratio were evaluated. Figure 1-2 shows an overview of specimens used in the current multi-scale research. Figure 1-3 shows a similar overview for diagonal tension shear.

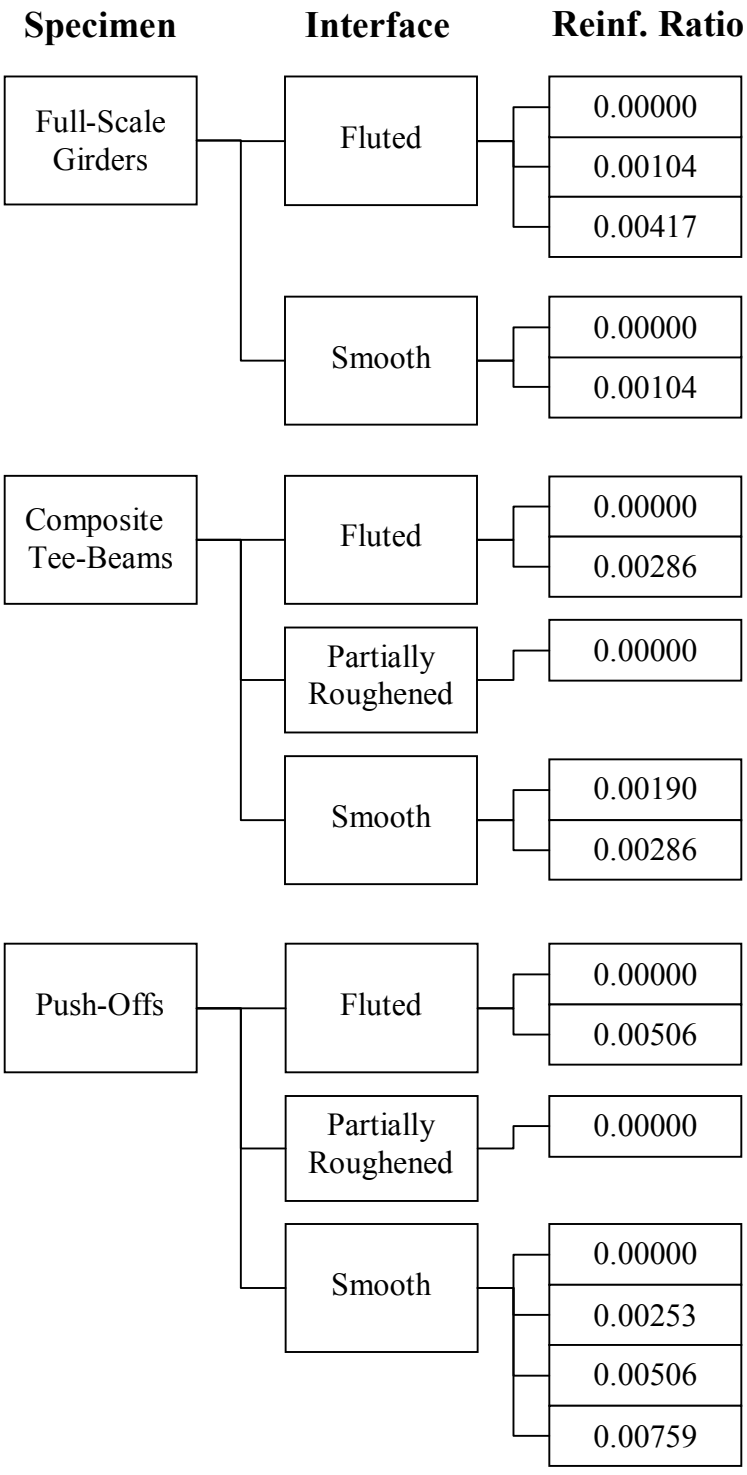

Figure 1-2: Overview of specimens used in multi-scale interface shear tests.

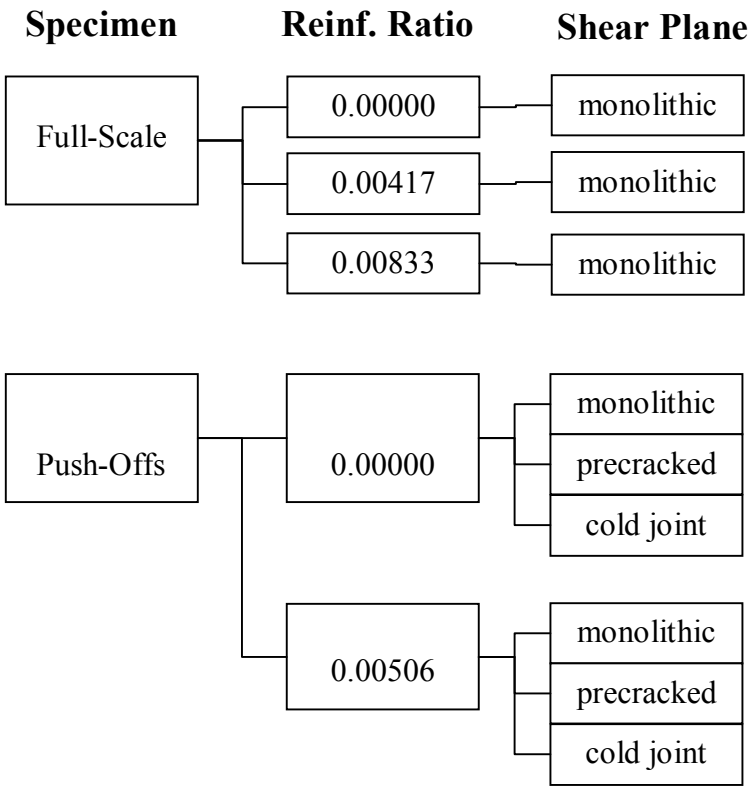

Figure 1-3: Overview of specimens used in multi-scale diagonal tension shear tests.

1.4 Thesis Organization

The research introduced and motivated in this chapter is fully detailed in the following chapters.

Chapter 2 presents the background literature applicable to the analysis and design of precast prestressed UHPC bridge girders with compositely cast reinforced concrete decks. Particular emphasis is placed on the behavior of interfaces between compositely cast concretes and diagonal tension shear in concrete structures.

Chapter 3 presents the results of 38 shear friction push-off tests. Twenty of these tests evaluate the interface shear capacity between precast UHPC and cast-in-place HPC.

Eighteen evaluate the how cracking and cold-joints affect the shear capacity of a defined shear plane in monolithic UHPC.

Chapter 4 presents the results of flexure tests performed on six 10-ft.-long conventionally reinforced UHPC beams with cast-in-place HPC decks. The effect of interface preparation and interface reinforcement ratio on interface shear capacity was studied.

Chapter 5 presents the interface shear results from six full-scale prestressed precast UHPC bridge girder tests. The interface preparation and reinforcement ratio were again varied to study their effect on interface shear capacity.

Chapter 6 presents the diagonal tension shear results of six full-scale prestressed precast UHPC bridge girder tests. The shear reinforcement ratio was varied to study the effect of passive shear reinforcement on the diagonal tension shear capacity of UHPC members.

Chapter 7 presents the results of the effect of fiber alignment on compressive strength of UHPC cores. Fiber alignment in triaxial cores from the webs of the full-scale precast prestressed bridge girders was studied and correlated to compressive strength in those three directions.

Chapter 8 gives conclusions from the current research, recommendations for design, and suggested areas for further research.

Chapters 3-7 are written as journal-style articles and are meant to be stand-alone documents related to one another by the common UHPC research program.

1.5 References

Garas, V. Y. (2009). Multi-Scale Investigation of Tensile Creep of Ultra-High Performance Concrete for Bridge Applications. *Civil and Environmental Engineering*. Atlanta, GA, Georgia Institute of Technology. Ph.D.

Graybeal, B. A. (2006). Structural Behavior of Ultra-high Performance Concrete Prestressed I-Girders. F. H. Administration. Mclean, VA, U.S. Department of Transportation.

CHAPTER 2
BACKGROUND

2.1 Material Characterization of Ultra-High Performance Concrete

Ultra High Performance Concretes (UHPCs), sometimes referred to as Reactive Powder Concretes (RPCs), comprise a class of concretes with compressive strengths above 22 ksi (150 MPa) made by elimination of large aggregate and refinement of the concrete microstructure (Shah and Weiss, 1998). These materials are designed using particle-packing models to densify the material microstructure leading to low porosities and high strengths (Delarrard and Sedran, 1994).

Currently, the only UHPC widely available in North America is Ductal® by Lafarge, Inc. (Graybeal, 2004). As part of the Federal Highway Administration's research in UHPC, extensive material property tests of this material have been performed in the general areas of strength, durability, and long-term stability (Graybeal, 2006). The research showed very high compressive strengths of 28.9 ksi (199 MPa) for UHPC thermally treated at 195°F (90°C) for 48 hours immediately following demolding as specified by Lafarge. The modulus of elasticity of the thermally treated material was 7600 ksi (52.5 GPa). Tensile strengths ranged from 1.2-1.7 ksi (8.3-11.7 MPa) for thermally treated UHPC. The variation in observed tensile strength was due to different tensile testing procedures.

Graybeal showed the compressive and tensile strengths as well as the modulus of the material to be highly dependent on the curing method (2006). For example, when no thermal curing was used, 28 day compressive strength was only 17.2 ksi (119 MPa).

When thermal treatment was delayed until 28 days after casting, the 30 day compressive strength was 24.7 ksi (170 MPa). When thermal treatment was performed at 140°F (60°C) for 72 hours, the 28 day compressive strength was 21.3 ksi (147 MPa). These compressive strengths are 15-40% lower than that seen when the recommended curing procedure was followed. Modulus decreased by 2-19% when the recommended procedure was not used. Tensile capacity decreased by up to 30% when no thermal treatment was used, but did not appear to be affected by type of thermal treatment.

Victor Garas (2009) details short and long-term compressive and tensile properties of UHPC.

2.2 Shear Friction

Very limited shear-friction or interface shear testing has been performed on UHPC (Banta, 2005), and no tests of this kind have been performed on UHPC beams or girders. No push-off shear testing has been done to date examining the interface shear capacity of monolithic UHPC with or without a pre-existing crack. Also no research has been done on interface shear capacity between cast-in-place normal strength, high-strength, or ultra-high strength concrete and precast UHPC. Further, no composite beams UHPC beams have been tested. The effects of reinforcement ratio, interface area, and surface preparation must be evaluated for each of these cases to have a complete understanding of interface shear in UHPC structures.

Two main types of interface shear tests were developed by Hanson (1960) for his research on composite action of precast prestressed bridge girders with cast-in-place decks performed for the Portland Cement Association. Since then, different forms of

these same tests have continued to be the basis for the majority of shear friction research. Push-off tests directly measure the shear capacity of an interface between two concretes by creating a shear force between two compositely or monolithically cast concrete blocks. Tests of composite beams create shear across the cold-joint interface between a precast beam and cast-in-place deck by bending the composite beam in flexure.

2.2.1 Push-off Tests

The original specimens (Figure 2-1) used for interface shear push-off tests were designed by Hanson and had interface areas varying from 48 to 192 in^2 (Hanson, 1960). The width of interface in shear was held constant at 8 in. and the length was varied between 6, 12, or 24 in. The amount of steel crossing the interface was varied between reinforcement ratios of .002 and .008. Both smooth and roughened surface preparations were investigated in both bonded and unbounded setups. In the unbounded setups, a silicone compound was applied to the surface of the girder prior to casting of the slab. Various means of removing surface paste and the use of shear keys were also evaluated in some specimens.

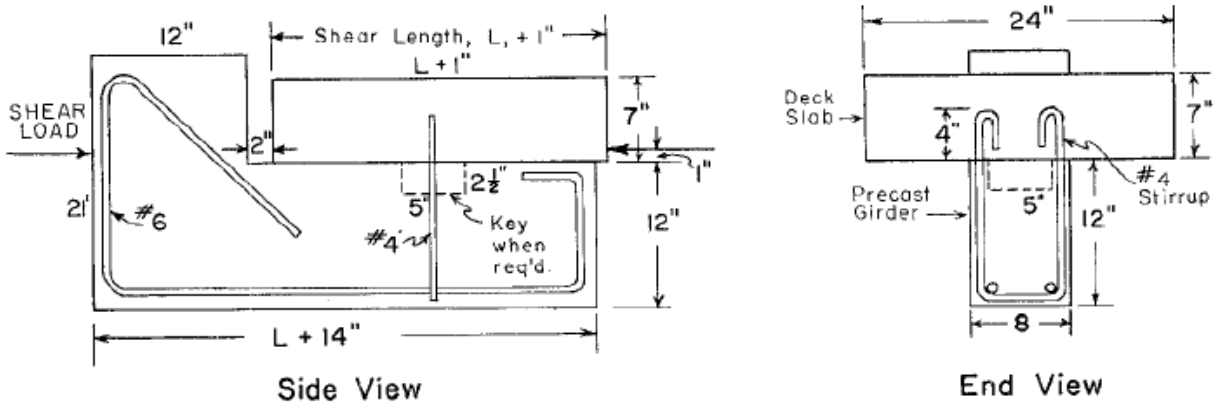

Figure 2-1: The push-off specimens used by Hanson (1960) varied the interface area between 48 and 192 in^2. The reinforcement ratios varied between 0.002 and 0.008.

Figure 2-2 shows the typical stress-slip curves observed by Hanson (1960) for various types of interfaces. In reporting the interface shear capacity of the push-off tests, the contribution of the steel stirrups was removed by subtracting a reference curve with the same amount of stirrups and a smooth unbounded interface from each experimental data set. This method was utilized in order to be able to compare data sets more directly; however, by subtracting the steel contribution, it was implicitly assumed that there were no linked effects of reinforcement and surface preparation. This assumption has been challenged by most researchers and a linked effect between surface preparation and reinforcement ratio is considered by both current ACI and AASHTO codes.

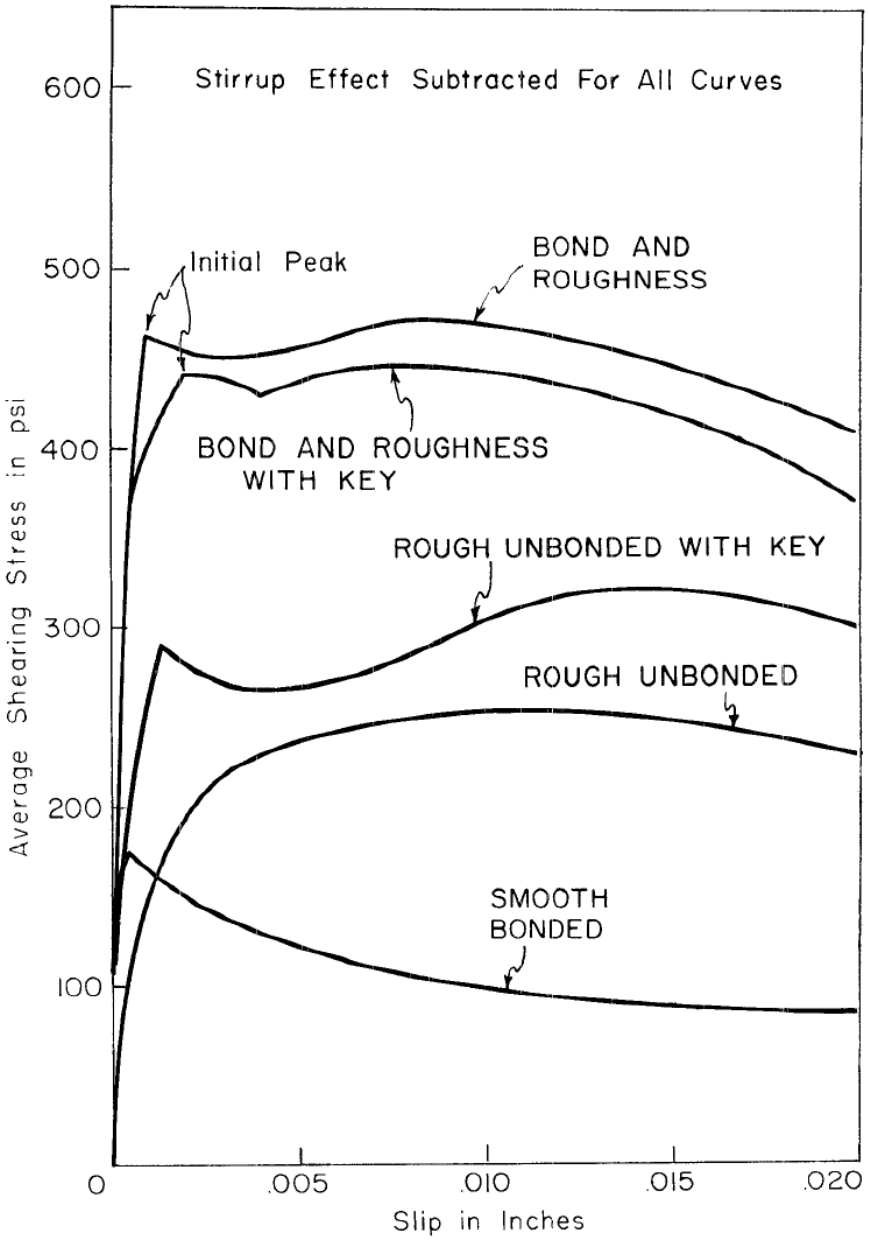

Figure 2-2: Typical stress-slip curves for push-off tests by Hanson (1960). Note that the effect of stirrups has been removed from these curves.

Based on his work, Hanson proposed a preliminary equation of the form:

$$v = A + 17500\rho \text{ (psi)} \tag{2-1}$$

where A is a constant based on surface roughness (300 psi for smooth, 500 psi for rough) and ρ is the shear reinforcement ratio across the interface. It should be noted that this

equation was not presented as a suggested design equation, but rather as an observation. Hanson further concluded that roughened bonded contact surfaces were the only advisable interface between precast beams and cast-in-place slabs.

Anderson (1960) performed similar tests on a slightly different specimen shape as shown in Figure 2-3. The advantage of this test shape is that it allows for the shear loads to be applied directly opposite one another, eliminating any moment due to load eccentricity. The interface area for all of these tests was100 in^2. These tests varied the reinforcement ratio across the interface between 0.002 and 0.0248. The effect of concrete strength was also evaluated. For the precast side of the push-off, the concrete strength was 7,500 psi for all specimens. For the cast-in-place portion of specimens, the concrete strength was either 3,000 psi or 7,500 psi. The precast surface of each push-off specimen was roughened prior to setting. Immediately before casting of the other half of the specimen, the roughened surface was coated with a neat cement slurry.

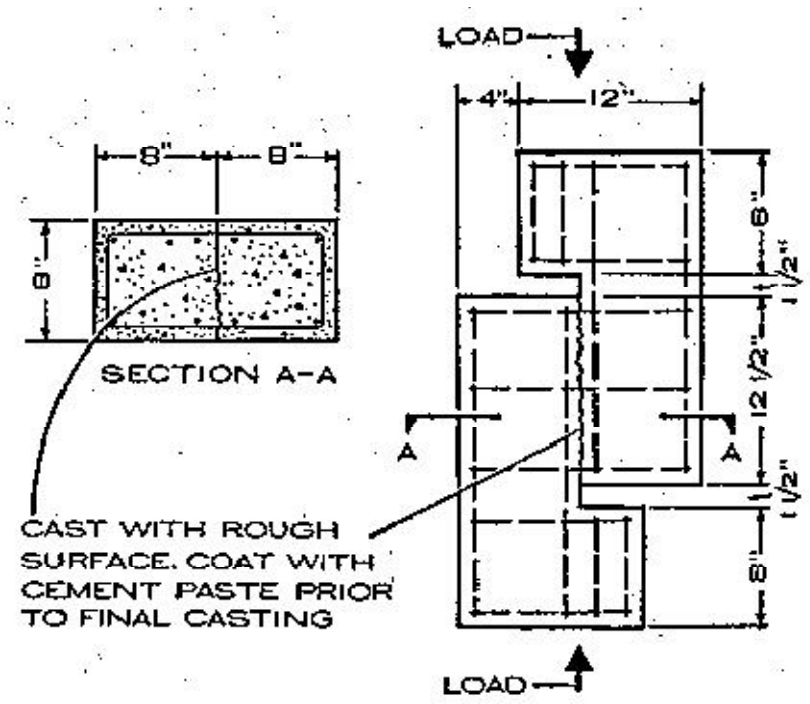

Figure 2-3: The push-off specimen used by Anderson (1960) had a 100 in^2 interface area and varied the reinforcing ratio between 0.002 and 0.0248.

The results of Anderson's tests are shown in Figure 2-4. Two clear trends can be seen from this data. As the concrete strength of the weaker concrete (in this case the cast-in-place concrete) increases, the interface shear capacity increases. Also, as the reinforcement ratio increases, the interface shear capacity increases. The trend lines provided by Anderson for 3000 psi concrete and 7500 psi concrete are approximately

$$v = 650 + 34{,}000\rho \text{ (psi)} \tag{2-2}$$

and

$$v = 800 + 41{,}000\rho \text{ (psi)} \tag{2-3}$$

respectively. These equations cannot be directly compared to Equation 2-1 because Hanson's data attempted to remove the effect of steel.

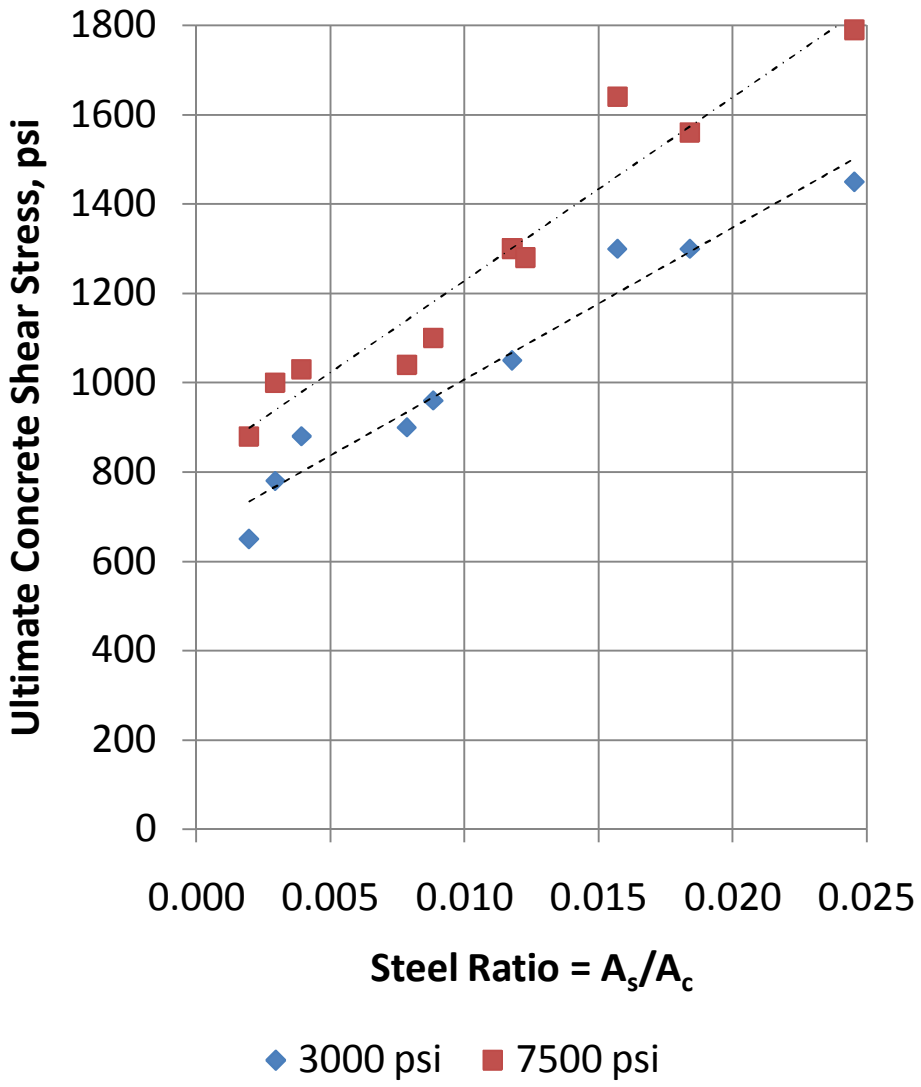

Figure 2-4: Push-off results from Anderson (1960) compare steel ratio to the ultimate interface shear stress in the concrete. Two different concrete strengths were used for the cast-in-place portion of specimens.

Birkeland and Birkeland proposed a shear friction hypothesis for explaining the mechanics of interface shear transfer (Birkeland and Birkeland, 1966). This theory views interface shear resistance as being provided by friction across a roughened surface. The friction force is therefore the product of the normal clamping force across the interface

and the tangent of the contact angle across the surface. This idea is depicted visually in Figure 2-5.

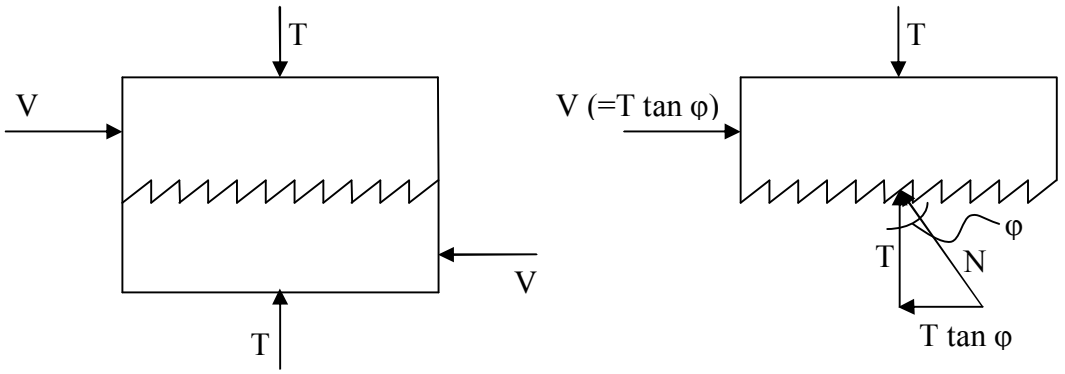

Figure 2-5: Shear friction hypothesis (Birkeland and Birkeland, 1966)

In the equation

$$V = T\tan\phi, \tag{2-4}$$

the force, T, is the force provided by the steel reinforcement crossing the interface, $A_s f_y$. The term, tan φ, can be thought of as the coefficient of friction, μ. This gives the shear friction equation as

$$V_n = \mu A_s f_y, \text{ or} \tag{2-5}$$

$$v_n = \mu \rho_s f_y. \tag{2-6}$$

This is the basic form of the equation currently used by both ACI 318 (2008) and AASHTO LRFD (2010) The friction factor, μ, varies depending on the surface preparation of the interface between the two concretes. Birkeland and Birkeland (1966) suggested values of 1.7, 1.4, and 0.8-1.0 for monolithic concrete, intentionally roughened construction joints, and smooth construction joints respectively.

The shear friction equation was validated by comparison to the work of both Hanson and Anderson (Hanson, 1960; Anderson, 1960; Birkeland and Birkeland, 1966). In order to compare these data sets, Birkeland and Birkeland added the steel effect into Hanson's data. Figure 2-6 shows these data plotted along with the values predicted by the shear friction equation. Based on unpublished tests by Mast, an upper bound of 800 psi was suggested when the shear friction equation was used.

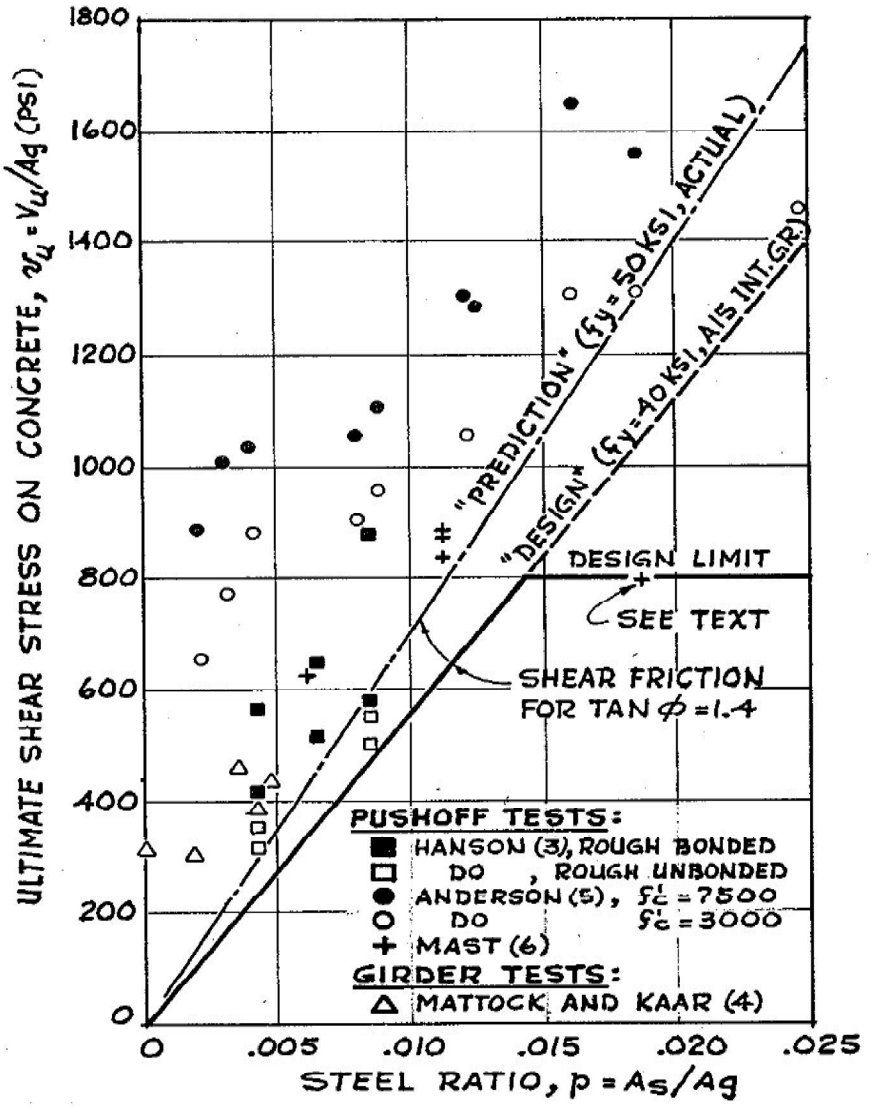

Figure 2-6: Shear friction equation compared to experimental data for push-off tests and girder tests from Birkeland and Birkeland (1966).

Mast (1968) expanded the use of the shear friction equation from existing interfaces to potential cracks. Using this design method, a notional crack is assumed at a given location and the reinforcement is design across that interface using shear friction. This process allows for safe design even when unplanned cracks are present. The values of tan φ suggested by Mast are 1.4, across a crack in monolithic concrete, 1.4 across roughened interfaces, and 0.7 across smooth interfaces.

Mast (1968) also suggested a change to the way interface shear stresses were calculated. Previously, most concrete researchers had calculated the shear stress at an interface via

$$v = \frac{VQ}{Ib}. \tag{2-7}$$

Mast noted that this equation was invalid outside of the elastic range and could not be used for shear stress calculations at ultimate. Instead, Mast suggested a force balance approach whereby the tension in the steel must be resisted by compression in the concrete. Therefore, if the compression block is on one side of the interface and the tension steel is on the other, the shear stress across the interface is simply the tension force (or compression force) divided by the interface area:

$$v = \frac{T}{A_i}. \tag{2-8}$$

Hofbeck et. al. (1969) tested Mast's theory that shear friction could be used to calculate interface shear capacity across a crack in monolithic concrete. Thirty-eight push-off specimens were cast similar to those used by Anderson (see Figure 2-3). Instead of being cast in two phases with a roughened cold joint between, the specimens were cast

monolithically. Most of the specimens then had a crack induced along the desired shear plane by placing opposing line loads on the section until a crack formed. Some of the monolithic specimens were left uncracked in order to evaluate whether push-off tests can be used to determine shear performance of monolithic concrete.

Figure 2-7 shows the results of Mast's (1968) tests plotted along with the shear friction equation proposed by Birkeland and Birkeland(1966). When a value of 1.4 was used for tan φ and the upper bound of 800 psi suggested by Birkeland and Birkeland was used, the shear friction equation was shown to provide a conservative lower bound for shear transfer across pre-existing cracks. It was also shown that, when uniaxial compressive capacity of the concrete was taken to be $0.85f'_c$, and the uniaxial tensile capacity of the concrete was taken to be $6\sqrt{f'_c}$, the results of the monolithic push-off tests very closely followed the Mohr circle failure envelope proposed by Zia (1961).

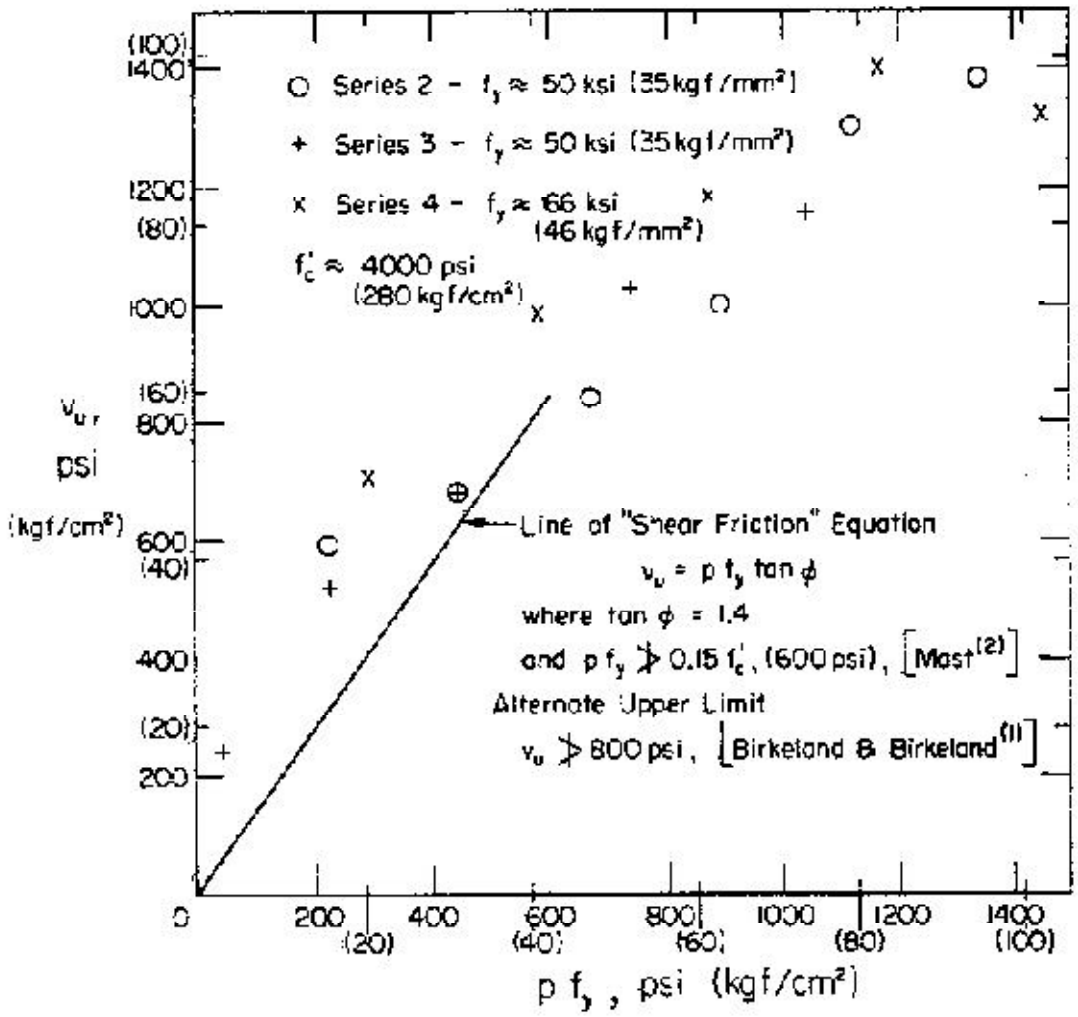

Figure 2-7: Results of precracked push-off shear tests compared to shear friction equation from Hofbeck et. al. (1969).

Mattock and Hawkins (1972) used a pull-off specimen and a modified push-off specimen to study the effects of tension parallel to the shear plane and additional compressive forces perpendicular to the shear plane. The pull-off specimens were similar to the push-offs previously used except that they had steel end pieces that allowed them to be tested in tension. The modified push-off tests created additional compression perpendicular to the shear plane by angling the shear plane from the load direction. The results of the pull-off tests showed that tensile stresses perpendicular to the shear plane

decreased the shear capacity of monolithic specimens, but had no effect on the capacity of precracked specimens. The results of the modified push-off tests showed that additional compressive forces perpendicular to the shear plane can be considered as additive to the clamping force provided by the steel reinforcement when using the shear friction equation. This research also suggested including a cohesion term in the shear friction equations when considering cracks in monolithic concrete given that certain minimum amounts of clamping force were maintained. Based on this suggestion, the shear friction equation suggested for design becomes:

$$v_u = 200psi + 0.8(\rho f_y + \sigma_{Nx}). \quad (2\text{-}9)$$

Hermansen and Cowan (1974) derived a similar formula, but suggested a cohesion term of 580 psi for monolithic concrete based on evaluation of corbel tests by Kriz and Raths (1965). In response to this work, Mattock (1974) pointed out that a cohesion term for monolithic concrete goes against the original basis for shear friction, i.e. that a pre-existing crack may form anywhere. Somerville (1974) also looked at the addition of a cohesion term for use with the shear friction equations when designing corbels, but noted that more research must still be done to determine what this term is at low reinforcement ratios.

Mattock (1974) further tested the validity of the shear friction hypothesis when applied to reinforcement crossing the shear plane at an angle. Twenty-three push-off tests were performed with stirrups at various angles to the shear plane. Some of these tests included two sets of stirrups that were at right angles to each other at various angles to the shear plane. It was found that the shear friction equations can adequately be used to predict behavior of shear interfaces with steel at an angle to the shear plane if both the

parallel and perpendicular components of the forces in these bars are included in the shear friction equation.

Paulay and Loeber (1974) examined the specific effects of aggregate interlock in transferring shear across an interface. Pre-cracked monolithic push-off specimens were created in which crack width opening could be controlled via external restraint. Three types of tests were performed as part of this research. For the first set of tests, push-off specimens with fixed crack width were tested under monotonic loading until failure occurred. The second set of tests used similar fixed width cracks, but tested the specimens under cyclical loading and unloading. The third set of tests increased the crack width as load was being applied. From these tests, it was determined that crack width was the single most important factor in determining interface shear performance of concrete push-off specimens.

Further tests by Paulay et. al. (1974) investigated the interaction of dowel action, surface roughness, reinforcement ratio, and cyclic loading on the push-off specimen shown in Figure 2-8. This specimen type is symmetric so that loading can be reversed in order to study the effect of cyclical loading of the interface. The portion of the specimen below the dashed line was precast and the remainder was cast-in-place. This research concluded that because of the large deformation required to develop dowel action, dowel action cannot be counted on for design purposes. This research also supported previous findings that roughening of the interface between precast and cast-in-place concrete is the best method for preventing large displacements in composite construction.

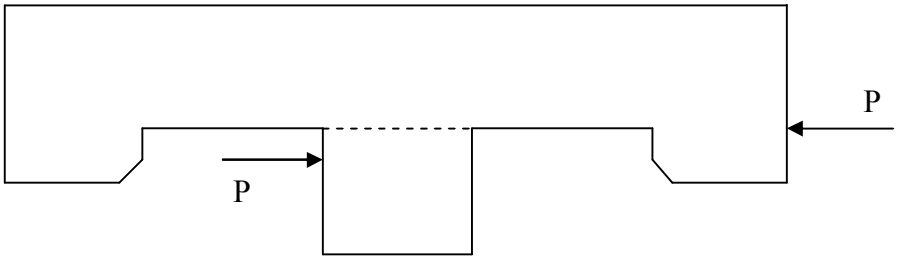

Figure 2-8: Push-off specimen for cyclic loading of interface. The dashed line represents the interface between precast and cast-in-place concretes (Paulay, Park et al., 1974).

Mattock et. al. (1975) studied the combined effects of moment and shear or tension and shear on interface shear capacity. Push-off tests with intentionally eccentric loads were used for creating moment and shear across the interface. For examining the effect of tension, push-off specimens were created with anchor bolt inserts that could be simultaneously be pulled during the interface shear test. The results of these tests showed that, while moments less than the ultimate capacity of the section do not decrease interface shear capacity, shear steel should be placed in the tension region of the interface if it is to be fully effective.

Mattock, et. al. (1976) expanded the research in interface shear transfer to include sand-lightweight and all lightweight concretes. They concluded that lightweight concretes had lower interface shear capacities than normal weight concretes of equivalent compressive strength. They recommended reducing the shear friction design capacity by adding a multiplier of 0.75 for all-lightweight concrete or 0.85 for sanded lightweight concrete.

Shaikh (1978) suggested a parabolic equation for the relationship between clamping stress and ultimate shear stress for the PCI design guideline. This equation was

based on class notes from H.W. Birkeland's course on "Precast and Prestressed Concrete." The proposed equation was

$$v_u = \sqrt{1000\mu(\rho_v f_y)} \text{ psi.} \quad (2\text{-}10)$$

The author notes that the units don't work out cleanly, but the curve fits the data more closely than the previously suggested linear equation.

Walraven (1981) suggested that the main mechanism for shear transfer across an interface was aggregate interlock. This aggregate interlock was either due to the protrusion of aggregates on a roughened interface or cracks propagating around aggregates (rather than through them) if a pre-existing crack was assumed. Using a mathematical model, the shear friction across an interface was related to the volume fraction, gradation, and size of the large aggregate. The model then derived a distribution of protruding spheres from the large aggregate distribution. Finally a contact model between protruding spheres of aggregate and indentations in the paste was used to predict shear capacity. This model was compared to data from push-off tests with varying aggregate fractions, gradations, and sizes. The model was observed to match the experimental data when a coefficient of friction of 0.4 was used. Note that this is different to the coefficient of friction in other models because it is the coefficient around each individual aggregate rather than across the interface. This changes the assumed geometry significantly and prevents this coefficient of friction from being compared with those suggested by previous researchers.

Walraven, et. al. (1987) evaluated the influence of concrete strength, load cycling, and load duration on interface shear capacity. Load duration and load cycling were found to not have significant effect on the ultimate interface shear capacity when the prolonged

load or cyclic load were kept below 82% and 66% of the ultimate static interface shear capacity respectively. Concrete strength, however, was found to have a large influence on interface shear capacity. A design chart was presented that could be used for including the influence of concrete strengths between 2,500 and 9,000 psi when clamping force across the interface was between 100 and 1500 psi. In discussion of this research, Mattock (1988) noted that this table was slightly unconservative for some previously published data and that explicit consideration of concrete strength may make design equations overly cumbersome.

Bass et. al. (1989) examined the effect of various surface preparations of existing concrete in order to determine the applicability of shear friction equations to interfaces between existing and new concretes. Unlike planned composite construction where the surface of the precast element can be roughened prior to set, this research evaluated sandblasting, chipping, and making shear keys in existing concretes prior to casting new concrete against the surface. For some specimens, holes were also drilled to varying depths in the existing concrete and dowels were epoxied into the holes prior to placement of new concrete. The results of the tests showed that 6 in. embedment was preferable for development of full shear capacity, but otherwise, shear friction equations provided a conservative estimate of experimental behavior.

Walraven and Stroband (1994) examined the use of shear friction equations for predicting interface shear performance in high-strength concretes. Previous research had been limited to concrete with cylinder strengths below 9,000psi. It was observed that, in higher strength concretes, the cracks tended to propagate through aggregates rather than around them. This crack mechanism does not allow for aggregate interlock to transfer

shear. Walraven and Stroband evaluated the applicability of shear friction equations for concretes with cylinder strengths up to 14,500psi. In push-off specimens with these higher concrete strengths, lower values of interface shear resistance are observed, or rather, the increase in concrete strength did not correlate to an equivalent increase in interface shear capacity. The basic form of the shear friction equation used in codes still provided an adequate lower bound for performance. This research did not suggest any modifications to the existing shear friction equations.

Ali and White (1999) proposed a contact model for calculation of interface shear capacity that included the effect of cracking aggregate in high-strength concretes. This mathematical model predicted behavior across concrete strengths very accurately, but was too cumbersome for design use. The simplified form of the equation was still shown to be more accurate than the basic shear friction equation, but it was still unconservative for high values of f'_c, with measured/theory values between 0.7 and 1.0 for compressive strengths of 13,600psi.

Valluvan et. al. (1999) evaluated the upper limits placed on the shear friction equation: $v_u \leq 0.2f'_c \; and \; 800psi$. Based on new research and an extensive evaluation of previous research, it was suggested that the upper limits be changed to $v_u \leq 0.25f'_c \; and \; 800psi$. This suggested change significantly decreased the overconservatism in the shear friction equations for the presented data without giving unconservative estimates.

Hwang et. al. (2000) suggested a departure from shear friction theory in calculating interface shear capacity. Instead, they showed how a softened strut-and-tie model can be used to predict failure along the interface by a mechanism similar to shear

in monolithic concrete. This method has not been adopted by current codes, presumably because of the significant increase in complexity of the equations. The authors also note that method presented for calculating the shear angle is not applicable to high-strength concretes or highly roughened interface surfaces.

Mattock (2001) suggested a change to the form of the shear friction equation that could account for some contribution of concrete strength, making the predicted values of interface shear in high-strength concrete better match experimental data. A variable related to concrete strength and cohesion was defined for existing cracks as $K_1 = 0.1f'_c$ but not more than 800psi. When $\rho_{vf} f_y < \frac{K_1}{1.45} psi$, insufficient data exists to consider the effects of concrete strength, so the shear friction capacity across an existing crack is taken as

$$v_n = 2.25(\rho_{vf} f_y + \sigma_{Nx}) psi. \quad (2\text{-}11)$$

When reinforcement ratios are higher, the shear friction capacity across an existing crack is

$$v_n = K_1 + 0.8(\rho_{vf} f_y + \sigma_{Nx}) psi \quad (2\text{-}12)$$

but not greater than $K_2 f'_c$ nor $K_3\ psi$,

where K_1 is defined above, K_2 = 0.3, and K_3=*2,400psi*. For normal weight concrete cast against intentionally roughened normal weight concrete, equations 8 and 9 can still be used, but K_1 = 400psi, K_2 = 0.3, and K_3=*2,400psi.* For sand-lightweight concrete, K_1 = 250psi, K_2 = 0.2, and K_3=*1,200psi.* For all lightweight concrete, K_1 = 200psi, K_2 = 0.2, and K_3=*1,200psi*. For concrete placed against concrete but not intentionally roughened,

$$v_n = 0.6\lambda A_{vf} f_y \quad (2\text{-}13)$$

but not more than 0.2*f'*$_c$ nor 800 psi.

where λ = 0.85 for sand lightweight concrete and 0.75 for all lightweight concrete.

Kahn and Mitchell (2002) tested 50 push-off specimens with concrete strengths up to 17,000 psi. These tests were performed using specimens (Figure 2-9) with interface areas of 60 in^2 and reinforcement ratios between .0037 and .0147. Roughened surfaces as well as precracked and monolithic shear planes were evaluated. In all cases, the shear friction equation (4) with the upper bounds of 800 psi and $0.2f'_c$ imposed by ACI318-99 was found to be a conservative predictor of behavior. It was suggested that the upper bound of 800 psi be removed, but the upper bound of $0.2f'_c$ be kept in order to make better use of increased concrete strengths. An alternative equation that more closely matched test data was also proposed:

$$v_n = 0.05f'_c + 1.4\rho_v f_y \leq 0.2f'_c \text{ [psi]}. \quad (2\text{-}14)$$

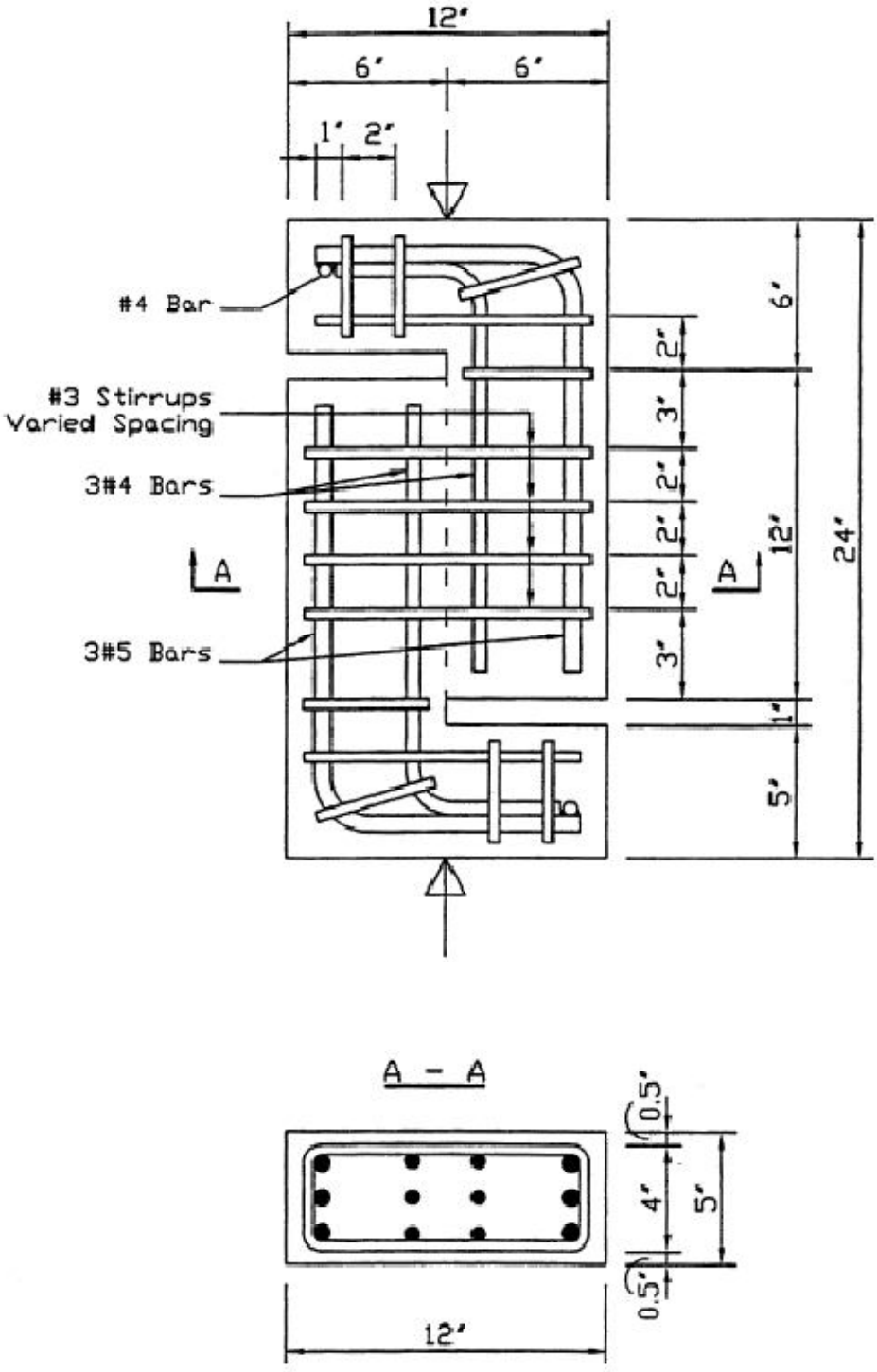

Figure 2-9: The push-off specimens used by Kahn and Mitchell (2002) had interface areas of 60 in and reinforcement ratios varying from 0.0037 and 0.0147.

The effect of steel fibers in monolithic steel-fiber reinforced concrete has also been evaluated by push-off testing (Barragán, Gettu et al., 2006). In these tests, concrete blocks were monolithically poured and then cuts were made to form a shear push-off specimen. This preparation method prevented preferential fiber alignment around extraneous formwork as well as wall effects. The specimens were then tested with LVDTs measuring both slip and crack width opening. Two different mixes with different concrete strength, fiber type, and fiber volume ratio were used. Increasing fiber volume fraction showed increased shear capacity and shear toughness for both normal and high-strength steel fiber reinforced concretes as shown in Figure 2-10. The increased ability of concretes to continue carrying shear over large crack openings was of particular interest. The authors noted that fiber orientation is a critical parameter in determining this interface shear strength, so push-off specimens should be formulated to mimic fiber orientation in actual members.

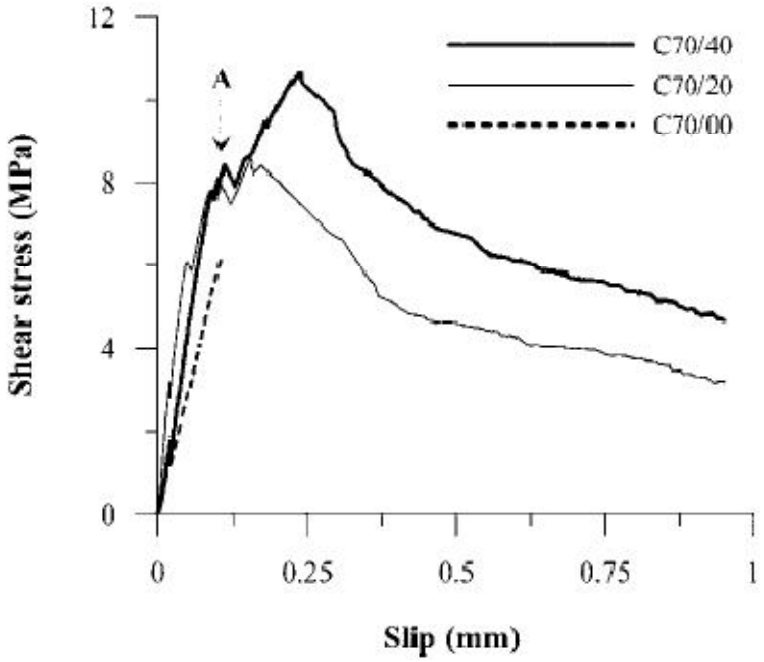

Figure 2-10: Shear stress versus slip of high performance concrete with varying amounts of steel fiber. C70/00 contains no steel, C70/20 contains 33.7 lb of steel fibers per cubic yard, and C70/40 contains 67.4 lb of steel fibers per cubic yard. Point A denotes first peak. (Barragán, Gettu et al., 2006)

Recent research has evaluated the use of shear friction equations for describing the interface shear capacity of lightweight concrete against ultra-high performance concrete (UHPC) (Banta, 2005). Three main variables were considered: amount of reinforcing steel (1, 2, 4, or 6 #3 bars across interface), the interface area (120, 180, or 240 in^2), and the preparation of the UHPC surface (smooth, deformed with half rounds, shear keys, or chipped surface). The UHPC used for these tests was Ductal® by Lafarge.

The setup of the test specimen is shown in Figure 2-11. The test setup measured the load being created by the actuator and the displacement of the lightweight concrete block. It did not measure the displacement of the UHPC block to normalize the results. Strains in the rebar were also measured close to the interface. In addition to shear across the interface, this setup also creates a moment due to the P forces not acting along the

same line of action. The thesis does not fully describe the placement of forces (other than to say that they are non-concurrent) during the test so this moment can't be quantified with the information given. Strain in the steel was affected by the presence of this moment. In the specimens with 6 stirrups, the rear stirrups experienced compression causing up to 850 microstrain due to this moment. This moment was present in all tests so it may have been manifest as a reduction (or increase) in strain in the reinforcement of the other specimens.

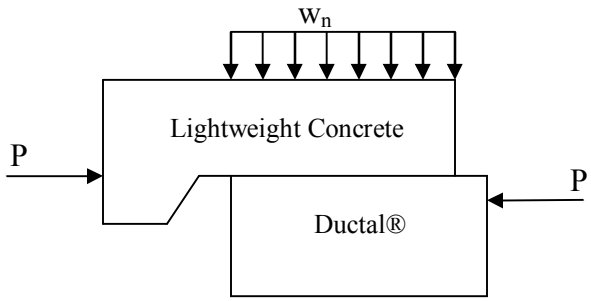

Figure 2-11: Setup for interface shear tests conducted by Banta (2005). The normal force (w_n) mimics the dead load on the structure and the P forces create shear across the interface between the two materials.

Table 2-1 shows the average results for the different interface types. The failure mechanism was slightly different for each. The smooth and deformed both sheared cleanly across the interface without cracking either surface. In the keyed specimen, the lightweight concrete keys sheared during failure. In the chipped specimen, the fibers ruptured or pulled out of the lightweight concrete. All of these failures were brittle with negligible resistance experienced after failure.

Table 2-1: Effect of Surface Preparation on Max Load and Slip at Failure

Surface Preparation	Max Load (180 in^2 interface) [k]	Slip at Failure [in]
Smooth	16	.12
Deformed	29	.11
Keyed	50	.12
Chipped	65	.28

The specimens with varying amounts of shear reinforcement failed in different ways depending on the amount of reinforcement used. Those with 4 or more #3 bars failed in a ductile manner. Those with only 1 or 2 #3 bars failed in a brittle manner (accompanied by large amounts of slip) before regaining some strength. It was not clear from the paper whether this was due to low reinforcement ratios or just lack of redundancy. Larger scale tests would be necessary to determine this. Crushing occurred adjacent to the rebar in the lightweight concrete in all tests. In the tests with more rebar, some crushing occurred in the UHPC but in the less heavily reinforced specimens, only minor spalling was observed.

The results are compared to a strut and tie model similar to that suggested by Hwang et. al. (2000). Banta notes, however, that more research needs to be done in this area to determine a rational for choosing the strut angles. The results were also compared to ACI, AASHTO LRFD, and AASHTO Standard codes. Each of the codes conservatively predicted the results observed even when no reduction factor is used for lightweight concrete. No new equations or changes to existing equations are suggested for improving accuracy.

2.2.2 Composite Beams

While shear friction specimens allow for a direct testing of interface shear capacity, they do not exactly mimic the shear that exists across an interface in a precast

beam with cast-in-place deck. In order to validate shear push-off tests and the interface shear equations, several researchers have tested composite beams; however, no composite beam tests have been performed with UHPC, so little is known about the interface shear performance of these beams. Particularly, the higher strength of this material allows for much higher moment and shear capacities at ultimate. It is unclear if interface shear capacity will increase along with these properties. It is important to study these phenomena in order to avoid a situation in which a beam with very high expected moment and shear capacities fails prematurely due to low interface shear strength.

In addition to the tests mentioned in the previous section, Hanson (1960) performed tests of compositely cast T-beams. Two lengths of girder were used with the same cross section (see Figure 2-12). The interface shear stress reported in these tests was calculated from the elastic equation (5), and is compared to the push-off data in Figure 2-13. This comparison is not the most helpful because of the method used for calculating the shear stress, but the comparison between tests still shows a good correlation between test types. From the test results of the push-off and beam tests, the author suggested a maximum slip of .005 in. for determining the loss of composite action between the girder and deck.

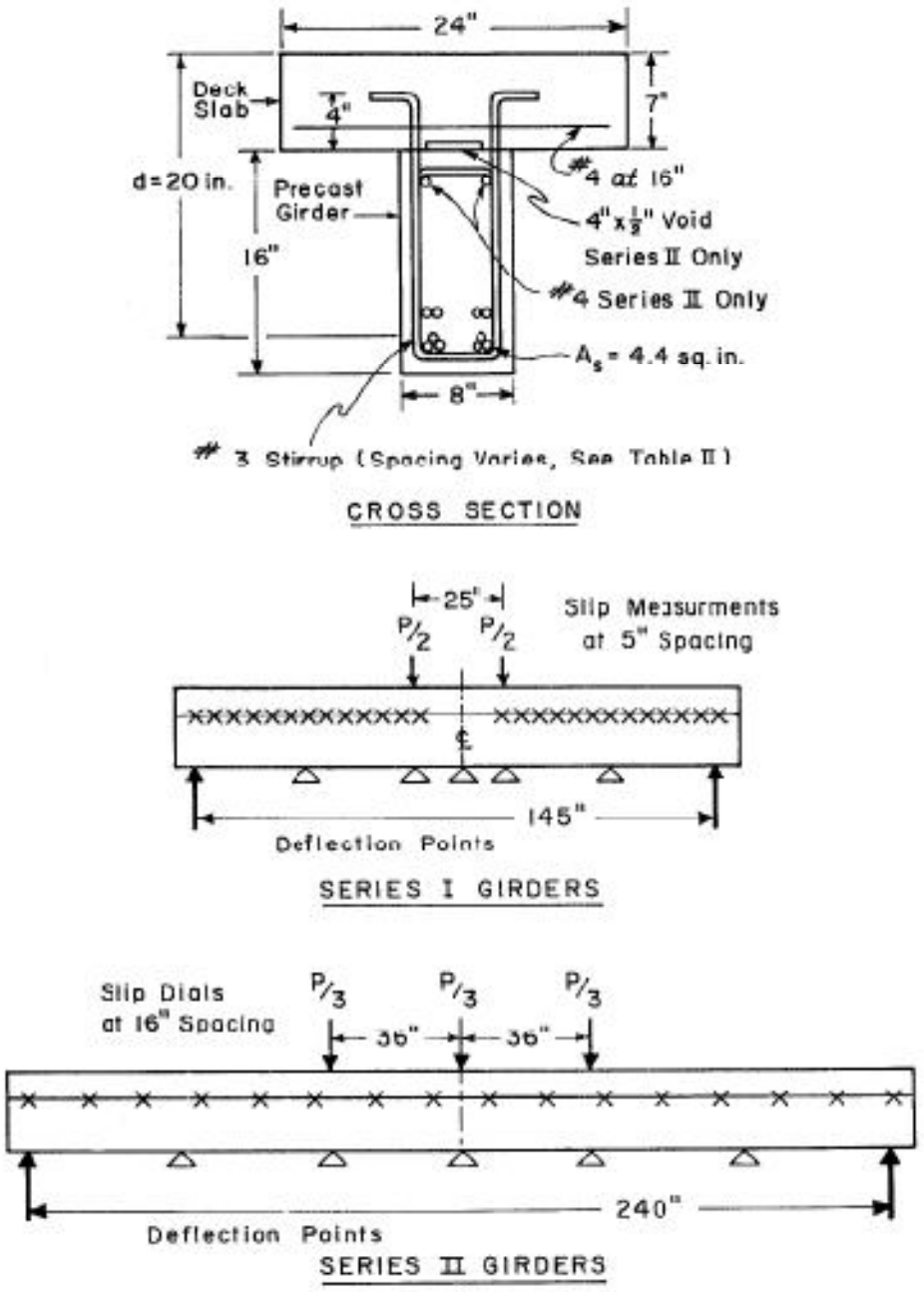

Figure 2-12: Design for composite girder casting and testing performed by Hanson (1960). In the elevation view, the X's indicate slip dial locations and the triangles indicate deflection measurement locations.

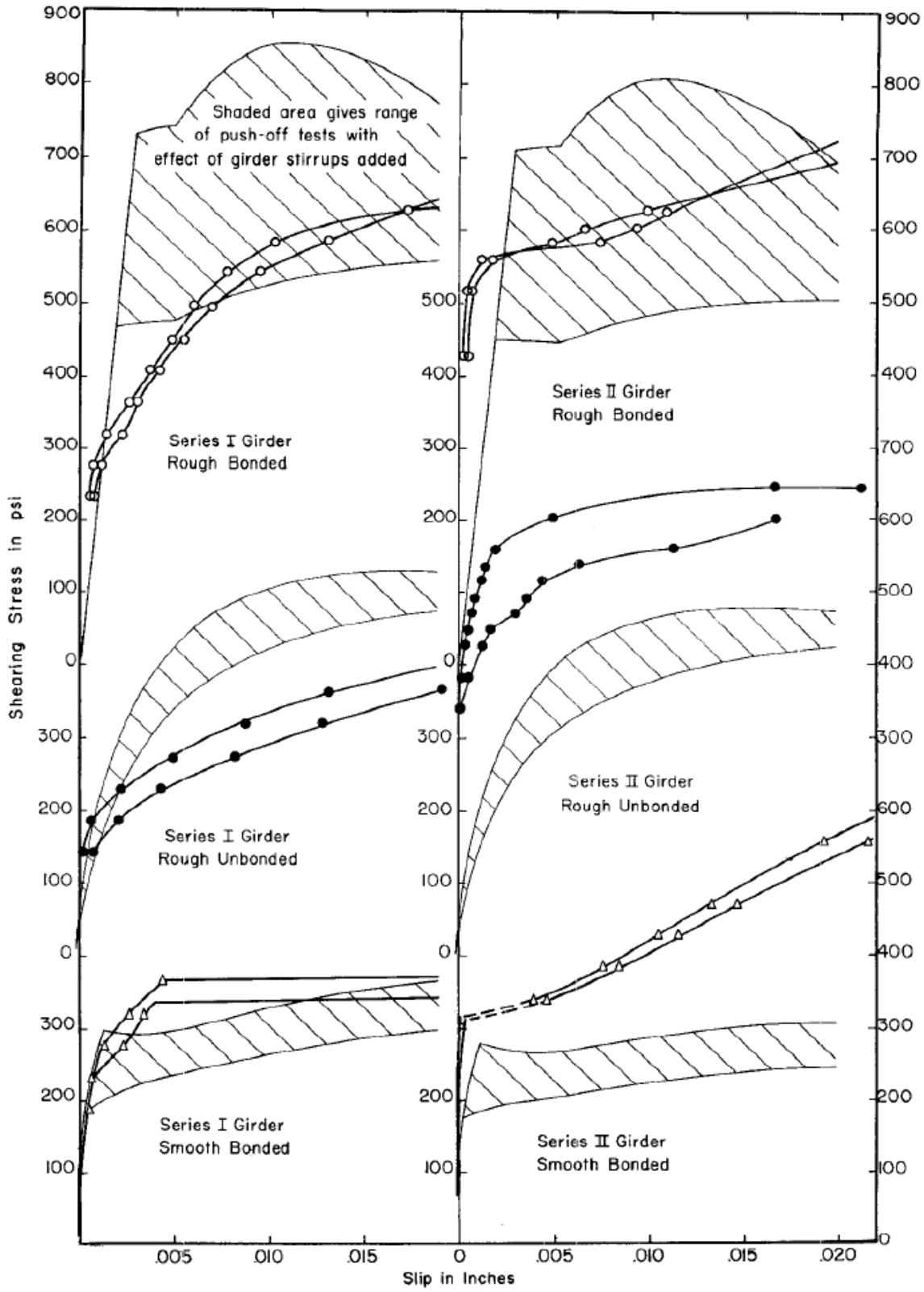

Figure 2-13: Comparison of push-off and T-beam results by Hanson (1960).

Grossfield and Birnstiel (1962) performed similar tests of eight 10-foot-long T-Beams. The results of these test showed that it is difficult to separate the effects of slip and shear cracking from dial gauge readings in beam tests. Push-off tests, however, did not capture the effects of web cracking. They also noted that this cracking effect may make a maximum slip value unrealistic for composite concrete design.

Saemann and Washa (1964) performed a comprehensive study of 42 composite T-beams. The influence of surface roughness, neutral axis position, shear span length, reinforcement ratio, shear keys, and concrete strength were evaluated. Beams with lengths of 8 and 11 ft were more likely to fail in interface shear than 20 ft beams. In these two shorter beam lengths, it was found that increasing the roughness of the interface increased the interface shear capacity. Also, when some surface roughness was present, increasing the amount of steel across the interface dramatically increased the interface shear capacity. From these tests, the following equation was suggested:

$$Y = \frac{2700}{X+5} + 300P\left(\frac{33-X}{X^2+6X+5}\right), \tag{2-15}$$

where Y is the shear stress in psi, P is the interface reinforcement ratio, and X is the shear span to depth ratio. The authors used the elasticity solution for shear stress found in equation(5) for calculating stresses at failure.

Loov and Patnaik (1994) tested 16 composite T-Beams with a length of 126 in. and a span of 120 in. Half of the beams had their flanges discontinued 15.75 in. from each end of the beam (12.80 in. from the support); the other half had flanges that continued to the end of the beam. The surfaces of all beams were left as cast with protruding large aggregate, and the reinforcement ratio was varied from 0.1% to 1.9%. The authors found that slip was insignificant up to the point when the shear stress equaled

220 to 290 psi as calculated by equation (5). After this point, slip and shear stress both increased up to a slip of 0.01 to 0.03 in. at which time slip continued to increase, but shear stress began to decrease. They suggested a departure from the shear friction methodology with the use of the equation:

$$v_n = k\lambda\sqrt{(15 + \rho_v f_y)f'_c} \leq 0.25f'_c. \quad (2\text{-}16)$$

In this equation, k is a constant defined as 0.5 for compositely cast concrete and 0.6 for monolithic concrete.

Patnaik (1999) conducted additional tests on 6 composite beams with roughened interfaces and no interface shear reinforcement. Based on these tests, he suggested a lower bound interface shear capacity of:

$$v_n = 4.215\sqrt{f'_c}\ (psi) \quad (2\text{-}17)$$

when no shear reinforcement is present. This expression was only validated for concrete strengths below 8,700 psi. Patnaik also suggested the use of the equilibrium equation (6) for calculating the shear stress, particularly in prestressed beams where the "elastic equation will produce unrealistic stresses."

Patnaik (2001) also investigated the interface shear strength of composite beams with smooth interfaces and varying interface areas and interface shear reinforcement ratios. He showed that existing codes for smooth interfaces are conservative, but suggested the equation:

$$v_u = 87 + \rho_v f_y \leq 0.2f'_c \ and\ 800\ psi, \text{ or} \quad (2\text{-}18)$$

$$v_u = 0 \ \text{ when } \ \rho_v f_y < 50psi. \quad (2\text{-}19)$$

He also noted that composite action was usually maintained up to about 65% of the factored design load for each beam. Below this load, the use of the cracked composite

section was valid for calculating deflections, but after this, the deflections increased dramatically. Figure 2-14 compares observed deflection behavior with that predicted by ACI for a monolithic section.

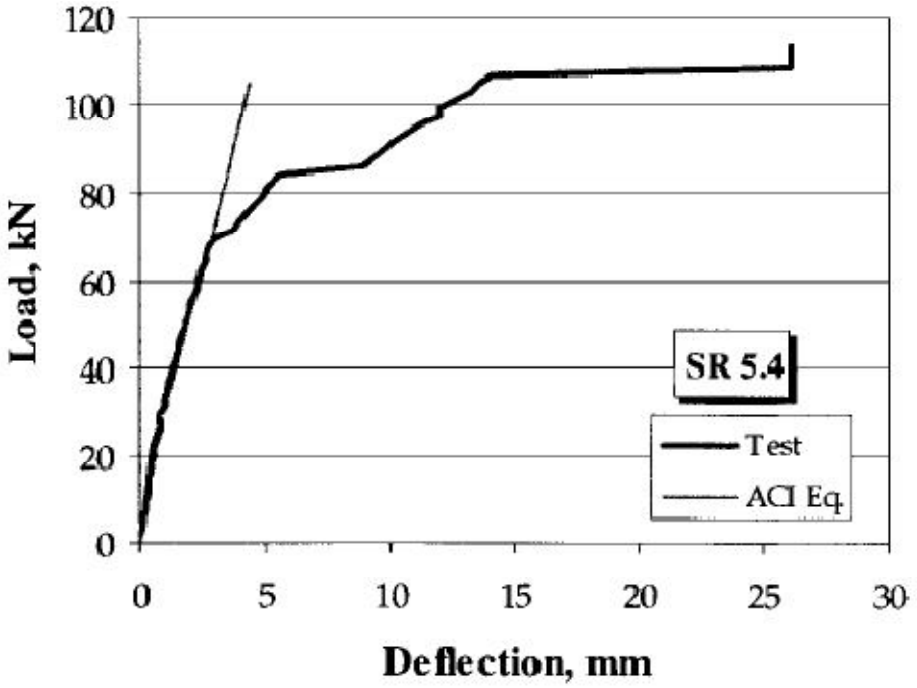

Figure 2-14: Typical load deflection curve for a composite beam with smooth interface compared to ACI predicted behavior (Patnaik, 2001).

Kahn and Slapkus (2004) studied interface shear capacity of 6 composite beams cast with high performance concretes with strengths up to 11,300 psi. Interface shear reinforcement ratios were varied from 0.186% to 0.371%. The results of these tests showed the equation proposed by Kahn and Mitchell (2002) as well as the equation proposed by Loov and Patnaik (1994) to be good predictors of interface shear capacity in composite high-strength concrete beams. The ACI and AASHTO code equations were also shown to be conservative for these higher concrete strengths.

2.3 Diagonal Tension Shear

ACI 426R-74 (1973) and ACI 445R-99 (1998) describe many methods for calculating shear capacity of concrete members including Compression Field Theory (CFT), Modified Compression Field Theory (MCFT), and various truss analogies. Most of these assume a minimum amount of transverse reinforcement or a minimal shear capacity of concrete without transverse reinforcement. None of the methods in these documents, however, deal explicitly with the shear capacity of fiber-reinforced concrete or ultra-high performance concrete.

A preliminary French code for the use of UHPC (Association Française de Génie Civil, 2002) suggests an additive relationship between the shear resistances provided by the concrete, the steel fibers, prestressing strands, and any other passive reinforcement present. This is similar to the $V_n = V_c + V_s$ relationship allowed in ACI 318-08 code.

The Federal Highway Administration performed three shear tests on prestressed UHPC AASHTO Type II girders with varying shear spans (Graybeal, 2006). Based on the results of this research, Graybeal showed that the French code underestimates the shear capacity by more than 50% in prestressed UHPC girders with no shear stirrups. This code also doesn't account for shear carried in a cracked section.

Graybeal suggested using a simplified model for shear failure that bases the shear capacity on the diagonal tension carried by the UHPC. Using this method, he back-calculated a tensile capacity for the UHPC in the section where shear failure occurs. This value was 2.3 ksi and 1.8 ksi for girders 24S and 14S respectively. This tensile capacity was 38% to 77% greater than Graybeal's best estimate of tensile cracking strength (f_{ct})

from small-scale tests of 1.3 ksi. Thus this method would provide a lower bound for shear capacity, but may be overly conservative for this material.

The research only focused on girders without shear stirrups, so the effect of additional mild reinforcement was not evaluated. Graybeal's research also focused only on shear capacity of the girder, rather than looking at the girder-deck system used in most bridge construction.

Mast (1968) applied shear friction principles to diagonal tension shear stresses in concrete members. Mast (1968) originally suggested that any given plane in concrete should be considered a potential interface because a pre-existing crack could exist in this location. Based on this principle, the shear transfer required at any given section could be designed by assuming it to be a cracked interface.

Krauthammer (1992) used the shear friction theory to propose an alternative method for minimum shear reinforcement. It was suggested that the minimum shear reinforcement be the amount that provides the same magnitude of interface shear resistance as full aggregate interlock. This guideline would require a reinforcement ratio of at least 0.001 in all areas subject to shear. This is one of the first uses of shear friction theory to explain shear transfer in areas other than along interfaces or pre-defined shear planes.

2.4 References

AASHTO (2010). *AASHTO LRFD bridge design specifications*. Washington, D.C., American Association of State Highway and Transportation Officials.

ACI Committee 318 (2008). *Building code requirements for structural concrete : (ACI 318-08) ; and commentary (ACI 318R-08)*. Farmington Hills, Mich., American Concrete Institute.

Ali, M. A. and R. N. White (1999). "Enhanced Contact Model for Shear Friction of Normal and High-Strength Concrete." *ACI Structural Journal* 96(3): 348-360.

Anderson, A. R. (1960). "Composite designs in precast and cast-in-place concrete." *Progressive Architecture* 41(9): 8.

ASCE-ACI Committee 426 (1973). *The Shear Strength of Reinforced Concrete Members: (ACI 426R-74)*. Farmington Hills, Mich., American Concrete Institute.

ASCE-ACI Committee 445 (1998). *Recent Approaches to Shear Design of Structural Concrete: (ACI 426R-99)*. Farmington Hills, Mich., American Concrete Institute.

Association Française de Génie Civil (2002). Interim recommendations for ultra high performance fibre-reinforced concretes. France.

Banta, T. E. (2005). Horizontal shear transfer between Ductal and lightweight concrete. *Civil Engineering*. Blacksburg, VA, Virginia Polytechnic Institute and State University. Masters of Science: 132.

Barragán, B., R. Gettu, et al. (2006). "Shear Failure of Steel Fiber-Reinforced Concrete Based on Push-Off Tests." *Aci Materials Journal* 103(4): 251.

Bass, R. A., R. L. Carrasquillo, et al. (1989). "Shear Transfer Across New and Existing Concrete Interfaces." *ACI Structural Journal* 86(4): 383-393.

Birkeland, P. W. and H. W. Birkeland (1966). "Connections in precast concrete construction." *ACI Journal* 63(3): 345-367.

Delarrard, F. and T. Sedran (1994). "Optimization of Ultra-High-Performance Concrete By the Use of a Packing Model." *Cement and Concrete Research* 24(6): 997-1009.

Garas, V. Y. (2009). Multi-Scale Investigation of Tensile Creep of Ultra-High Performance Concrete for Bridge Applications. *Civil and Environmental Engineering*. Atlanta, GA, Georgia Institute of Technology. Ph.D.

Graybeal, B. A. (2004). Fabrication of an optimized UHPC bridge. *PCI National Bridge Conference*. Atlanta, GA.

Graybeal, B. A. (2006). Material Property Characterization of Ultra-High Performance Concrete. F. H. Administration. McLean, VA, U.S. Department of Transportation.

Graybeal, B. A. (2006). Structural Behavior of Ultra-high Performance Concrete Prestressed I-Girders. F. H. Administration. Mclean, VA, U.S. Department of Transportation.

Grossfield, B. and C. Birnstiel (1962). "Tests of T-Beams with Precast Webs and Cast-in-Place Flanges." *ACI Journal* 59(6): 843-851.

Hanson, N. W. (1960). "Precast-Prestressed Concrete Bridges: 2. Horizontal Shear Connections." *Journal of the PCA Research and Development Laboratories* 2(2): 38-58.

Hermansen, B. R. and J. Cowan (1974). "Modified Shear-Friction Theory for Bracket Design." *ACI Journal* 71(2): 55-60.

Hofbeck, J. A., I. O. Ibrahim, et al. (1969). "Shear transfer in reinforced concrete." *ACI Journal* 66(2): 119-128.

Hwang, S.-J., H.-W. Yu, et al. (2000). "Theory of Interface Shear Capacity of Reinforced Concrete." *Journal of Structural Engineering* 126(6): 700-707.

Kahn, L. F. and A. D. Mitchell (2002). "Shear Friction Tests with High-Strength Concrete." *ACI Structural Journal* 99(1): 98-103.

Kahn, L. F. and A. Slapkus (2004). "Interface Shear in High Strength Composite T-Beams." *PCI Journal* 49(4): 102-110.

Krauthammer, T. (1992). "Minimum Shear Reinforcement Based on Interface Shear Transfer." *ACI Structural Journal* 89(1): 99-105.

Kriz, L. B. and C. H. Raths (1965). "Connections in Precast Concrete Structures - Strength of Corbels." *PCI Journal* 10(1): 18-61.

Loov, R. E. and A. K. Patnaik (1994). "Horizontal Shear Strength of Composite Concrete Beams." *PCI Journal* 39(1): 48-67.

Mast, R. F. (1968). "Auxiliary reinforcement in concrete connections." *Journal of the Structural Division, ASCE* 94(6): 1485-1504.

Mattock, A. H. (1974). "Discussion of the paper "Modified Shear Friction Theory for Bracket Design," by B. R. Hermansen and J. Cowan." *ACI Journal* 71(8): 421-423.

Mattock, A. H. (1974). Shear Transfer in Concrete Having Reinforcement at an Angle to the Shear Plane. *ACI Special Publication 42, Shear in Reinforced Concrete 2*. Detroit, Michigan, American Concrete Institute: 17-42.

Mattock, A. H. (1988). "Discussion of the paper "Influence of Concrete Strength and Load History on teh Shear Friction Capacity of Concrete Members," by Walraven, et. al." *PCI Journal* 33(1): 165-166.

Mattock, A. H. (2001). "Shear Friction and High-Strength Concrete." *ACI Structural Journal* 98(1): 50-59.

Mattock, A. H. and N. M. Hawkins (1972). "Shear Transfer in Reinforced Concrete - Recent Research." *PCI Journal* 17(2): 55-75.

Mattock, A. H., L. Johal, et al. (1975). "Shear Transfer in Reinforced Concrete with Moment or Tension Across the Shear Plane." *PCI Journal* 20(4): 76-93.

Mattock, A. H., W. K. Li, et al. (1976). "Shear Transfer in Lightweight Reinforced Concrete." *PCI Journal* 21(1): 20-39.

Patnaik, A. K. (1999). "Longitudinal Shear Strength of Composite Concrete Beams with a Rough Interface and No Ties." *Australian Journal of Structural Engineering* 1(3): 157-166.

Patnaik, A. K. (2001). "Behavior of Composite Concrete Beams with Smooth Interface." *Journal of Structural Engineering* 127(4): 359-366.

Paulay, T. and P. J. Loeber (1974). Shear Transfer by Aggregate Interlock. *ACI Special Publication 42, Shear in Reinforced Concrete 2*. Detroit, Michigan, American Concrete Institute: 1-15.

Paulay, T., R. Park, et al. (1974). Horizontal Construction Joints in Cast-in-place Reinforced Concrete. *ACI Special Publication 42, Shear in Reinforced Concrete 2*. Detroit, Michigan, American Concrete Institute: 17-42.

Saemann, J. C. and G. W. Washa (1964). "Horizontal shear connections between precast beams and cast-in-place slabs." *American Concrete Institute -- Journal* 61(11): 1383-1409.

Shah, S. P. and W. J. Weiss (1998). Ultra High Performance Concrete: A Look to the Future. *1998 ACI Spring Conference*. Houston, TX.

Shaikh, A. F. (1978). "Proposed Revisions to Shear-Friction Provisions." *PCI Journal* 23(2): 12-21.

Somerville, G. (1974). The Behavior and Design of Reinforced Concrete Corbels. *ACI Special Publication 42, Shear in Reinforced Concrete 2*. Detroit, Michigan, American Concrete Institute: 477-502.

Valluvan, R., M. E. Kreger, et al. (1999). "Evaluation of ACI 318-95 shear-friction provisions." *ACI Structural Journal* 96(4): 473-481.

Walraven, J. and J. Stroband (1994). *Shear Friction in High-Strength Concrete*. ACI International Conference, High-Performance Concrete, Singapore, American Concrete Institute.

Walraven, J. C. (1981). "Fundamental Analysis of Aggregate Interlock." *Journal of the Structural Division, ASCE* 107(11): 2245-2270.

Walraven, J. C., J. Frenay, et al. (1987). "Influence of Concrete Strength and Load History on the Shear Friction Capacity of Concrete Members." *PCI Journal* 32(1): 66-84.

Zia, P. (1961). "Torsional Strength of Prestressed Concrete Members." *ACI Journal* 57(4): 1337-1360.

CHAPTER 3
SHEAR FRICTION PUSH-OFF TESTS WITH ULTRA-HIGH PERFORMANCE CONCRETE

3.1 Introduction

The purpose of this experimental study was to determine if the ACI 318 (2008) and AASHTO LRFD (2007) code equations for shear friction are applicable for ultra high performance concrete (UHPC) and for cold joints between UHPC and cast-in-place high performance concrete (HPC). The concept of shear friction uses the idea of a coefficient of friction to quantify shear transfer across a given plane, especially at a cold joint or at an existing or potential crack. The current ACI shear friction equations is:

$$V_n = \mu A_v f_y \qquad (3\text{-}1)$$

not greater than the smaller of:

$0.2 f_c' A_{cv}$,

$(480 + 0.08 f_c') A_{cv}$,

or $1600 A_{cv}$

where

μ = coefficient of friction

A_{vf} = area of steel crossing interface

f_y = yield stress of steel

f'_c = concrete compressive strength

A_c = area of concrete contact across interface

The AASHTO equation is:

$$V_{ni} = cA_{cv} + \mu(A_{vf} f_y + P_c) \text{, lb.} \qquad (3\text{-}2)$$

not to exceed the smallest of:

$K_1 f_c' A_{cv}$,

and $K_2 A_{cv}$.

where

V_n = nominal shear strength, lb

c = cohesion factor,

75 psi (0.52 MPa) for a clean concrete surface, not roughened,

280 psi (1.9 MPa) for a roughened surface with a ¼-in. (6 mm) amplitude,

400 psi (2.76 MPa) for concrete cast monolithically

A_{cv} = area of concrete considered to be engaged in interface shear transfer ($b_{vi}d_v$), in^2

μ = friction factor

1.0 for a roughened surface with a ¼-in. (6 mm) amplitude,

0.6 for a not intentionally roughened surface

1.4 for concrete cast monolithically

A_v = area of interface shear reinforcement crossing the shear plane within the area A_{cv}, in^2

f_y = yield stress of transverse reinforcement, psi

P_c = permanent net compressive force normal to the shear plane, lb

b_{vi}= interface width considered to be engaged in shear transfer, in.

d_v= the distance between the centroid of the tension steel and the mid-thickness of the slab to compute a factored interface shear stress.

K_1 = concrete cohesion term that is related to strength,

0.3 for cast in place slab cast against roughened girder

0.25 for normalweight concrete placed monolithically, normalweight and lightweight concrete with a roughened surface,

0.2 for normal weight concrete placed against non-roughened surface or cast against studded steel girders

K_2 = maximum allowable interface stress

1.8 ksi for normal-weight concrete deck cast against roughened girder,

1.5 ksi for normal-weight concrete cast against roughened concrete or placed monolithically

1.3 ksi for lightweight concrete deck cast against roughened girder,

1.0 ksi for lightweight concrete cast against roughened concrete or placed monolithically

0.8 ksi for concrete cast against studded steel girders

Using Equations (3-1) and (3-2), shear stress is calculated by dividing nominal shear strength by the area of the concrete engaged in shear transfer as follows in Equations (3-3) and (3-4)

$$v_{ni} = \mu \rho_v f_y \tag{3-3}$$

$$v_{ni} = c + \mu(\rho_v f_y + P_c/A_{cv}) \tag{3-4}$$

where,

ρ_v = interface shear reinforcement ratio

Equation (3-1) was derived from what was originally proposed by Birkeland-Birkeland (1966) and has since been modified based on experimental research (Mast, 1968; Hofbeck et al., 1969; Kahn and Mitchell, 2002).

The current ACI and AASHTO code provisions need to be validated in order to determine if current provisions can be used for UHPC girder shear resistance and for UHPC/HPC interface shear resistance for composite structures. Because of

UHPC's high tensile capacity and the presence of steel fibers in the matrix, it has been proposed that UHPC girders require no transverse shear reinforcement to carry shear forces (Graybeal, 2005). Also, the amount of shear reinforcement required to develop shear transfer across the interface between a precast UHPC bridge girder and a cast-in-place deck slab is unknown. The interface connection is further complicated by the high flowability of the UHPC and by the presence of the fibers, both of which make roughening the UHPC surface by brooming or raking impossible.

3.2 Research Significance

New ultra high performance concretes (UHPCs) have begun being used in precast prestressed concrete bridge girders. Some precast prestressed I-girders rely on composite action with a cast-in-place concrete deck for carrying live loads. The shear capacity of the interface between precast UHPC and cast-in-place concrete must be understood if this structural system is to be used safely. Further, the shear friction capacity across a crack in a UHPC girder is unknown. These shear friction strengths must be known before UHPC with its advantages of high strength and durability can be fully utilized.

3.3 Experimental Procedure

The 38 push-off specimens were designed and cast similar to those used by Hanson (1960), Anderson (1960), Hofbeck et al. (1969), and Kahn and Mitchell (2002) so that the results could be compared directly to the previous tests. The main difference in the current specimens is the dimensions, which were about 45% larger to allow for development of the larger internal steel reinforcement with larger bend diameters required. Twelve specimens were cast monolithically from UHPC with a compressive strength, f_c', of 28,900 psi (200 MPa) as shown in Figure 3-1. The

specimens were cast in such a way as to limit the preferential alignment in any one axis, so that the amount of fibers crossing the interface was considered to be random and isotropic. This was qualitatively verified by examining the interface surfaces after failure, which confirmed a substantial portion of the fibers crossed the interface. Chapter 7 presents the results of research on fiber alignment in long beams, and Appendix C presents the results of a small fiber alignment study performed on cast rectangular specimens that had similar lengths in all three dimensions.

Twenty-six composite specimens were manufactured by first casting one-half from the same UHPC. After this half had cured, the other half was cast against the cold joint using either HPC or UHPC. Figure 3-2 shows the design of the composite specimens. The HPC had a design strength of 8,000 psi but achieved an actual compressive strength of 12,200 psi (84.4 MPa), and the UHPC had compressive strength of 28,900 psi (200 MPa). For all specimens, the interface shear plane was rectangular with width of 7 1/4 in. (174 mm) and length of 12 in. (288mm). The formwork for the monolithic and composite specimens is shown in Figure 3-3.

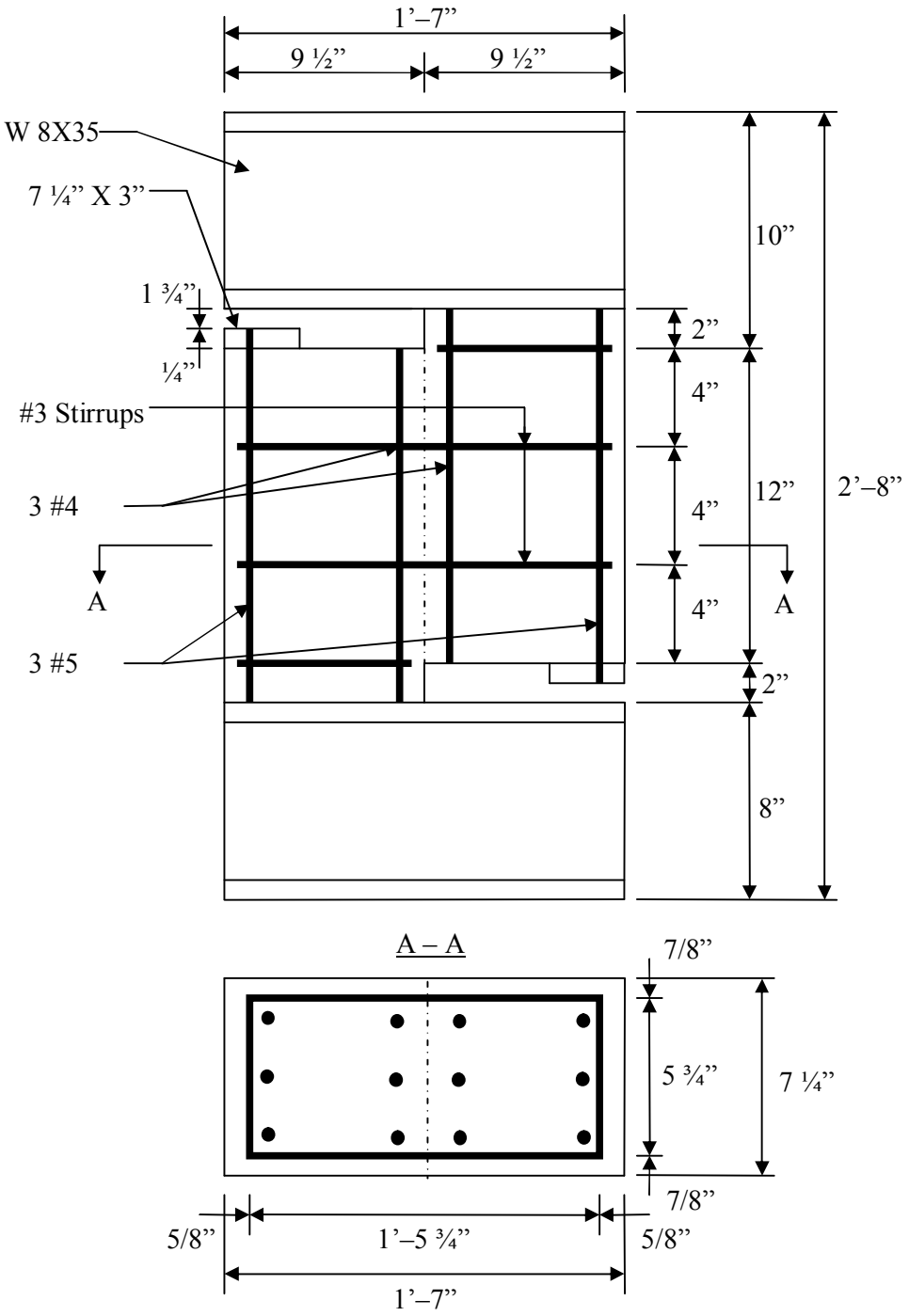

Figure 3-1: Design of monolithically cast specimens using only UHPC. The dot-dashed line indicates the shear plane and where a crack was created on pre-cracked specimens. 1 in.=25.4mm.

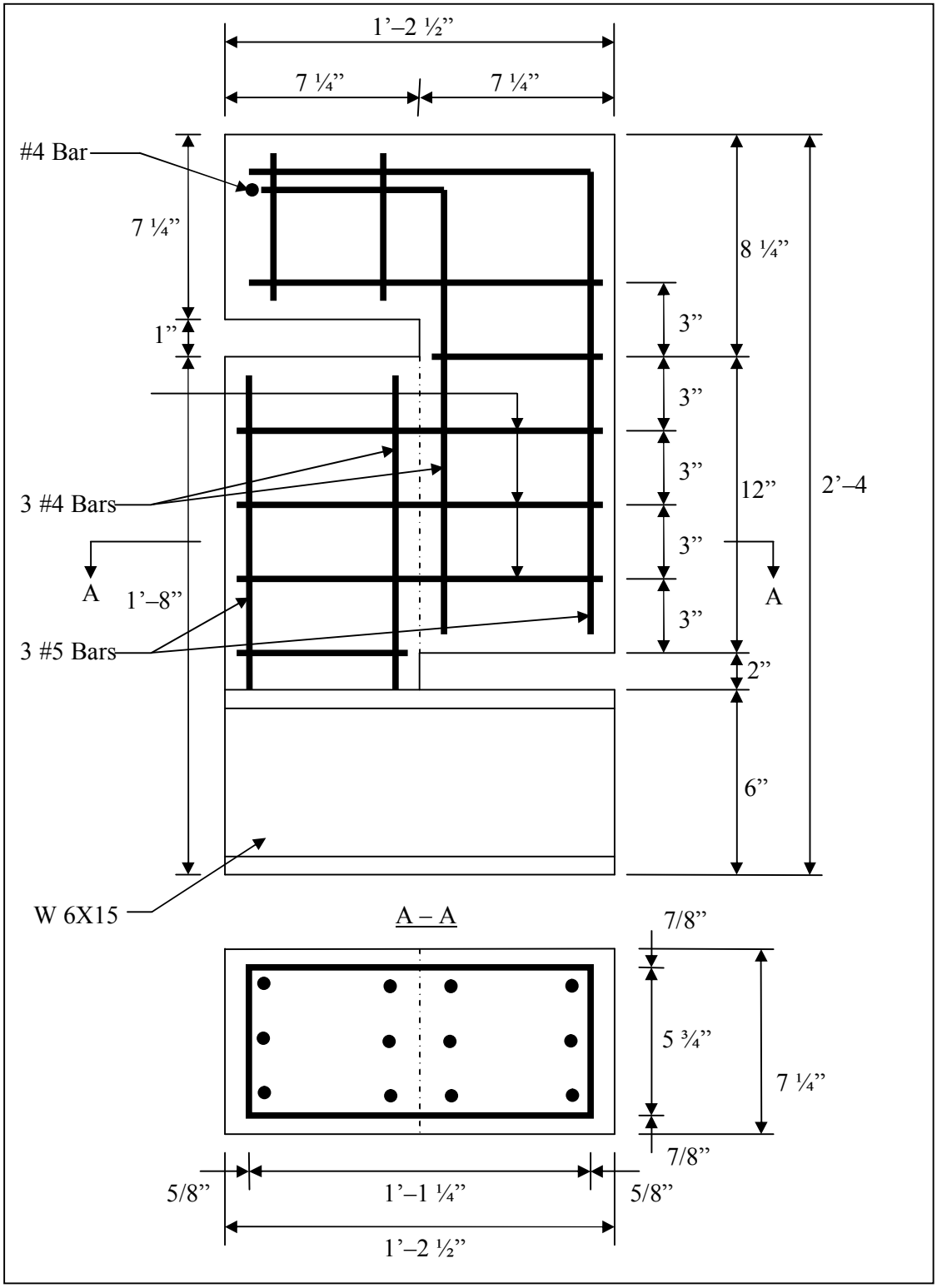

Figure 3-2– Design of composite push-off specimen. The dot-dashed line indicates the shear plane and the cold joint location. 1 in.=25.4mm.

a)

b)

Figure 3-3– Specimen formwork for (a) monolithic pour (b) composite pour.

The monolithic specimens and the first half of the composite specimens were cast during the second of three full-scale castings performed at the Tindall Corporation, Georgia Division Plant in Conley, GA. The UHPC used was Ductal® manufactured by Lafarge Corp. Once the specimens were cast, they were allowed to cure in ambient conditions for 48 hours. After 48 hours, the specimens were demolded and underwent a thermal treatment for an additional 48 hours at 95% relative humidity and 203°F (95°C) as recommended by Lafarge (Crane and Kahn, 2009).

In the all-UHPC specimens, the two variables evaluated were the interface surface and transverse reinforcement ratio. The monolithic specimens were either left uncracked or were pre-cracked; the composite specimens had a smooth cold joint to represent a UHPC girder in which concrete placement was delayed and an accidental cold joint was created. The monolithic pre-cracked specimens were prepared by placing a specimen on its front side while aligning a knife-edge plate perpendicular to the shear plane as shown in Figure 3-4. Load was applied at an initial rate of 500 lbs per second and continued until a 3000 lb. drop in load was observed. For each surface preparation, either 0 or 2 two-leg No. 3 stirrups crossing the shear plane were used giving reinforcement ratios of 0% or 0.5%.

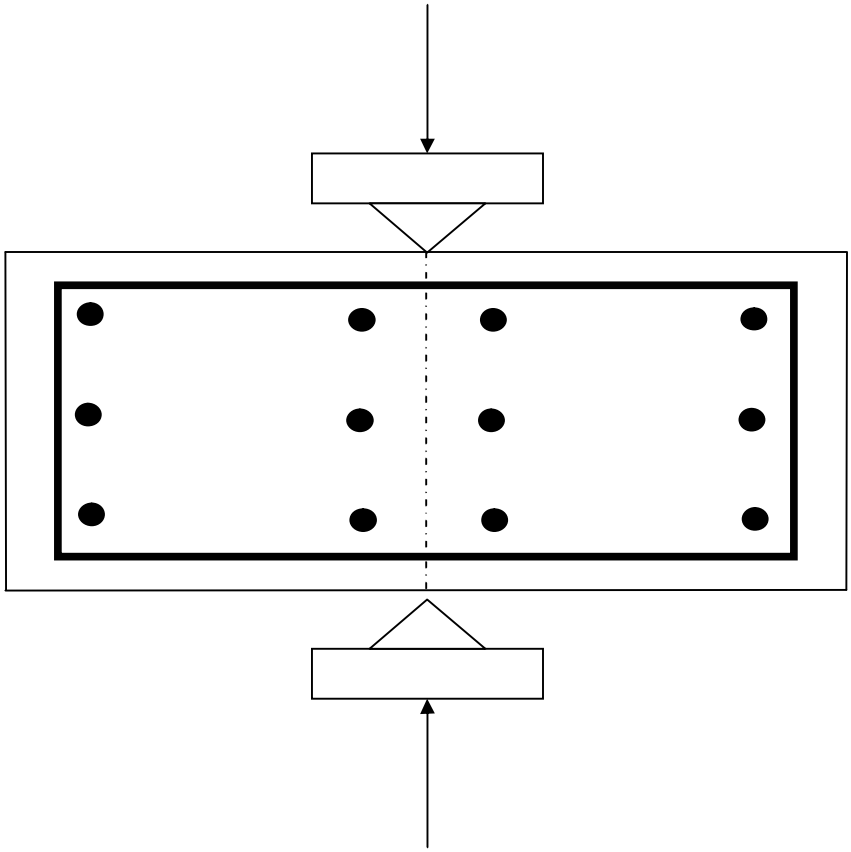

Figure 3-4: Section cut showing loading and position of monolithic specimen during pre-cracking.

Similarly, in the UHPC/HPC cold joint composite specimens, the interface surface preparation and interface reinforcement ratio were varied. Three surface preparations were used. The first interface used a 1/4 in. (6 mm) deep form liner which was pressed into the surface of the UHPC to create a fluted, "roughened" condition. In the second interface, burlap was placed on the cast UHPC to create a mildly rough surface. The third surface was the smooth, as-cast cold joint surface; no troweling, brooming, or raking was used. Either 0, 1, 2, or 3 two-leg No. 3 stirrups crossed the shear plane to give reinforcement ratios of 0%, 0.25%, 0.5%, and 0.75%.

The Grade 60 No. 3 reinforcing bars used for all closed stirrup transverse reinforcement had an average yield stress of 73.5 ksi (506.8 MPa); however, the ACI-

318 recommended maximum f_y of 60 ksi (413.7 MPa) was used in the following calculations of predicted shear stress values.

Table 3-1 summarizes the details of all specimens. The first two letters represents the type of concrete on either side of the shear plane, U for UHPC and H for HPC. The third set of letters indicates the interface type: monolithic uncracked (MU), monolithic precracked (MC), fluted cold joint (F), burlap-roughened cold joint (B), smooth cold joint (S). The last character indicates the number of stirrups crossing the shear plane (0,1, 2, or 3). Three identical push-off specimens termed A, B, and C were constructed for each type except for U-H-F-0 which had only specimens A and B. The formwork for specimen C leaked prior to setting of the UHPC making the specimen useless.

Table 3-1: Specimen Specification

Specimen Identification	Concrete 1	Concrete 2	Interface Type	Transverse Reinforcement Ratio, ρ_v
U-U-S-0	UHPC	UHPC	Smooth Cold Joint	0%
U-U-S-2	UHPC	UHPC	Smooth Cold Joint	0.50%
U-U-MC-0	UHPC	UHPC	Pre-Cracked Monolithic	0%
U-U-MC-2	UHPC	UHPC	Pre-Cracked Monolithic	0.50%
U-U-MU-0	UHPC	UHPC	Un-Cracked Monolithic	0%
U-U-MU-2	UHPC	UHPC	Un-Cracked Monolithic	0.50%
U-H-S-0	UHPC	HPC	Smooth Cold Joint	0%
U-H-S-1	UHPC	HPC	Smooth Cold Joint	0.25%
U-H-S-2	UHPC	HPC	Smooth Cold Joint	0.50%
U-H-S-3	UHPC	HPC	Smooth Cold Joint	0.75%
U-H-B-0	UHPC	HPC	Burlap-Roughened Cold Joint	0%
U-H-F-0	UHPC	HPC	Fluted Cold Joint	0%
U-H-F-2	UHPC	HPC	Fluted Cold Joint	0.50%

All push-off specimens were tested using the set up illustrated in Figure 4-5. Each specimen was centered in a 400 kip (1,780 kN) capacity hydraulic testing machine. Load was applied at a rate of 100, 200, or 500 lb/s (445, 890, or 2,224 N/s) depending on the expected interface shear capacity. Relative slip movement across the interface was measured by dial gages located at center of the interface on both front and back of the specimen. Prior to testing, the width and height of the interface shear surface were measured and recorded for determining interface shear stress.

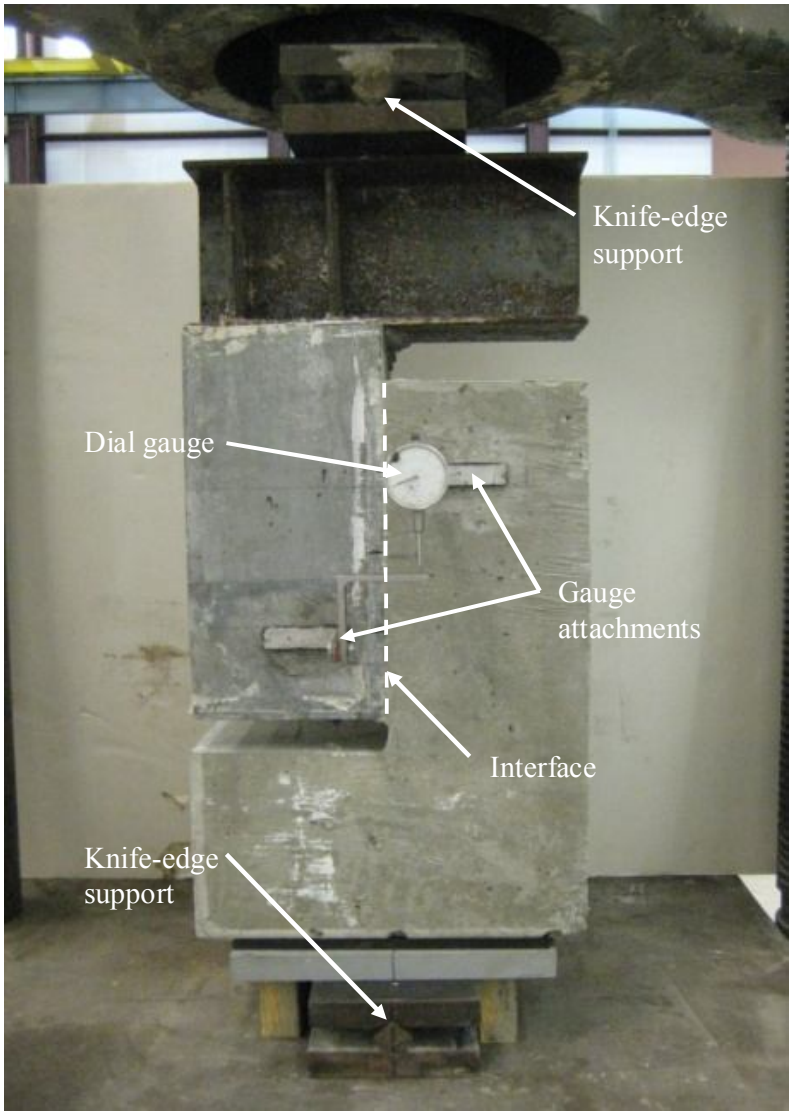

Figure 3-5: Typical loading and push-off test of a composite specimen.

3.4 Experimental Results and Discussion

3.4.1 Monolithic UHPC Results

The ultimate interface shear force recorded for each of the all-UHPC specimens is presented in Table 3-2 along with the predicted capacities from Equation (3-1) and (3-2). Figure 3-6 shows typical load slip behavior of these specimens. The monolithic uncracked specimens with and without shear reinforcement behaved similarly. Initial cracks were observed at loads between 20% and 65% of the peak ultimate capacity and were only visible when alcohol was applied. These cracks were between 1 to 4 in (25 to 102 mm) long and oriented diagonally between 0 to 30 degrees to the shear plane from top and bottom as illustrated in Figure 3-7. This behavior was similar to what was observed by Hofbeck et al. (1969) and Kahn and Mitchell (2002). The unreinforced specimens showed ultimate capacities that were approximately 33% lower than those with the 2-double leg #3 bar stirrup reinforcement.

Table 3-2: Monolithic push-off specimen ultimate shear experimental and predicted values, 1kN=0.225 kip

Specimen Identification		Test value V_{exp} [kip]	ACI[1] predicted Eq. (1) [kip]	AASHTO[2] predicted Eq. (2) [kip]	V_{exp} / V_{ACI} predicted	V_{exp} / V_{AASHTO} predicted
U-U-S-0	A	20.5	0.0	6.9	N/A	3.0
	B	16.5	0.0	7.0	N/A	2.3
	C	17.3	0.0	6.6	N/A	2.6
U-U-S-2	A	49.4	15.8	22.6	3.1	2.2
	B	51.1	15.8	22.6	3.2	2.3
	C	45.7	15.8	22.4	2.9	2.0
U-U-MC-0	A	142.0	0.0	35.3	N/A	4.0
	B	205.5	0.0	35.2	N/A	5.8
	C	148.0	0.0	34.6	N/A	4.3
U-U-MC-2	A	240.5	37.0	72.1	6.5	3.3
	B	129.0	37.0	72.0	3.5	1.8
	C	314.0	37.0	72.7	8.5	4.3
U-U-MU-0	A	226.0	0.0	35.6	N/A	6.4
	B	225.0	0.0	35.9	N/A	6.3
	C	250.3	0.0	35.2	N/A	7.1
U-U-MU-2	A	330.0	37.0	72.8	8.9	4.5
	B	351.0	37.0	71.9	9.5	4.9
	C	369.0	37.0	71.6	10.0	5.2

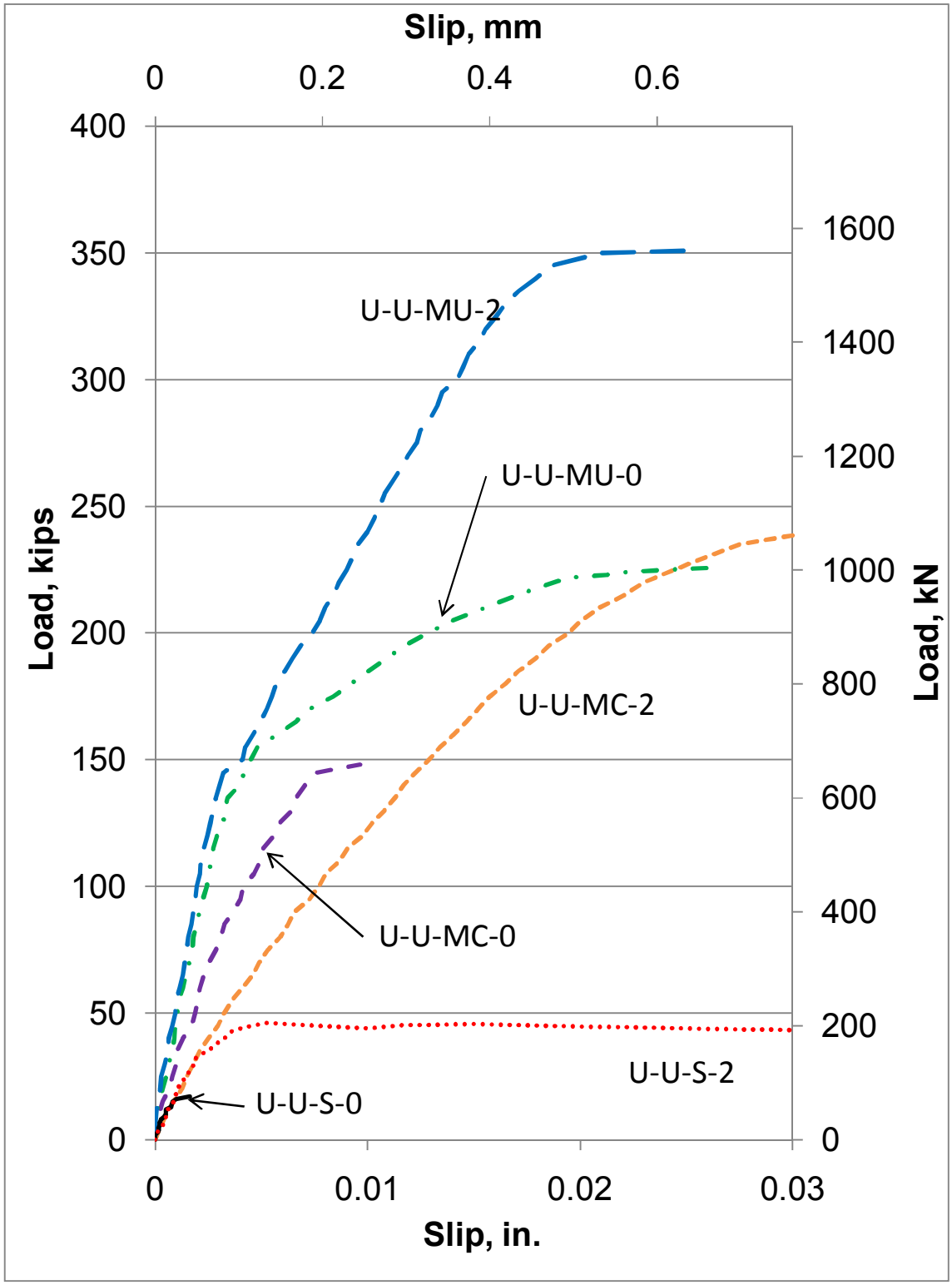

Figure 3-6: Typical load-slip curves for all-UHPC push-off specimens.

Figure 3-7: (a) Overall specimen setup, (b) initial cracking of a typical specimen, (c) & (d) crack initiating at an angle of 0° to 30° to shear plane.

In the pre-cracked monolithic specimens, measurable slip was observed at much lower loads and increased at a greater rate than in the uncracked specimens. As the load approached ultimate, the pre-existing cracks became wider and caused the failure to be localized. The ultimate load in the pre-cracked specimens was 30-35% less on average than the corresponding uncracked specimens, but it varied widely

between specimens. Inconsistent crack width between specimens may have caused this variation. Specimen U-U-MC-2-B in particular was considered to be an outlier as it had less capacity than those cracked specimens without any additional reinforcement. The all-UHPC specimens with a smooth cold joint at the interface showed ultimate capacities that were only 10-20% of those of the uncracked or pre-cracked monolithic UHPC push-offs.

Neither the ACI not AASHTO equations considered the fibers crossing the shear plane. The specimens with "0" stirrups demonstrated that fibers developed high shear friction strengths as further discussed in section 3.4.4.

3.4.2 UHPC/HPC Cold Joint Results

Table 3-3 gives the results of the UHPC/HPC push-off specimens. Figure 3-8 shows typical load slip curves for these tests. The UHPC/HPC specimens with reinforcement all tended to have more gradual changes to the slope of the load-slip curve than did the all-UHPC specimens. This could be due to a more gradual transfer of force from cohesion to shear friction. The fluted UHPC specimens were the exception to this trend. They exhibited much more consistent stiffness up to failure loads. The reinforced fluted specimens carried the most load of the UHPC/HPC specimens, and even the unreinforced fluted specimens carried more load than all but the most heavily reinforced smooth specimens. In general, the unreinforced UHPC/HPC specimens exhibited very brittle failures at much lower loads than their reinforced analogs. Figure 3-9 shows the typical interface crack after loading.

Table 3-3: Experimental and predicted shear capacities of UHPC/HPC push-off specimens, 1kN=0.225 kip

Specimen Identification		Test value V_{exp} [kN]	ACI[1] Predicted Eq. (1) [kN]	AASHTO[2] predicted Eq. (2) [kN]	V_{exp} / V_{ACI} predicted	V_{exp} / V_{AASHTO} predicted
U-H-F-0	A	45.8	0.0	21.0	N/A	2.2
	B	46.6	0.0	21.4	N/A	2.2
U-H-F-2	A	88.0	3.3	47.1	3.3	1.9
	B	117.0	4.4	47.4	4.4	2.5
	C	83.0	3.1	47.5	3.1	1.7
U-H-S-0	A	12.5	0.0	6.8	N/A	1.8
	B	11.8	0.0	6.8	N/A	1.7
	C	18.0	0.0	6.7	N/A	2.7
U-H-S-1	A	26.6	3.3	14.3	3.4	1.9
	B	29.1	3.7	14.6	3.7	2.0
	C	26.9	3.4	14.5	3.4	1.9
U-H-S-2	A	49.0	3.1	22.5	3.1	2.2
	B	40.3	2.5	22.6	2.5	1.8
	C	41.4	2.6	22.5	2.6	1.8
U-H-S-3	A	56.0	2.4	30.4	2.4	1.8
	B	42.4	1.8	30.3	1.8	1.4
	C	60.8	2.6	30.4	2.6	2.0
U-H-B-0	A	33.0	0.0	6.7	N/A	4.9
	B	27.0	0.0	6.6	N/A	4.1
	C	36.0	0.0	6.6	N/A	5.5

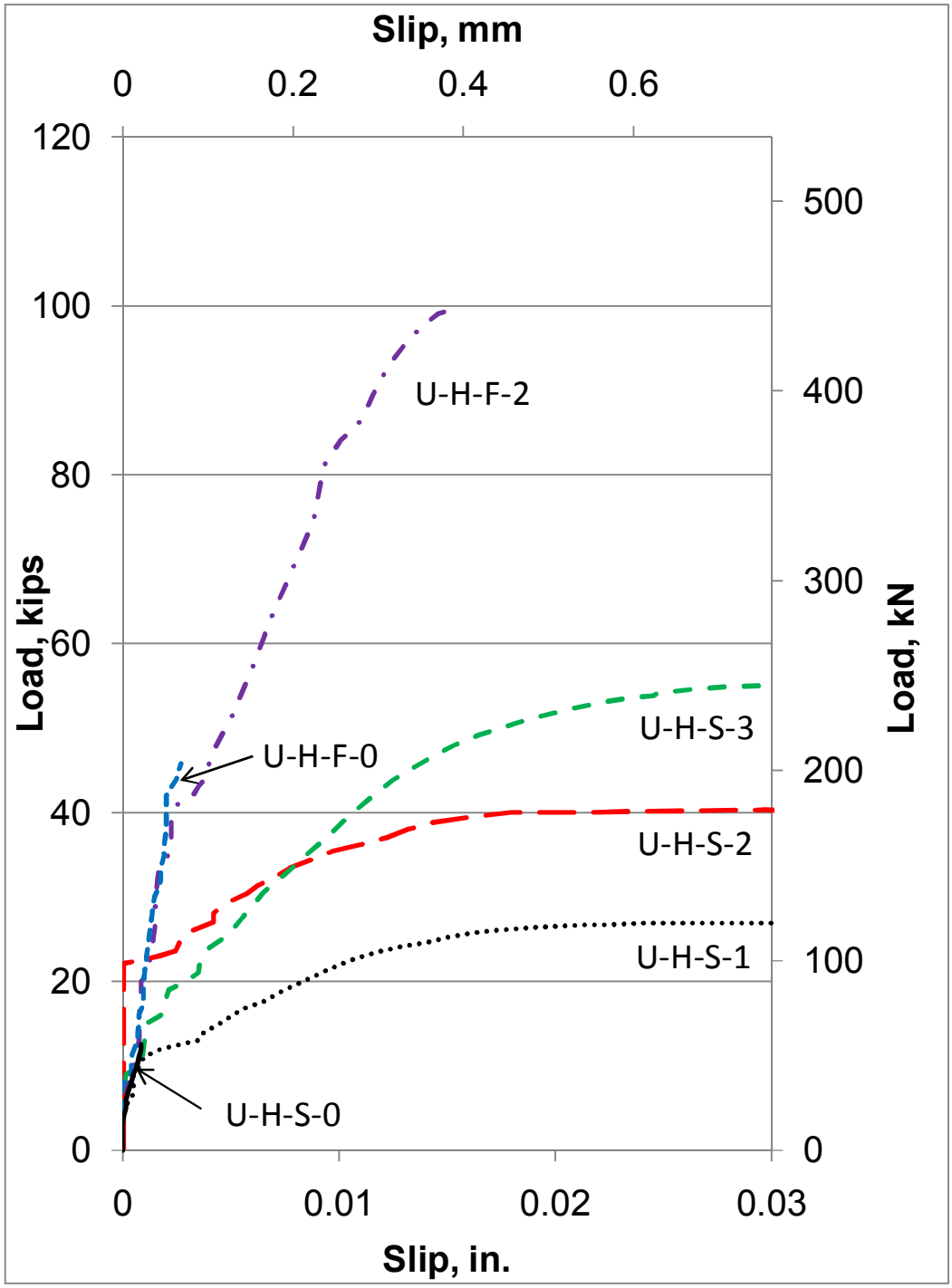

Figure 3-8: Typical load-slip curves for UHPC/HPC push-off specimens. The curves for the unreinforced specimens had approximately the same slope as that shown for U-H-S-0 with maximum values listed in Table 3-2.

a) 

b) 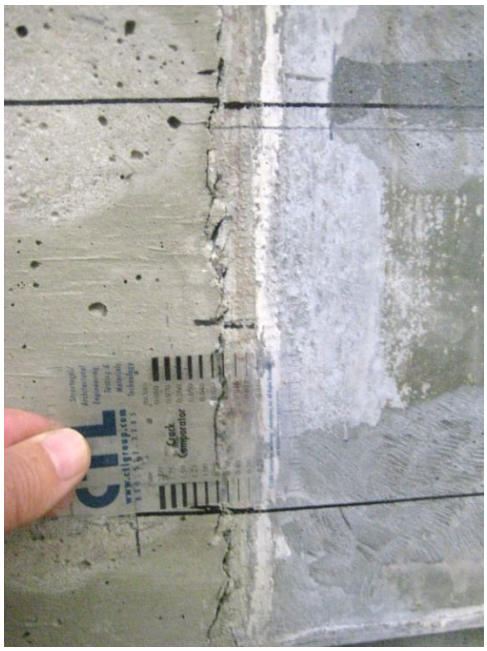
c) 

Figure 3-9: (a) Specimen after testing, (b) slip at joint visible at reinforcement markings, (c) failed fluted interface.

3.4.3 Comparison with Code Equations

Figures 3-10 and 3-11 show the ultimate shear stress, v_u, as a function of the clamping stress, $\rho_v f_y$, for the all-UHPC and UHPC-HPC push-off tests, respectively. For all of these, f_y is limited to 60 ksi (413.7 MPa) as specified by the code. The solid and dashed lines represent equation 3-1 with varying coefficients of friction. All shear stresses are greater than those predicted by equation 3-1 with coefficient of friction, μ, of 1.0. Figure 3-10 shows that the ACI equation is conservative when extended to UHPC.

Figures 3-12 and 3-13 show the same experimental results for all-UHPC and UHPC-HPC specimens, respectively, compared to the equation 3-2. These equations also provide a conservative estimate of the experimental results in all cases.

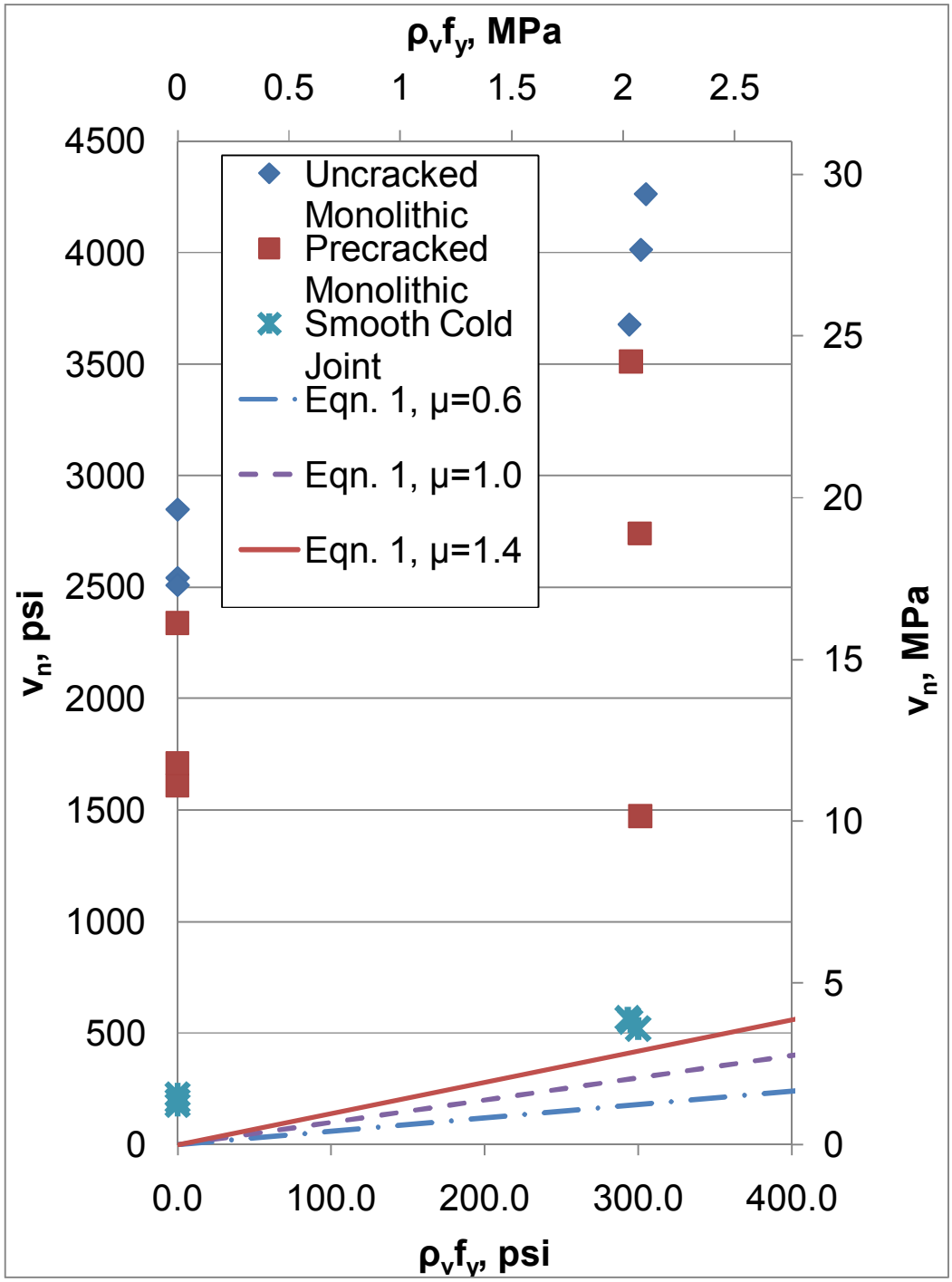

Figure 3-10: Comparison of all-UHPC push-off specimens to ACI shear friction equation, Equation (3-1).

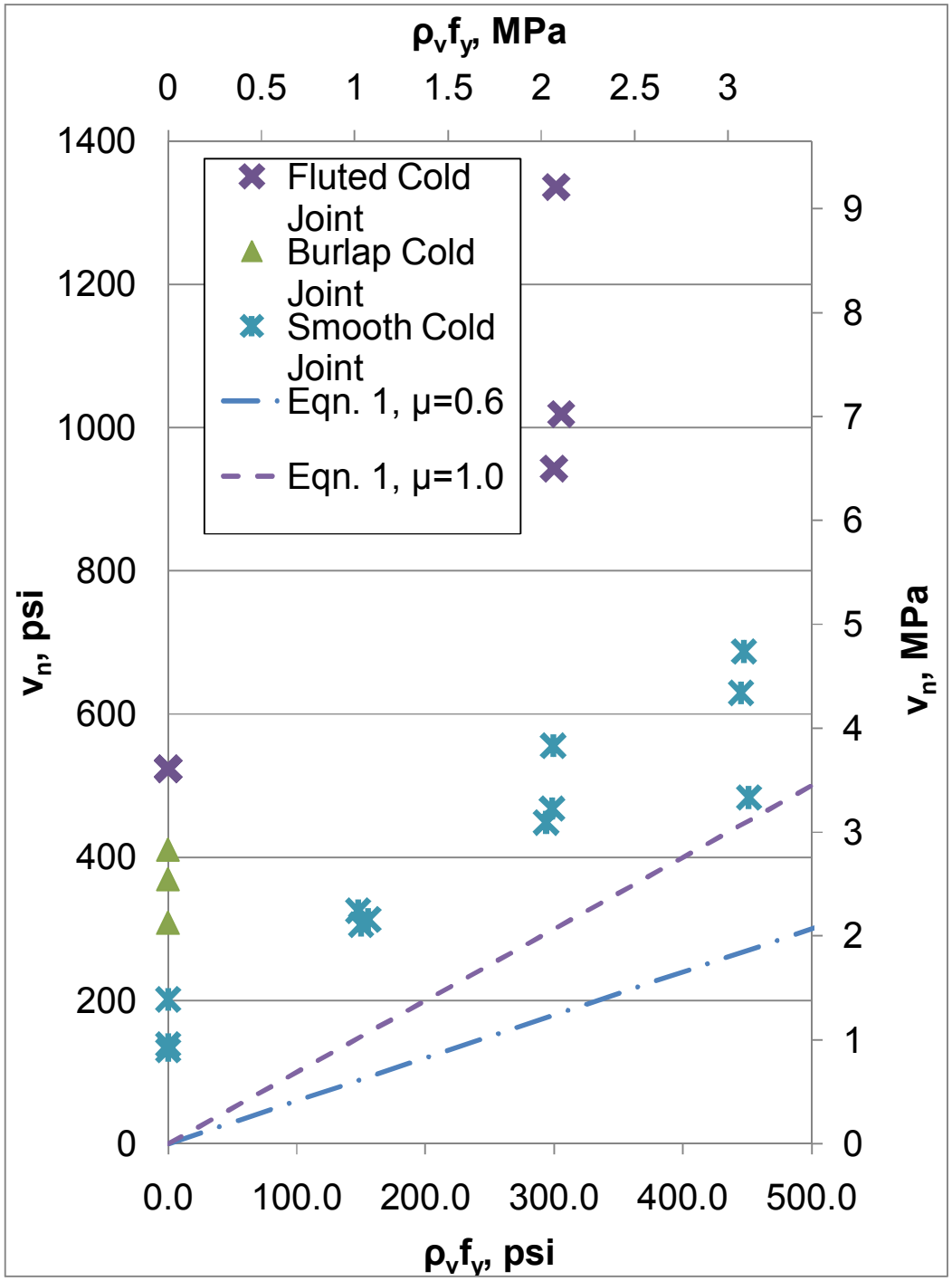

Figure 3-11: Comparison of UHPC-HPC push-off specimens to ACI shear friction equation, Equation (3-1).

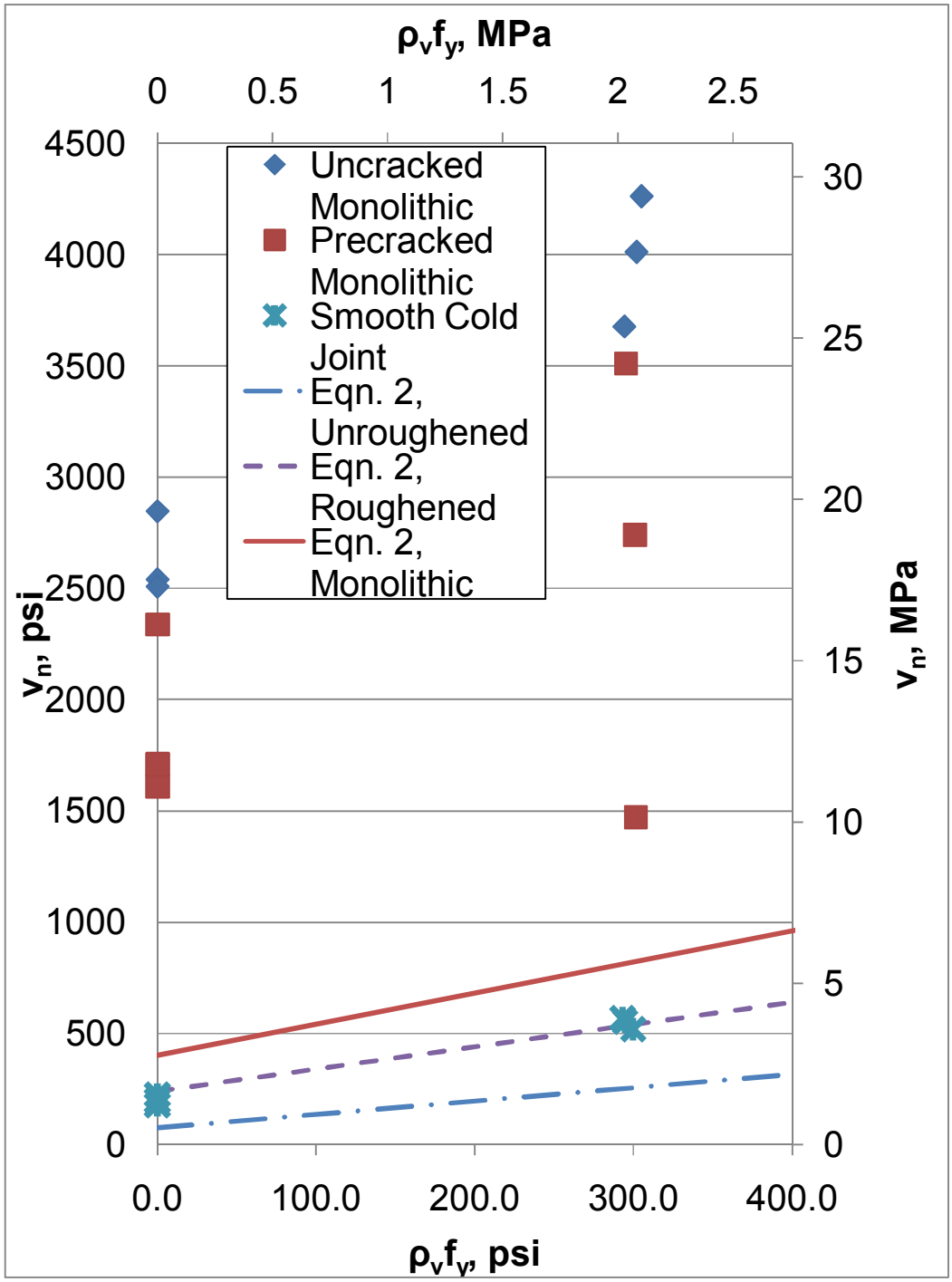

Figure 3-12: Comparison of all-UHPC push-off specimens to AASHTO shear friction equation, Equation (3-2). (1 MPa=145 psi)

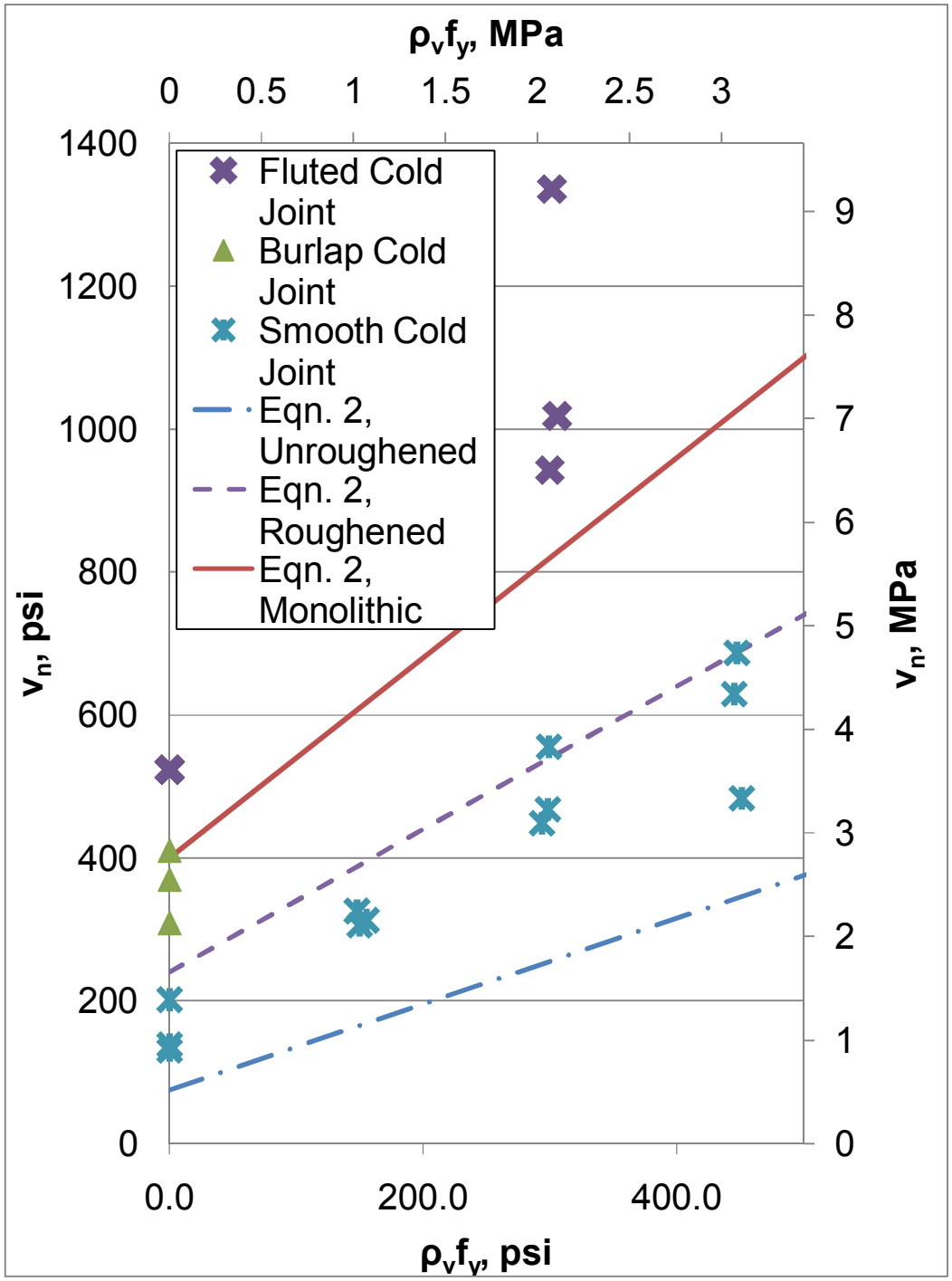

Figure 3-13: Comparison of all-UHPC push-off specimens to AASHTO shear friction equation, Equation (3-2). (1 MPa=145 psi)

3.4.4 Proposed Shear Friction Constants for Monolithic UHPC

Figures 3-10 and 3-12 clearly show that ACI and AASHTO shear friction provisions grossly underestimate the capacity of monolithic UHPC with and without pre-existing cracks. A linear regression analysis was performed on each of these data sets in order to calculate values of c and μ for these cases. These values are beyond the reasonable range for shear friction theory. They are presented as a design guide with the understanding that they are not reasonable "friction coefficients" from a phenomenological level.

Figure 3-14 shows the linear regression for the monolithic uncracked UHPC specimens. The equation of the line was:

$$2,629 + 4.527\rho_v f_y . \tag{3-5}$$

Based on the regression data, a 90% confidence interval for an individual predicted value was also plotted in Figure 3-14. The lower bound of this confidence interval represents the level below which only 5% of samples are predicted to lie. For ease of use and consistency with existing equations, a linear approximation of this line is suggested for design use. For use of ACI and AASHTO shear friction equations, μ = 4.5 and c = 2,000. These values should be limited to clamping forces below 300 psi until further testing can be performed at higher reinforcement ratios.

Figure 3-15 shows the linear regression for the monolithic cracked UHPC specimens excluding test U-U-MC-2-B, which was determined to be an outlier. The equation of the line was:

$$v_u = 1888 + 4.140\rho_v f_y . \tag{3-6}$$

Equation values were predicted as detailed above yielding μ = 4.0 and c = 650. Again these values should be limited to use when clamping force is less than 300 psi.

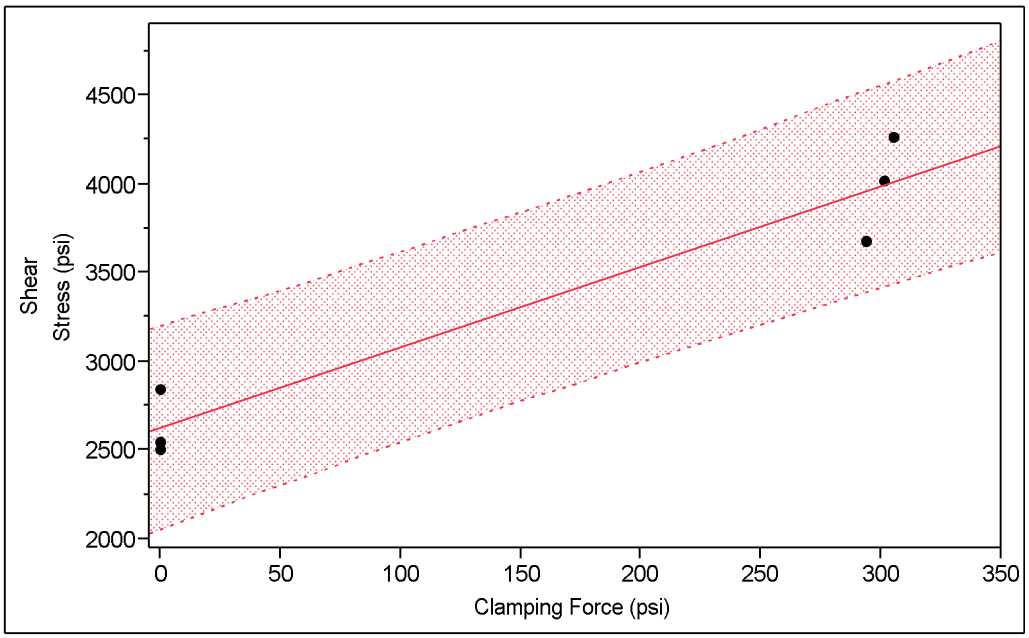

Figure 3-14: Linear regression analysis of uncracked monolithic push-off capacities with 90% confidence interval for an individual predicted value.

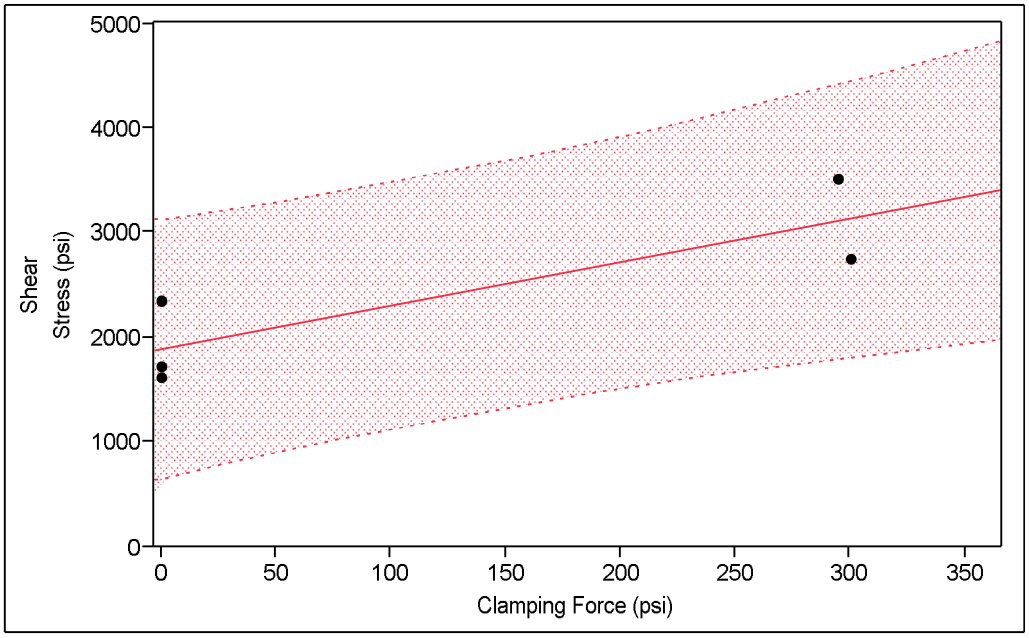

Figure 3-15: Linear regression analysis of precracked monolithic push-off capacities with 90% confidence interval for an individual predicted value.

3.4.5 Effect of Interface on Performance of All-UHPC Specimens

Based on Figure 3-6, it was observed that the pre-cracked specimens and cold-joint specimens exhibited similar initial slopes, both of which were less than those slopes observed for the uncracked specimens. This difference in slope suggests that microslipping began across the pre-cracked and cold joint interfaces even at very low loads. The pre-cracked specimens with and without stirrup reinforcement had capacities that were 150-180 kip (670-800 kN) greater than their cold joint counterparts. This increase in capacity shows the large contribution of the steel fibers in transferring shear across the interface. It also emphasizes the very low UHPC to UHPC bond developed when surfaces are left smooth.

3.4.6 Effect of Reinforcement Ratio on Performance of All-UHPC Specimens

As expected, the specimens with reinforcement exhibited much more ductile failures than the unreinforced all-UHPC specimens. The reinforced specimens also exhibited increased load carrying capacity with the uncracked, pre-cracked, and cold joint specimens with reinforcement carrying 50, 38, and 170% more load than the equivalent specimens without reinforcement. The increase in clamping force acts in the way predicted by shear friction theory. For smooth cold joints, a friction coefficient, μ = 0.6, was a conservative predictor of performance as clamping force increased. For monolithic specimens with and without existing cracks, μ = 1.4 provided an overly conservative prediction, underestimating the capacity by at least 300%. The suggested values from section 3.4.4 give a prediction that is 65% of the observed value on average.

3.4.7 Effect of Surface Preparation on Performance of Cold Joint UHPC/HPC Specimens

From Figure 3-8 it was obvious that surface roughness of these specimens had a large impact on the interface shear capacity. In unreinforced specimens, the burlap-roughened surface increased the interface shear capacity over the smooth cold joint by 127% while the fluted surface increased the shear capacity by 228%. In specimens with 0.5% reinforcement ratios, the fluted surface increased the interface shear capacity of the specimens by 120%. For all fluted surfaces specimens, the ACI recommended friction coefficient, = 1.0, was conservative. Even when the coefficient was taken as 1.4, the ACI and AASHTO codes provided conservative estimates.

3.4.8 Effect of Reinforcement Ratio on Performance of UHPC/HPC Specimens

In specimens with a smooth interface, the shear capacity appeared to increase linearly with the increase in reinforcement ratio. This supports the shear friction theory and its applicability to UHPC/HPC interfaces even when a smooth joint is used with a friction coefficient = 0.6. When a fluted joint was used, the use of a 0.5% reinforcement ratio increased the interface shear capacity by 108%. For both types of fluted-joint specimen, the shear friction theory was conservative with the ACI specified friction coefficient = 1.0.

3.5 Conclusions

Based on the current research in shear transfer in monolithic and cold-joint push-off specimens, the following conclusions were made:

1. Current ACI and AASHTO provisions are conservative for estimating interface shear capacity of composite UHPC/HPC structures. For monolithic UHPC, these equations vastly underestimate performance. New constants suggested by this research increase the accuracy of the performance measurement while maintaining conservatism.
2. Formliners can be successfully used to create a fluted surface finish in UHPC that is comparable to the 6 mm (1/4-in.) surface roughness recommended by current codes for composite construction. This surface finish provides significant increase in interface shear capacity, particularly when used in conjunction with reinforcing steel crossing the interface.
3. In monolithic UHPC, steel fibers allow for significant shear transfer across pre-existing cracks even when no additional shear reinforcement is used; however, smooth cold joints in UHPC have very low interface shear capacities when transverse shear reinforcement is not used.

3.6 References

AASHTO (2007). *AASHTO LRFD bridge design specifications*. Washington, D.C., American Association of State Highway and Transportation Officials.

ACI Committee 318 (2008). *Building code requirements for structural concrete : (ACI 318-08) ; and commentary (ACI 318R-08)*. Farmington Hills, Mich., American Concrete Institute.

Anderson, A. R. (1960). "Composite designs in precast and cast-in-place concrete." *Progressive Architecture* 41(9): 8.

Birkeland, P. W. and H. W. Birkeland (1966). "Connections in precast concrete construction." *ACI Journal* 63(3): 345-367.

Crane, C. K. and L. F. Kahn (2009). Field Evaluation of Ultra-High Performance Concrete, Task 4 Report, Ultra-High Performance Concrete for Precast Prestressed Bridge Girders. Georgia Department of Transportation, Atlanta, GA.

Graybeal, B. A. (2005). Characterization of the Behavior of Ultra-High Performance Concrete. *Civil and Environmental Engineering*. Doctor of Philosophy Thesis. University of Maryland, College Park.

Hanson, N. W. (1960). "Precast-Prestressed Concrete Bridges: 2. Horizontal Shear Connections." *Journal of the PCA Research and Development Laboratories* 2(2): 38-58.

Hofbeck, J. A., I. O. Ibrahim, et al. (1969). "Shear transfer in reinforced concrete." *ACI Journal* 66(2): 119-128.

Kahn, L. F. and A. D. Mitchell (2002). "Shear Friction Tests with High-Strength Concrete." *ACI Structural Journal* 99(1): 98-103.

Mast, R. F. (1968). "Auxiliary reinforcement in concrete connections." *Journal of the Structural Division, ASCE* 94(6): 1485-1504.

CHAPTER 4
INTERFACE SHEAR CAPACITY OF SMALL COMPOSITE T-BEAMS

4.1 Introduction

The purpose of this research was to evaluate AASHTO LRFD and ACI interface shear requirements for composite T-beams with a "precast" ultra high performance concrete (UHPC) web and a cast-in-place high performance concrete (HPC) deck. The goals were to compare the results obtained with current code provisions and to determine if the current codes can be used to satisfy strength and serviceability requirements in precast UHPC girders with HPC decks.

The scope of the research was restricted to five T-beams cast using UHPC for the web with a compressive strength of 29 ksi (200 MPa) and HPC for the deck with a design compressive strength of 8 ksi (55 MPa), which yielded an actual strength of 12 ksi (83 MPa). Each beam was constructed with either a smooth interface (no roughening), burlap roughened, or a fluted form liner (¼-in. (6 mm) roughened) interface between the web and the deck slab. The transverse reinforcement ratio ranged between 0 and 0.286 percent for all beams.

4.2 Research Significance

Ultra high performance concretes (UHPCs) are being considered for construction of precast pretensioned highway bridge girders. These concretes have self-consolidating properties, include steel fiber reinforcement, and use a maximum size aggregate of less than 2mm. These properties create a smooth surface upon placement and prevent the

concrete surface from being roughened by raking. Therefore, it is not possible to create, in the usual manner, the ¼-in. (6 mm) surface roughness specified by ACI 318 (2008) and AASHTO LRFD (2010). The interface properties between UHPC girder and cast-in-place concrete deck must be investigated to determine if current shear friction concepts can be utilized in design with UHPC.

4.3 Background

AASHTO LRFD (2010) provides an equation for shear friction along an interface between two concretes cast at different times. As long as minimum transverse reinforcement requirements are met, the nominal shear resistance of the interface plane is given in Eq. (4-1):

$$V_n = cA_{cv} + \mu[A_v f_y + P_c] \leq V_{n\,max} \tag{4-1}$$

where

V_n = nominal shear strength, lb

c = cohesion factor,

75 psi (0.52 MPa) for a clean concrete surface, not roughened,

280 psi (1.9 MPa) for a roughened surface with a ¼-in. (6 mm) amplitude,

400 psi (2.76 MPa) for concrete cast monolithically

A_{cv} = area of concrete considered to be engaged in interface shear transfer ($b_{vi}d_v$), in^2

μ = friction factor

1.0 for a roughened surface with a ¼-in. (6 mm) amplitude,

0.6 for a not intentionally roughened surface

1.4 for concrete cast monolithically

A_v = area of interface shear reinforcement crossing the shear plane within the area A_{cv}, in^2

f_y = yield stress of transverse reinforcement, psi

P_c = permanent net compressive force normal to the shear plane, lb

b_{vi}= interface width considered to be engaged in shear transfer, in.

d_v= the distance between the centroid of the tension steel and the mid-thickness of the slab to compute a factored interface shear stress.

K_1 = concrete cohesion term that is related to strength,

0.3 for cast in place slab cast against roughened girder

0.25 for normalweight concrete placed monolithically, normalweight and lightweight concrete with a roughened surface,

0.2 for normal weight concrete placed against non-roughened surface or cast against studded steel girders

K_2 = maximum allowable interface stress

1.8 ksi for normal-weight concrete deck cast against roughened girder,

1.5 ksi for normal-weight concrete cast against roughened concrete or placed monolithically

1.3 ksi for lightweight concrete deck cast against roughened girder,

1.0 ksi for lightweight concrete cast against roughened concrete or placed monolithically

0.8 ksi for concrete cast against studded steel girders

ACI 318 (2008) gives a similar equation for shear friction along an interface with minimum transverse reinforcement. This equation is given in Eq. (4-2) in customary in.-lb units:

$$V_n = \left(260 + 0.6\rho_v f_y\right)\lambda b_v d \le 500 b_v d \tag{4-2}$$

where

s = spacing of transverse reinforcement, in.

ρ_v = transverse reinforcement ratio, $\frac{A_v}{b_v s}$

b_v = interface width considered to be engaged in shear transfer, in.

d = distance from top of slab to centroid of bottom tensile reinforcement, in. (note difference from d_v in AASHTO equation).

Furthermore, both AASHTO LRFD (2010) and ACI (2008) permit the shear friction equation given in Eq. (4-3) to be used when evaluating interface shear strength:

$$V_n = \mu A_v f_y \tag{4-3}$$

not greater than the smaller of:

$0.2 f_c' A_{cv}$,

$(480 + 0.08 f_c') A_{cv}$,

or $1600 A_{cv}$

where

μ = coefficient of friction, 1.4 for a monolithic concrete connection,

1.0 for a cold joint with ¼ in. (6 mm) roughness amplitude, and

0.6 for a cold joint at a smooth concrete interface

A_{cv} = area of shear reinforcement across shear plane, in^2

f_y = yield stress of transverse reinforcement (≤ 60,000 psi)

f_c' = weaker compressive strength of the flange or web concrete, psi.

Neither Eq. (4-1) nor Eq. (4-2) takes into account the concrete compressive strength (f_c'), and Eq. (4-3) only uses compressive strength as an upper boundary. Yet several authors have investigated the influence of f_c' on nominal shear strength of beams. Loov and Patnaik (1994) performed tests on 16 composite beams with varying concrete strengths, web widths, stirrup spacing and two different flange lengths. They also made sure that the surface between the flange and web was left rough and that course aggregate was protruding. Loov and Patnaik proposed Eq. (4-4), which calculates nominal shear stress capacity and takes into account the roughed surface as well as f_c':

$$v_n = k\lambda\sqrt{(15 + \rho_v f_y) f_c'} \tag{4-4}$$

where

v_n = nominal shear stress, psi

k = roughness constant equal to 0.6 for rough surfaces and 0.5 for smooth surfaces

λ = correction factor related to concrete density

Loov and Patnaik concluded that the stirrups did not attribute to shear resistance until the horizontal shear stress reached 220 to 290 psi (1.5 to 2 MPa), suggesting that the roughened surface provided adequate shear resistance before this stress range.

Fifty push-off specimens were tested by Kahn and Mitchell (2002) to determine if current design standards may be used for high strength concretes. Concrete compressive strengths ranged between 6,800 and 17,900 psi (47 and 123 MPa), and transverse reinforcing ratios between 0.0037 and 0.0147. Testing concluded that both AASHTO and ACI were conservative estimates for shear resistance when using high strength concretes.

Kahn and Mitchell introduced Eq. (4-5) that is applicable for both monolithic concrete and as-cast cold joints, with a friction coefficient equal to 1.4:

$$v_n = 0.05 f_c' + 1.4 \rho_v f_y \leq 0.2 f_c' \tag{4-5}$$

where

f_y = yield stress of transverse reinforcement (≤60,000psi).

Kahn and Slapkus (2004) tested 6 composite beams with precast, high strength concrete webs with compressive strengths of 12,120 psi (83.6 MPa), and cast-in-place decks with compressive strengths of either 7,280 or 11,290 psi (50.2 or 77.8 MPa). The tests concluded that both AASHTO and ACI provisions were a conservative estimate for interface shear resistance of composite beams with high strength concrete made with an intentionally roughed interface with protruding aggregate.

4.4 Test Setup

The five composite beams were constructed to replicate the tests run by Kahn and Slapkus and to compare shear friction push-off results with the interface shear results of these composite beam tests. Each beam was 120-in. (3.05 m) long with 114-in. (2.9 m) span between supports. The cast-in-place deck slab had a reduced length of 88 in. (2.2 m) in order to force an interface shear failure. The "precast" web had a depth of 10-in. (254 mm) and a width of 6-in. (152 mm) while the slab depth was 5½-in. (140 mm) deep by 16.5-in. (419 mm) wide as shown in Figures 4-1 and 4-2. The confined area under the compressive load was not assumed to resist interface shear so the interface area, A_{cv}, of each beam was calculated to be 462 in^2 (0.298 m^2).

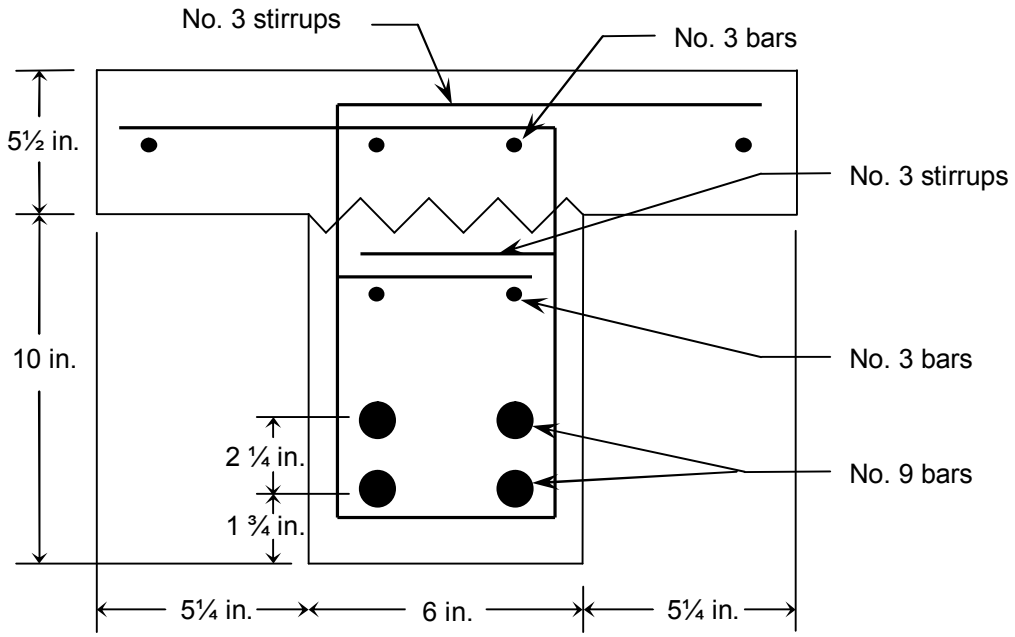

Figure 4-1: Typical T-beam cross section. Note: 1 in. = 25.4 mm; No. 3 bar = 10 M; No. 9 bar = 29 M.

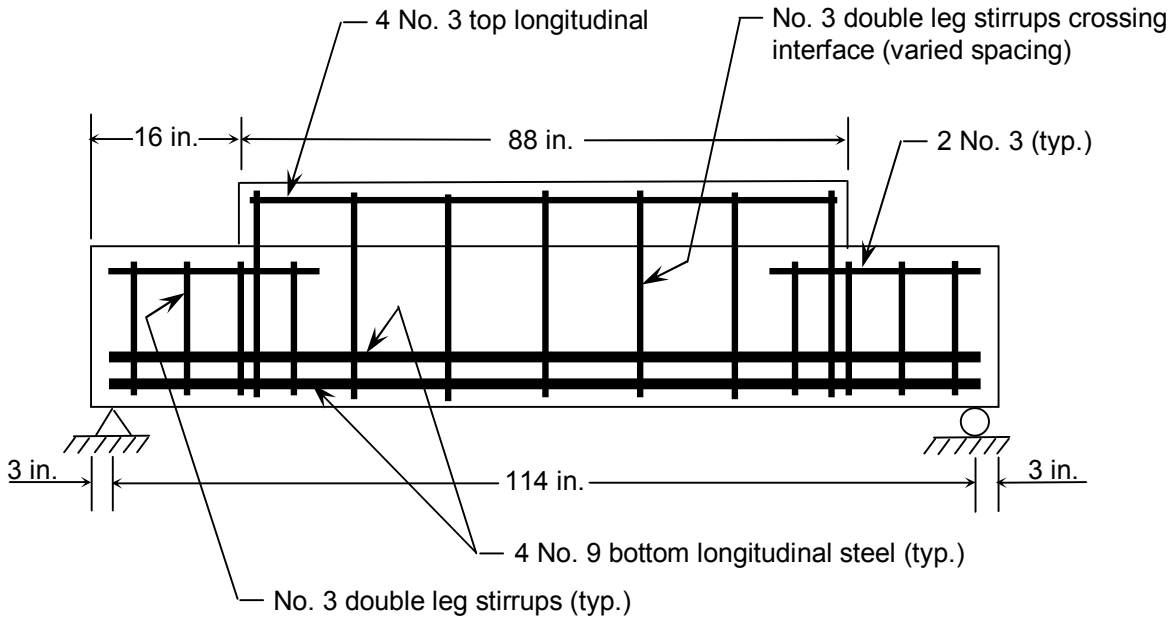

Figure 4-2: Typical reinforcement for all beams. Note: 1 in. 25.4 mm; No. 3 bar = 10 M; No. 9 bar = 29 M.

The web was cast using UHPC at Tindall Corporation precast concrete plant, Conley GA. Two days after casting, the web was thermally treated at 194°F (90°C) for 48 hours. The UHPC was Lafarge Ductal® using 2% by volume steel fiber reinforcement. The 28-day mean compressive strength was 28,930 psi (199.5 MPa). Three hundred and forty two days after casting the web, the deck was placed using conventional high performance concrete (¾-in. (19 mm) maximum size aggregate) delivered by ready-mix. The HPC had a compressive strength at the time of testing of 12,170 psi (83.9 MPa). All reinforcement was A615, Grade 60 (415 MPa). The elastic modulus for both the No. 9 (29 M) and No. 3 (10 M) bars was taken as 29,000 ksi (200 GPa).

The main variation between each composite beam was the interface between the web and the flange and the number of stirrups. The top surface of the UHPC beams proved impossible to roughen by raking, brooming, or cutting with a trowel. To make a rough interface, a form liner was used to create 0.25 in. (6 mm) flutes analogous to the roughness amplitude required by codes. The variations between all five of the beams tested can be seen in Table 4-1. At the suggestion of Mr. Peter Calcetas of Lafarge North America, burlap was placed atop the interface of one beam containing no reinforcement. The burlap was supposed to create a textured surface, which was to provide an improved bond to the deck slab. The burlap proved difficult to remove from the surface after the initial 48-hour cure and significant wire brushing was required. Further, during moving of a sixth beam intended to be tested that contained a smooth interface and no reinforcement, the deck fell off; that is, there was little bond between the web and slab. The latter beam was not included in any tables but data for the non-composite UHPC section by itself are included in load-deflection results.

Table 4-1: Summary of Experimental Results

Beam	ρ_v (percent)	Clamping Stress (psi)	Maximum Load (lb)	Load at slip (lb)	Number of Stirrups	Type of Interface
0-B	0.000	0	63,067	13,724	0	Smooth
4-S	0.190	114	64,754	14,719	4	Smooth
7-S	0.286	171	71,083	17,890	7	Smooth
0-FL	0.000	0	66,657	49,270	0	Fluted
7-FL	0.286	171	93,321	93,321	7	Fluted

The beams were designated using the following convention X-Y where the first term indicates the number of double-legged No. 3 (10 M) stirrups crossing the interface and the second term indicates the type of interface between the web and the flange. B denotes a burlap interface, S denotes a smooth cold joint interface and FL denotes a form liner interface with ¼-in deep by ½-in. wide (6 by 13 mm) flutes.

Each beam was tested between 697-703 days after web casting and 355-361 days after deck casting. Each beam was loaded in three-point bending as illustrated in Figure 4-3. Four mechanical strain gauges made with linear variable displacement transducers (LVDTs) were placed at the midspan of the beam on both sides near the bottom and top of the web. Each had a gauge length of 16-in. (406 mm). Along with the strain gauges, two LVDT slip gauges were placed on one side of the beam. The body of the LVDT was attached to the web while the extension portion of the LVDT was attached to the underside of the cast-in-place deck to measure slip between the beam and deck. Finally, the midspan deflection was measured using a string potentiometer.

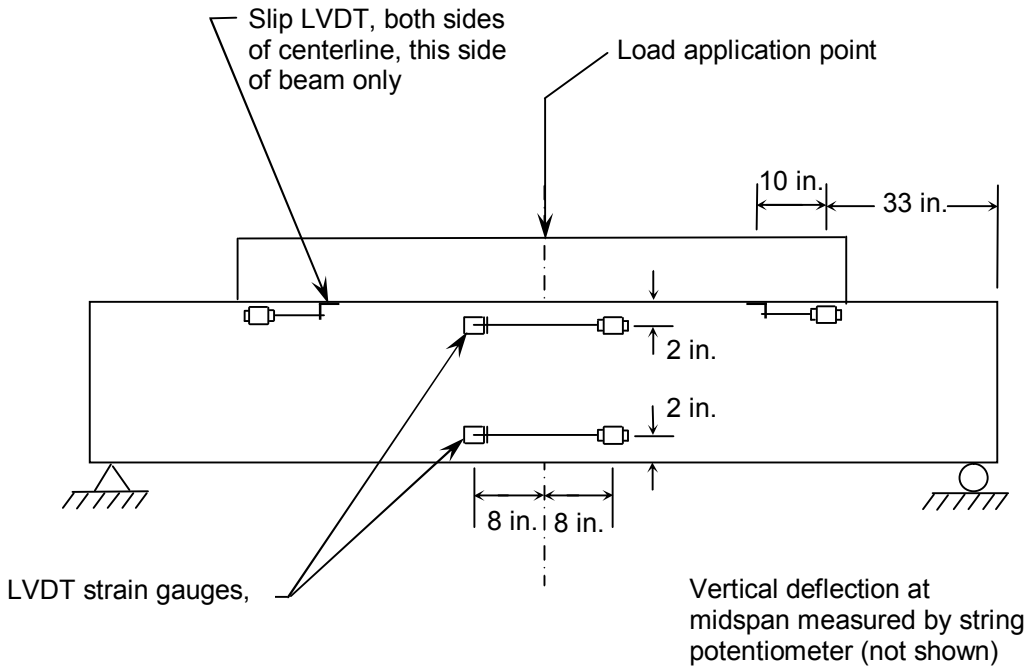

Figure 4-3: Typical loading test set-up and instrumentation.

4.5 Experimental Results and Discussion

For all five beams, the primary failure mode was cracking and slipping between the web and the flange – interface shear failure. Figure 4-4 compares the load deflection curves for all five composite beams plus a plain beam without a deck. Interface failure was assumed to occur when there was a significant decrease in flexural stiffness and a sudden jump in the slip between web and flange. This interface failure is denoted on Figure 4-4 with a circle on each load deflection curve.

Even prior to the noted interface slip, there were distinct differences in the slopes of the load-deflection (P-Δ) curves for each specimen. Table 4-2 gives the stiffnesses for each specimen prior to the interface slip marked in Figure 4-4. Based on these values, it

is clear that even prior to loss of full composite action or gross slipping of the deck, only partial composite action was attained in the beams with smooth interfaces. Among these beams, the preliminary stiffness increased as the reinforcement ratio increased. This trend suggests that larger amounts of interface steel do reduce initial slippage. The two beams with fluted interfaces showed the highest stiffnesses initially. This shows that the fluted surface creates a more fully composite connection than does a smooth surface.

Based on a transformed moment of inertia of 2,422 in^4 ($1.008x10^{-3}$ m^2) and an elastic modulus of 7,860 ksi (54.2 GPa) for UHPC, the expected initial composite stiffness was $19.0x10^6$ kip-in^2 (54,500 kN-m^2). This was more than twice the highest observed experimental value. For the plain beam, the expected initial stiffness was $4.36x10^6$ kip-in^2 (12,500 kN-m^2), which was almost twice that observed. Several possible causes of this discrepancy were suggested including geometric differences, but no conclusive cause was discovered.

There was a drastic difference between the slip load for beams that had a smooth or burlap interface and the beams that had fluted interfaces. It was observed that the greatest interface shear capacity was obtained from the beam that contained a form liner interface along with 7 stirrups crossing the interface. The beam with a burlap-roughened interface and no stirrups had the least interface shear capacity. After composite action was lost, the beams behaved similarly to the plain beam as can be seen in Figure 4-4.

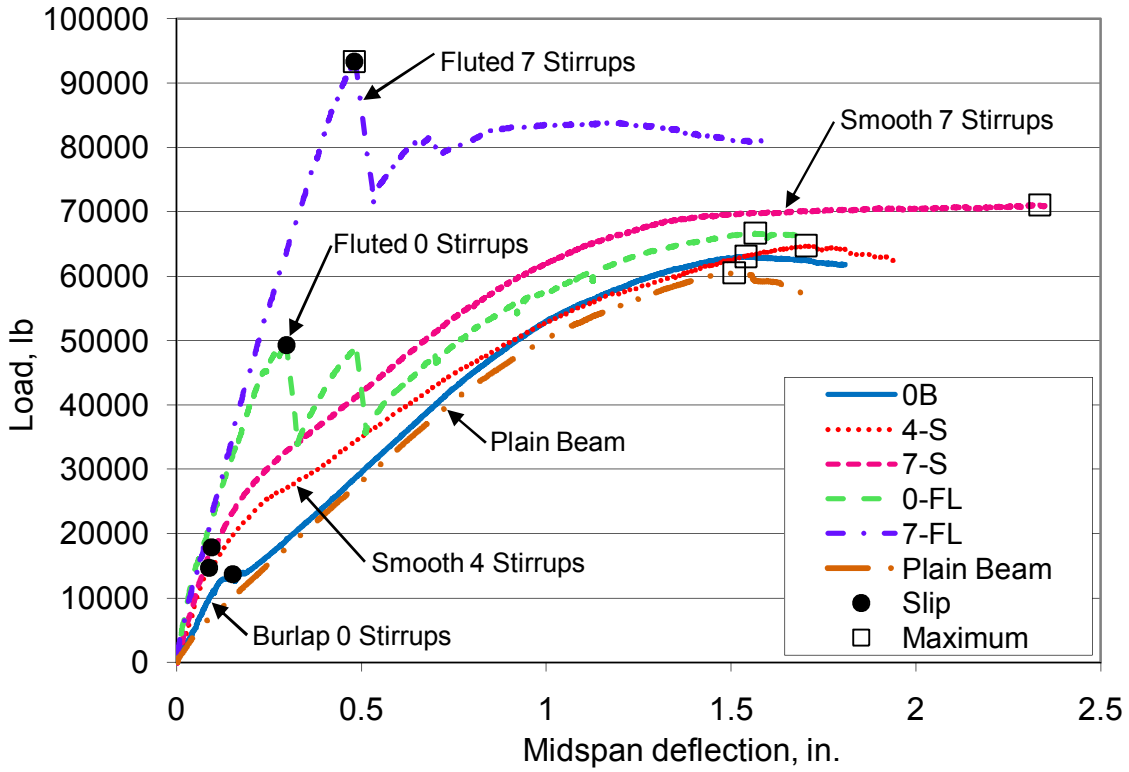

Figure 4-4: Load-deflection plots for beams with slip and max load denoted. Note: 1 in. = 25.4 mm; 1 lb = 4.45 N

Table 4-2: Initial stiffnesses of composite t-beams.

Beam	Interface Surface Preparation	Interface Reinforcement Ratio, ρ_v, percent	Initial Slope of Load-Deflection Curves, lb/in (kN/m)	Initial Composite Stiffness [EI], kip*in^2*10^6 (kN*m^2)
Plain Beam	N/A	N/A	89.2 (15.6)	2.67 (7,700)
0-B	Smooth	0.000	111 (19.4)	3.41 (9,800)
4-S	Smooth	0.190	179 (31.3)	5.52 (15,800)
7-S	Smooth	0.286	197 (34.5)	6.09 (17,500)
0-FL	Fluted	0.000	286 (50.1)	8.83 (25,300)
7-FL	Fluted	0.286	271 (47.5)	8.36 (24,000)

Figure 4-5 compares the moment curvature diagrams for four of the composite beams and the plain beam to the theoretical moment curvature calculated using the computer program Response 2000 developed by Bentz (2000). The beam designated 0-FL is not included because there was insufficient data to calculate an experimental curvature. Stiffer behavior in experimental beams than predicted by Response 2000 can be explained by the non-negligible tensile capacity of the UHPC.

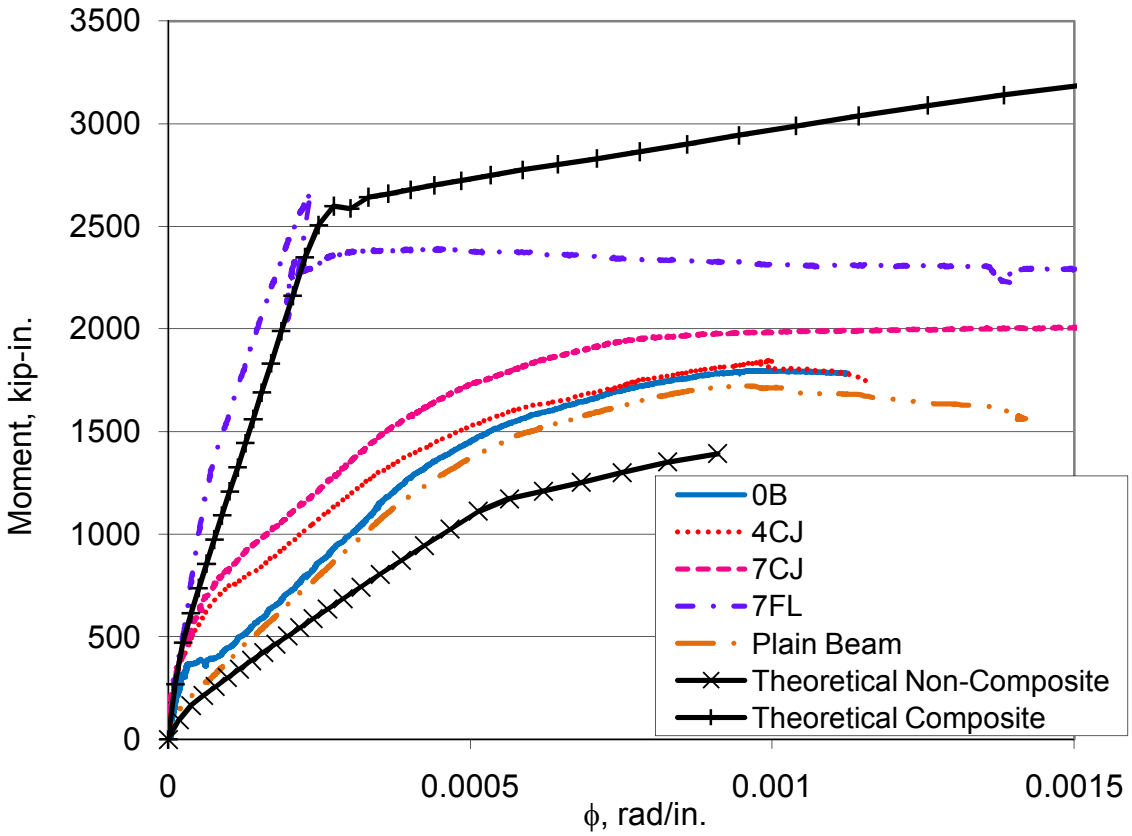

Figure 4-5: Moment-curvature plots for beams with theoretical moment-curvature curves plotted. Note: 1 in = 25.4 mm; 1 lb = 4.45 N

The grooves made with the form liner were the key component in providing composite strength. The beams that did not use form liner failed at an average load of

15,444 lbs (68,698 N), while the beams that did use form liner failed at an average load of 71,296 lbs (317,140 N). For the beam containing both stirrups and form liner, the maximum load was the load at interface failure; therefore, this combination provided the greatest composite interface shear capacity.

Table 4-2 compares the experimental interface shear stress based on two loads: the load at interface failure and the maximum load. These two criteria were chosen because, while there is still a substantial amount of strength remaining in the beam once the interface has failed, the stiffness has been substantially reduced. The experimental interface shear stress was obtained using ACI interface stress from Equation (4-2):

$$v_{\exp} = \frac{V_u}{b_v d} \tag{4-6}$$

where

V_u = shear at failure load being considered, lb.

b_v = interface width considered to be engaged in shear transfer, in.

d = distance from top of slab to centroid of bottom tensile reinforcement, in.

Along with the experimental interface shear stress, Table 4-3 contains the interface shear stress capacities calculated using the equations 4-1 through 4-5.

Table 4-3: Experimental and predicted interface shear stresses, psi (MPa)

Beam	Experimental (Max) v_{exp}	Experimental (Slip) v_{exp}	ACI Shear Friction Eq. (4-3)	Kahn and Mitchell Eq. (4-5)	Loov and Patnaik Eq. (4-4)	AASHTO LRFD Eq. (4-1)	ACI Eq. (4-2)
0-B**	416 (2.87)	86 (0.59)	0	608* (4.19)	214* (1.48)	75 (0.52)	260* (1.79)
4-S	427 (2.94)	97 (0.67)	68 (0.47)	768* (5.30)	626* (4.32)	143 (0.99)	328* (2.26)
7-S	469 (3.23)	117 (0.81)	103 (0.71)	848* (5.85)	752* (5.19)	178 (1.23)	363* (2.50)
0-FL	440 (3.03)	325 (2.24)	0	608 (4.19)	214 (1.48)	280 (1.93)	260 (1.79)
7-FL	616 (4.25)	616 (4.25)	171 (1.18)	848 (5.85)	752 (5.19)	451 (3.11)	363 (2.50)

*These equations assume a roughened interface that was not provided.

**0-B assumed unroughened surface because ¼ in. amplitude was not achieved with the burlap interface.

Figures 4-6 through 4-10 compare the experimental interface shear stress (both maximum and slip loads) to the interface shear stress calculated from the five equations. Table 4-4 and Table 4-5 give the ratio of the experimental interface shear stress (both maximum and slip loads) to the theoretical interface shear stress calculated using the equations 4-1 through 4-5 above. It was observed that the ACI equation (4-2) provided the best conservative estimate for stress along the interface when compared to the experimental interface shear stress due to maximum loads. At the experimental interface shear stress due to slip loads, the ACI interface shear equation (4-3) was the only equation to provide consistently conservative performance estimates. It should be noted that ACI equation (4-2) assumed a roughened surface and was conservative for specimens with fluted surfaces.

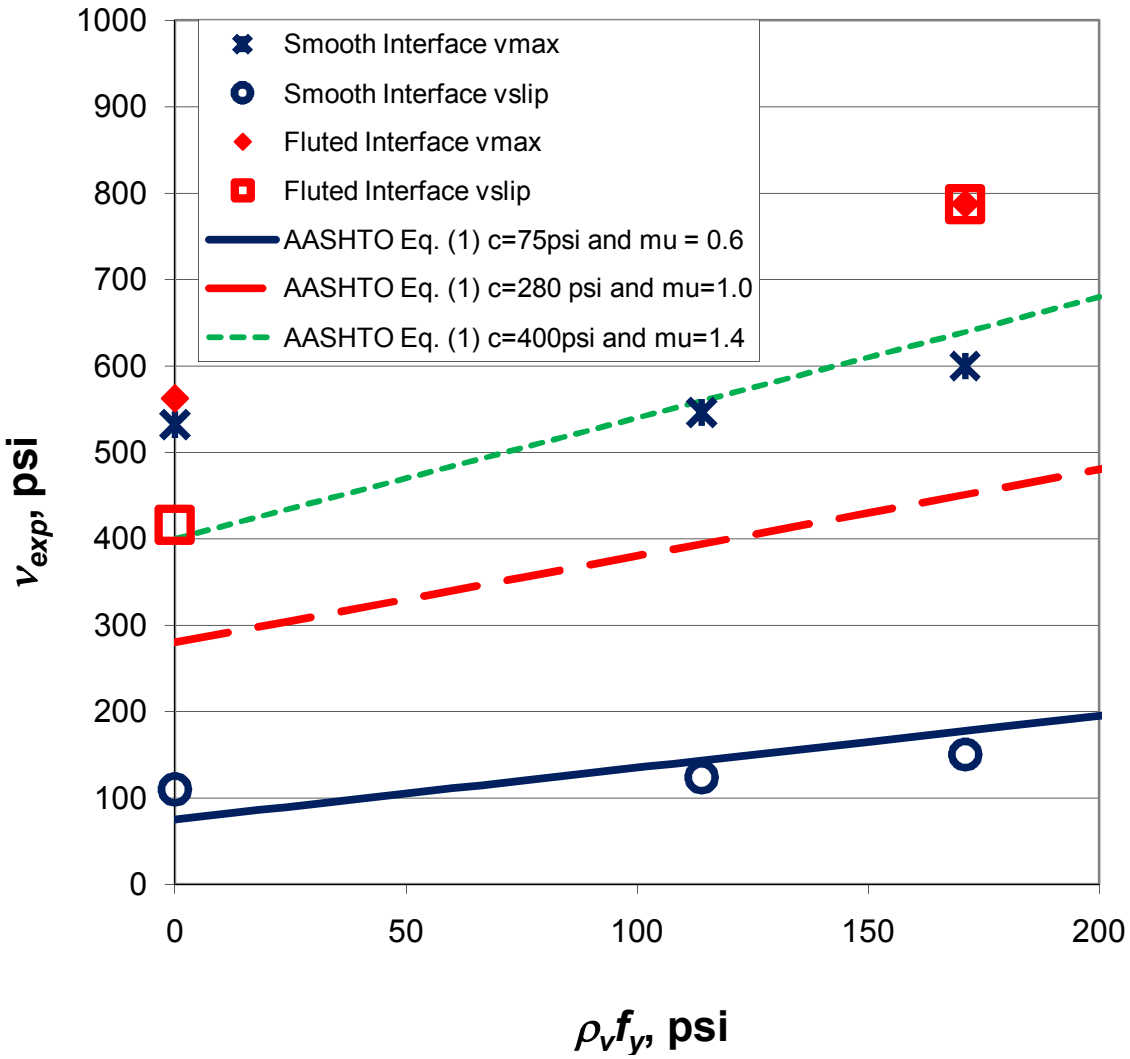

Figure 4-6: Comparison of interface shear stress results to predictions using AASHTO LRFD Eq. (4-1). Note: 1 psi = 0.0069 MPa.

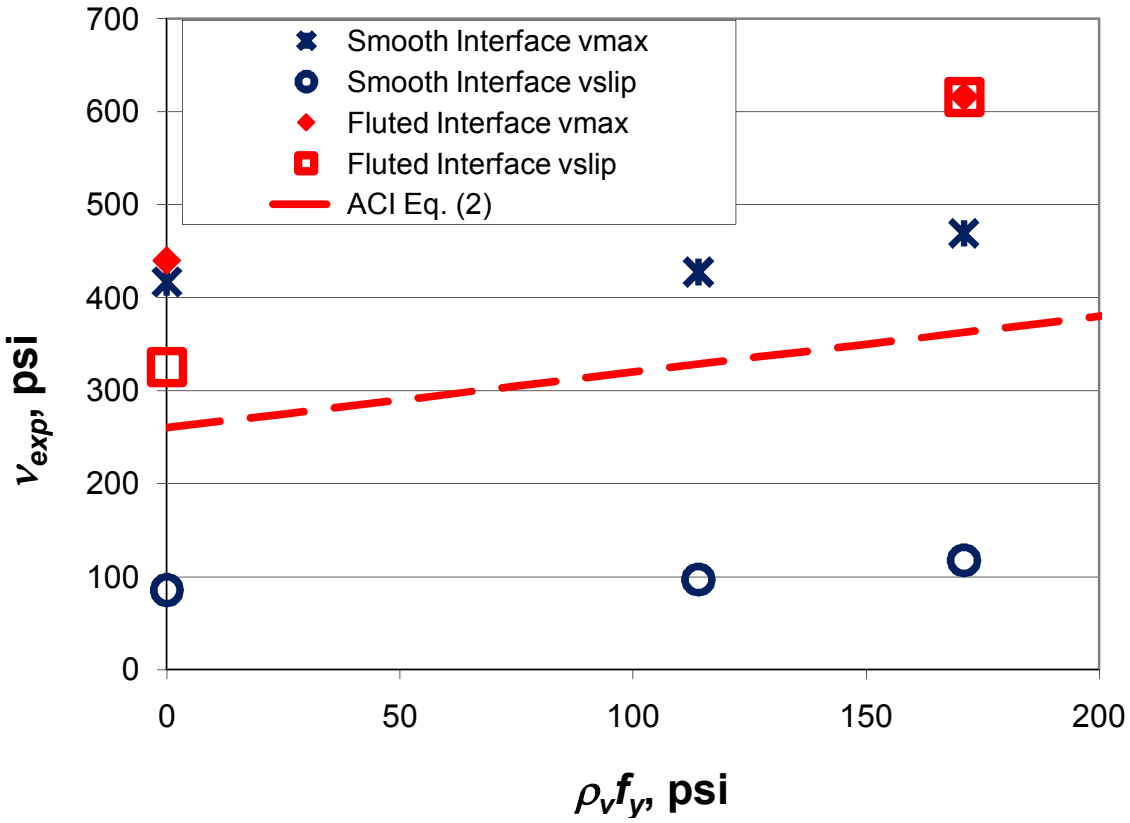

Figure 4-7: Comparison of interface shear stress results to predictions using ACI Eq. (4-2). Note: 1 psi = 0.0069 MPa.

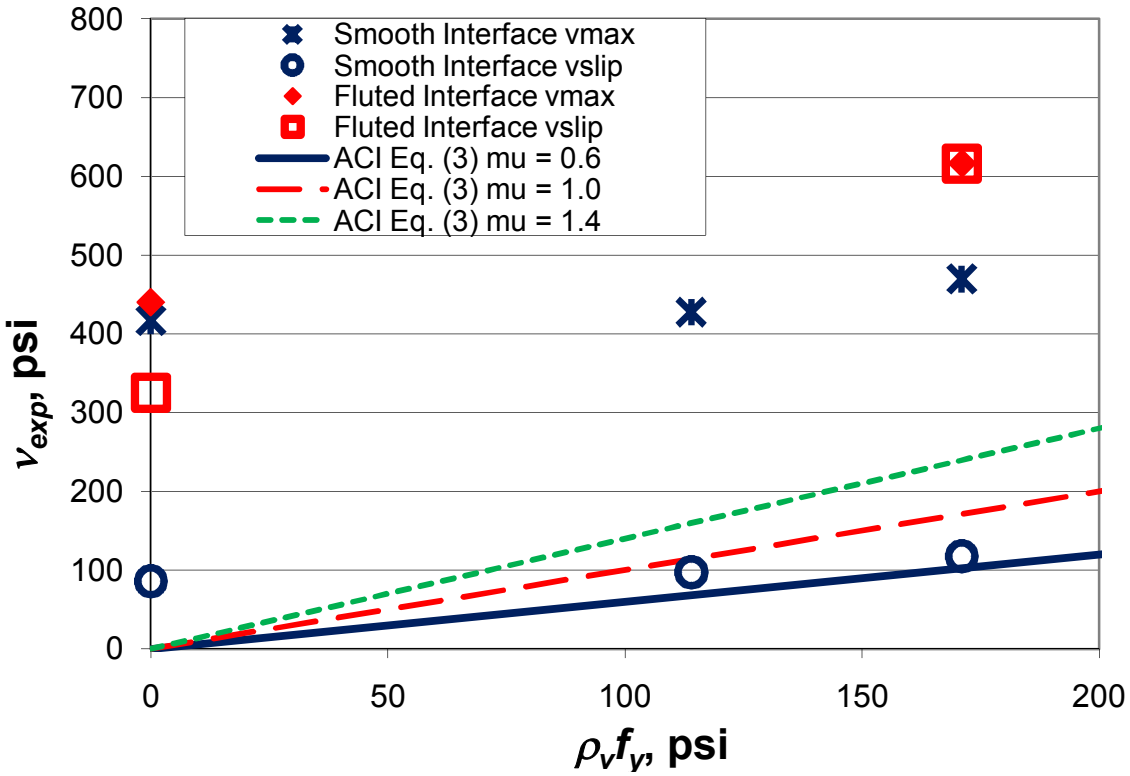

Figure 4-8: Comparison of interface shear results with ACI Shear Friction Eq. (3). Note: 1 psi = 0.0069 MPa.

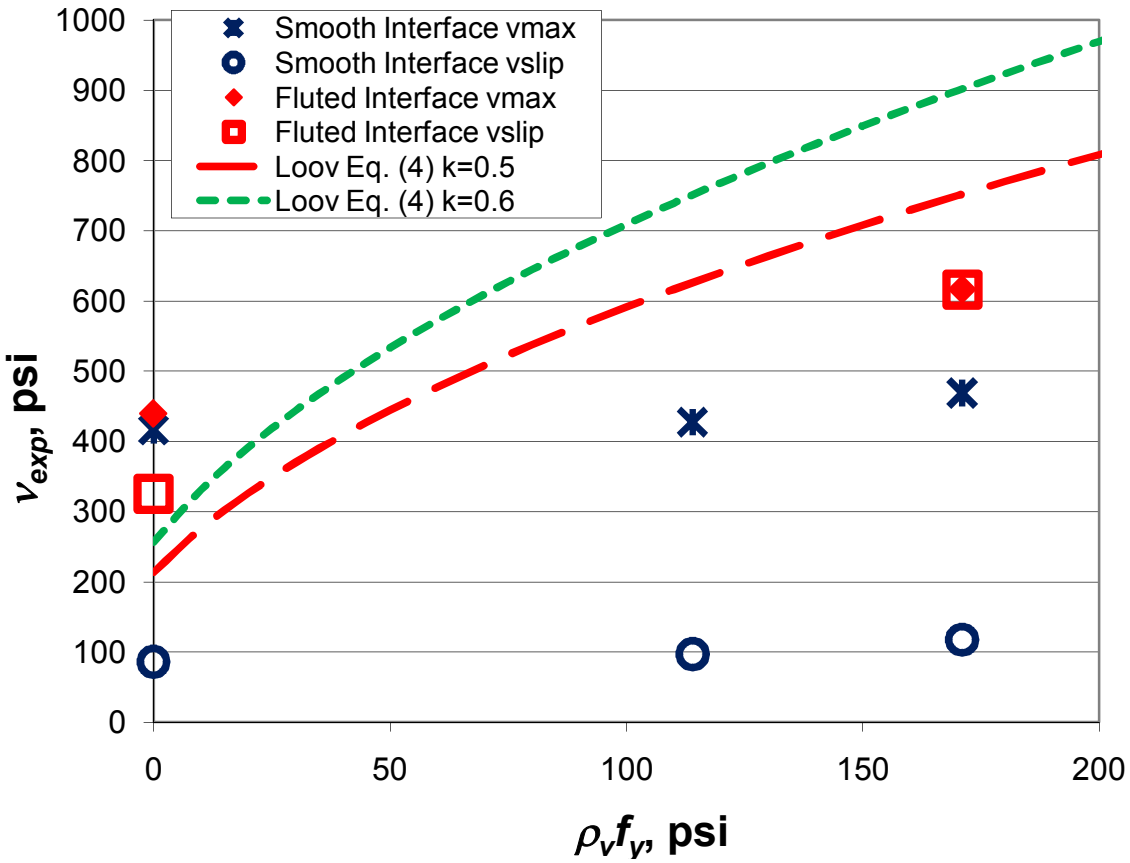

Figure 4-9: Comparison of interface shear stress results to predictions using Loov and Patnaik Eq. (4). Note: 1 psi = 0.0069 MPa

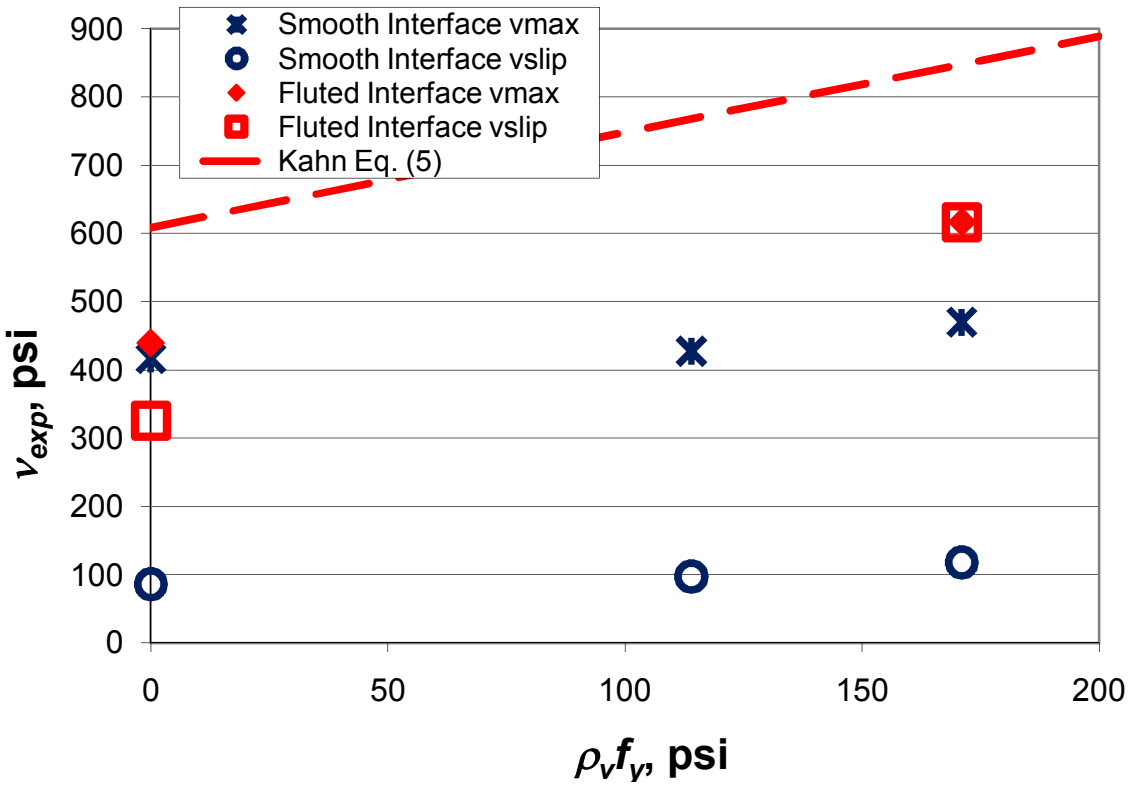

Figure 4-10: Comparison of interface shear results with Kahn and Mitchell Eq. (5). Note: 1 psi = 0.0069 MPa.

Table 4-4: Ratio of $v_{exp\ max}$, experimental interface shear stress at maximum load to predicted interface shear stress

Beam	$v_{exp\ max}$ /ACI Shear Friction Eq. (4-3)	$v_{exp\ max}$ /Kahn and Mitchell Eq. (4-5)	$v_{exp\ max}$ /Loov and Patnaik Eq. (4-4)	$v_{exp\ max}$ /AASHTO LRFD Eq. (4-1)	$v_{exp\ max}$ /ACI Eq. (4-2)
0-B**	-	0.68*	1.94*	5.55	1.60*
4-S	6.28	0.56*	0.68*	2.99	1.30*
7-S	4.55	0.55*	0.62*	2.63	1.29*
0-FL	-	0.72	2.06	1.57	1.69
7-FL	3.60	0.73	0.82	1.37	1.70
Mean	4.81	0.65	1.22	2.82	1.52
Standard Deviation	1.36	0.08	0.64	1.49	0.18
Coefficient of Variation	28.2%	12.1%	52.0%	53.0%	12.0%

*These equations assume a roughened interface that was not provided.
**0-B assumed unroughened surface because ¼ in. amplitude was not achieved with the burlap interface.

Table 4-5: Ratio of $v_{exp\ slip}$, experimental interface shear stress at slip load to predicted interface shear stress

Beam	$v_{exp\ slip}$ /ACI Shear Friction Eq. (3)	$v_{exp\ slip}$ /Kahn and Mitchell Eq. (5)	$v_{exp\ slip}$ /Loov and Patnaik Eq. (4)	$v_{exp\ slip}$ /AASHTO LRFD Eq. (1)	$v_{exp\ slip}$ /ACI Eq. (2)
0-B**	-	0.14*	0.40*	1.15	0.33*
4-S	1.43	0.13*	0.15*	0.68	0.30*
7-S	1.14	0.14*	0.16*	0.66	0.32*
0-FL	-	0.53	1.52	1.16	1.25
7-FL	3.60	0.73	0.82	1.37	1.70
Mean	2.05	0.33	0.61	1.00	0.78
Standard Deviation	1.35	0.25	0.52	0.28	0.58
Coefficient of Variation	65.6%	75.0%	84.4%	28.3%	75.0%

*These equations assume a roughened interface that was not provided.
**0-B assumed unroughened surface because ¼ in. amplitude was not achieved with the burlap interface.

4.6 Comparison to Push-off Tests

Interface shear push-off specimens made from UHPC and HPC have previously been discussed in Chapter 3. Both smooth and fluted interfaces were tested with varying levels of interface shear reinforcement. Figures 4-11 and 4-12 summarize the results of these tests in comparison with the results from the composite beams as well as equations 4-1 and 4-2. For each set of push-off tests, both the initial slip stress and the ultimate stress are given with their corresponding standard deviations. The initial slip stress was defined as the point at which the load-slip curve for each push-off changed slope. This point was usually accompanied by audible cracking during testing. For each composite beam, only the slip stress is shown since that value is a better indicator of the composite system performance.

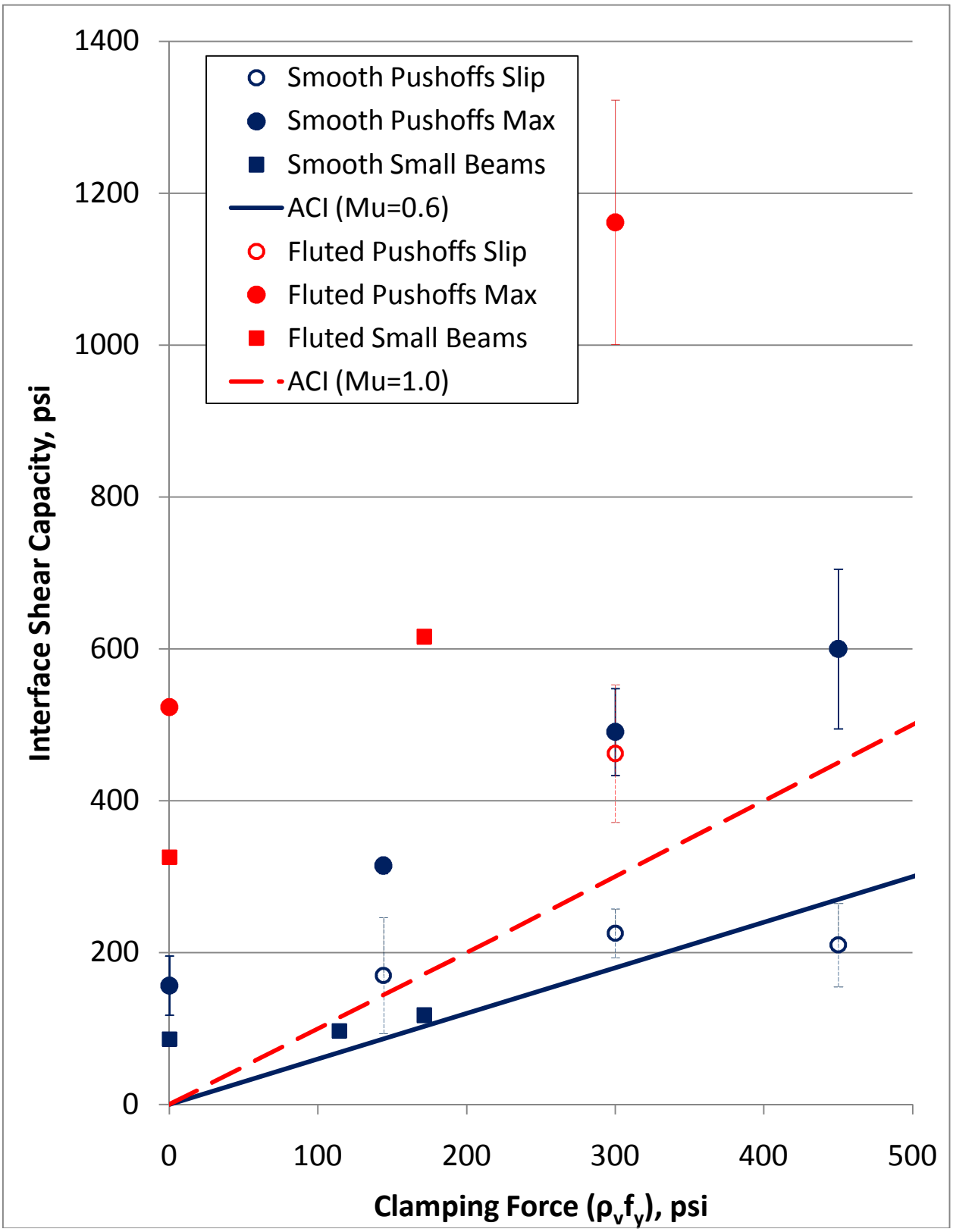

Figure 4-11: Comparison of interface shear push-off tests and composite small beam tests with ACI interface shear equation (4-2).

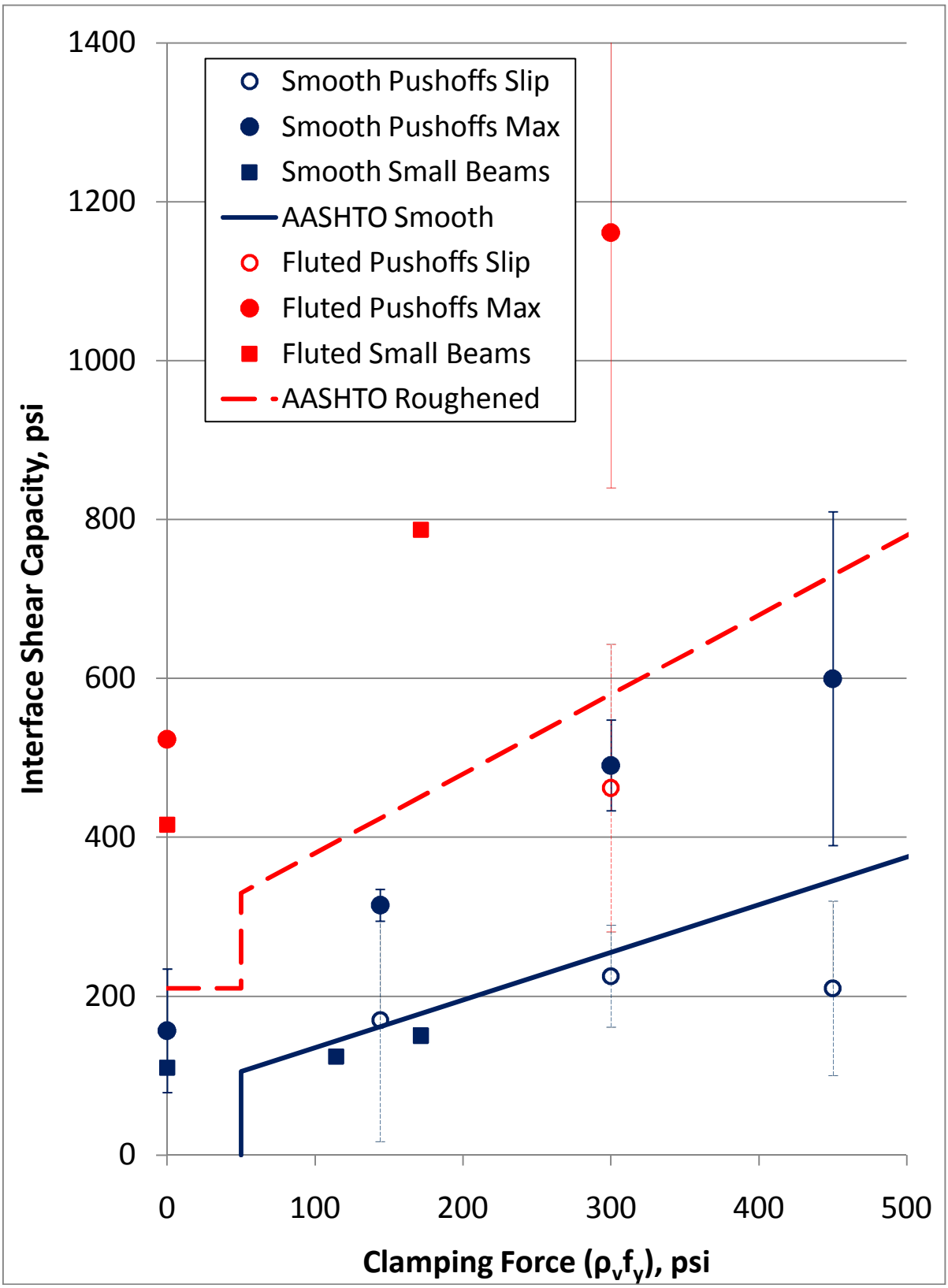

Figure 4-11: Comparison of interface shear push-off tests and composite small beam tests with AASHTO interface shear equation (4-1).

Whether the composite beam failure corresponded more closely to slip stress or ultimate stress in the push-offs depended on interface preparation. In comparing the smooth push-off test to the small composite beams the slip stresses, the smooth push-off slip stresses corresponded much more closely to the composite beam stresses than did the smooth push-off ultimate stresses. For the fluted case, the ultimate push-off stresses corresponded more closely to the composite beams than did the fluted slip stresses. From a phenomenological level this makes sense because the flutes continued to carry significant load after initial cracking, while the smooth interface did not carry as much load after slip.

4.7 Conclusions and Recommendations

It is evident that a smooth UHPC interface, even when reinforcement is present, does not provide the interface shear capacity anticipated by equation 4-1. Based on these small beam tests, equation 4-2 was a close indicator of performance of smooth interfaces in composite beams, but it is not recommended for use in design due to the high variability of smooth interface performance. Smooth interfaces were also shown to create only quasi-composite action even prior to full slip . Therefore, it is recommended that any cold-joint between UHPC and HPC use a form liner or other technique to create a fluted surface. Under these conditions, both equation 4-1 and 4-2 with constants based on roughened interfaces can be used to conservatively design UHPC-HPC interfaces.

UHPC-HPC interface shear push-off tests can also be accurately used for determining the performance of small composite UHPC beams. When smooth interfaces are being considered, it is recommended that the slip load, rather than the maximum load,

of the push-off be used as the maximum interface shear design capacity of the beam. System characteristics after this point should be based only on the non-composite beam properties.

4.8 References

AASHTO (2010). *AASHTO LRFD Bridge Design Specifications*. Washington, D.C., American Association of State Highway and Transportation Officials.

ACI Committee 318 (2008). *Building code requirements for structural concrete : (ACI 318-08) ; and commentary (ACI 318R-08)*. Farmington Hills, Mich., American Concrete Institute.

Bentz, E. C. (2000). Sectional Analysis of Reinforced Concrete Members. *Civil Engineering*. Doctor of Philosophy Thesis. University of Toronto, Toronto.

Kahn, L. F. and A. D. Mitchell (2002). "Shear Friction Tests with High-Strength Concrete." *ACI Structural Journal* 99(1): 98-103.

Kahn, L. F. and A. Slapkus (2004). "Interface Shear in High Strength Composite T-Beams." *PCI Journal* 49(4): 102-110.

Loov, R. E. and A. K. Patnaik (1994). "Horizontal Shear Strength of Composite Concrete Beams." *PCI Journal* 39(1): 48-67.

CHAPTER 5
INTERFACE SHEAR PERFORMANCE OF FULL-SCALE UHPC BRIDGE GIRDERS WITH CAST-IN-PLACE HPC DECKS

5.1 Introduction

Ultra-high performance concretes allow for a significant decrease in material usage such that bridge girders can be lighter and shallower than traditional prestressed concrete bridge girders. Specialized shapes have been created that optimize the performance of this material by using a modified double-tee girder shape with no need for structural concrete decks (Keierleber et al., 2008; Graybeal, 2009b; Graybeal, 2009a), but these girders represent a significant capital investment in formwork and a change from traditional concrete bridge girder design in the U.S. In lieu of a totally unique shape, Georgia Department of Transportation is interested in using UHPC with traditional I-girder shapes. If these shapes are to be used effectively, however, composite action with a cast-in-place deck is needed for carrying live loads and satisfying AASHTO deflection criteria. The objectives of this research were to determine the interface shear capacity of prestressed UHPC bridge girders with cast-in-place high performance concrete (HPC) decks and to determine if existing ACI (2008) and AASHTO (2010) code equations may be used conservatively for design with these materials.

5.2 Previous Research

Little full-scale research has investigated interface shear in composite beam systems. The majority of work has been done on shear friction specimens as described in Chapter 2. The current ACI 318 (2008) and AASHTO (2010) code cite several studies

performed on composite beams between 8.2 and 10-ft (2500 to 3050 mm) long that were 13.6 to 15.5 in (350 to 394 mm) deep, which are discussed further in Chapters 2 and 4 (Loov and Patnaik, 1994; Patnaik, 1999; Kahn and Slapkus, 2004; Grossfield and Birnstiel, 1962). Saemann and Washa tested composite beams up to 20 ft (6096mm) long but their total depths were only 17 in. (432 mm) (1964). These beams are still shorter and much shallower than beams conventionally used in concrete bridge girder construction.

5.3 Specimen Design

Three full-scale precast prestressed UHPC bridge girders with cast-in-place HPC decks were designed to test the flexural strength, diagonal tension shear capacity, and the interface shear capacity of composite UHPC / HPC bridge girders. One 54-ft-long girder was cast to test the flexural capacity of the composite system in four-point symmetrical bending. After the flexural test, the span length could be adjusted to test the diagonal tension shear strength and the interface shear capacity of each end of the beam by subjecting it to asymmetrical 3-point bending. Two 34-ft-long girders were cast to investigate diagonal tension and interface shear. Each end of each of these beams was designed to be subjected to asymmetrical 3-point bending in order to force shear failure.

The girders were constructed using existing forms. The amount of prestressing and specific beam cross-sections (Figure 5-1 and 5-2) were designed to emulate a girder that would be used in a 90-ft (27.4m) long highway bridge. If this section were used with a girder spacing of 7.5 ft (2.3) and HL-93 loading, AASHTO (2010) gives an ultimate interface shear stress demand, v_{ui}, of 241 psi (1.66 MPa). At service, the interface stress demand, v_{si}, would be 124 psi (0.86 MPa).

The interface between the UHPC girder and HPC deck was varied along each of the six shear spans of these beams. Differing amounts of interface stirrup reinforcement, shear areas, and concrete surface "roughness" were used in order to test the effect of these parameters on interface shear capacity. Table 5-1 lists the variations between each of the shear tests. For the smooth interface preparation, the surface was left unfinished and allowed to cure with plastic covering as recommended by the UHPC manufacturer. The "roughened" surface was created by depressing a formliner into the surface of the plastic concrete to create transverse ¼-in. (6 mm) deep flutes. This method of deforming the surface was chosen because the self-leveling properties of the UHPC. The steel fibers were known to prevent traditional roughening by brooming or raking of the surface. Figure 5-3 shows the formliner dimensions and Figure 5-4 shows the surface of the girder after formliner removal. The formliner used had regular deformations that were ¼-in. wide and ¼-in. deep. This formliner was chosen to replicate the ¼-in. deformations required by ACI 318 Section 17.5.3.3 (2008) and AASHTO LRFD Section 5.8.4.3 (2007). Differing amounts of shear reinforcement also protruded from the surface of the beams to vary the interface shear reinforcement. A reinforcement ratio, ρ_v, of .00104 was chosen for tests 1-1 and 2-2 because it allowed for the maximum spacing to be used while still satisfying the minimum interface reinforcement ratio of .00083 required by Equation 5.8.4.4-1 of the AASTHO LRFD code. This requirement is greater than the minimum reinforcement ratio of .00047 required by section 17.6 of ACI 318. Figures 5-5, 5-6, and 5-7 show the detailed elevations of the girders along with their surface preparations and reinforcement specifications.

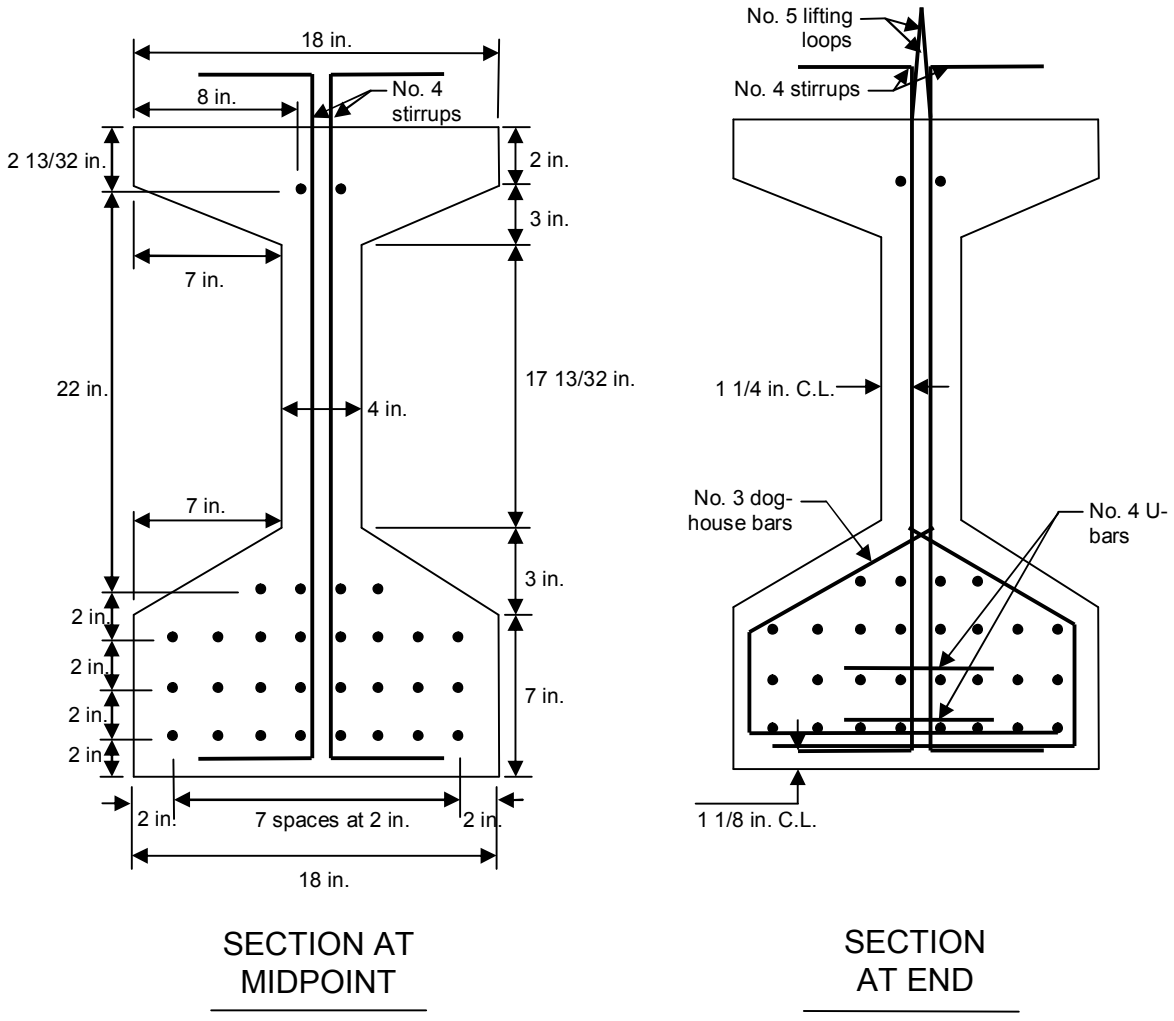

Figure 5-1: Design cross section for Girder 1 and Girder 2. As-built sections shown in Chapter 6.

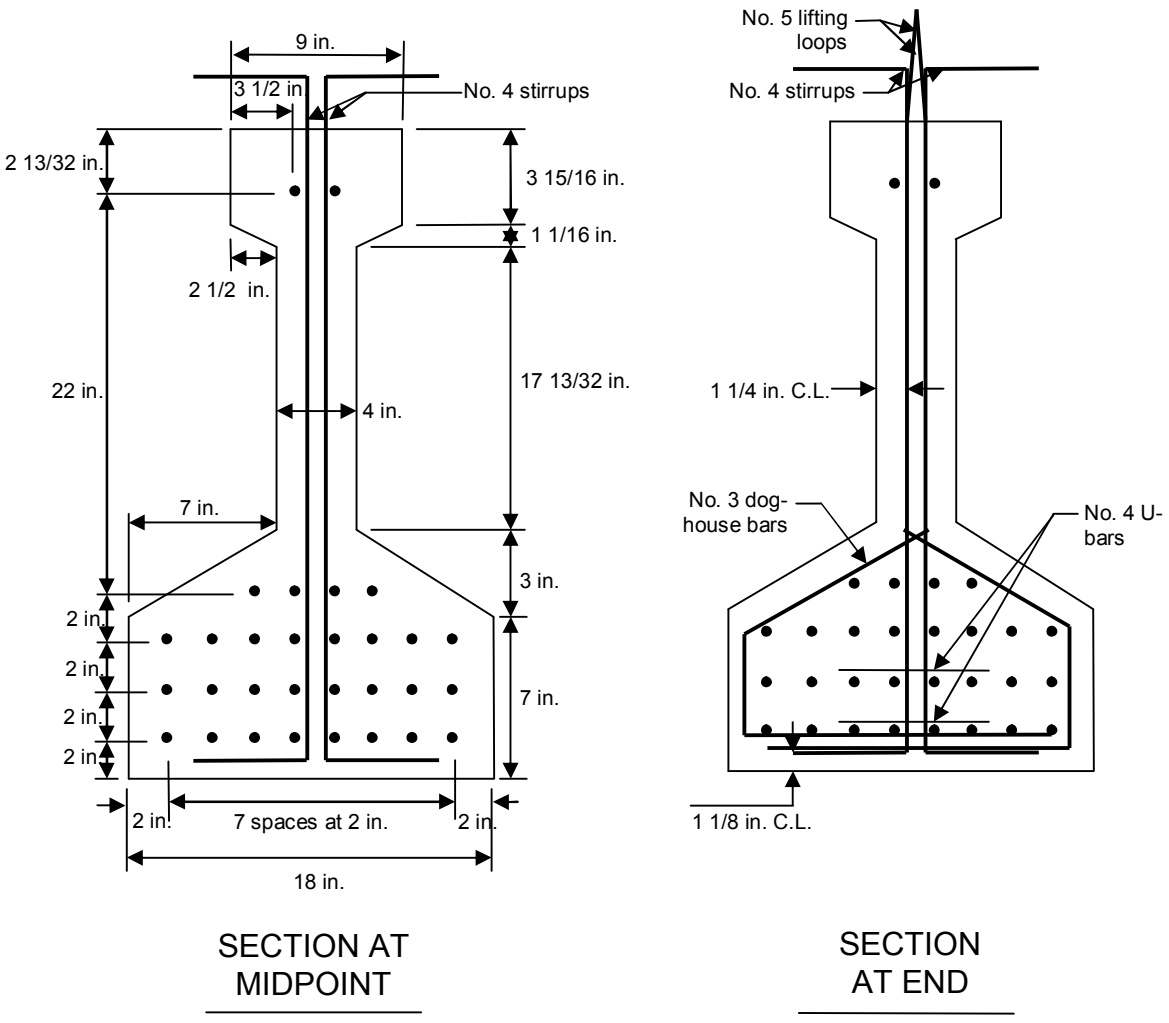

Figure 5-2: Design cross section for Girder 3 (reduced top flange). As-built sections shown in Chapter 6.

Table 5-1: Comparison of interface steel and surface preparation for shear tests

Shear Test	Surface Preparation	Stirrup Spacing, s	Reinforcement Ratio, ρ_v
1-1	smooth	24 in.	.00104
1-2	fluted	N/A	0
2-1	smooth	N/A	0
2-2	fluted	24 in.	.00104
3-1	fluted	N/A	0
3-2	smooth	12 in.	.00417

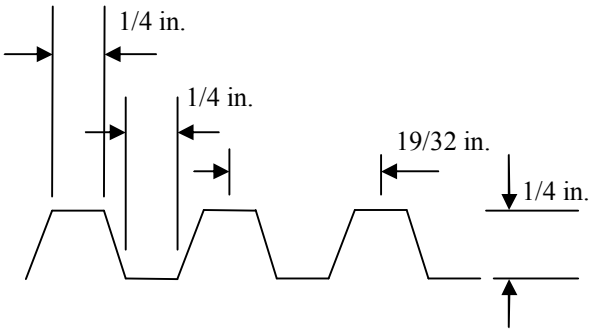

Figure 5-3: Dimensioned drawing of formliner used in creating fluted UHPC surface.

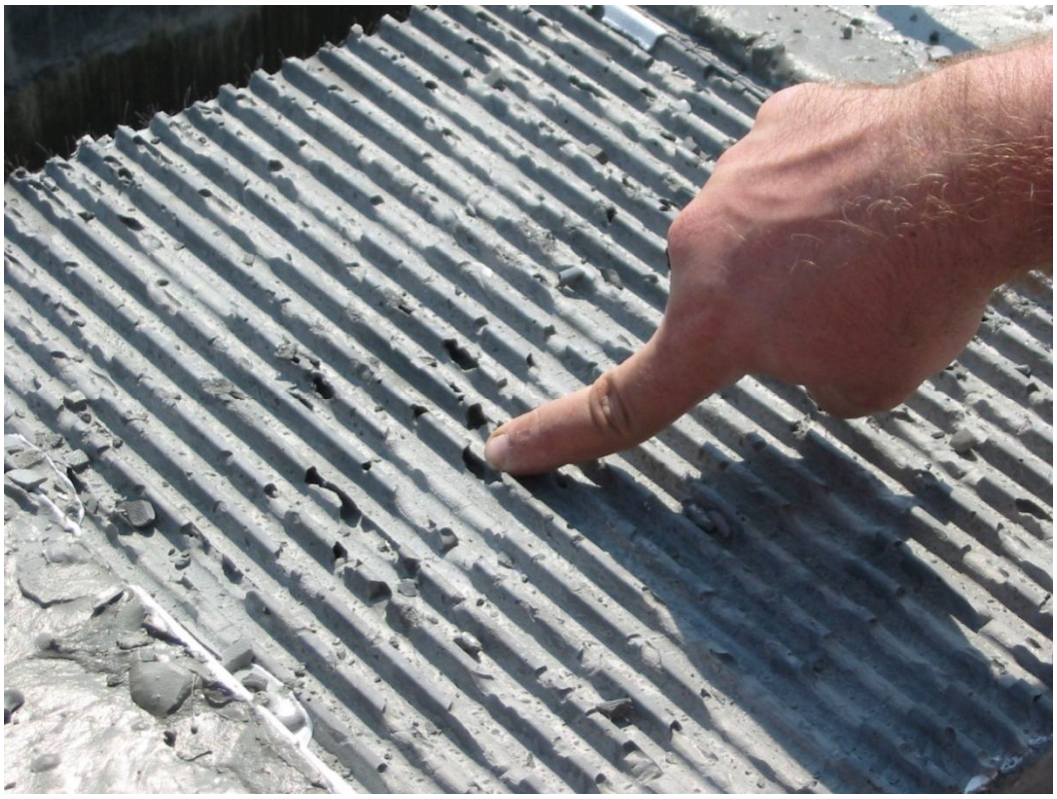

Figure 5-4: Fluted surface of UHPC girder after removal of formliner.

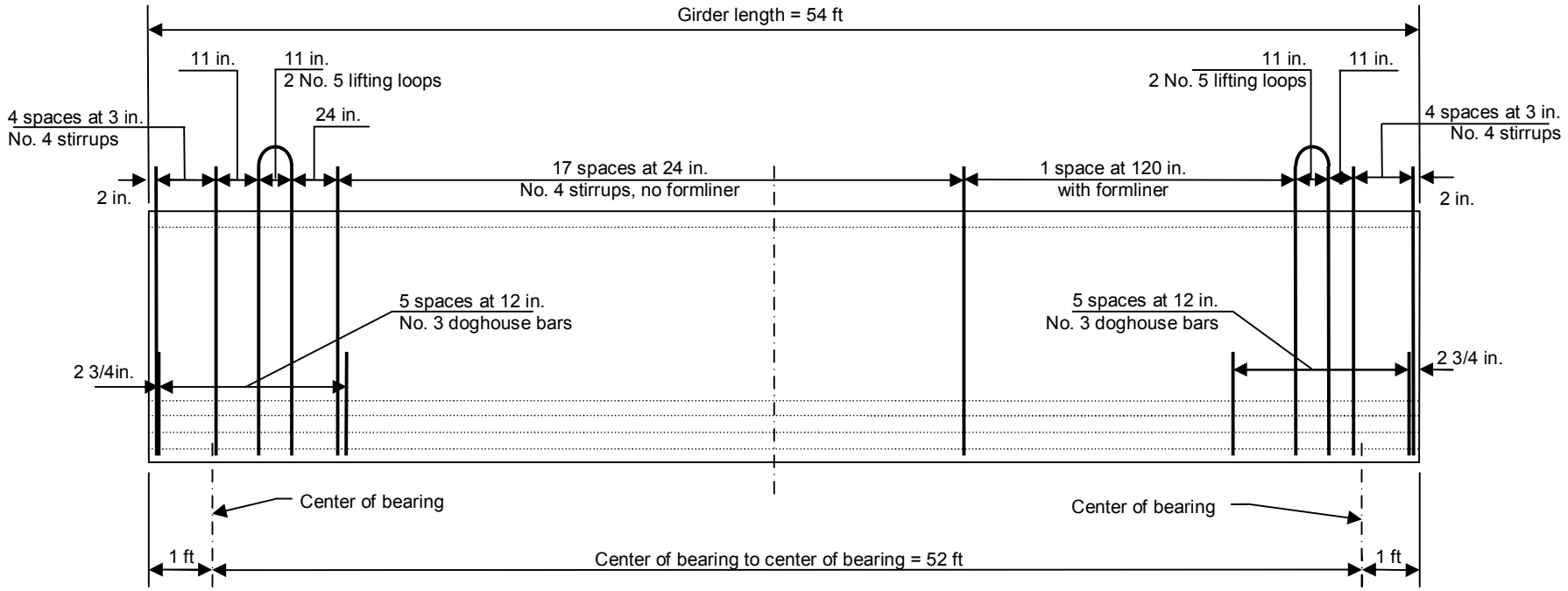

Figure 5-5: Girder 1 elevation.

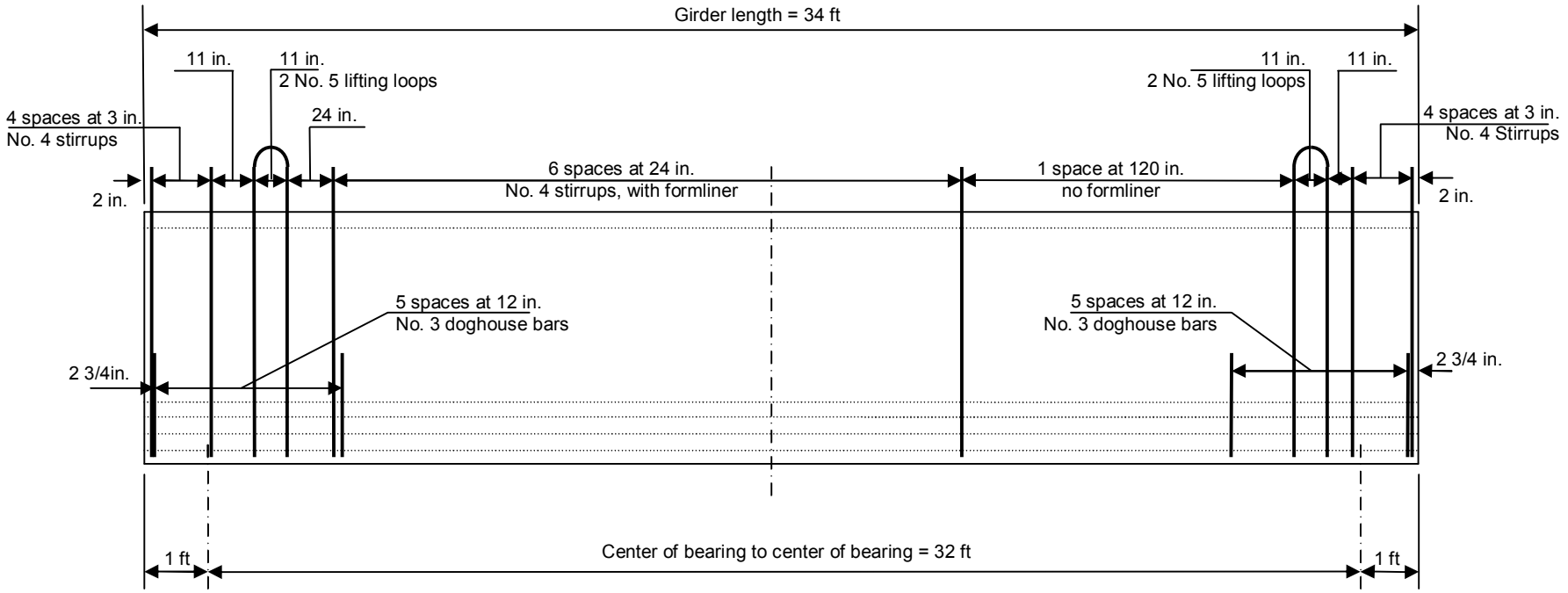

ELEVATION VIEW

Figure 5-6: Girder 2 elevation.

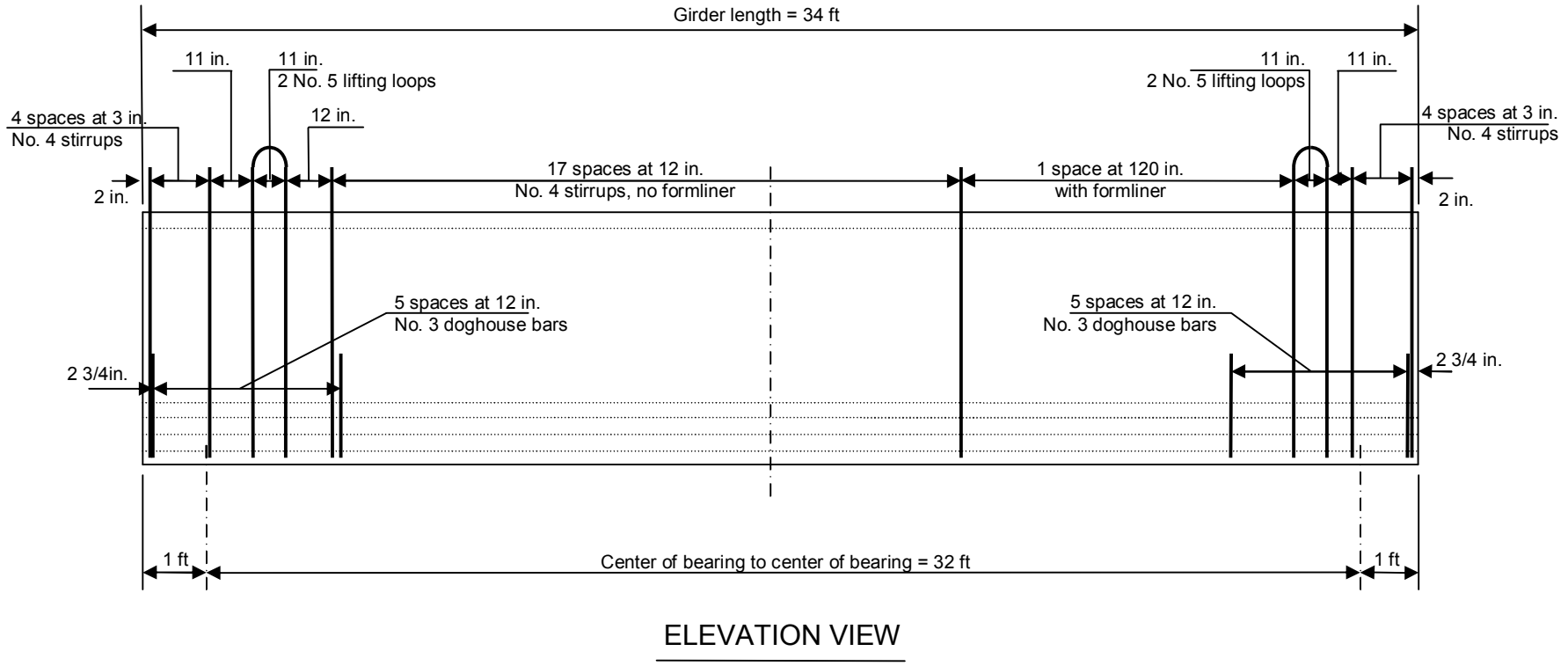

ELEVATION VIEW

Figure 5-7: Girder 3 Elevation.

A 5-ft wide, 8-in. thick HPC deck was cast on top of each of the girders as shown in Figures 5-8 and 5-9. The formwork for the deck was completely supported by the girder, which was simply supported during this construction. This unshored deck construction mimicked that which would most likely occur in bridge construction. The decks were discontinued 3 feet from each end of the girders in order to facilitate testing of the girders, to force interface shear failure, and to omit the lifting hooks and end bursting stirrup reinforcement from the interface shear zone.

Temperature and shrinkage reinforcement were provided in the form of 7 No. 4 bars placed longitudinally in the decks and No. 4 bars at 10 inches on center running transversely. The steel was chaired 5 inches from the bottom of the decks. Figures 5-8 and 5-9 show the deck reinforcement, and Figure 5-10 shows Girder 1 with formwork prior to pouring of the deck.

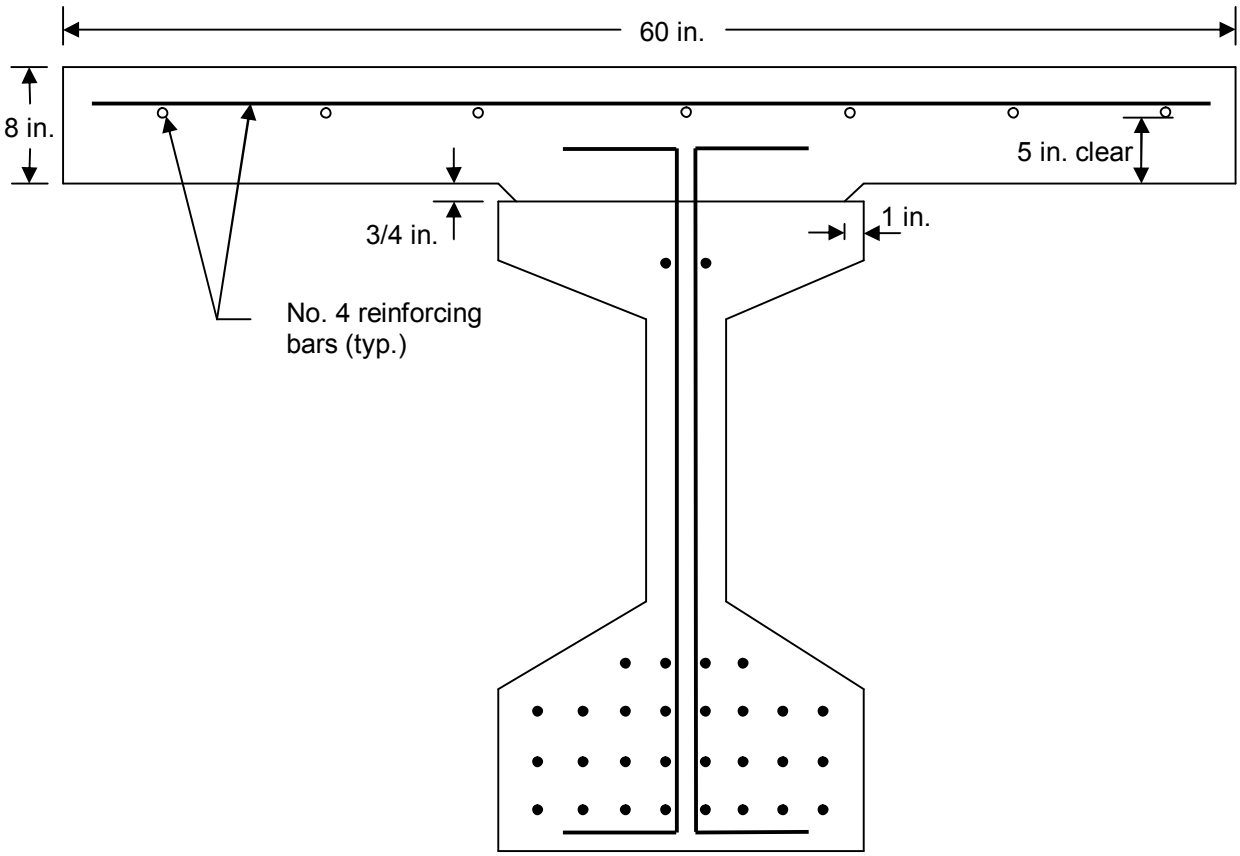

Figure 5-8: Girder 1 and 2 with composite HPC deck. Notice 3/4-in. haunch.

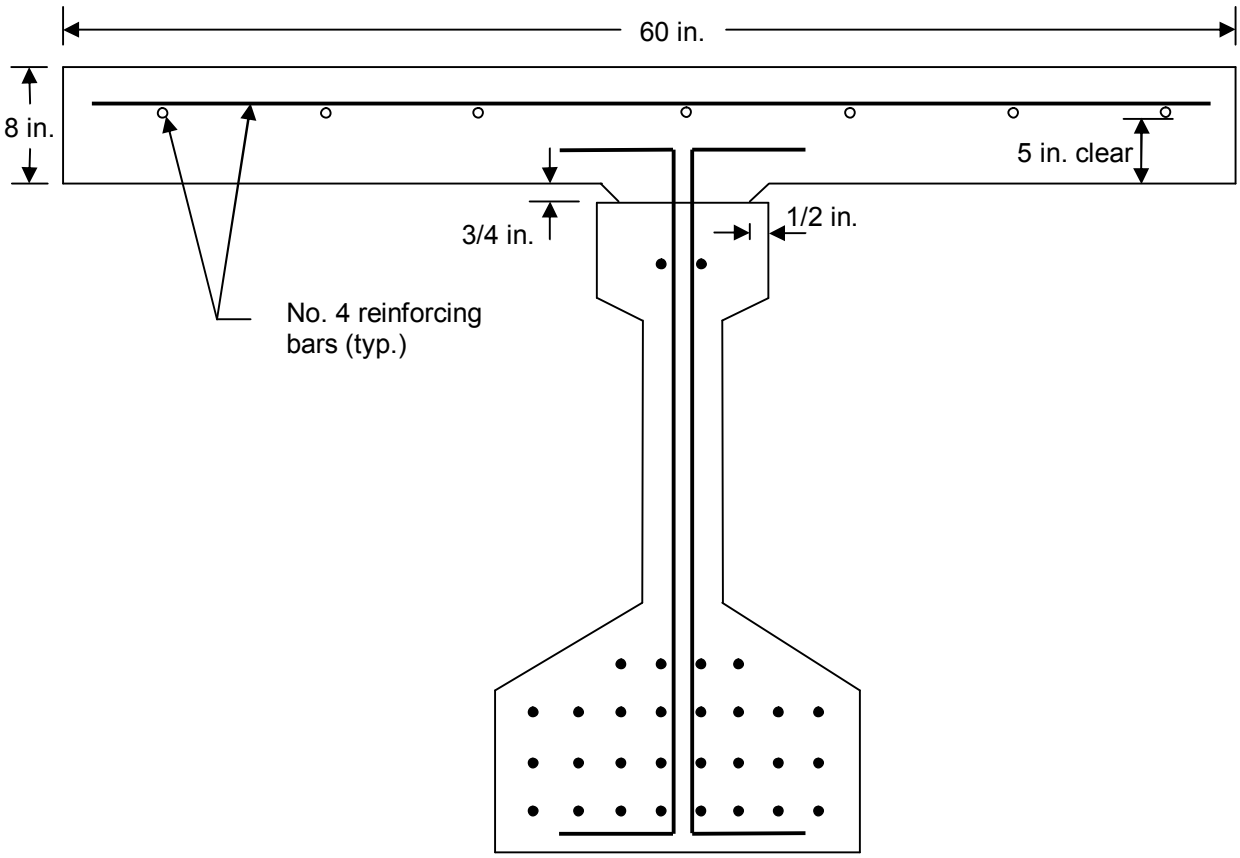

Figure 5-9: Girder 3 with composite HPC deck. Notice 3/4-in. haunch.

Figure 5-10: Temperature and shrinkage reinforcement for HPC deck on Girder 1.

Table 5-1 compares the different shear reinforcement and surface preparation combinations used on the interfaces of the three test beams. Test specimens were designated as follows: the first number represents the beam number; the second number represents the different ends of the beams. Shear tests 1-1, 1-2, 2-1, and 2-2 were designed to analyze the interaction of steel interface reinforcement and surface preparation on the overall interface shear performance. Shear test 3-1 was designed to analyze the effect of increased steel reinforcement on the interface shear performance. Shear test 3-2 was designed to analyze the effect of a decreased interface shear area. Comparison of tests 2-2, 1-1, and 3-1 was designed to find the effect of interface reinforcement ratio on interface shear capacity of girders with smooth interfaces. Comparison of tests 1-2 and 2-1 was designed to find the effect of interface reinforcement ratio on shear capacity of girders with fluted interfaces. Tests 2-2 and 1-1 were designed to evaluate the shear capacity of interfaces without reinforcement.

5.4 Beam Testing

For each of the beam shear tests, interface failure was determined by two criteria. The first was a jump or change in the slope of the shear – slip curve. The second was a drop or change in slope of the load-deflection curve. The presence of both of these factors allowed for interface shear failure to be defined in terms of structural performance rather than a more arbitrary definition based on a certain magnitude of slip between the deck and UHPC beam.

The first full-scale test performed was the flexural test of a 54-ft long girder in 4-point bending. The flexural test was not intended to be a test of the interface shear

capacity of the girder and deck, but the interface between the deck and girder was instrumented in case any slippage occurred during the test. Figures 5-11 and 5-12 show the test setup and instrumentation. The load was applied at a rate of approximately 15 kips/minute. Every 15 kips, the loading was paused to check measurements and look for new cracks in the structure.

At a load of 70 kips corresponding to a shear of 35 kips, the east end of the beam (left half of Figure 5-3) experienced an instantaneous interface slip of 0.01 in. Figure 5-13 shows the shear-slip curve for the east end of the beam. This end of the beam was smooth with an interface shear reinforcement ratio of 0.00104; the calculated clamping force was 62.4 psi at reinforcement yielding (f_y = 60 ksi). The initiation of slip was accompanied by a change in the slope of the load-deflection curve from 121 kip/in. to 66 kip/in. At this load, the strain at the bottom of the concrete was calculated to be -0.0003, so the concrete was not near flexural cracking. Therefore the change in the slope of the load deflection curve can be solely attributed to the beginning of interface shear failure. Figure 5-14 shows the complete load-deflection curve for the flexural test with the linear curve fits of the first two regions of the data set. Based on an applied shear of 35 kips and the AASHTO LRFD computation for interface shear stress, the interface capacity was 73 psi. This is based on:

$$v_n = \frac{V_n}{A_{cv}} \tag{5-1}$$

where

A_{cv} = area of concrete considered to be engaged in interface shear transfer ($b_{vi}d_v$), in^2

b_{vi} = interface width considered to be engaged in shear transfer, in.

d_v= the distance between the centroid of the tension steel and the mid-thickness of the slab to compute a factored interface shear stress.

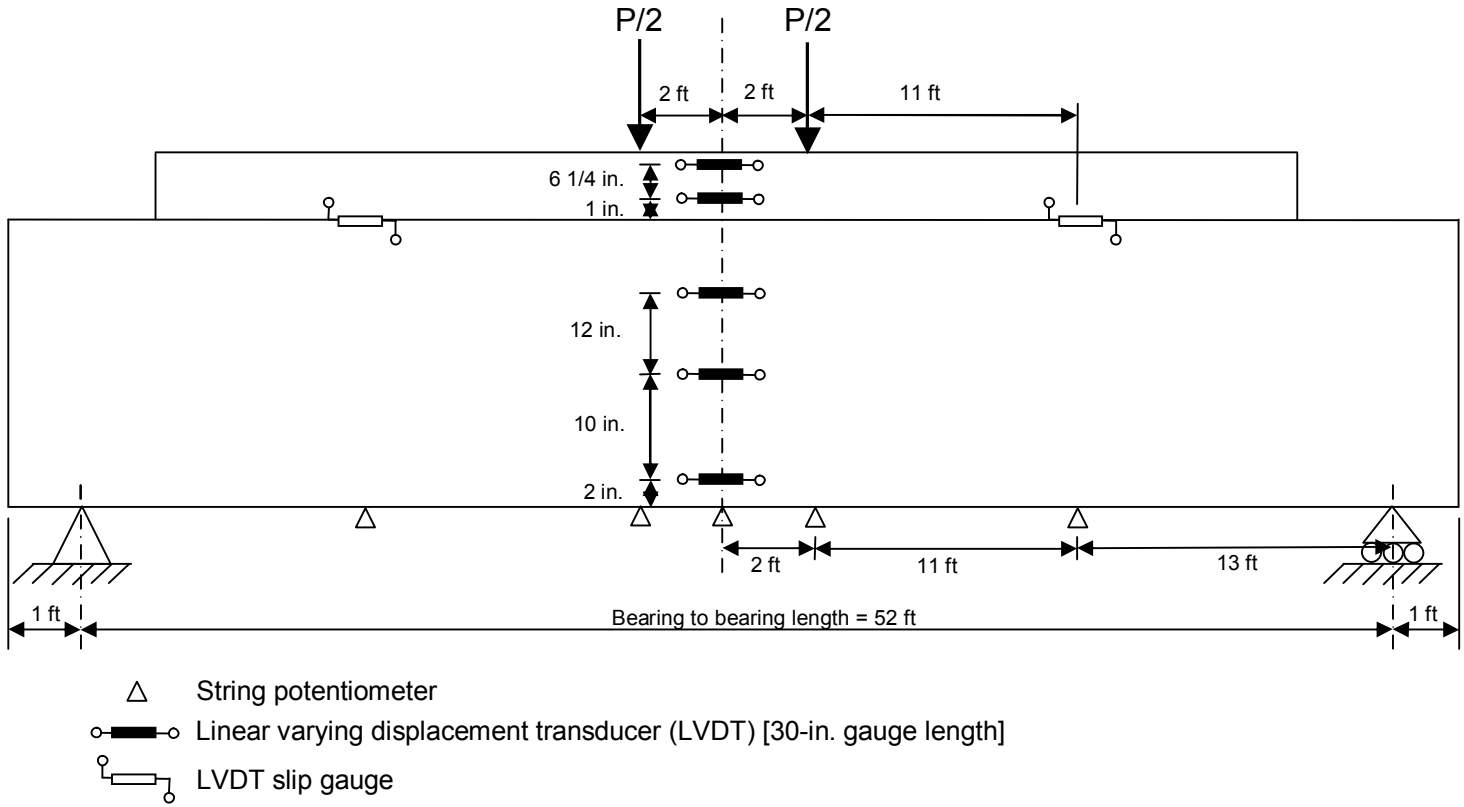

Figure 5-11: Elevation view of external instrumentation for flexure testing of Girder 1. (All instrumentation except string potentiometers is mirrored on other side of beam.)

Figure 5-12: Beam 1 prior to flexural testing.

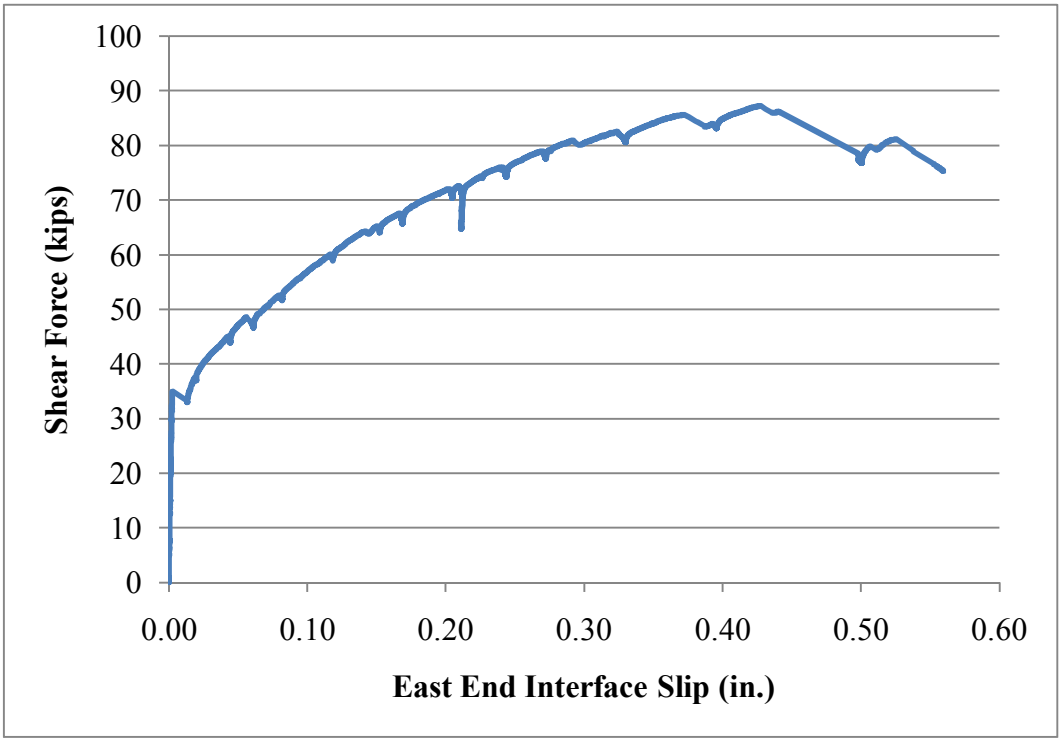

Figure 5-13: Shear-slip curve for east end of beam. Note the initiation of slip at approximately 35 kips.

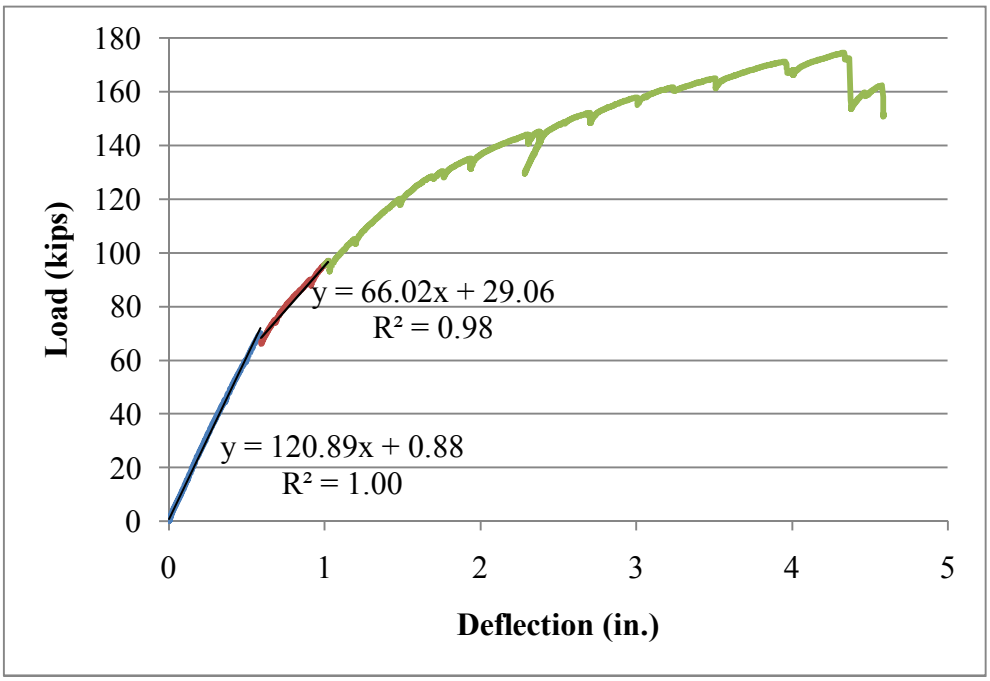

Figure 5-14: Load-deflection curve for flexural test with linear curve fits before and after deck slip.

After the flexural test, the 54-ft beam was saw cut into two segments, lengths of 20-ft and 34-ft. Shear test 1-2 tested the interface of the 34-ft length, the original west end of girder 1. This portion of the beam had a fluted interface with no shear reinforcement. The setup for this test is shown in Figures 5-15 and 5-16. During the test, slip initiation was observed at a load of 391 kips as seen in Figure 5-17. This correlated to a shear force of 261 kips on the high-shear end of the beam or an interface shear stress of 540 psi at failure. Figure 5-18 shows the shear – slip diagram for the high-shear end of the beam in test 1-2. Test 1-2 ultimately failed in diagonal tension web shear at a load of 647 kips (2,880 kN) which was a shear force of 431 kips (1,920 kN).

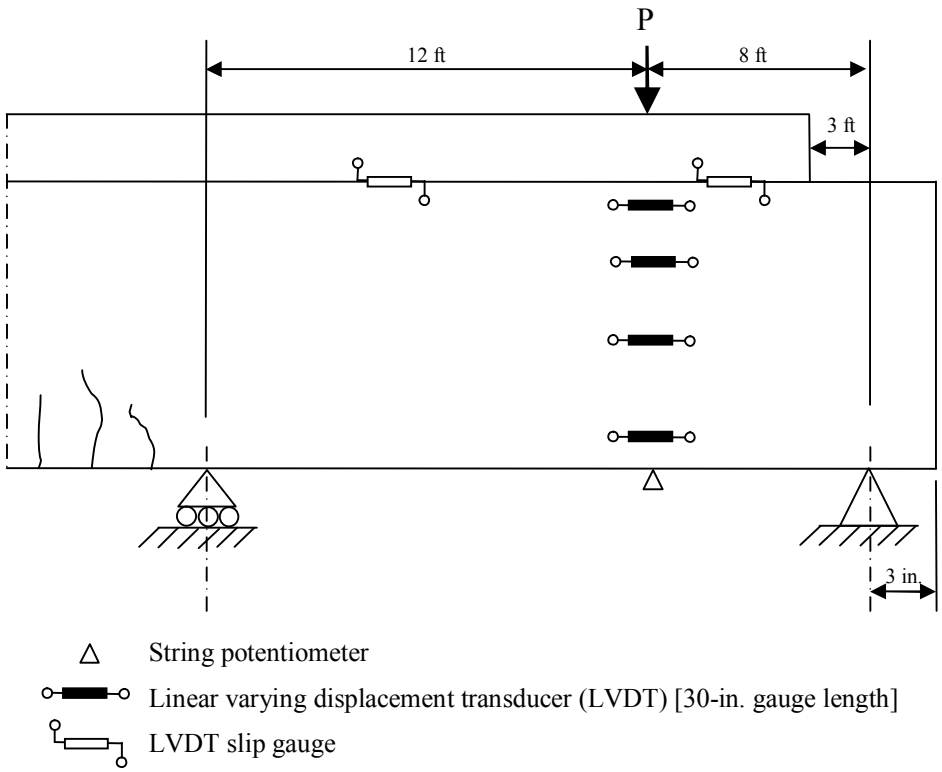

Figure 5-15: Instrumentation and setup for shear test 1-2.

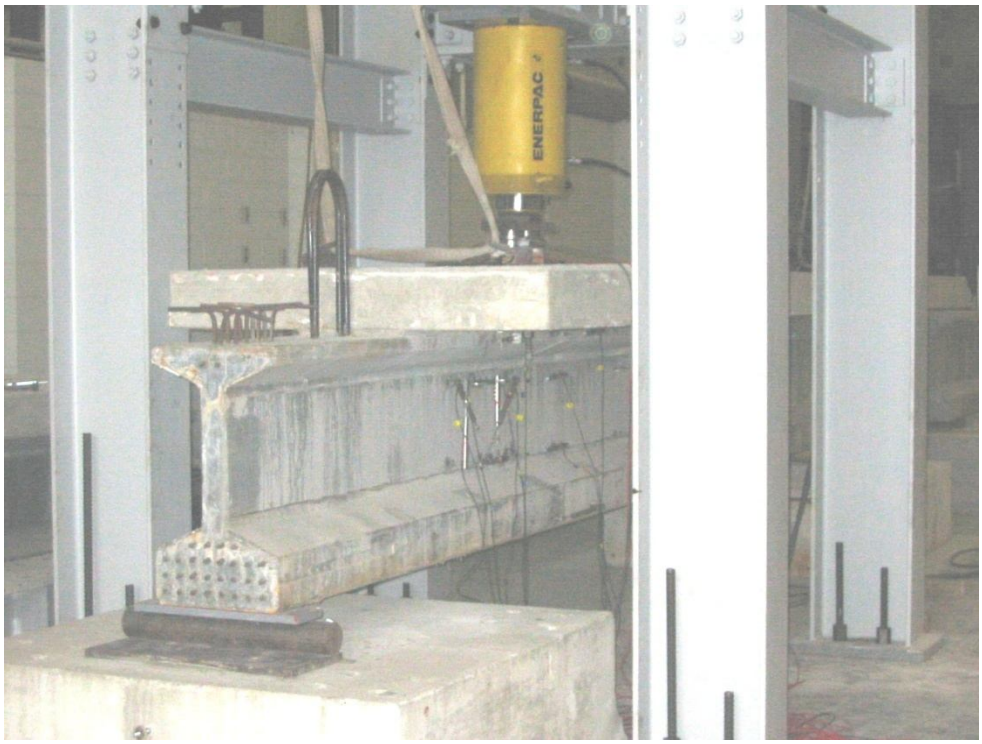

Figure 5-16: Setup for shear test 1-2.

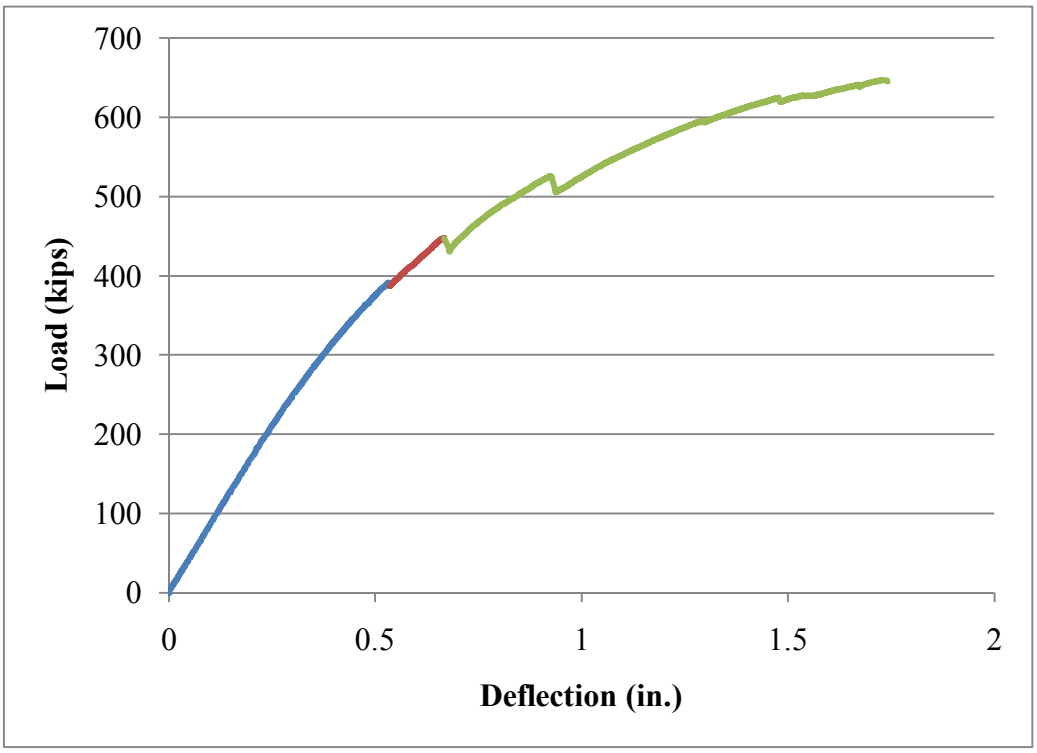

Figure 5-17: Load – deflection curve for shear test 2-1. Note the change in slope at a load of 391 kips.

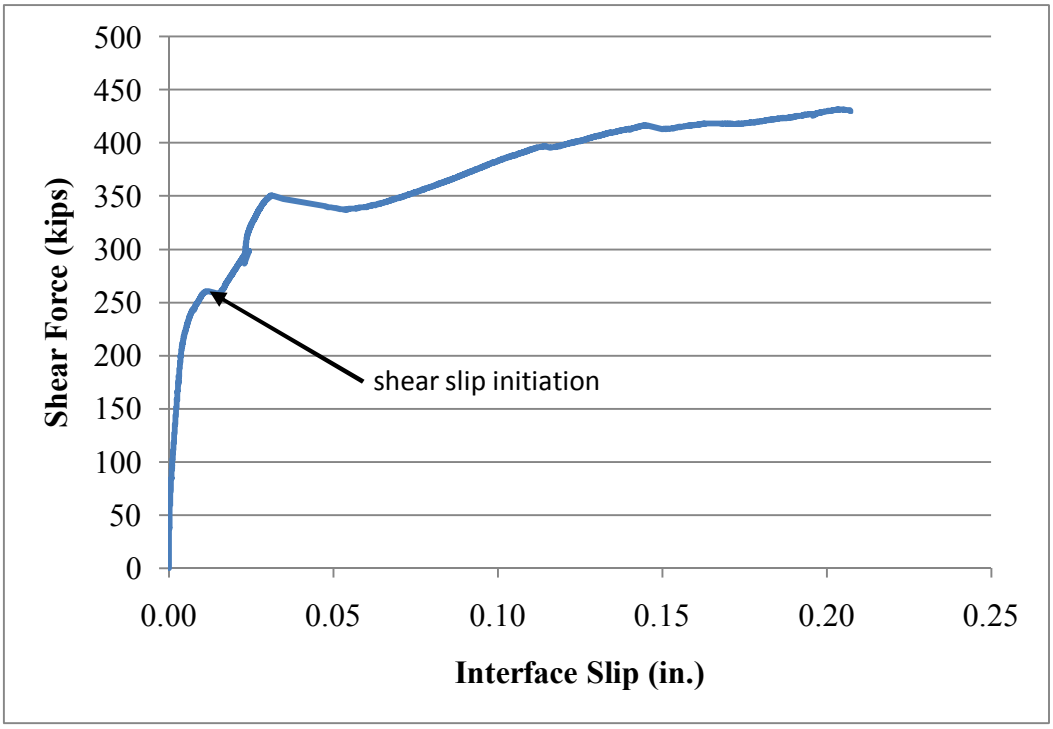

Figure 5-18: Shear – slip curve for test 1-2.

For tests 2-1, 2-2, 3-1, and 3-2, the setup shown in Figure 5-19 was used. In test 2-1, there was a smooth interface with no reinforcing steel. This allowed slip to initiate as soon as the beam was loaded (Figure 5-20). Any composite stiffness provided by cohesion between the girder and deck was negligible, giving an interface shear stress of 0 psi at slip initiation. Test 2-1 ultimately failed in flexural compression at a load of 699 kips (2,880 kN) with a bending moment of 3,728 kip-ft (5,050 kN-m).

Figure 5-21 shows the shear – slip curve for test 2-2. A shear force of 421 kips was observed at interface failure. This shear force correlated to a load of 632 kips which was where a major slope change is seen in the load – deflection curve for this test (Figure 5-22). The interface shear stress capacity was calculated to be 873 psi. Test 2-2 ultimately failed in diagonal tension web shear at a load of 720 kips (2,880 kN) which was a shear force of 480 kips (2,140 kN).

Due to the results of the flexure test that showed the initiation of slip beginning earlier in smooth reinforced interfaces than rough unreinforced interfaces, test 3-2 was run before test 3-1. As predicted, slip initiated on the east end of the beam where the interface was smooth and had a reinforcement ratio of 0.00417. Slip initiated at a shear force of 143 kips as shown in Figure 5-23, at a total load of 215 kips. As the load was increased further, the west end of the beam that was fluted with no reinforcement began to slip as well. This occurred at a shear force of 153 kips, which correlates to a load of 460 kips (Figure 5-24). Figure 5-25 shows the complete load deflection curve for the shear test 3-2 with the initiation of slip on each end denoted. Test 3-2 ultimately failed in flexural compression at a load of 666 kips (2,960 kN) with a bending moment of 3,552 kip-ft (4,820 kN-m).

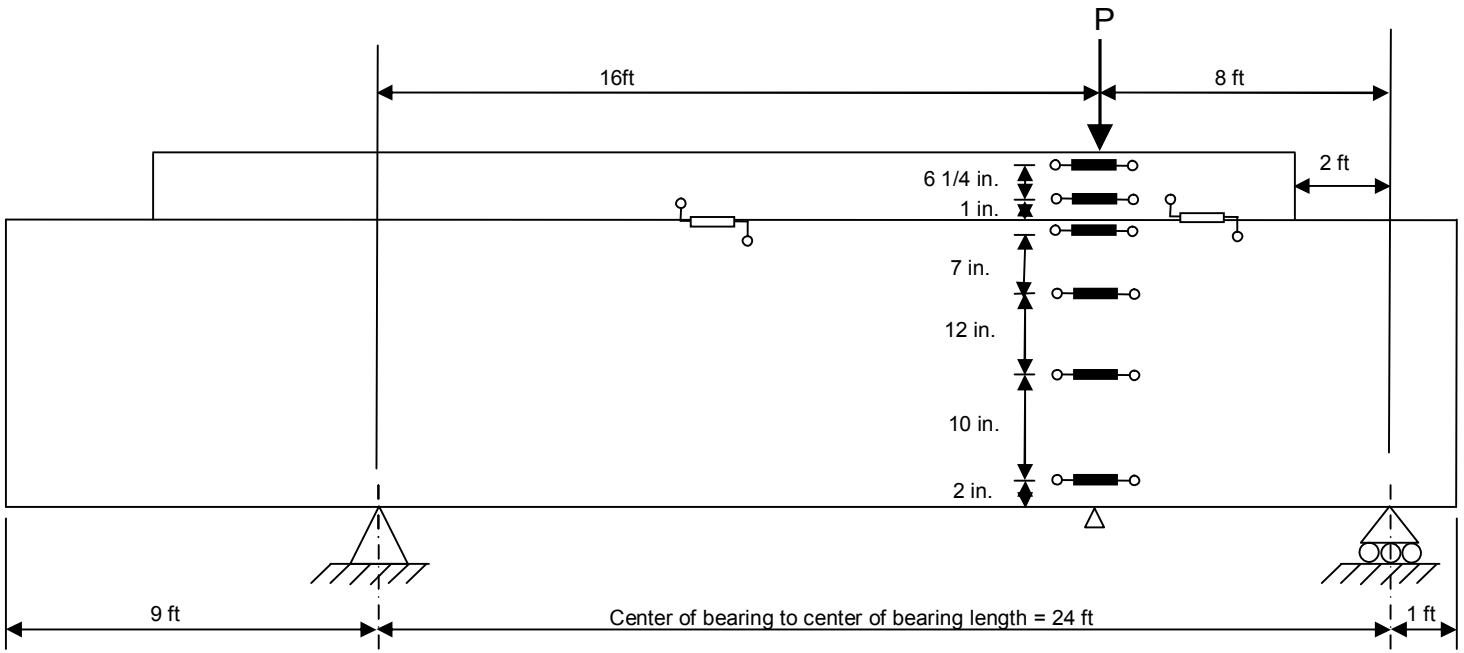

Figure 5-19: Instrumentation and setup for tests 2-1, 2-2, 3-1, and 3-2.

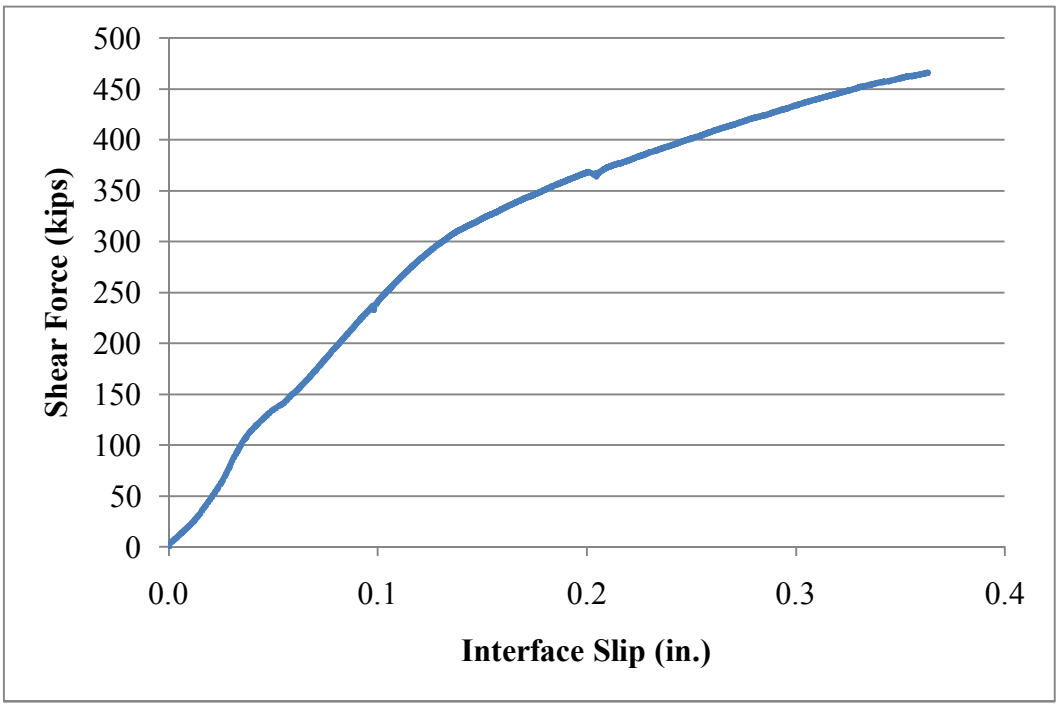

Figure 5-20: Shear – slip curve for shear test 2-1. Note that slip initiated immediately from the time of loading.

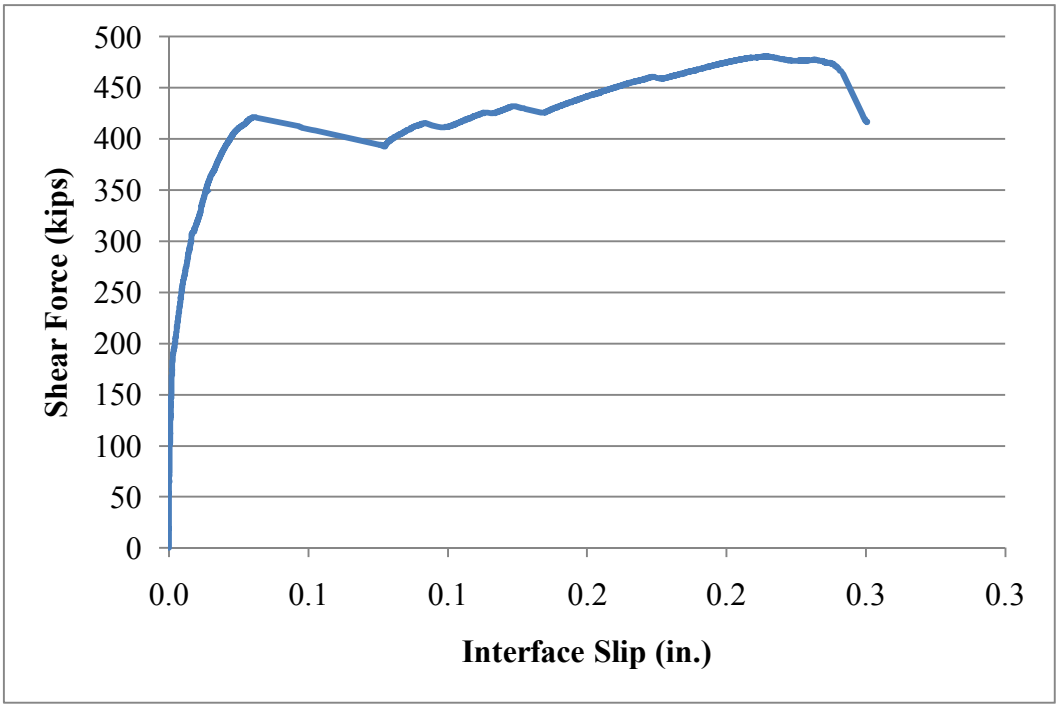

Figure 5-21: Shear – slip curve for shear test 2-2. Note the initiation of slip at 421 kips of shear force.

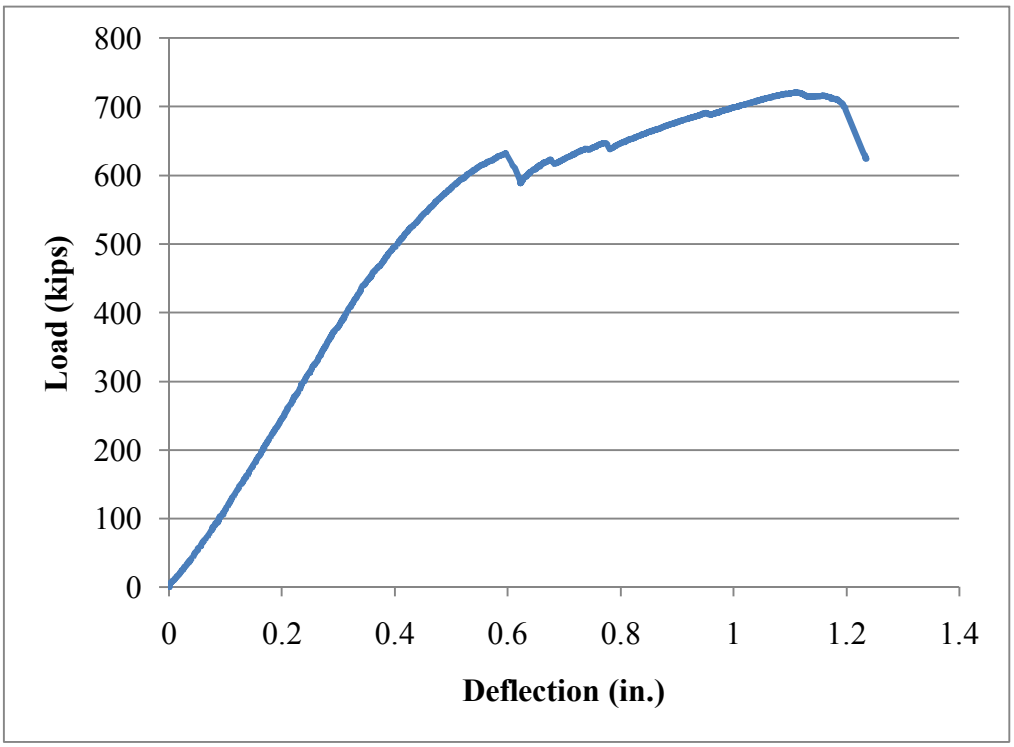

Figure 5-22: Load- deflection curve for shear test 2-2. Note that slip initiation coincided with a load drop and slope change at a load of 632 kips.

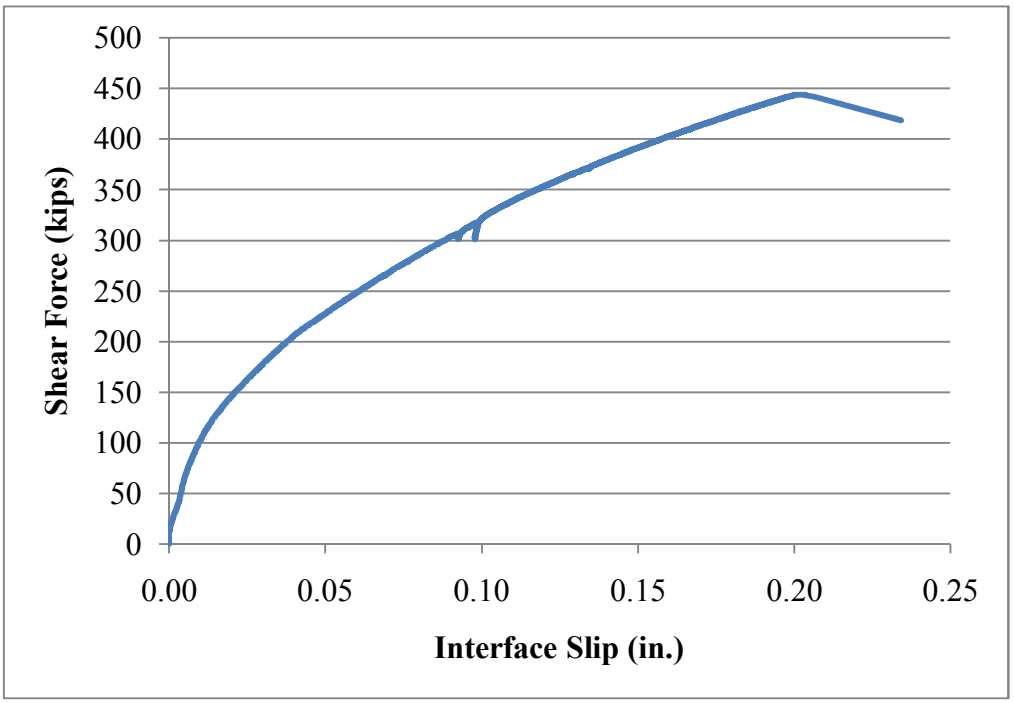

Figure 5-23: Shear – slip curve for shear test 3-2, east end of the beam. Slip was determined to initiate at a shear force of 143 kips.

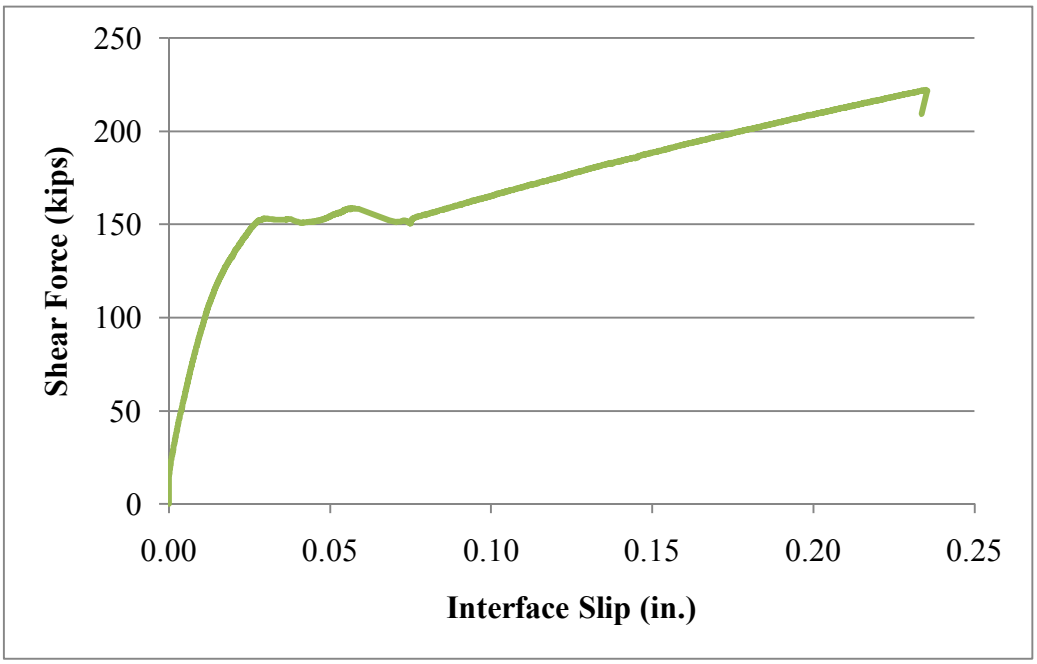

Figure 5-24: Shear – slip curve for shear test 3-2, west end of the beam. Slip was determined to initiate at a shear force of 153 kips.

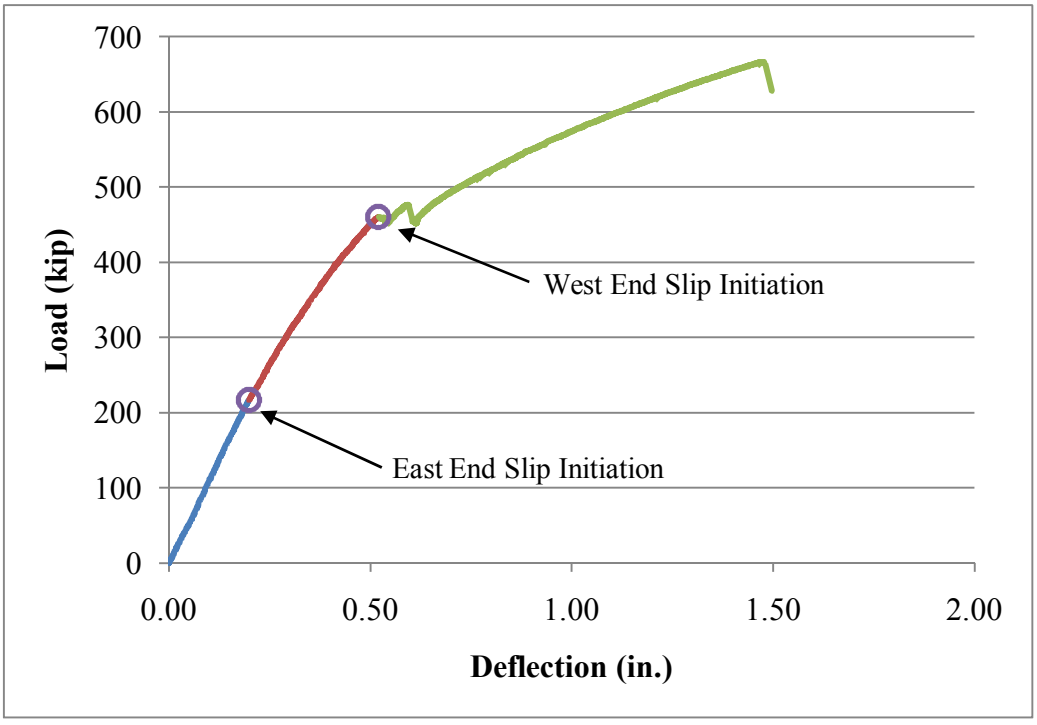

Figure 5-25: Load deflection curve for shear test 3-2.

5.5 Results and Analysis

5.5.1 Comparison to Code Equations

Table 5-2 compares the interface shear capacities of the beams with the theoretical values predicted by the AASHTO and ACI codes. AASHTO LRFD gives an interface shear transfer equation based on shear friction theory:

$$V_n = cA_{cv} + \mu[A_v f_y + P_c] \tag{5-2}$$

not to exceed the smallest of:

$K_1 f_c' A_{cv}$,

and $K_2 A_{cv}$.

where

c = cohesion factor,

400 psi (2.76 MPa) for concrete cast monolithically,

280 psi (1.9 MPa) for a roughened surface with a ¼-in. amplitude,

75 psi (0.52 MPa) for a clean concrete surface, not roughened.

A_{cv} = area of concrete considered to be engaged in interface shear transfer ($b_{vt}d_v$), in^2

μ = friction factor,

1.4 for concrete cast monolithically,

1.0 for concrete with a roughened surface with a ¼-in. (6 mm) amplitude,

0.7 for concrete cast against structural steel with headed studs,

0.6 for concrete without an intentionally roughened surface.

A_v = area of interface shear reinforcement crossing the shear plane within the area A_{cv}, in^2

f_y = yield stress of transverse reinforcement (not to exceed 60 psi), psi

P_c = permanent net compressive force normal to the shear plane, lb

b_{vi}= interface width considered to be engaged in shear transfer, in.

d_v= the distance between the centroid of the tension steel and the mid-thickness of the slab to compute a factored interface shear stress.

K_1=fraction of concrete strength available to resist interface shear

0.3 for slab cast against girder with ¼" surface roughness,

0.25 for monolithic concrete, lightweight concrete cast against roughened concrete, or normal-weight concrete with ¼" surface roughness

0.2 for concrete placed against smooth concrete or steel

K_2=limiting interface shear resistance

1.8 ksi for normal-weight slab cast against girder with ¼" surface roughness

1.5 ksi for normal-weight concrete placed monolithically or with ¼" surface roughness

1.3 ksi for light-weight slab cast against girder with ¼" surface roughness

1.0 ksi for light-weight concrete placed monolithically or with ¼" surface roughness

0.8 ksi for concrete placed against smooth concrete or structural steel with headed studs

ACI presents two different methods for calculating interface shear capacity. Section 11.6 gives the shear friction equation:

$$V_{ni} = \mu A_{vf} f_y, \text{ lb} \quad (5\text{-}3)$$

not to exceed the smallest of:

$.2f'_c A_c$, lb,

$(480 + 0.08f'_c)A_c$, lb,

and $1600A_c$, lb.

where μ is the same as given for the AASHTO equation. For composite beams with minimum reinforcement and a surface intentionally roughened to ¼", Section 17 gives the equation:

$$V_{nh} = (260 + 0.6\rho_v f_y)\lambda b_v d, \text{ lb.} \quad (5\text{-}4)$$

not to exceed:

$500 b_v d$, lb.

When the surface is intentionally roughened but minimum reinforcement is not provided, or when minimum reinforcement is provided, but the surface is not intentionally roughened, the interface shear capacity is limited to:

$$V_{nh} = 80 b_v d, \text{ lb.} \quad (5\text{-}5)$$

Figures 5-26 and 5-27 graphically compare the experimental results with the AASHTO Eq. 5-2 and ACI shear friction Eq. 5-3. The ACI composite section interface shear Eqs. 5-4 and 5-5 do not lend themselves to this kind of graphical representation. Table 5-3 gives the ratio of the experimental results with each of the three code equations. These data show that the existing codes are conservative for most cases, but that when a smooth surface with a low reinforcement ratio is used, the equations can over-predict the interface capacity, potentially leading to unconservative design. For the

beams with fluted interfaces, the existing code equations under-predict the interface shear capacity by 60 to 90%.

Table 5-2: Experimental interface shear stresses compared to ACI and AASHTO code predictions

Shear Test	Interface Type	Clamping Stress [$\rho_v f_y$] (psi)	AASHTO Exp. Stress (psi)	ACI Exp. Stress (psi)	AASHTO Eq. 5-2 Theoretical Stress (psi)	ACI 318 Eq-5-3 Theoretical Stress (psi)	ACI 318 Eq. 5-4 Theoretical Stress (psi)
1-1	smooth	62	73	64	112	37	80
1-2	fluted	0	540	474	210	0	80
2-1	smooth	0	0	0	0	0	0
2-2	fluted	62	873	766	342	62	297
3-1	fluted	0	594	521	210	0	80
3-2	smooth	250	635	558	225	150	80

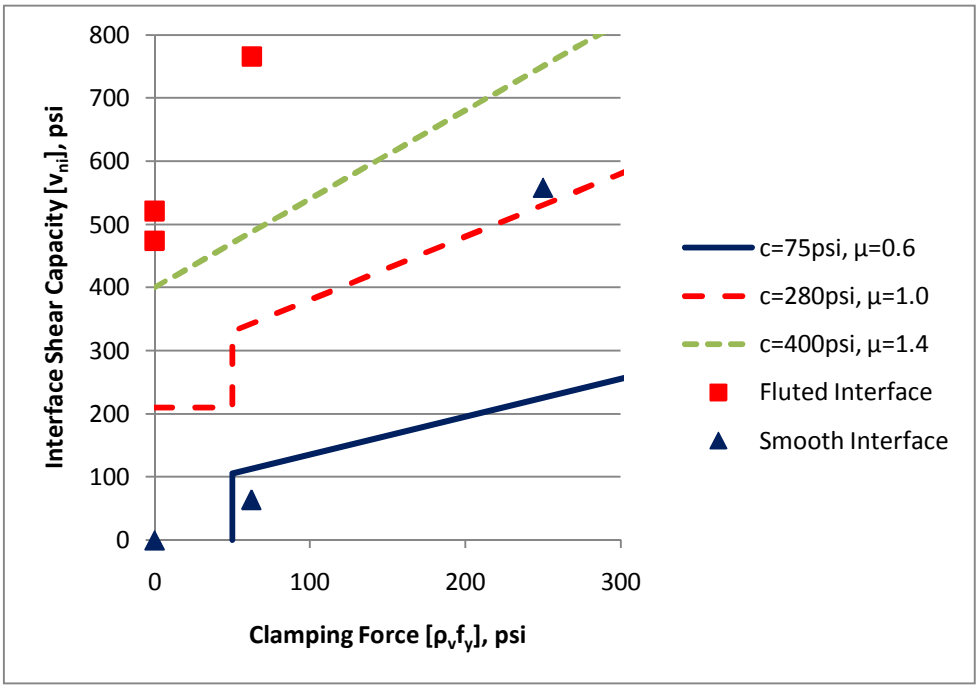

Figure 5-26: Comparison of full-scale composite beam shear tests to AASHTO LRFD shear friction provisions.

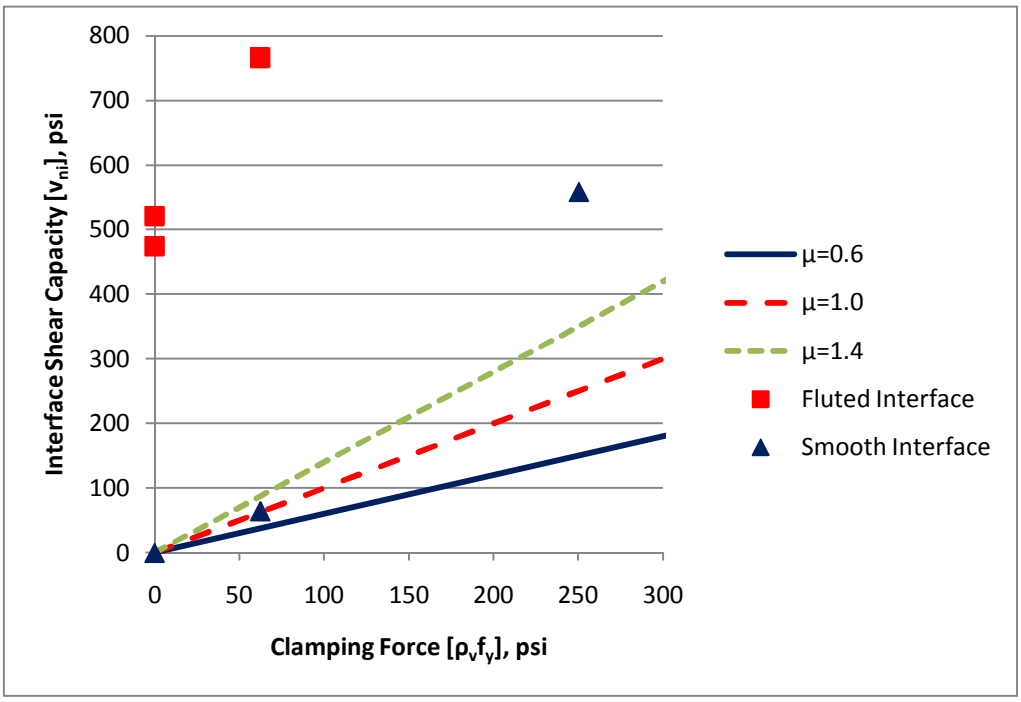

Figure 5-27: Comparison of full-scale composite beam shear tests to ACI shear friction Equation 5-3.

Table 5-3: Ratio of experimental shear interface shear stresses to code predictions

Shear Test	Exp. / AASHTO Eq. 5-2	Exp. / ACI 318 Eq. 5-3	Exp. / ACI 318 Eq. 5-4
1-1	0.65	1.71	0.80
1-2	2.57	N/A	5.93
2-1	N/A	N/A	N/A
2-2	2.55	12.28	2.58
3-1	2.83	N/A	6.51
3-2	2.82	3.72	6.98

5.5.2 Comparison to Push-Off and Small Composite Beam Results

Figure 5-28 compares the results of the full-scale composite beam interface shear tests to research performed on small composite beams and push-off specimens as well as to AASHTO (2010) equations. For both sizes of beam, interface failure was determined based on both observed slip and change in slope of the load-deflection curve. There is no

such phenomenological rationale for choosing the failure slip of the push-off specimens, so both the load at initial slip as well as the load at failure are denoted on the graph. Also for the push-off specimens, the 95% confidence intervals are given based on the assumption of a normal distribution of results. For the push-off case with no reinforcement and for a fluted interface, there were only two specimens, so statistics were not available.

It should be noted that the clamping force is based on the assumption of yielding of the steel reinforcement. This assumption may not be accurate for the tests with smooth interfaces as it is based on the surface roughness creating a separation across the interface that strains the steel to its yield point. Previous researchers have used strain gauges on interface steel to try to quantify the actual clamping force. This approach was not used in the current research due to the complex state of strain of the steel as it crossed the interface as well as the possibility of changing the interface performance via the presence of gauges.

For all of the tests in which the surface was fluted, the AASHTO (2010) equation for an intentionally roughened interface provided a conservative estimation of performance. For a majority of the tests with a smooth interface, the AASTHO equation for a reinforced smooth interface was not a conservative estimator of interface shear performance.

Figure 5-29 shows the same data compared to the ACI shear friction equation. The ACI equation provides a conservative estimator of the observed test results for specimens with smooth interfaces and roughened interfaces. For the roughened

interfaces, the ACI equations may be overly conservative as they under-predict the capacities by more than 300 psi (2.07 MPa).

Other authors have proposed equations for interface shear transfer. Kahn and Mitchell (2002) proposed an equation based on shear friction theory that incorporated a term for concrete cohesion based on the concrete strength:

$$v_u = 0.05 f'_c + 1.4 \rho_v f_y \leq 0.20 f'_c . \tag{5-6}$$

They found this equation to be conservative for as-cast concrete surfaces with traditional and high performance concretes. Loov and Patnaik (1994) proposed a different type of equation that is based on a parabolic rather than linear shear friction theory. It combined an initial cohesion based on a roughened surface with the effect of reinforcement and concrete strength. The resulting equation was:

$$v_n = k\lambda \sqrt{(15 + \rho_v f_y) f'_c} \leq 0.25 f'_c , \tag{5-7}$$

where k is a constant equaling 0.5 for composite construction. Since both of these equations assume a roughened interface, Figure 5-30 compares them to the specimens with fluted surfaces. The Kahn and Mitchell equation gives a conservative estimate of the shear stress at clamping stresses above 200 psi (1.38MPa). The Loov and Patnaik equation is conservative over all of the test data points, but does not provide a 95% confidence given the limited number of tests in the data set.

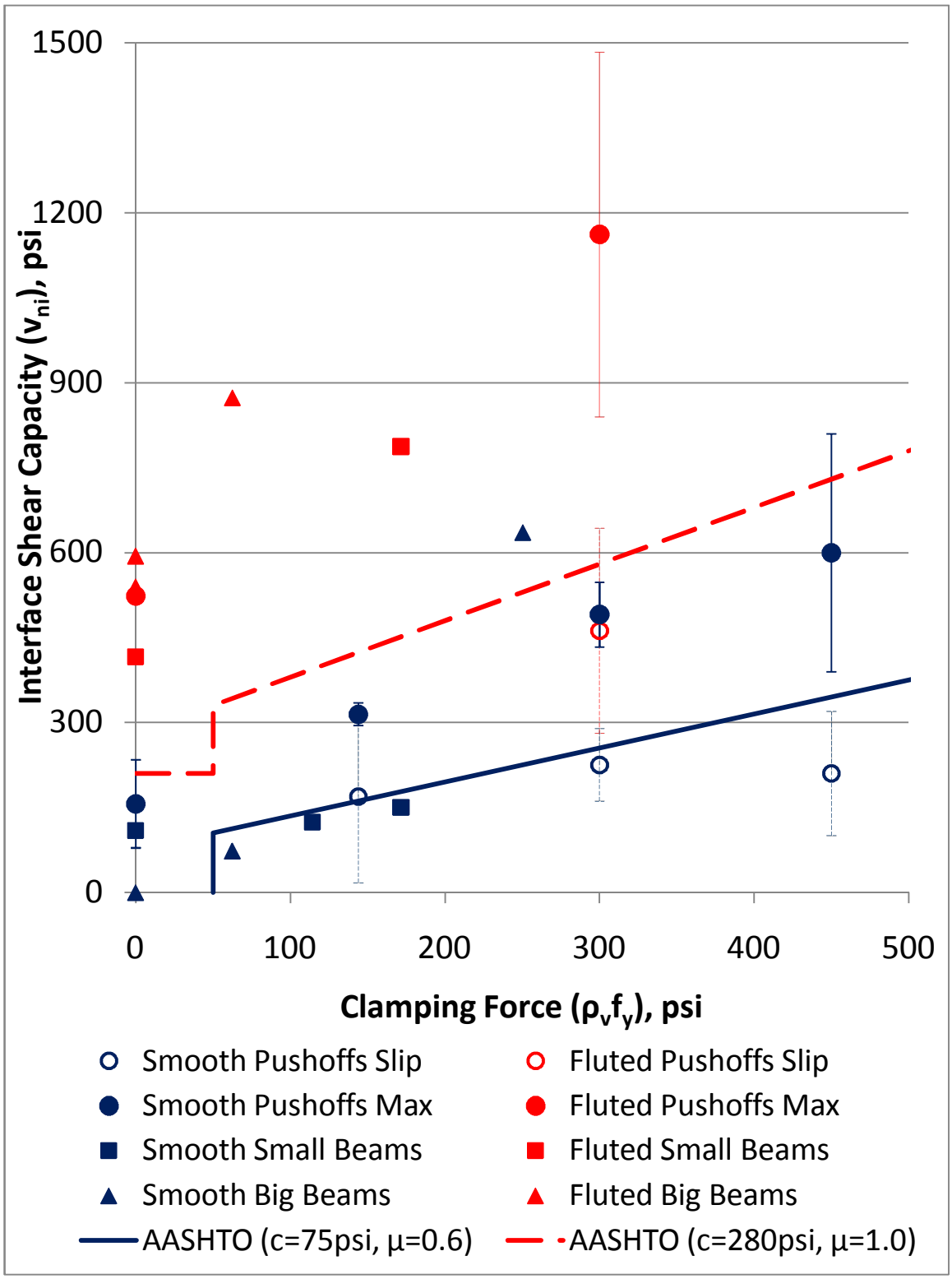

Figure 5-28: Results of push-off, small beam, and full-scale beam interface shear tests compared to Equation 5-2.

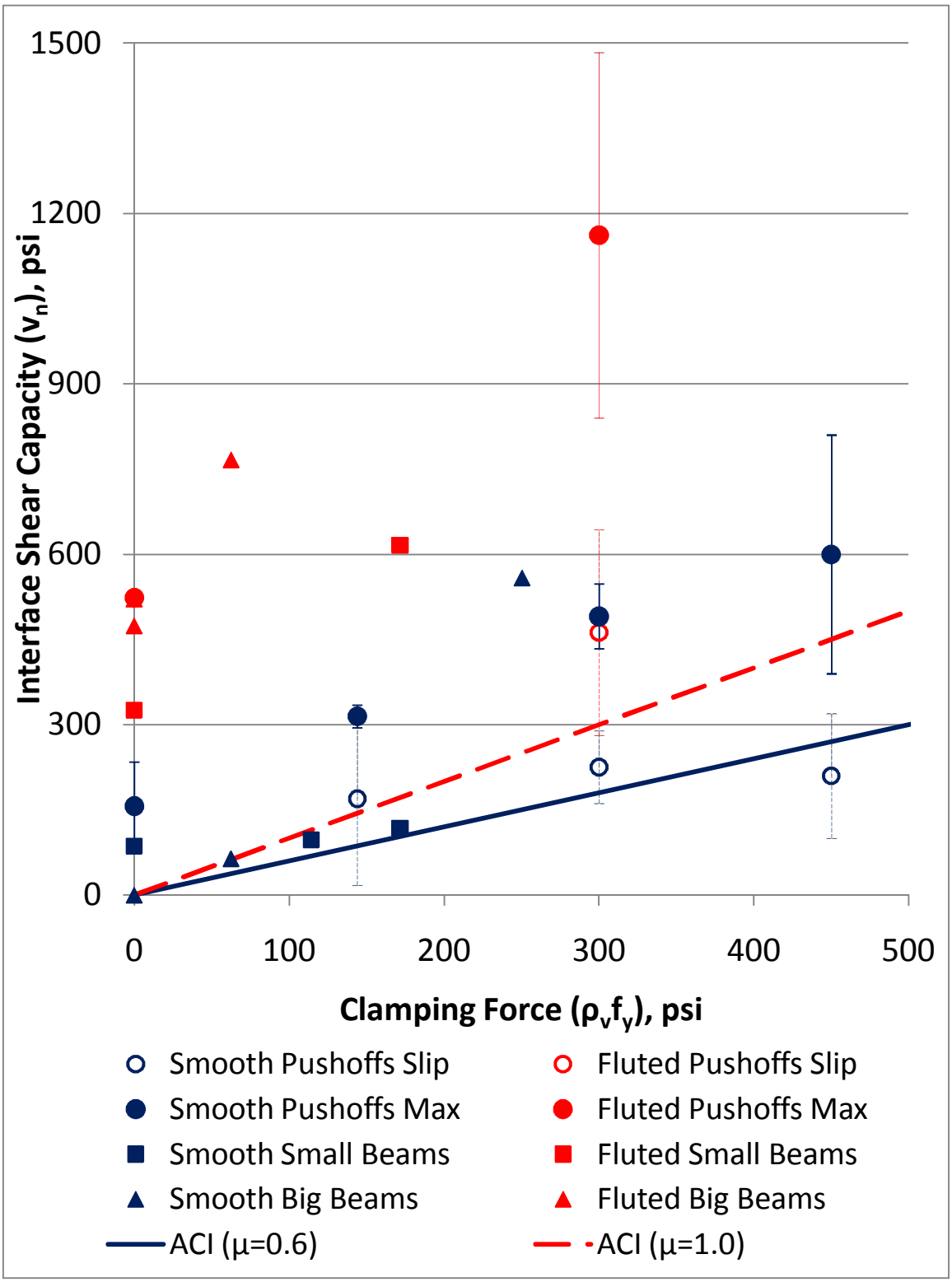

Figure 5-29: Results of push-off, small beam, and full-scale beam interface shear tests compared to Equation 5-3.

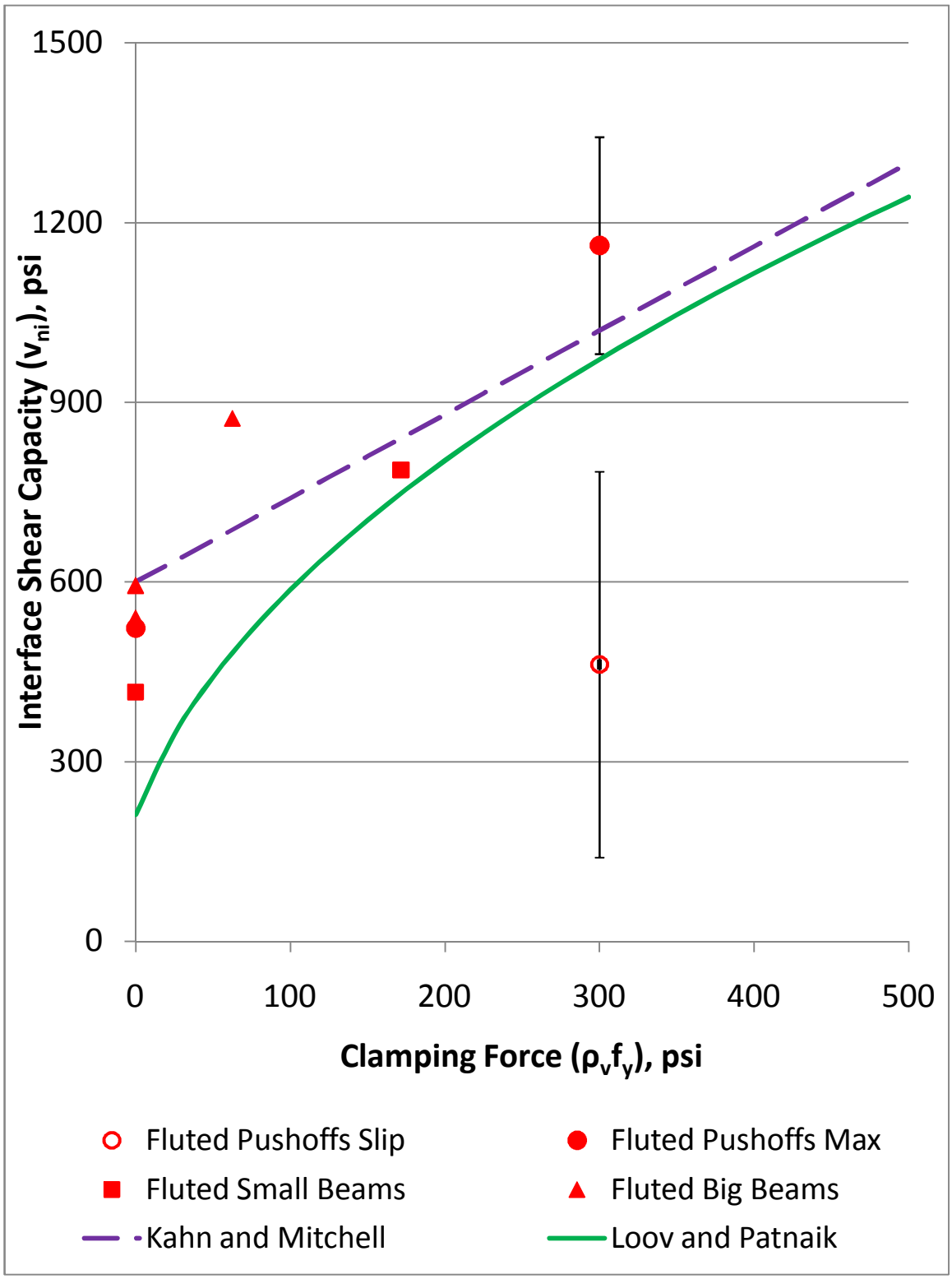

Figure 5-30: Results of push-off, small beam, and full-scale beam interface shear tests compared to Equations 5-6 and 5-7 proposed by Kahn and Mitchell (2002)and Loov and Patnaik (1994), respectively.

5.6 Conclusions

1. The six interface shear tests of full-scale prestressed UHPC bridge girders with cast-in-place HPC decks showed that AASHTO (2010) equations cannot safely be used to design interface connections with as-cast, smooth UHPC surfaces. ACI 318 shear friction equations do provide a lower bound for these smooth-interface connections using a friction coefficient, μ, of 0.6, but smooth interfaces are still not recommended for design of composite systems.
2. A fluted interface can be created in UHPC by depressing formliners into the surface of the beam prior to the concrete setting. This fluted surface can make a roughness similar to that suggested by the ACI and AASHTO codes.
3. When using a fluted interface, both ACI and AASHTO codes were conservative for all specimens tested. This type of interface provides performance similar to roughening the surface of traditional concrete and is suggested for all design applications where composite action is desired.
4. The equation suggested by Loov and Patnaik (1994) provides the most accurate estimation of performance of fluted interfaces between UHPC and HPC while still maintaining conservatism.
5. Small beam tests provide a conservative estimate for full-scale girder tests. In some cases, results of small beams may be overly conservative estimates of full-scale behavior.
6. For smooth beams, push-off slip stresses provide a good estimate of small beam and big beam performance; however, the variability of smooth interface capacities is high so smooth interfaces are not recommended for design of new structures.

Ultimate capacities of fluted push-off specimens were good predictors of performance in both small and large composite beams.

7. Based on a hypothetical bridge design with 90-ft. long, 32-in. deep (27.4 m x 813 mm) UHPC BT-shaped beams spaced at 90-in. (2.3 m) on centers, the fluted surface with #4 (M13) bar stirrups spaced at both 12-in. and 24-in. on center and the smooth surface with stirrups spaced at 12-in. on center satisfy the expected ultimate interface shear stress of 241 psi (1.66 MPa). The smooth surface with minimum stirrup reinforcement would not satisfy the expected ultimate interface stress.

5.7 References

AASHTO (2010). *AASHTO LRFD bridge design specifications*. Washington, D.C., American Association of State Highway and Transportation Officials.

ACI Committee 318 (2008). *Building code requirements for structural concrete : (ACI 318-08) ; and commentary (ACI 318R-08)*. Farmington Hills, Mich., American Concrete Institute.

American Association of State Highway and Transportation Officials (2007). *AASHTO LRFD bridge design specifications*. Washington, D.C., American Association of State Highway and Transportation Officials.

Graybeal, B. A. (2009a). Structural Behavior of a 2nd Generation Ultra-High Performance Concrete Pi-Girder. F. H. Administration. McLean, VA, U.S. Department of Transportation.

Graybeal, B. A. (2009b). Structural Behavior of a Prototype Ultra-High Performance Concrete Pi-Girder. F. H. Administration. McLean, VA, U.S. Department of Transportation.

Grossfield, B. and C. Birnstiel (1962). "Tests of T-Beams with Precast Webs and Cast-in-Place Flanges." *ACI Journal* 59(6): 843-851.

Kahn, L. F. and A. D. Mitchell (2002). "Shear Friction Tests with High-Strength Concrete." *ACI Structural Journal* 99(1): 98-103.

Kahn, L. F. and A. Slapkus (2004). "Interface Shear in High Strength Composite T-Beams." *PCI Journal* 49(4): 102-110.

Keierleber, B., D. Bierwagen, et al. (2008). Design of Buchanan County, Iowa, bridge, using ultra high-performance concrete and pi beam cross section. *PCI-FHWA National Bridge Conference*. Orlando, FL.

Loov, R. E. and A. K. Patnaik (1994). "Horizontal Shear Strength of Composite Concrete Beams." *PCI Journal* 39(1): 48-67.

Patnaik, A. K. (1999). "Longitudinal Shear Strength of Composite Concrete Beams with a Rough Interface and No Ties." *Australian Journal of Structural Engineering* 1(3): 157-166.

Saemann, J. C. and G. W. Washa (1964). "Horizontal shear connections between precast beams and cast-in-place slabs." *American Concrete Institute -- Journal* 61(11): 1383-1409.

CHAPTER 6
DIAGONAL TENSION SHEAR CAPACITY OF PRECAST PRESTRESSED ULTRA-HIGH PERFORMANCE CONCRETE BRIDGE GIRDERS

Current AASHTO (2010) code does not provide for use of Ultra-High Performance Concretes (UHPCs) in bridge design and construction. Specifically, this code does not consider contribution of fiber reinforcement to tension or shear capacities. The few UHPC bridges currently in service in the U.S. make use of fiber reinforcement to eliminate transverse shear reinforcement. If UHPC is going to gain wider usage in U.S. bridge construction, code equations for quantifying the shear capacity of fiber-reinforced UHPC must be developed. The objectives of this chapter are to quantify the diagonal tension shear capacity of prestressed UHPC girders with fiber reinforcement and varying amounts of non-prestressed transverse shear reinforcement and to develop provisional equations for the UHPC beam shear capacity.

6.1 Background

6.1.1 Previous Research

Hegger et. al. (2004) studied the shear capacity of precast prestressed UHPC beams that were 11.8 in. (30 cm) deep, 137.8 in. (350 cm) long, and had a shear span of 53.2 in. (135 cm). Figure 6-1 shows the cross section of the tested shear beams. Each beam was prestressed with eight 7-wire 0.6 in (15.2 mm) diameter strands stressed to 153 ksi (1,000 MPa). If the strands were standard 270 ksi (1,862 MPa) ultimate strength, this was a prestressing stress of approximately 57% the strength of the strand. While it was

not stated explicitly, due to the very specific round number reported for stress, it was assumed that this stress was before strand release and did not account for any time-dependent losses. The average ultimate shear force carried by these beams was 61.4 kips (273 kN) which produced a moment at shear failure of 270 kip-ft (366 kNm). The AASHTO (2010) specification uses the following equation for calculating shear stress at failure:

$$v_u = \frac{V_u}{\phi b_v d_v}, \tag{6-1}$$

where

V_u = shear force at failure,

φ = resistance factor (taken as 1.0),

b_v = width of web adjusted for the presence of ducts (not to be confused with interface width which is also denoted by b_v in AASHTO)

d_v = effective shear depth, not to be taken as less than the greater of $0.72h$ or $0.9d_e$

h = depth of girder and deck (when present)

d_e = distance from centroid of steel to extreme compression fiber.

Based on this equation, the average shear stress of the Hegger tests at failure was 2,490 psi (17.2 MPa).

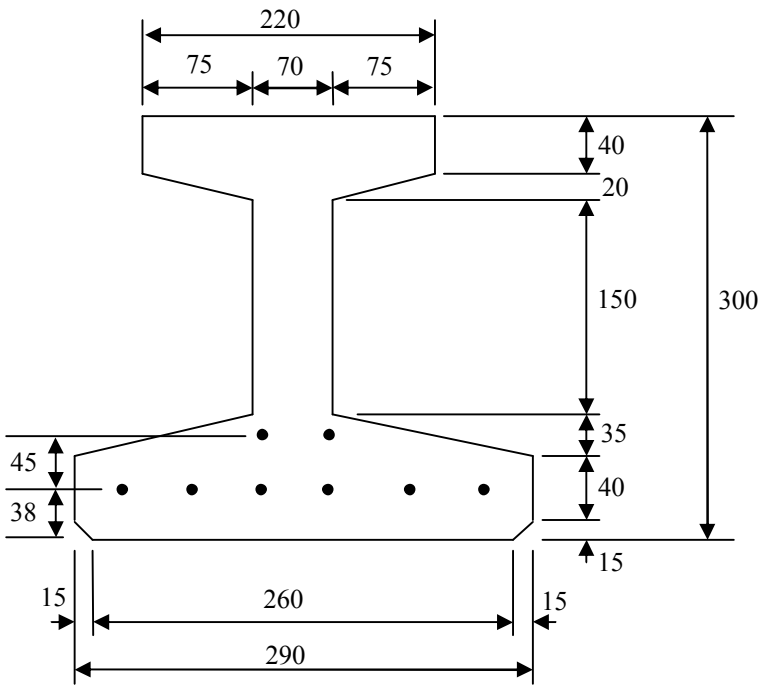

Figure 6-1: Cross-section of UHPC beam tested by Hegger et. al. (2004). All units in mm. Note: 1 in = 25.4mm.

As previously stated, AASHTO (2010) makes no provision for the use of UHPC or any other fiber-reinforced concrete; however, for completeness, the experimental results are compared to these equations. Using a resistance factor of 1, the AASHTO general procedure (5.8.3.4.2) based on the Simplified Modified Compression Field Theory (S-MCFT) (Bentz et al., 2006) predicted a shear capacity of 27.7 kip (1,080 psi) [123kN, 7.45 MPa], which was 56% lower than the average observed failure stress. For the S-MCFT calculation, a maximum aggregate size of 0 was used based on fine sand being the largest aggregate. Using the AASHTO simplified procedure (5.8.3.4.3), a predicted ultimate shear capacity of 30.5 kip (1,190 psi) [135kN, 8.22 MPa] was calculated. This value was 52% lower than the average observed value.

At this point the AASHTO nomenclature should be clarified. The provisions of section 5.8.3.4.2 are the *general* procedure based on the *simplified* modified compression field theory (here abbreviated S-MCFT). This should not be confused with the *simplified* procedure for prestressed and nonprestressed sections presented in section 5.8.3.4.3 of the code (AASHTO, 2010).

Graybeal (2005) performed three shear tests on sections of an 80-ft. (24.38 m) long and a 30-ft (9.14 m) long AASHTO Type II UHPC girder. Table 6-1 gives the details of each of the three shear tests. The ultimate shear stress reported was calculated using Eq. 6-1. Graybeal noted that girder 28S had a longitudinal hairline crack running down the entire shear span at the joint of the web and the bottom flange prior to testing. It was suggested that this initial crack was the reason for the lower ultimate shear load on this test. For girder 14S, a portion of the shear span also included strands that were intentionally debonded to prevent end bursting. This reduced prestressing could have decreased the ultimate shear carried by this girder.

For each of the tests performed by Graybeal (2005), AASHTO (2010) general procedure (5.8.3.4.2) estimated an ultimate shear capacity between 84 and 86 kips (548 and 552 psi) [381 to 383 kN, 3.78 to 3.80 MPa] depending on the girder length. These values are approximately 78% less than the lowest observed experimental stress. AASHTO simplified procedure (5.8.3.4.3), predicts a capacity of 108 kips (689 psi) [479 kN, 4.75 MPa), which is 72% less than the lowest observed experimental stress.

Graybeal (2009) also performed shear tests on three girders with an optimized shape, called the pi-girder. These tests showed even less correlation to current code with capacities that were almost seven times greater than those predicted byAASHTO (2010).

Table 6-1: AASHTO Type II UHPC girder shear test results (Graybeal, 2005)

Test	Supported Length, ft. (m)	Shear Span, ft. (m)	Shear span to depth ratio	Ultimate Shear Load, kips (kN)	Ultimate Shear Stress, psi (MPa)
28S	28 (8.5)	6.5 (2.0)	2.17	384 (1710)	2,460 (17.7)
24S	24 (7.3)	7.5 (2.3)	2.5	502 (2230)	3,210 (22.1)
14S	14 (4.3)	6 (1.8)	2.0	438 (1950)	2,800 (19.3)

Hegger and Bertram (2008) conducted eight shear tests on four prestressed UHPC beams. Figure 6-2 shows the cross section of the beams. Each beam was 185 in. (4.7m) long. For test "a" on each beam, the span length was 173 in. (4.39 m) and the shear span was 47 in. (1.19 m). After each of these tests, the support on the damaged end of the beam was moved in past the damaged area, and test "b" was conducted on the undamaged end. For beams T1 through T3, a shear span of 47 in. (1.19 m) was used. Test T4b used a shear span of 55 in. (1.40 m). Table 6-2 shows the variation between test specimens. Note that test T3a is not included because the test had to be aborted.

Figure 6-3 shows the experimental results from these four studies along with the theoretical capacities predicted by AASHTO general (S-MCFT) and AASHTO simplified procedures. Note that both procedures are conservative in all cases shown. The only tests where the predicted values were close to those observed were the T2 tests, which did not include steel fibers in the concrete. These results emphasize the need for fiber contribution to be considered when looking at ultimate shear capacities.

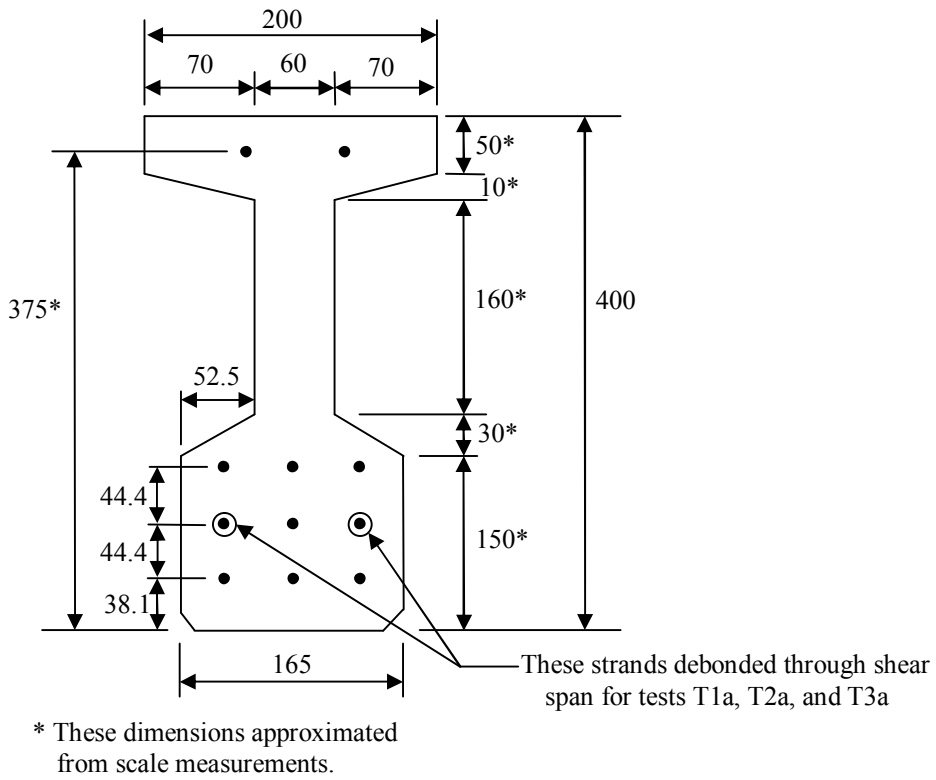

Figure 6-2: Cross-section of UHPC beam tested by Hegger and Bertram (2008). All prestressing strands were 0.5-in (13 mm) diameter 7-wire strands prestressed to 125kN (28.1 kips) each. All units in mm. Note: 1 in = 25.4mm.

Table 6-2: Test parameters for shear tests performed by Hegger and Bertram (2008)

Test	f_c', ksi (MPa)	f_r, ksi (MPa)	Fiber Content, %	Fiber Length, in. (mm)	Stressed Strands	Span / Depth
T1a	21.9 (151)	3.29 (22.7)	0.9	0.69 (17.5)	9	3.8
T1b	25.2 (174)	3.08 (21.2)	0.9	0.69 (17.5)	11	3.8
T2a	19.4 (134)	1.78 (12.3)	0	N/A	9	3.8
T2b	19.4 (134)	1.78 (12.3)	0	N/A	11	3.8
T3b	24.7 (170)	3.50 (24.1)	2.5	0.35 (9)	11	3.8
T4a	25.5 (176)	2.77 (19.1)	0.9	0.69 (17.5)	11	3.8
T4b	26.5 (183)	2.93 (20.2)	0.9	0.69 (17.5)	11	4.4

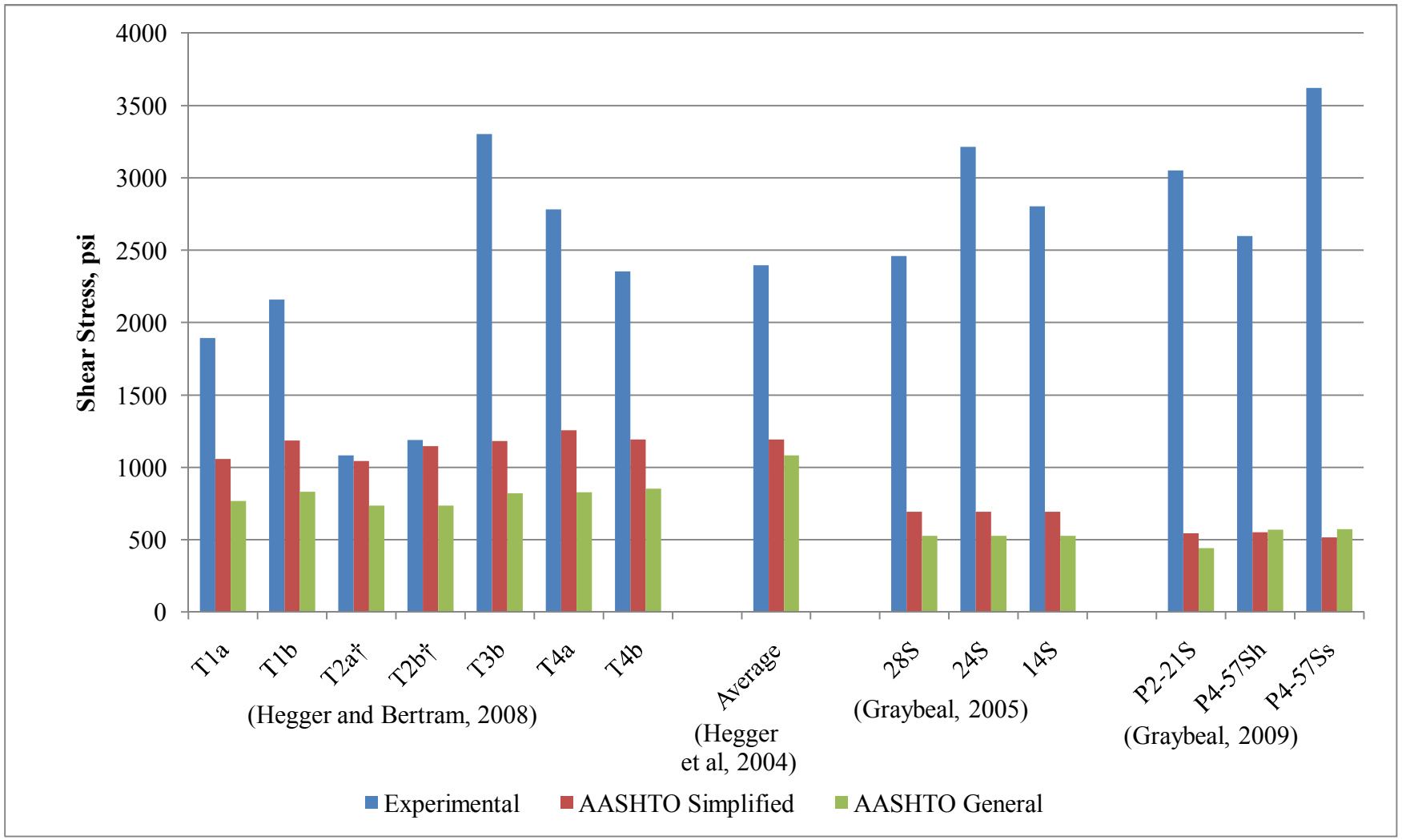

Figure 6-3: Comparison of previous research with current AASHTO (2010) code equations.

6.1.2 Current UHPC Recommendations

Currently, there are three sets of provisional recommendations for the use of UHPC worldwide. The Japanese recommendations (JSCE, 2006) specify that normal shear design procedures be followed for UHPC but that "no deformed bars are permitted, except at special locations such as joints between members." This provision would require shear forces to be carried entirely by the fiber-reinforced matrix along with any prestressed reinforcement.

The Australian recommendations (Gowripalan and Gilbert, 2000) define a maximum tensile stress to be carried by the fiber reinforced concrete:

$$\sigma_1 = \frac{\sigma_x}{2} + \sqrt{\left(\frac{\sigma_x}{2}\right)^2 + \tau^2} \tag{6-2}$$

based on the axial stress due to prestressing, dead and live loads,

$$\sigma_x = -\frac{P}{A} - \frac{Pey}{I} + \frac{My}{I}\ , \tag{6-3}$$

and the shear stress,

$$\tau = 2\sigma_{xy} = \frac{VQ}{Ib}\ . \tag{6-4}$$

This maximum tensile stress is then limited to:

$$5.0 + 0.13\sqrt{f_c'}\ \text{, MPa, or} \tag{6-5}$$

$$0.725 + 0.0495\sqrt{f_c'}\ \text{, ksi.} \tag{6-6}$$

This limit corresponds to a tensile stress of 1 ksi (6.8 MPa) for a typical UHPC with a compressive strength of 29 ksi (200 MPa).

The French design guidelines (AFGC, 2002) and additional information (AFGC, 2003) for the use of UHPC are the most extensive recommendations to date. Using a philosophy similar to that in the AASHTO LRFD simplified procedure, the French guidelines combine a term for concrete contribution, V_{Rb}, with a fiber contribution, V_f, and a passive, transverse reinforcement contribution, V_a. Excluding load and resistance factors,

$$V_{Rb} = 0.24\sqrt{f_{cj}}b_0 z \text{ with } f_{cj} \text{ in MPa, or} \tag{6-7}$$

$$V_{Rb} = 0.0914\sqrt{f_{cj}}b_0 z \text{ with } f_{cj} \text{ in ksi.} \tag{6-8}$$

where

f_{cj} = concrete compressive strength (f'_c)

b_0 = minimum width of web carrying shear (b_v)

z = shear depth (d_v).

The fiber contribution without safety factors is given as

$$V_f = \frac{S\sigma_p}{\tan(\beta_u)} \tag{6-9}$$

where

S = the effective shear area ($b_v d_v$),

σ_p = average tensile stress carried by fibers after cracking until a limiting strain of 0.003. Based on previous research by Graybeal (2005) , this is taken as 1 ksi.

β_u = angle of maximum compressive stress measured from longitudinal axis.

Using the French code, Graybeal (2005) predicted an ultimate shear capacity for his girders of 247 kips, which was more than twice the value predicted by either AASHTO equation, but the prediction was still 36% less than the lowest failure load observed.

6.2 Experimental Program

For the current research program, six shear tests were performed on 32-in. deep, BT-shaped precast prestressed UHPC bridge girders with cast-in-place HPC decks. With the exception of test 1-1a and 3-1, these tests were conducted simultaneously with the interface shear tests detailed in Chapter 5. Test 1-1a was performed on the end of girder 1 that had experienced interface failure during the flexural test. This girder was then tested without a deck in order to determine the beam's web shear capacity. Shear test 3-1 was performed on the end of girder 3 which had a fluted interface. This interface failed during shear test 3-2. Figure 6-4 shows the as-built cross-section of the prestressed precast UHPC girders used for shear tests 1-1a, 1-2, 2-1, and 2-2. Shear tests 3-1 and 3-2 used a section that was identical except that the top flange was 9-in. (23 cm) wide (Figure 6-5). With the exception of shear test 1-1a, all shear tests were performed with a cast-in-place HPC deck that was 8.4 in. (21 cm) thick and 60 in. (152 cm) wide with a 0.63 in. (1.6 cm) haunch. Figure 6-6 shows a cross section of the reduced-flange UHPC girder with cast-in-place deck.

Table 6-3: Shear test properties

Test	Shear Reinforcement Ratio	Shear Reinforcement Spacing, in. (cm)	Surface Preparation	Shear Span Length, ft. (cm)	Shear Span to Depth Ratio
1-1a	0.41%	24 in. (61 cm)	N/A	6 ft. (183 cm)	2.2
1-2	0.00%	N/A	fluted	8 ft. (244 cm)	2.3
2-1	0.00%	N/A	smooth	8 ft. (244 cm)	2.3
2-2	0.41%	24 in. (61 cm)	fluted	8 ft. (244 cm)	2.3
3-1	0.00%	N/A	fluted	8 ft. (244 cm)	2.3
3-2	0.83%	12 in. (31 cm)	smooth	8 ft. (244 cm)	2.3

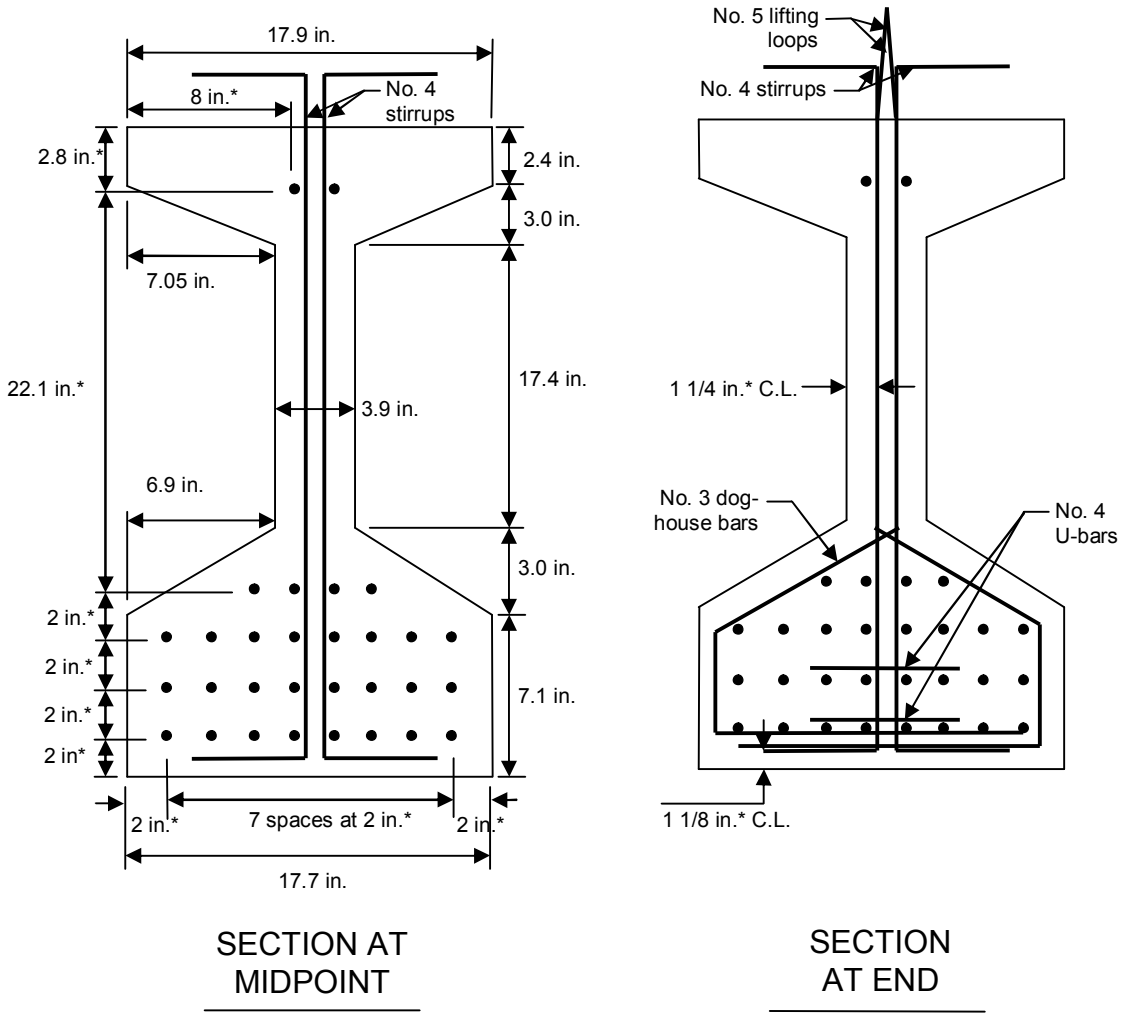

Figure 6-4: As built cross-section of precast prestressed UHPC girders 1 and 2. See Chapter 5 for design dimensions.
*approximate values

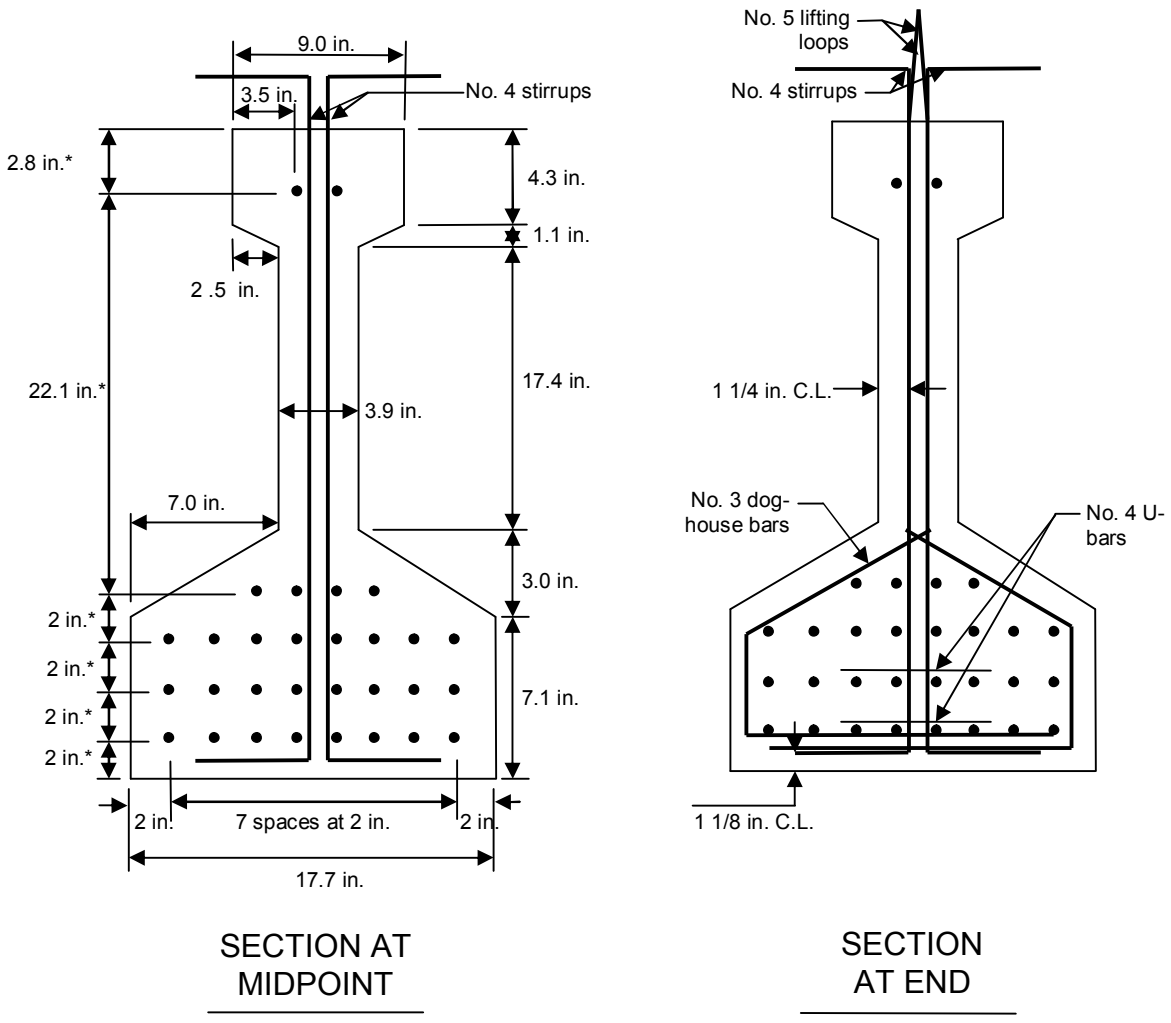

Figure 6-5: As built cross-section of precast prestressed UHPC girder 3 (reduced top flange). See Chapter 5 for design dimensions.
*approximate values

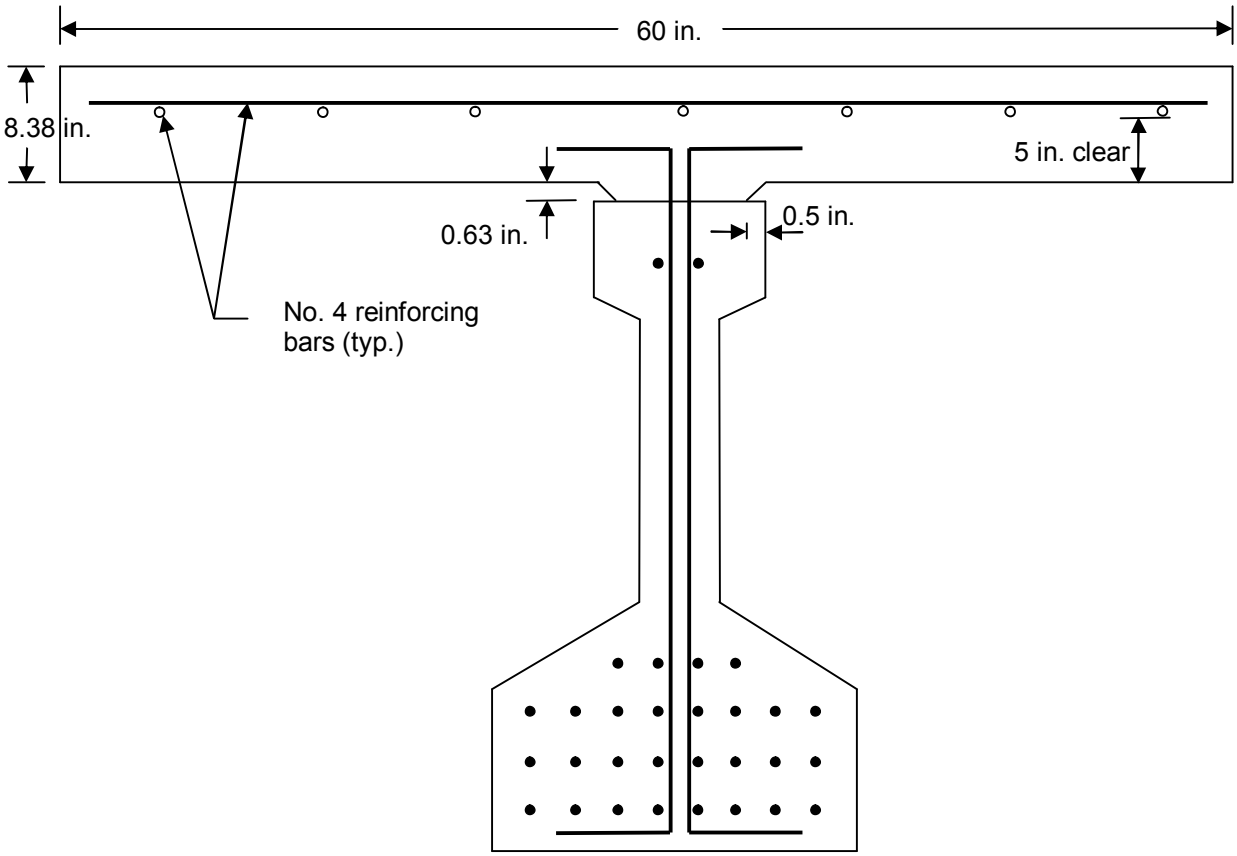

Figure 6-6: Cross-section of girder 3 with cast-in-place deck.

6.2.1 Shear Test 1-1a (non-composite girder with 2-#4 [M13] bars at 24-in. [0.61-m] spacing)

The purpose of shear test 1-1a was to analyze the shear performance of the UHPC girder without a deck and with 2-#4 (M13) bars at 24-in. (0.61-m) spacing. After the flexural test (presented in Chapter 5) led to an interface shear failure along the east end of the girder, the deck was removed from that end of the girder and the girder was cut in two. Figure 6-7 shows the test setup and instrumentation for this test, and Figure 6-8 shows the girder during testing.

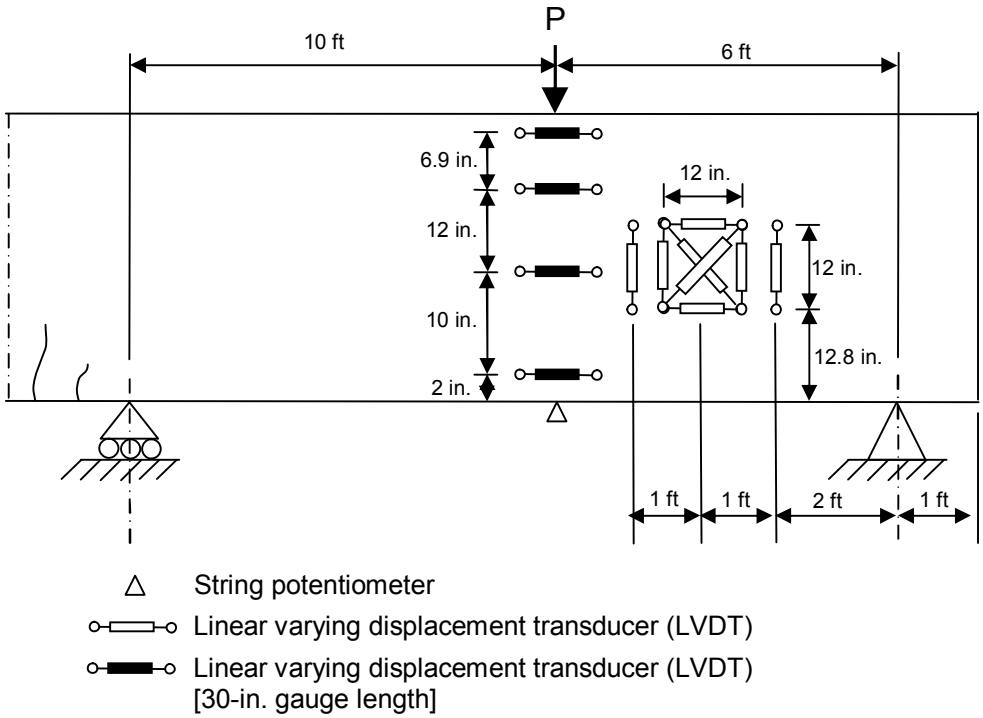

Figure 6-7: Elevation view of experimental setup and instrumentation for shear test 1-1a.

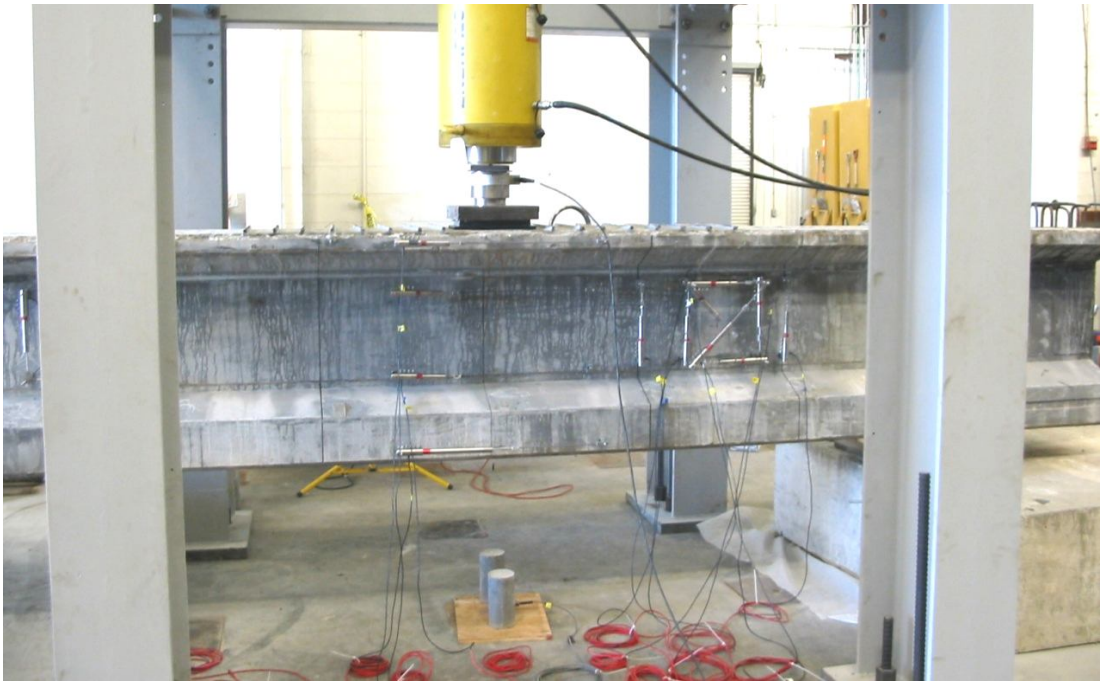

Figure 6-8: Shear test 1-1a during testing.

During the initial loading of this shear test 1-1, testing was stopped due to premature cracking that was observed at the load point with cracks running parallel to the girder's longitudinal axis. The top of the girder was retrofitted by epoxy bonding reinforcing bars to the top surface of the girder perpendicular to the girder's longitudinal axis in order to prevent crack growth. Because shear cracking had not been initiated, all data presented here are from the second loading of this beam section. Figure 6-9 gives the load deflection curve for the second loading.

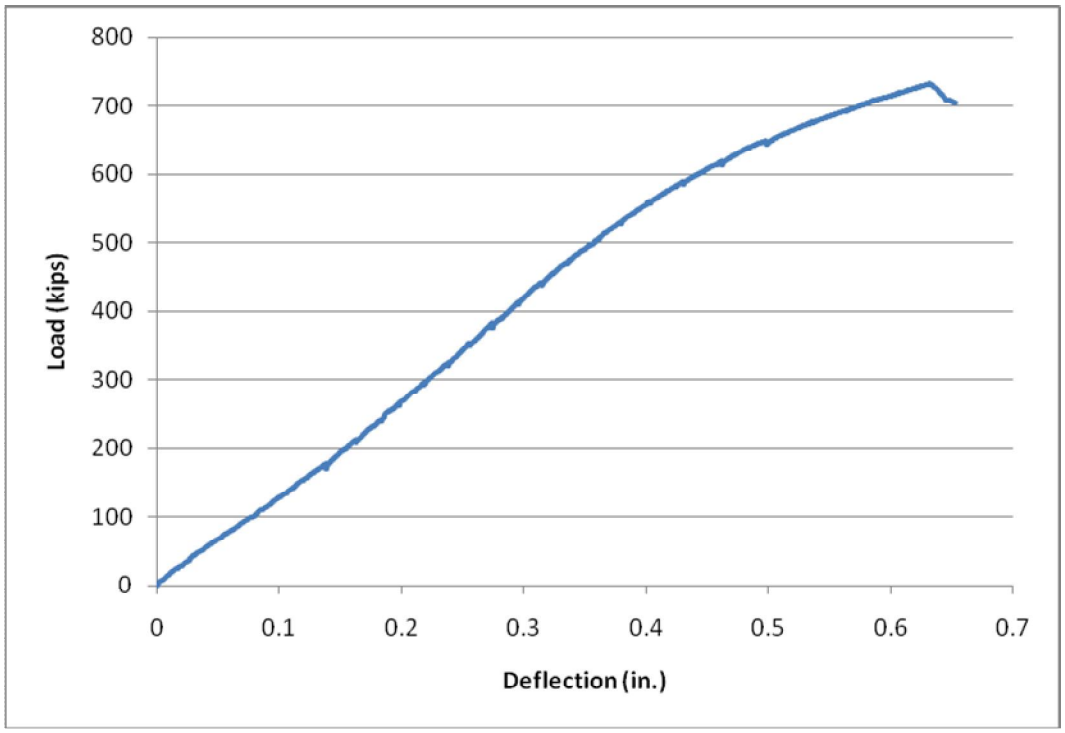

Figure 6-9: Load deflection curve for shear test 1-1a.

The first shear cracks were observed at a load of 325 kips (1,450 kN) which corresponded to a shear force of 200 kips (890 kN) as shown in Figure 6-10. These cracks were only visible when sprayed with a volatile solvent and examined very closely.

Cracks were not visually monitored in subsequent tests due to the danger posed by being under the deck while the girder was loaded. Figure 6-11 and Figure 6-12 show the principal strains and compressive strain angle calculated from the strain rosette. This strain rosette was 12 in x 12 in (305 mm x 305 mm) as shown in Figure 6-7. The size was chosen in order to maximize the potential to capture the shear crack when it formed. Also, since the neutral axis of the beams changed depending on the degree of composite action, the size of the array was large so that it would include the neutral axis throughout the test. Due to the large size of the gauge array, however, the strains and strain angles are averaged across a fairly large area. Based on data from vibrating wire strain gauges (VWSGs), initial compressive strains in the top and bottom external LVDT strain gauges were calculated as -0.000262 and -0.000590, respectively. Based on these strains and the assumption that there was negligible strain in the vertical direction, the initial strain in the diagonal rosette gauges was calculated to be -0.000213.

The principal tensile strain began increasing significantly at around 250 kips (1,110 kN) of shear force. This load also was where the compression principal strain angle began to decrease. Both of these events indicated the onset of diagonal tension shear cracking in the girder. This was supported by a softening of the load deflection curve past 400 kips (1,780kN). The observed tensile strain at cracking was around 0.0004. This is fairly consistent with the tensile cracking strain of 0.0003 assumed for steel fiber reinforced UHPC in the French recommendation (AFGC, 2002).

Figure 6-10: Initial shear cracks were first visible at a load of 325 kips (1,450 kN), which corresponded to a shear force of approximately 200 kips (890 kN).

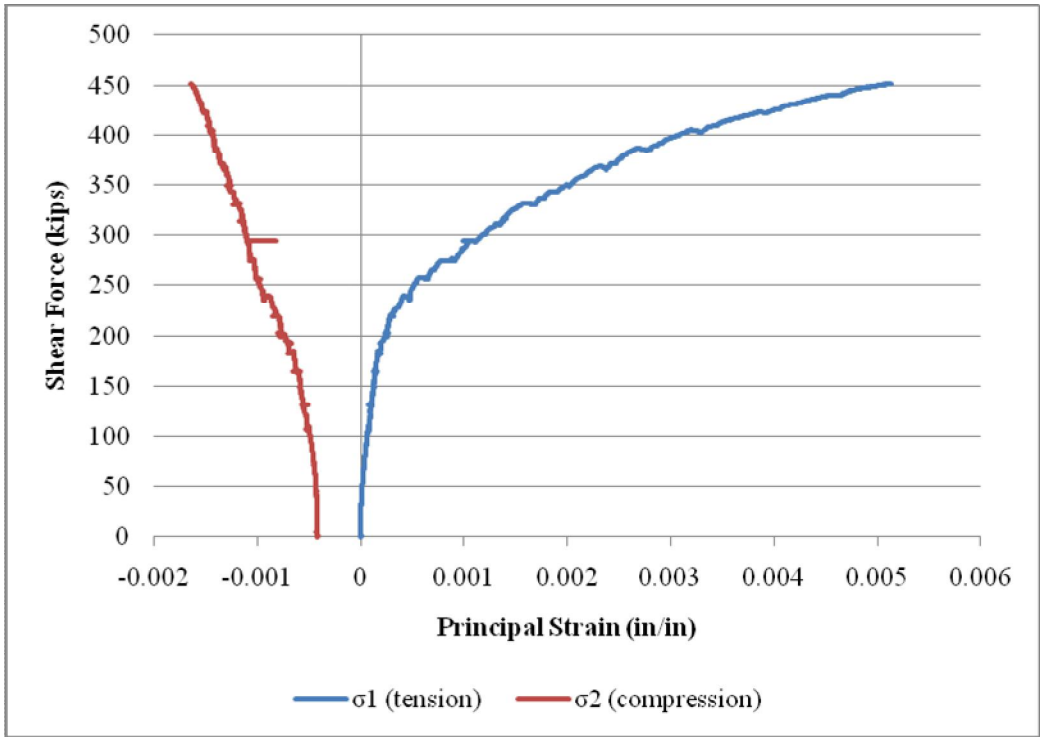

Figure 6-11: Principal strains for shear test 1-1a

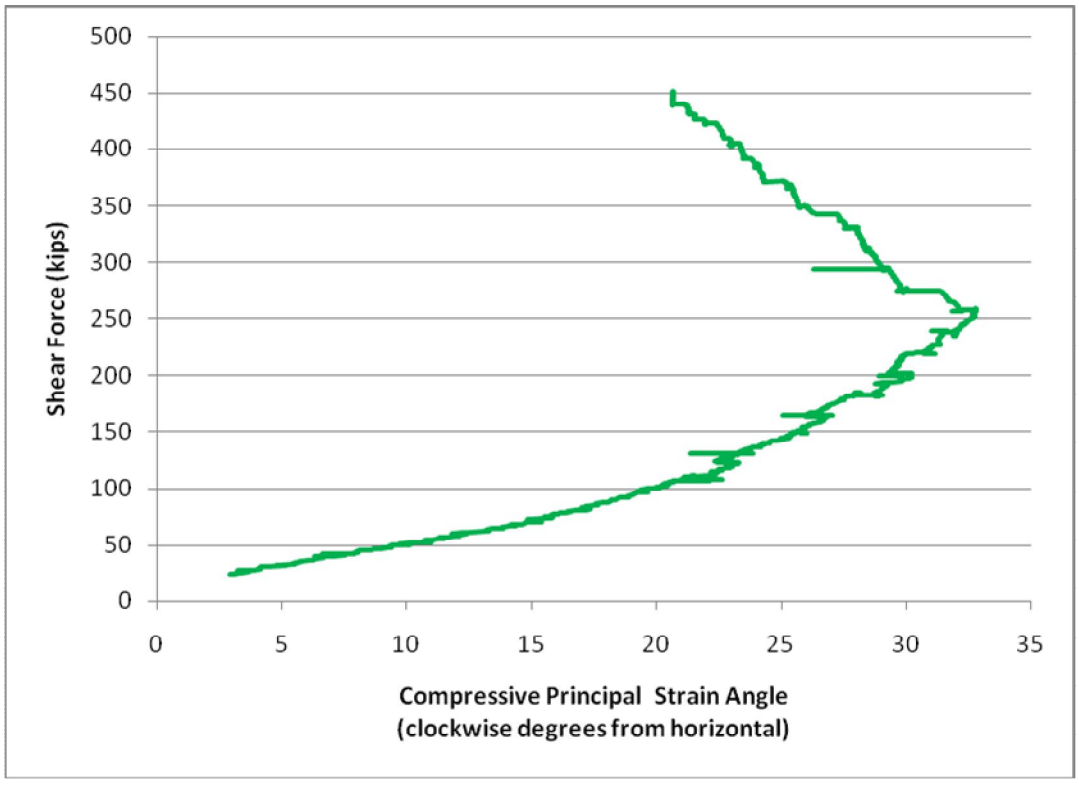

Figure 6-12: Principal compressive strain angle for shear test 1-1a.

Two LVDTs were oriented vertically and placed above the transverse shear reinforcement stirrup locations in midlength of the shear span to measure the strain in the stirrups. These data were paired with the stress-strain curve for the stirrups shown in Figure 6-13. Based on five reinforcing bar tests, the average yield stress was 66.8 ksi (461 MPa), and the modulus of elasticity was measured to be 26,400 ksi (182 GPa). The modulus was lower than expected, which was attributed to possible slippage in the extensometer during testing. Figure 6-14 shows the force in each double-leg No. 4 stirrup. The point at which the stirrups begin to carry load coincides with the shear cracking of the concrete discussed earlier.

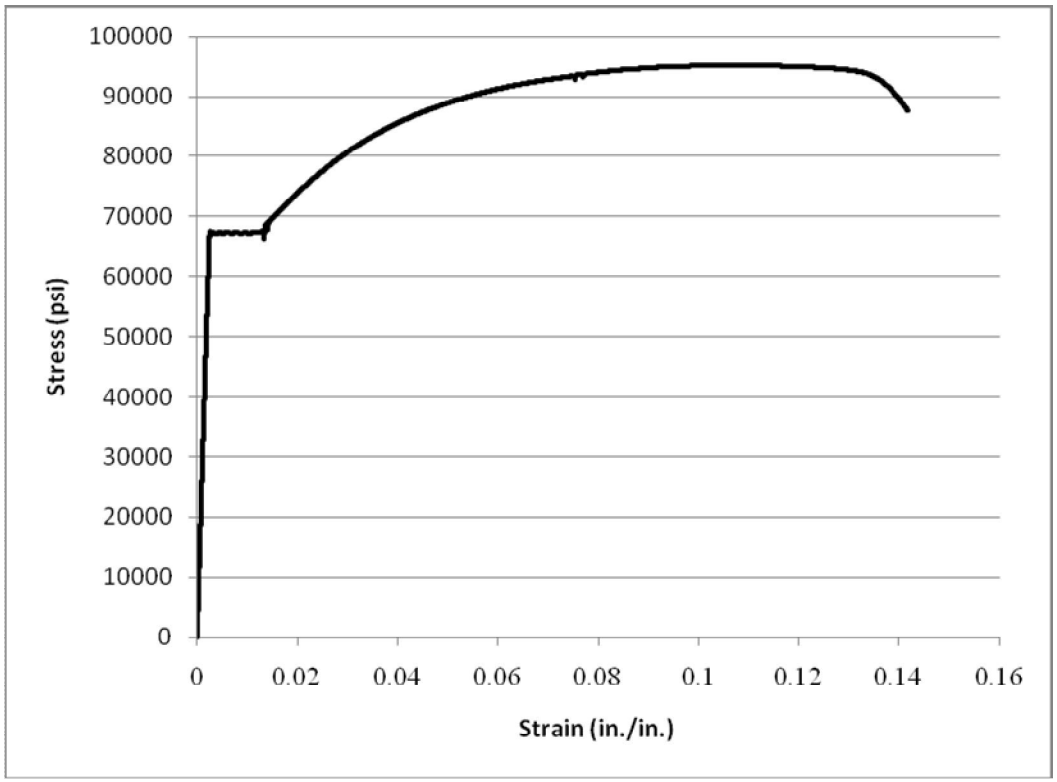

Figure 6-13: Stress-strain curve for No. 4 reinforcing bar used in girder stirrups.

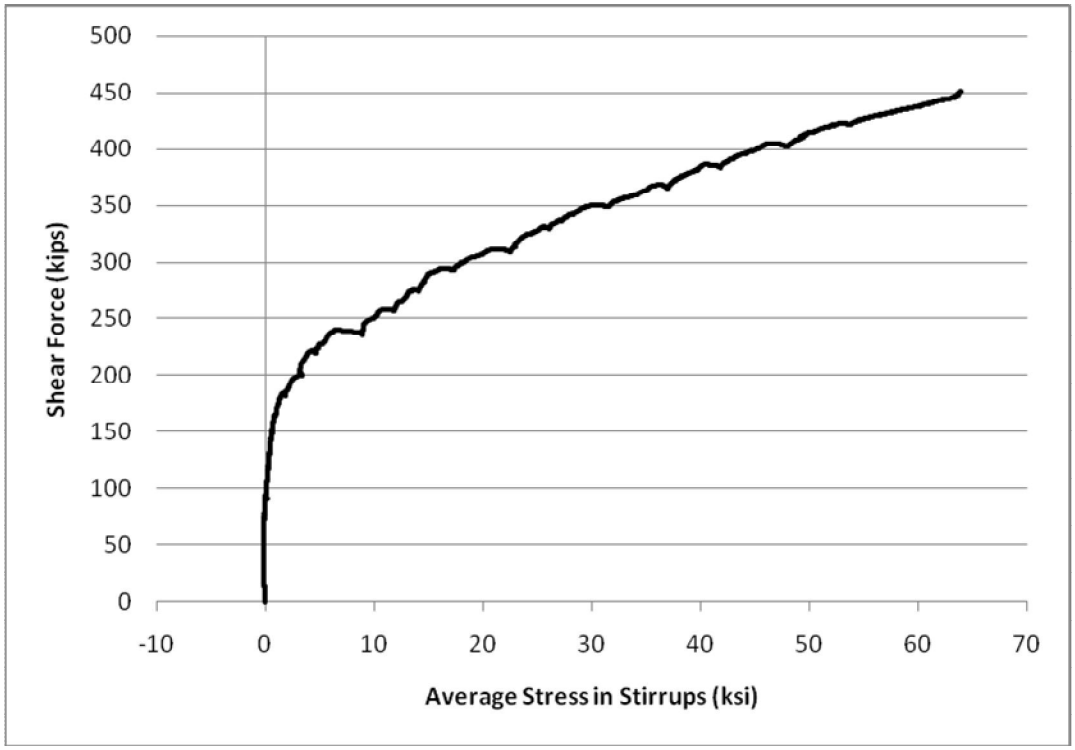

Figure 6-14: Force in shear stirrup.

Girder 1-1a failed in flexural compression at an applied load of 723 kips (2712 kip-ft) [3,216 kN, 3,677 kN-m]. The failure was brittle and was accompanied by loss of a large portion of the top flange of the beam underneath the load point as shown in Figure 6-15. Inspection of the failure surface revealed that a majority of the fibers were oriented parallel to the beam's longitudinal axis with very few crossing the failure planes. The maximum shear carried by the girder prior to the compression failure was 452 kips (4,890 psi) [2010 kN, 33.7 MPa]. The measured crack angle was 34° as shown in Figure 6-16, which was very close to the maximum angle of 33° calculated from the strain rosette. It was also observed that the cracks were very fine and that the spacing was very close (on the order of 0.2 in. [5 mm]) as the girders neared failure. Comparison of shear capacities of all tested girders is presented in section 6.3.

Figure 6-15: Flexural compression failure resulted in loss of a large piece of the top flange.

Figure 6-16: Shear cracks in test 1-1a.

6.2.2 Shear Test 1-2 (fluted interface with no reinforcement)

Shear test 1-2 was performed on the west end of the flexural girder 1 where there was no transverse reinforcement and a smooth interface between the deck and girder. Figures 6-17 and 6-18 show the experimental setup and instrumentation for this test.

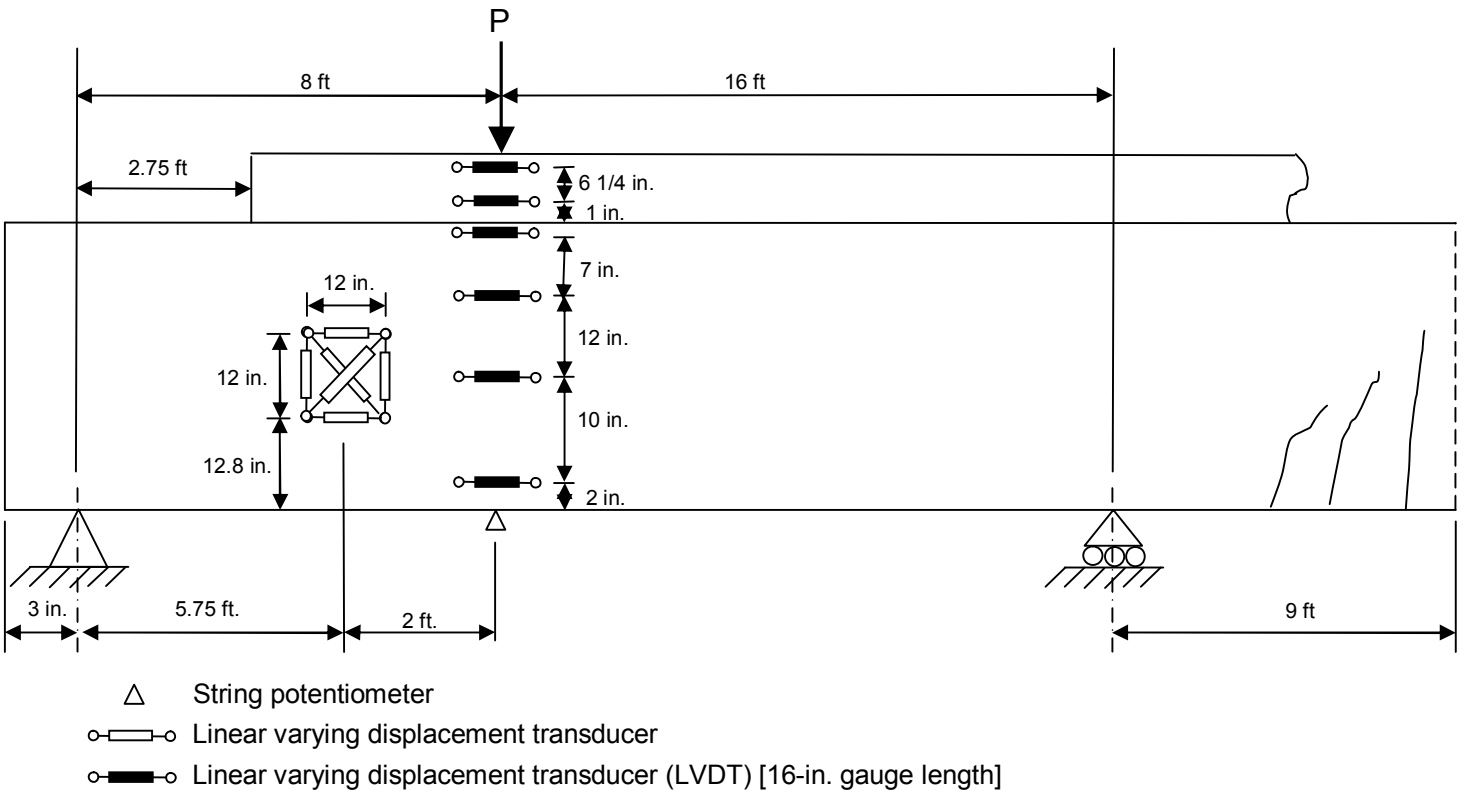

Figure 6-17: Elevation view of experimental setup and instrumentation for shear test 1-2. 1-in = 25.4 mm.

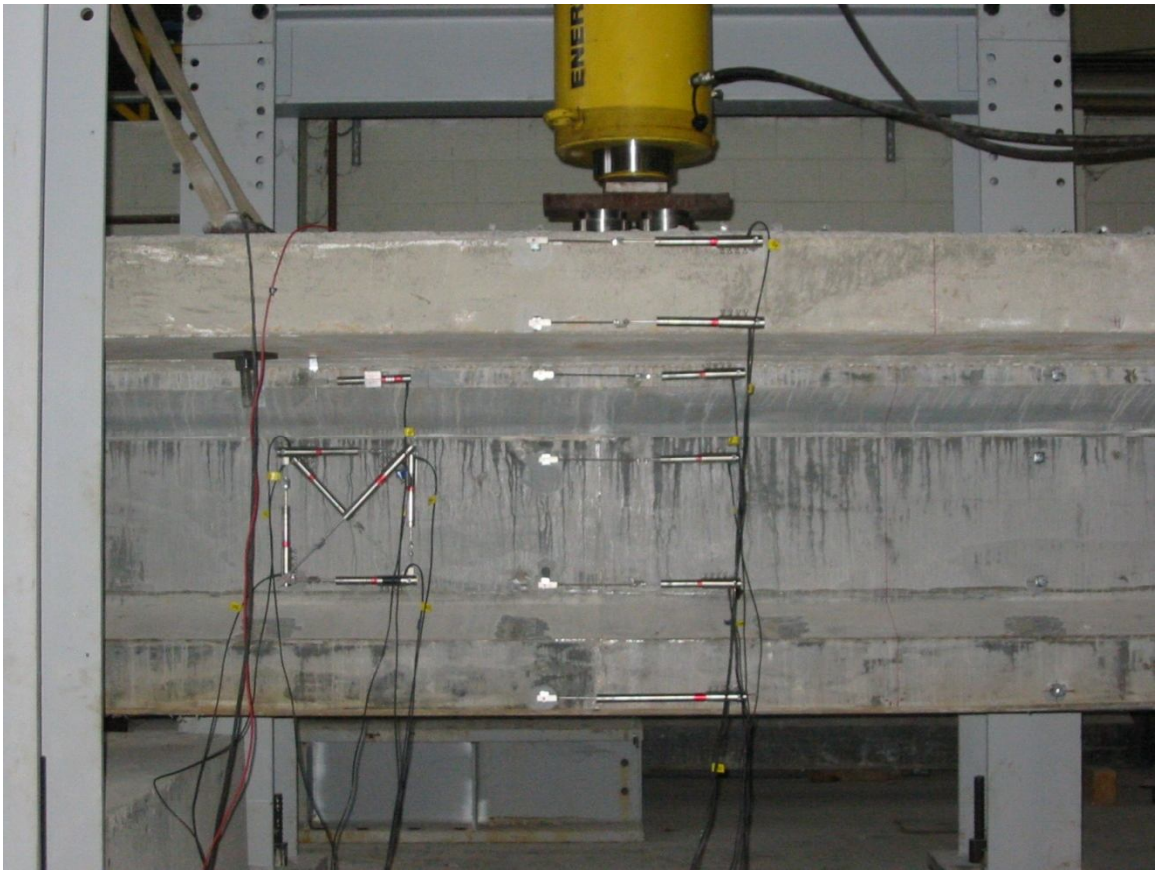

Figure 6-18: Instrumentation for shear test 1-2.

Figure 6-19 shows the load-deflection curve for shear test 1-2, also shown in Chapter 5. The drops in load at 390, 450, and 520 kips (1735, 2000, and 2310 kN) corresponded to progressive slipping of the interface between the girder and deck. Figures 6-20 and 6-21 give the principal strains and principal compressive strain angle for shear test 1-2. These strains were based on initial compressive strains of -0.000259, -0.000594, and -0.000212 in the top horizontal, bottom horizontal and diagonal gauges, respectively. It was also noted that each slip of the deck corresponded to an abrupt change in both principal strain magnitude and angle.

Evaluation of the maximum principal strain indicated a diagonal tension cracking strain of 0.0005. This was higher than the cracking strain of 0.0004 observed in shear

test 1-1a or the cracking strain of 0.0003 anticipated by French code (AFGC, 2002). The slope of the load-strain curve for this test was also lower than shear test 1-1a. Pre-existing cracks from the first shear loading may have caused a softening effect in this initial range.

At a load of approximately 615 kips (2,740 kN), one main diagonal shear crack was observed. At a load of 647 kips (2,880 kN) equal to a shear force of 431 kips (1920 kN), this crack opened suddenly accompanied by a loud cracking sound, a sharp drop in load of more than 400 kips (1,780 kN), and an instantaneous increase in deflection of approximately 0.5 in (1.3cm) deflection. Figure 6-22 shows the diagonal tension shear failure of this girder. The failure crack was measured to be 26 degrees. This was 5 degrees less than the principal compression strain angle shown in Figure 6-21. The difference between these two values was thought to be due to the strain rosette being outside of the center of the shear span. The failure crack went through the upper left portion of the strain rosette. Variations in the initial axial strains used in calculation of the angle could also account for the discrepancy.

The maximum principal tension strain at failure was 0.00464. This strain value was an average strain across the area of the rosette and did not account for strain localization at crack formation. Because of this, it can be used for comparison with subsequent tests, but should probably not be used as a value in design or analysis.

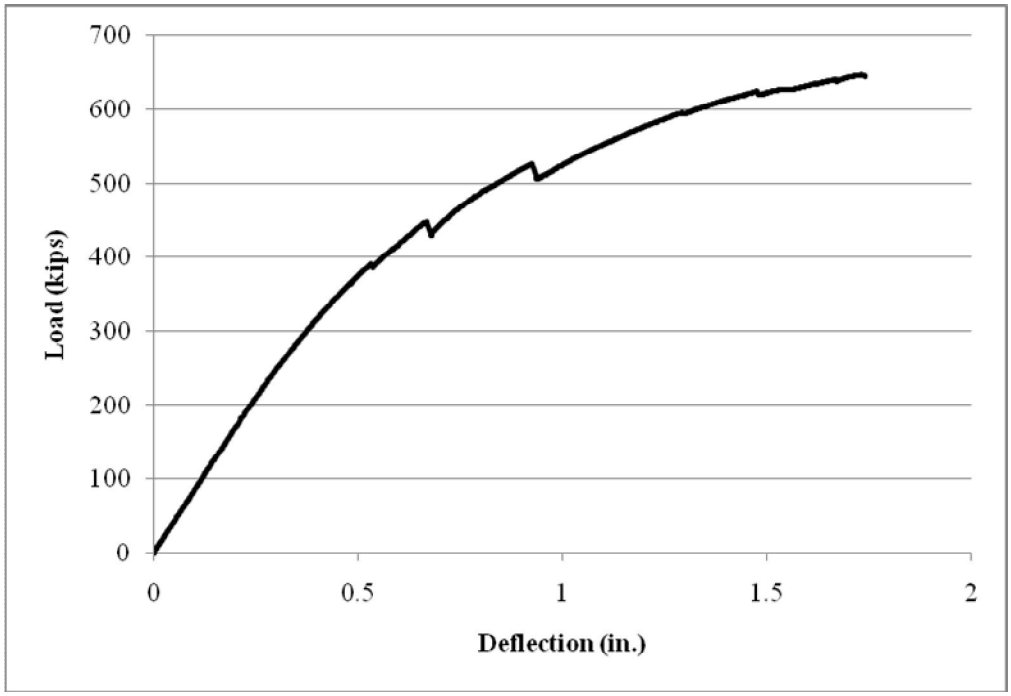

Figure 6-19: Load deflection curve for shear test 1-2.

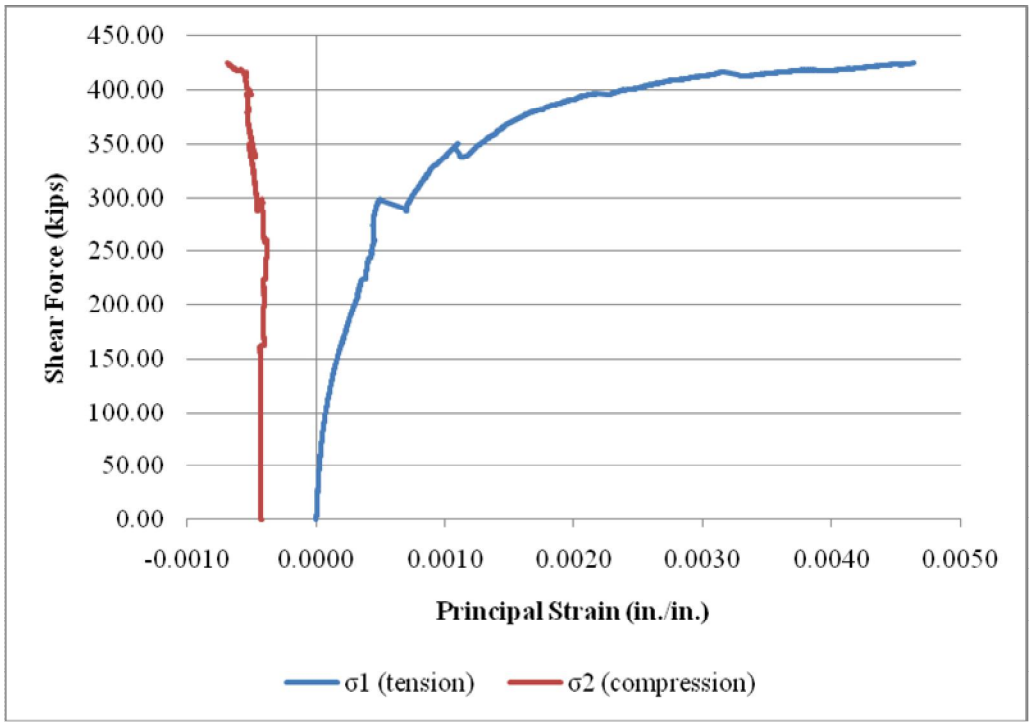

Figure 6-20: Principal strains for shear test 1-2.

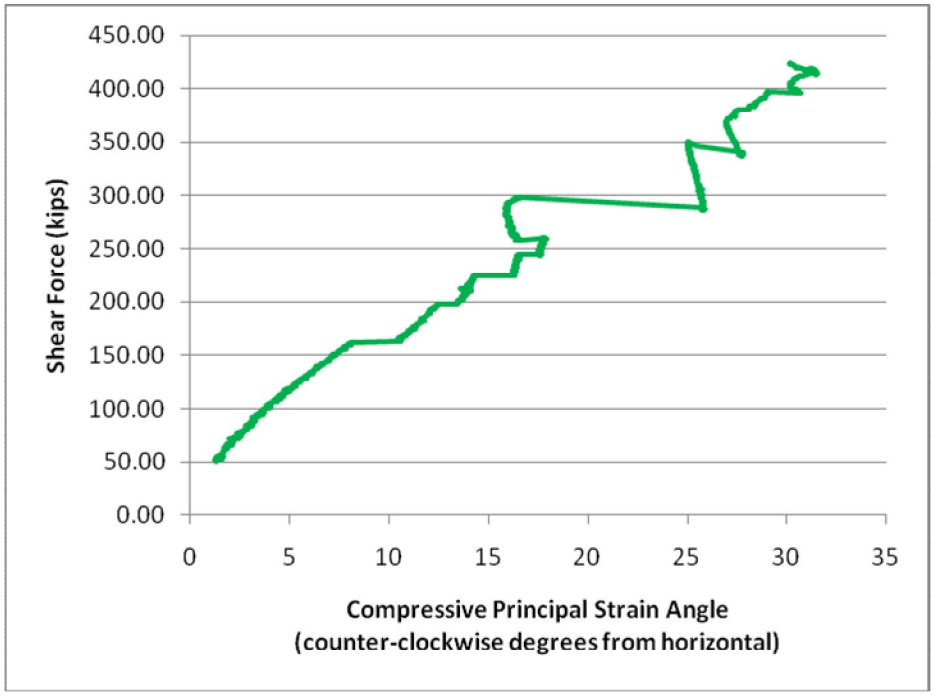

Figure 6- 21: Principal compressive strain angle for shear test 1-2.

Figure 6-22: Diagonal tension shear failure of shear test 1-2.

6.2.3 Shear Test 2-1 (smooth interface with no reinforcement)

The experimental setup and instrumentation for shear test 2-1 are shown in Figure 6-23. The deck began to slip at a very low load, so the response of the system was primarily due to the non-composite girder with no shear reinforcement. This can be seen in the load deflection curve in Figure 6-24. The slope was linear until flexural tensile cracking of the concrete at a moment of 2,400 kip-ft (3,254 kN-m) and a load of approximately 450 kips (2000 kN).

Figure 6-25 and 6-26 show the principal strains and compressive strain angle at the center of the shear span as calculated by the strain rosette with initial strains of -0.000143, -0.000523, and -0.000166 for the top horizontal, bottom horizontal, and diagonal strain gauges, respectively. An unexplained jump was seen in the magnitudes of the principal strains at a shear force of 226 kips (1,010 kN) or a load of 339 kips (1,510 kN). Upon further investigation, this appeared to be due to a stick-slip in the gauges. The principal strains and strain angles were adjusted based on this hypothesis and are presented in their adjusted forms in Figures 6-27 and 6-28. The data from these adjusted graphs is used in discussion and comparison.

Principal tensile cracking was observed to occur at a shear force of 275 kips (1,220 kN). The maximum principal strain at this point was 0.00026. The angle of the minimum principal strain (compression) was 14.5 degrees at this load. After the onset of diagonal tension shear cracking, the compression strain angle increased to a value of 20° at a shear force of 350 kips (1,560 kN). This angle continued to increase slowly up to 21 degrees at failure. The maximum shear carried by the girder was 466 kips (5,040 psi) [2,070 kN, 34.8 MPa] at the moment of flexural failure.

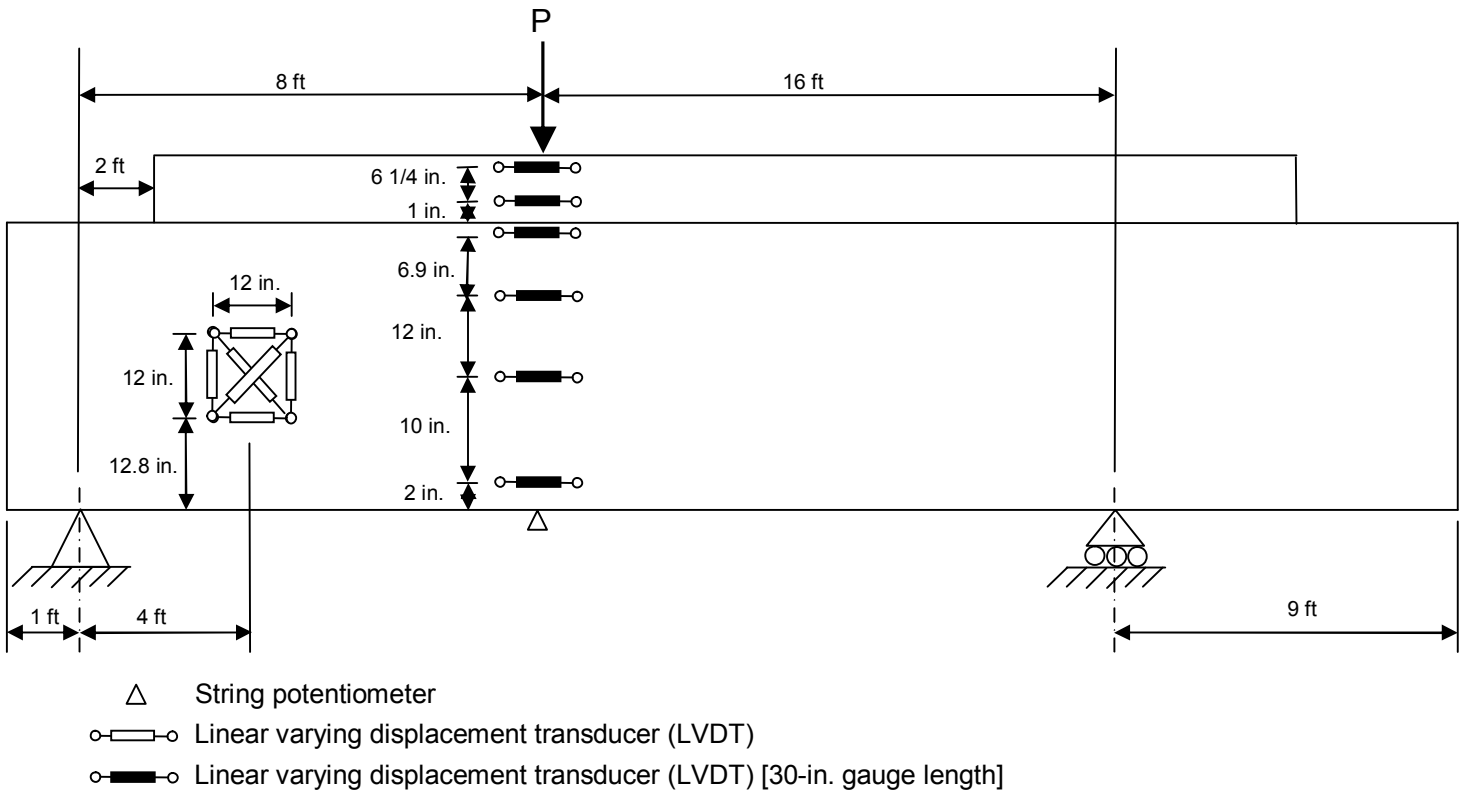

Figure 6-23: Experimental setup and instrumentation for shear test 2-1.

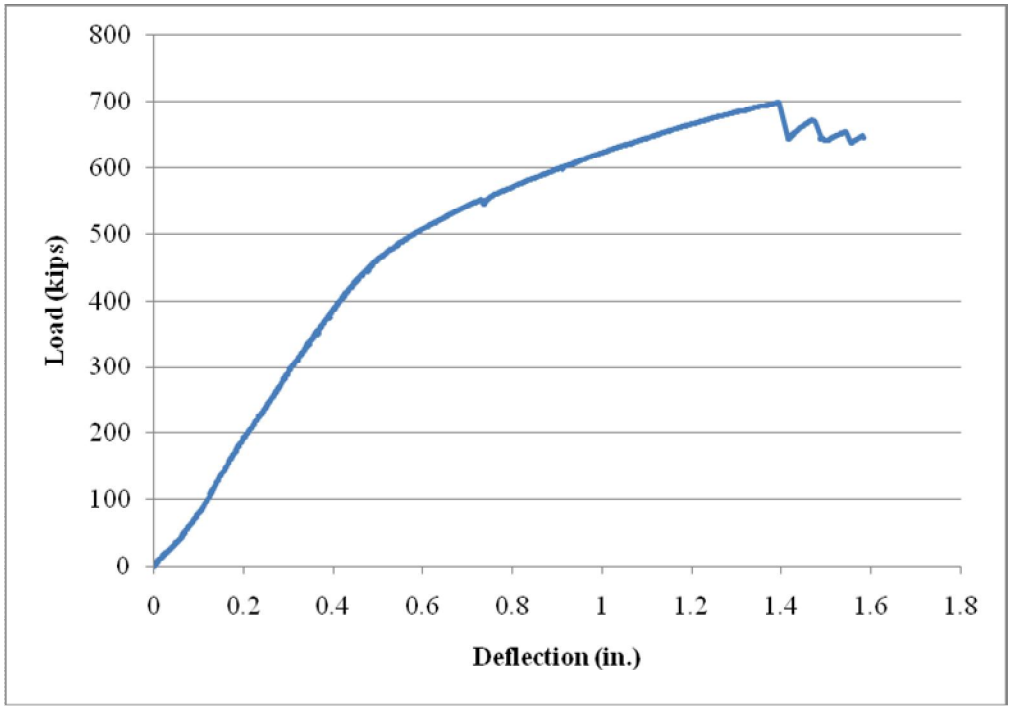

Figure 6-24: Load-deflection curve for shear test 2-1.

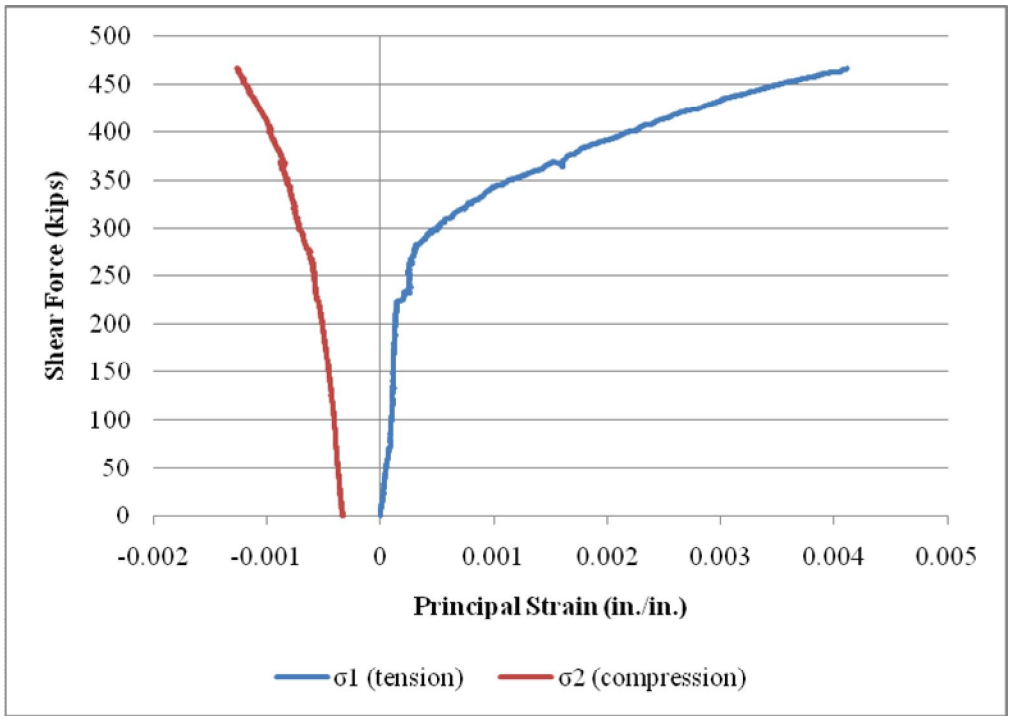

Figure 6-25: Principal strains for shear test 2-1.

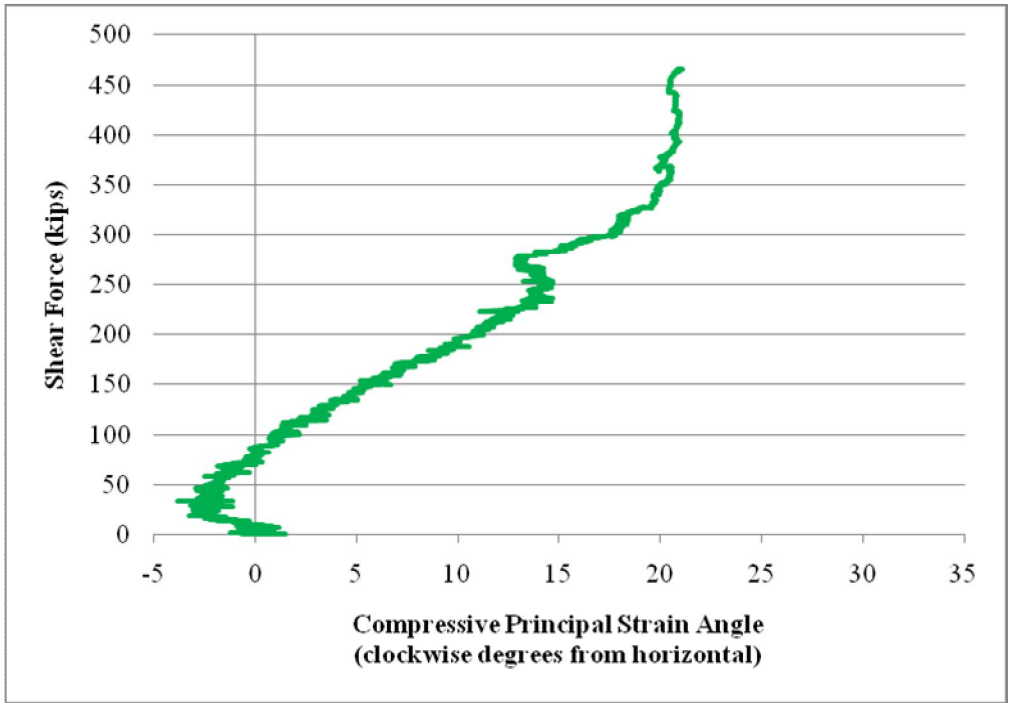

Figure 6-26: Principal compressive strain angle for shear test 2-1.

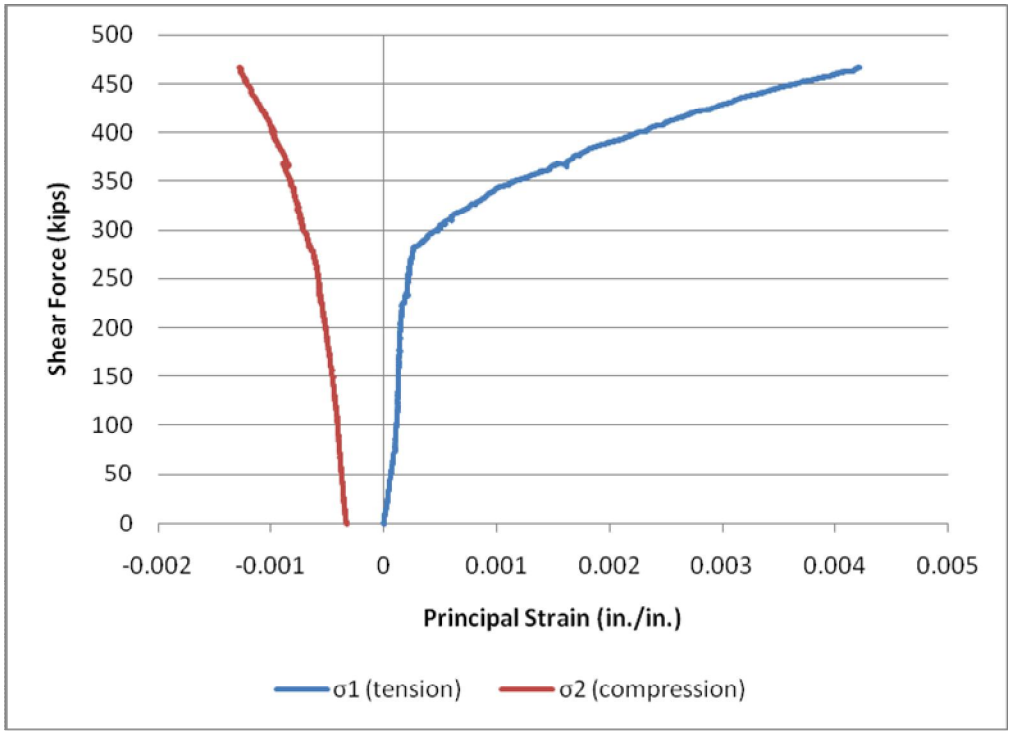

Figure 6-27: Adjusted principal strains for shear test 2-1.

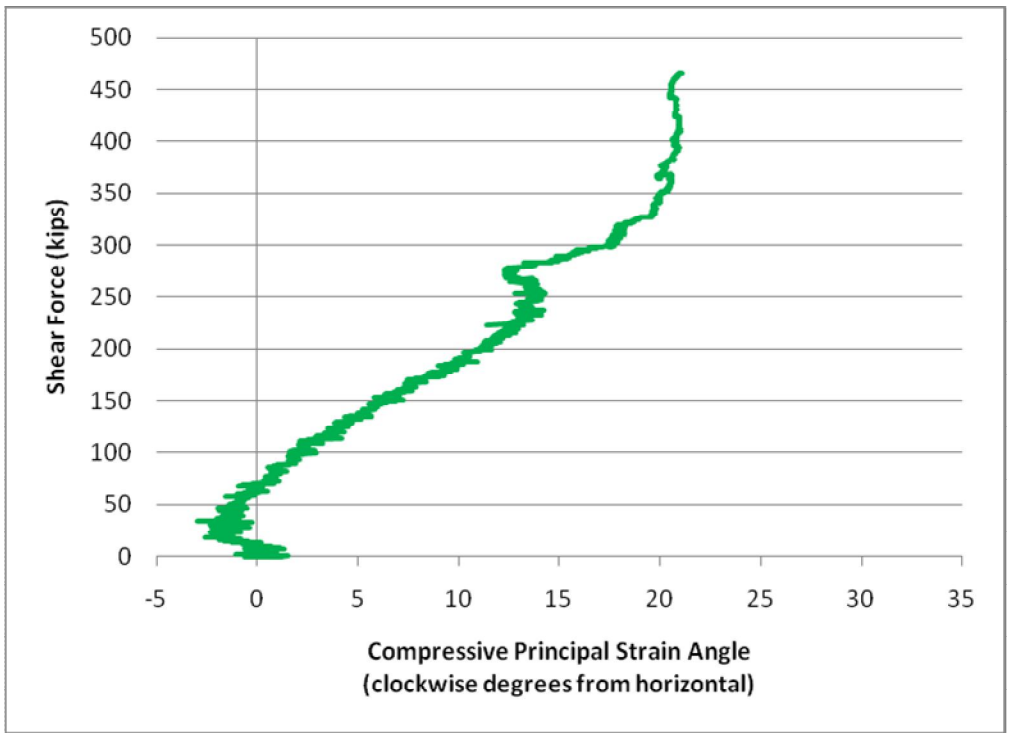

Figure 6-28: Adjusted principal compressive strain angle for shear test 2-1.

At a moment of 3,728 kip-ft (699 kips) [5,050 kN-m, 3,110 kN), girder 2-1 experienced compressive flexural failure directly under the loading point as shown in Figure 6-29. A large portion of the top flange was lost, similar to the failure in test 1-1a. Figure 6-30 shows the missing top flange following compression failure. Along the web, the compression failure site was observed to have a lamellar morphology. Plate-like sheets of the UHPC were oriented parallel to the surface of the web and looked as if they had been successively peeled away. This failure geometry was thought to be indicative of a lack of fibers running orthogonal to the web surface.

Figure 6-29: Flexural compression failure of shear test 2-1. Note the plate-like morphology of the UHPC failure surface.

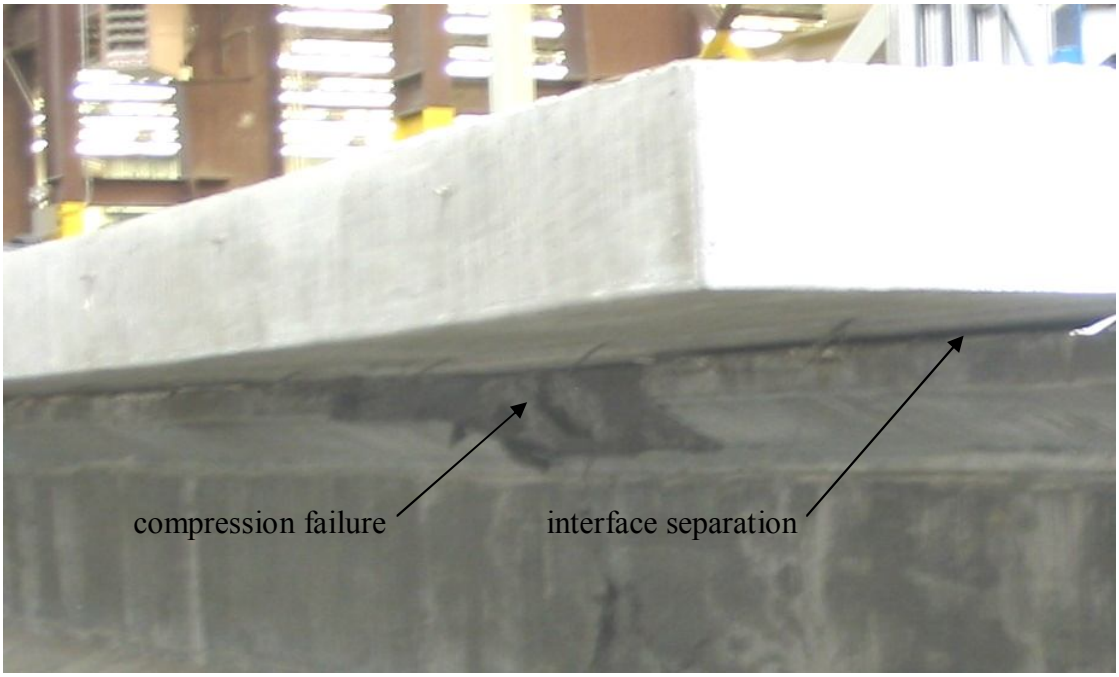

Figure 6-30: Top flange of girder 2 after shear test 2-1.

While the failure clearly occurred as a result of flexural compression, the maximum principal strain at the failure load was 0.00426, which was approaching the failure strain observed in test 1-2 at diagonal tension shear failure. Figure 6-31 shows the shear cracks after flexural failure. The angle of these cracks was measured to be 23°, which matched very closely with the maximum compressive strain angle of 21° from the strain rosette. Again, these shear cracks were hair width and spaced about 0.2 in. (5 mm) apart.

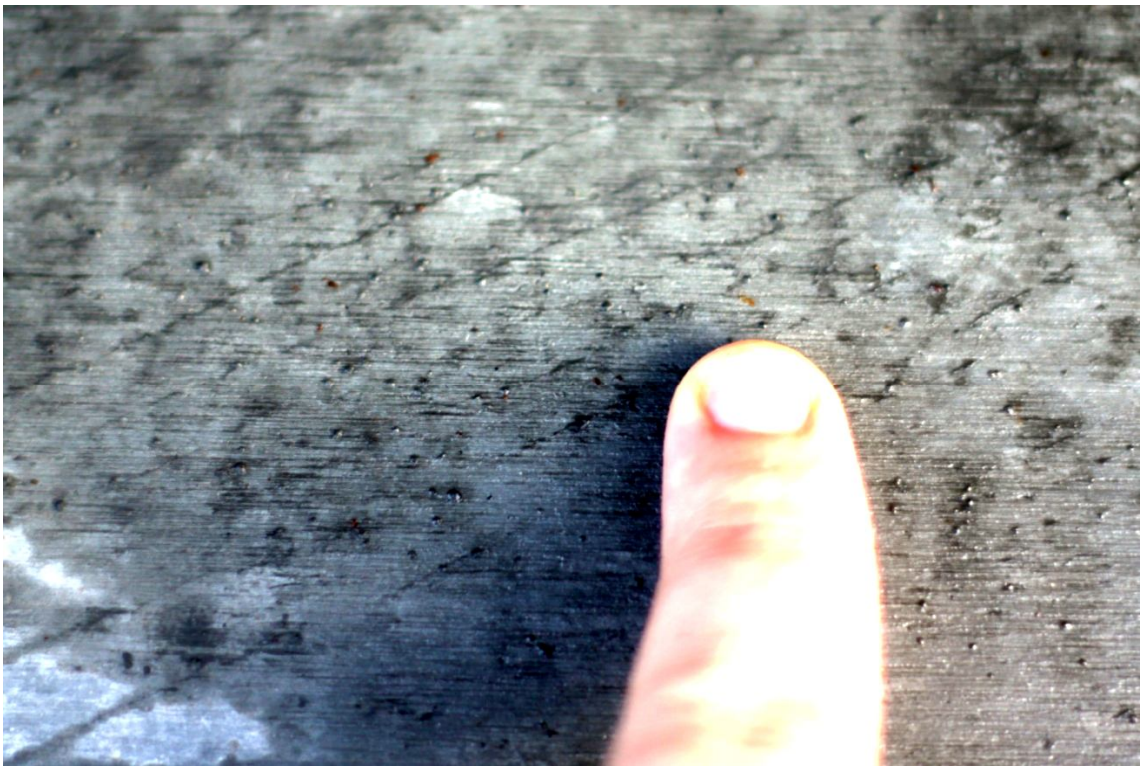

Figure 6-31: Shear cracks from shear test 2-1.

6.2.4 Shear Test 2-2 (fluted interface with 2-#4 [M13] bars at 24-in. [0.61m] spacing)

Shear test 2-2 was conducted on the east end of girder 2. Figures 6-32 and 6-33 show the experimental setup and instrumentation. This end of girder two had 2-#4 (M13) at 24-in. (0.61m) o.c. shear reinforcement and a fluted interface, so the interface between girder and deck did not fail until a load of 632 kips (2,810 kN) with a shear force of 421 kips (1,870 kN). This composite action caused a much stiffer load deflection behavior as shown in Figure 6-34. Even after the initiation of interface shear failure, the girder maintained limited composite action which allowed it to continue to carry increasing load past the point where girder 2-1 experienced flexural compression failure.

At a load of 466 kips (2,070 kN), which was a shear force of 311 kips (1,380 kN), the upper right LVDT gauge point detached, making the readings for the top horizontal strain, outside vertical strain, and tension diagonal strain unknown after this point. When interface shear initiated at a shear force of 421 kips (1,870 kN), which was a load of 632 kips (2,810 kN), it was accompanied by a loud cracking sound and a drop in load of 41 kips (182 kN). The shock of this event caused the entire strain rosette to detach, so no data were collected on principal strains past this load. Additionally, the bottom LVDT in the strain rosette was defective during the test, so the strain at this location had to be calculated based on the other five LVDTs. Figures 6-35 and 6-36 show the principal strains and compressive strain angle up until the gauges detached. These data are based on initial strains of -0.000143, -0.0005217, and -0.000166 for the top horizontal, bottom horizontal, and diagonal gauges, respectively.

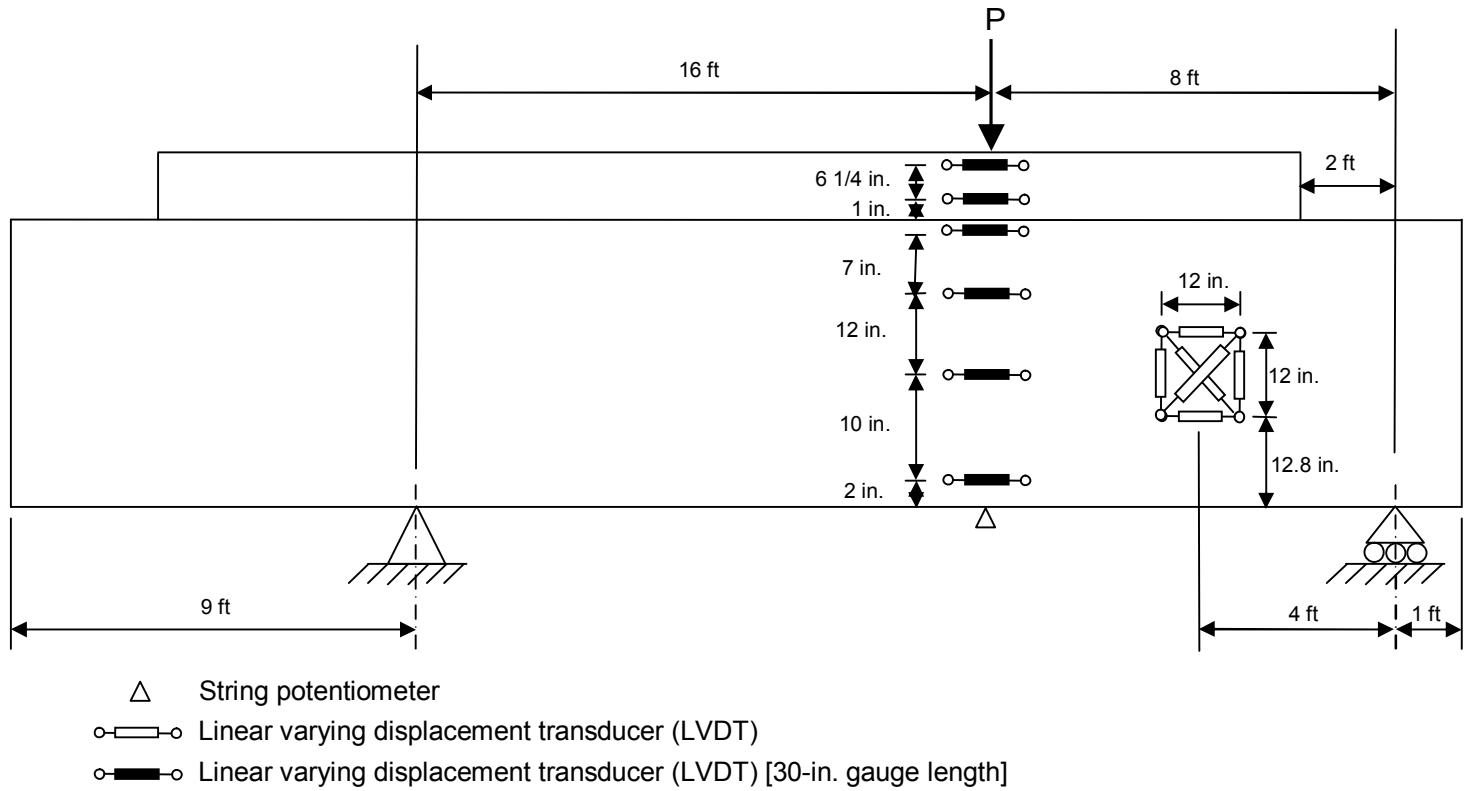

Figure 6-32: Experimental setup and instrumentation for shear test 2-2 and 3-2. East end is to the right of the figure.

Figure 6-33: Shear test 2-2 prior to loading.

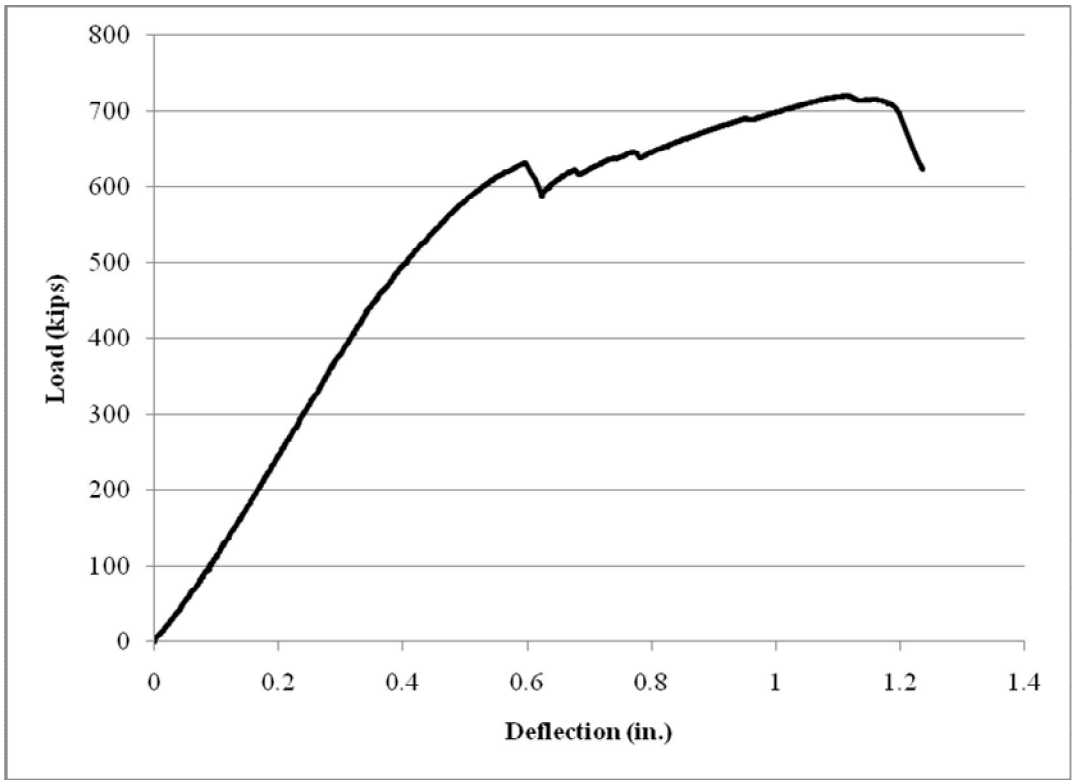

Figure 6-34: Load-deflection curve for shear test 2-2.

From the limited principal strain data, it was hard to determine the diagonal cracking strain of the concrete. There was a jump in principal tensile strain around 290 kips of shear force, but this corresponded to a strain of only 0.00005, which was much lower than any previously reported cracking strain for UHPC in this research or in the literature. It is possible that localized cracking began at this point, so the average strain was not an accurate representation of the local effect.

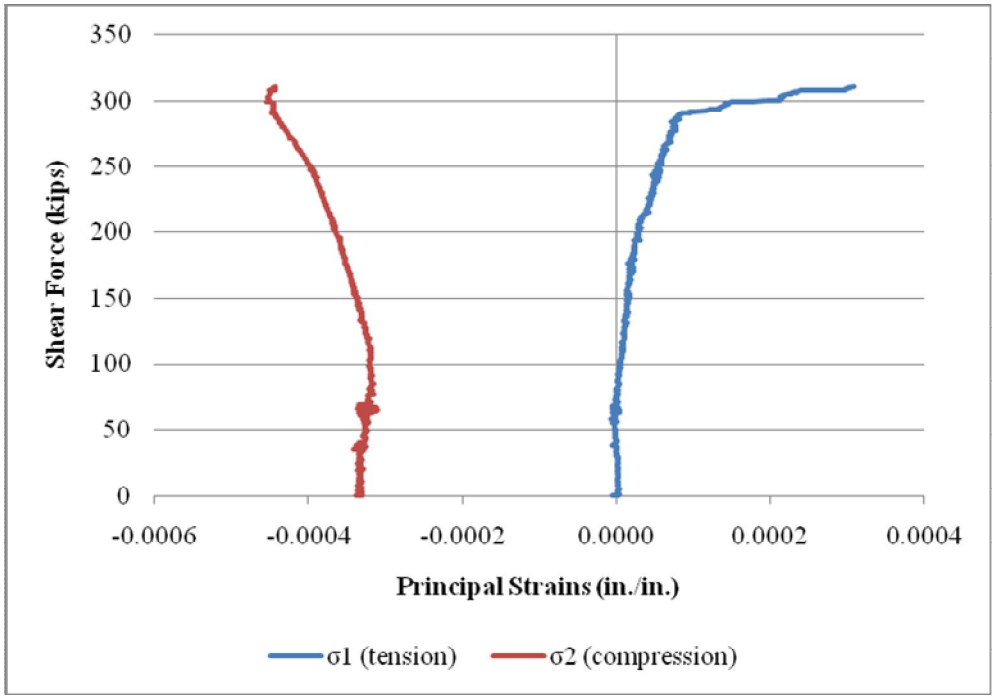

Figure 6-35: Principal strains for shear test 2-2. The gauges detached at a shear force of 420 kips, but shear failure did not occur until a shear force of 480 kips.

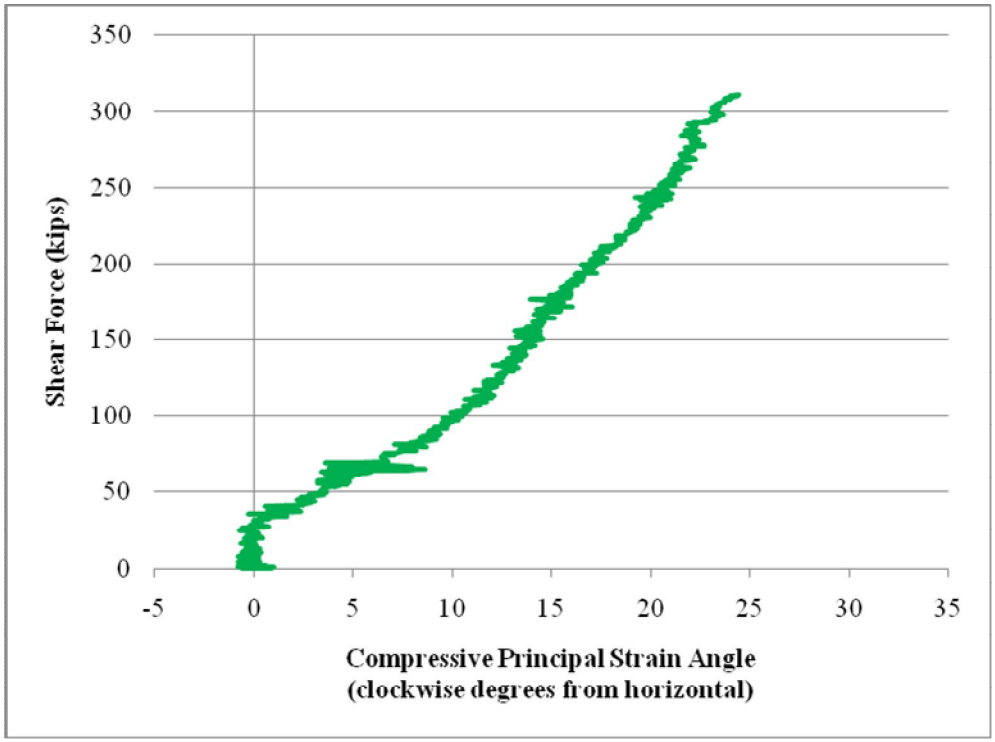

Figure 6-36: Principal compressive strain angle for shear test 2-2. The gauges detached at a shear force of 420 kips, but shear failure did not occur until a shear force of 480 kips.

Diagonal tension shear failure of shear test 2-2 occurred at a shear force of 481 kips (2,140 kN), a total load of 722 kips (3,210 kN). Figure 6-37 shows the failure location. The measured crack angle at failure was 28 degrees. Prior to losing the gauges, the maximum compressive strain angle was calculated to be 24 degrees. Considering the shear increase of 170 kips (756 kN) that occurred between gauge detachment and failure, these strain angles match very closely. It should also be noted that the failure angle seemed to be affected by the presence of shear stirrups as can be seen in Figure 6-37.

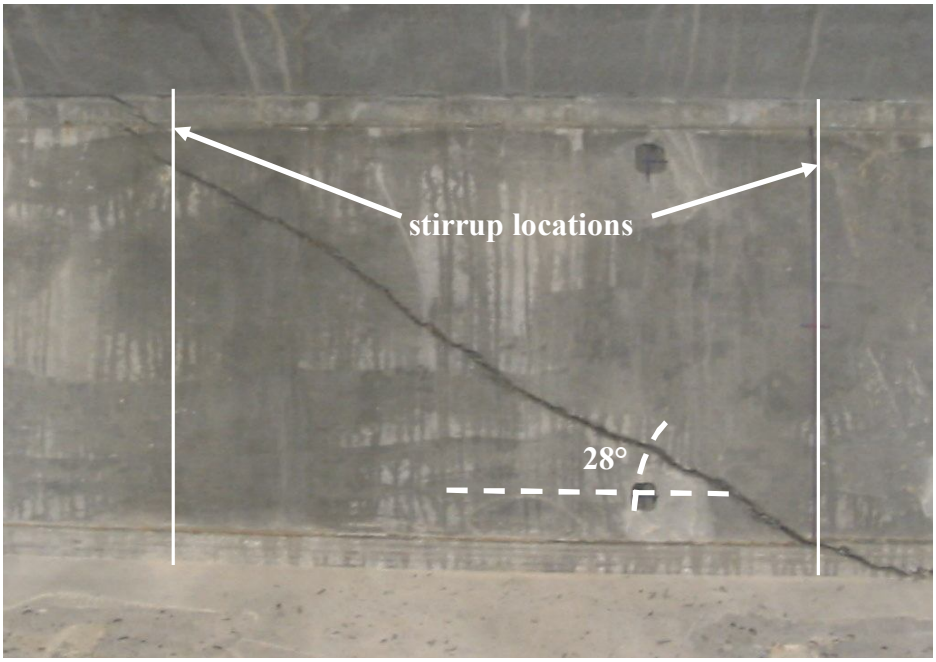

Figure 6-37: Diagonal tension shear failure of girder 2 during shear test 2-2.

6.2.5 Shear Test 3-1 (reduced flange width fluted interface with no reinforcement)

Shear test 3-1 was performed after shear test 3-2. During testing of shear girder 3-2, the interface on each side of the beam failed, so shear test 3-1 was similar to a non-composite beam. Shear test 3-1 had no shear stirrups and a fluted interface. The test setup for shear test 3-1 was identical to that used for shear test 2-1 (Figure 6-23).

Despite the interface slip initiated during shear test 3-2, the clamping force created by the application of load may have created limited interface connection, but the load deflection curve (Figure 6-38) still showed a linear behavior similar to that of shear test 2-1 shown in Figure 6-24. The lower stiffness seen in this test compared to shear test 2-1 was attributed to the reduced moment of inertia of the reduced-flange section as well as micro-cracking caused by the previous loading of girder test 3-2.

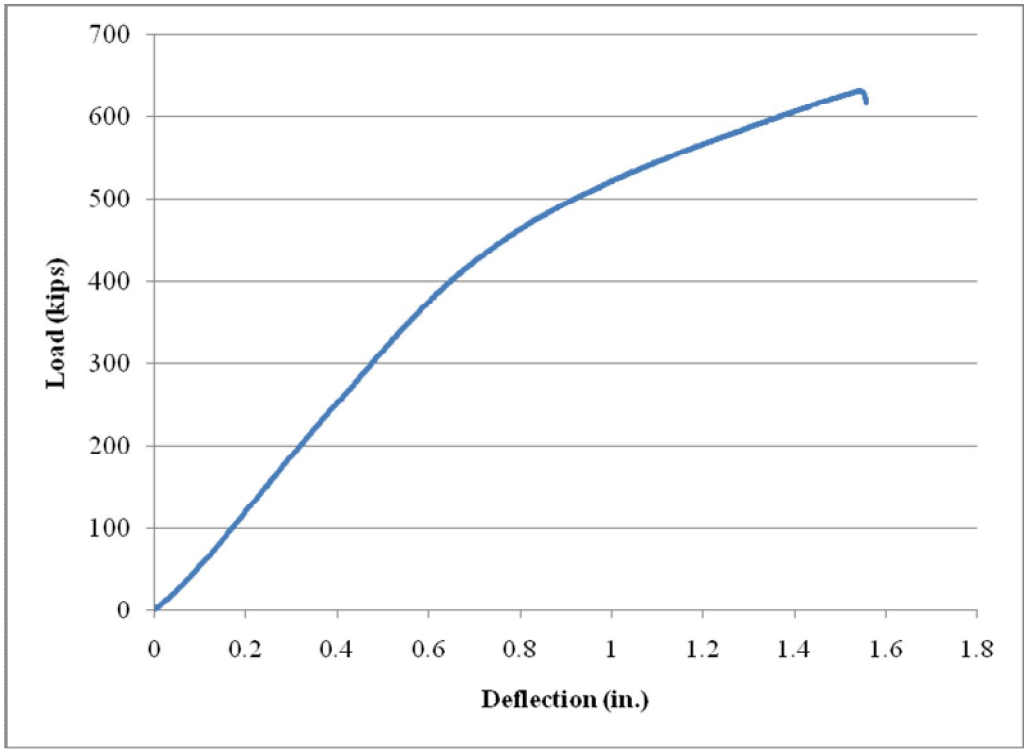

Figure 6-38: Load deflection curve for shear test 3-1.

Figures 6-39 and 6-40 show the principal strains and the compressive principal strain angle. These values were based on initial compressive strains of -0.000187, -0.000550, and -0.000184 in the top horizontal, bottom horizontal, and diagonal gauges, respectively, based on VWSG readings. The calculated maximum principal shear strain appeared to jump at a shear force of 228 kips and a strain of 0.0001. This strain was much lower than the expected onset of tensile cracking. This was thought to indicate an outside disturbance that may have affected the rosette values. Figures 6-41 and 6-42 show the adjusted principal strains and compressive principal strain angle. Based on these adjusted graphs, the slope change in the principal strain graph appears to occur in the range of 0.0002. Comparison between data is based on these adjusted values.

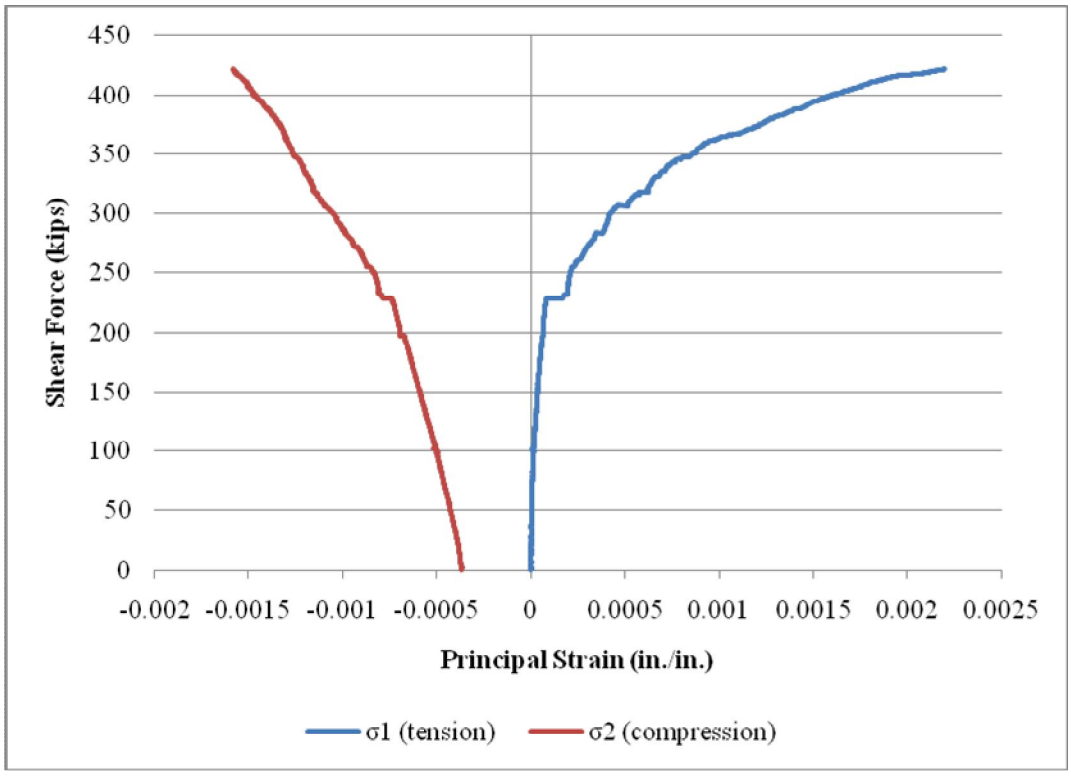

Figure 6-39: Principal strains for shear test 3-1.

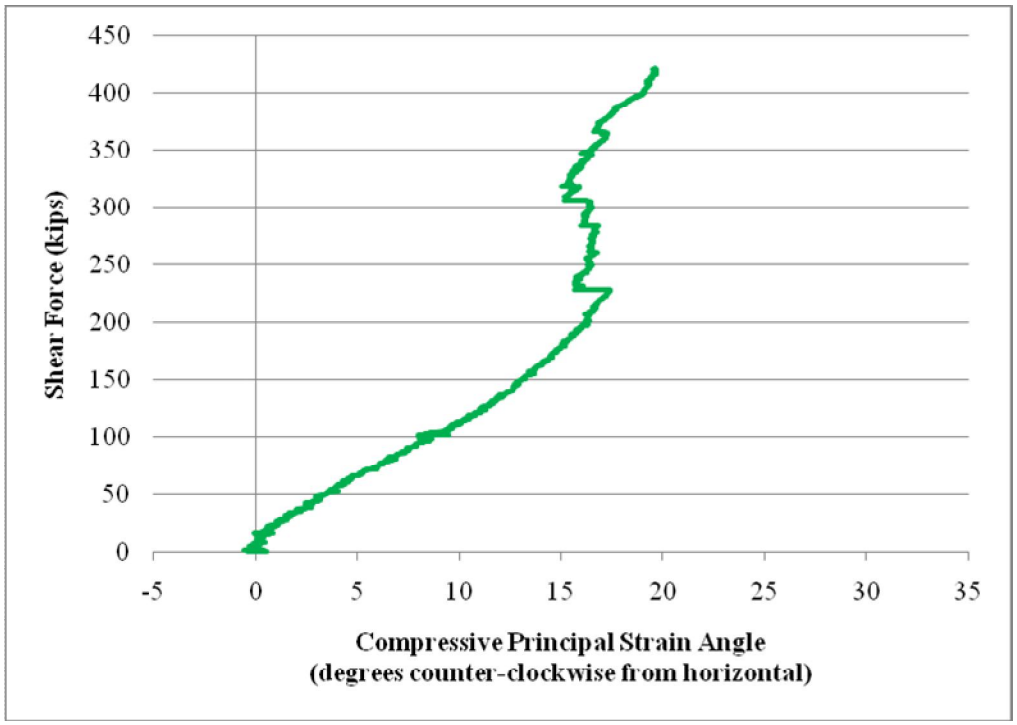

Figure 6-40: Principal compressive strain angle for shear test 3-1.

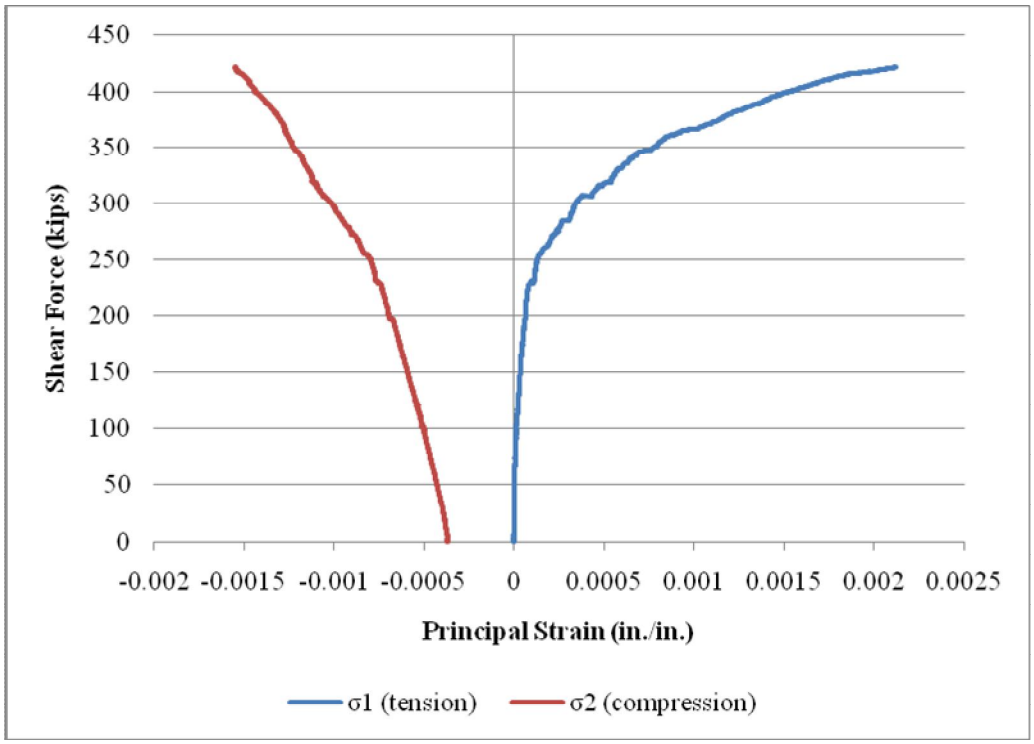

Figure 6-41: Adjusted principal strains for shear test 3-1.

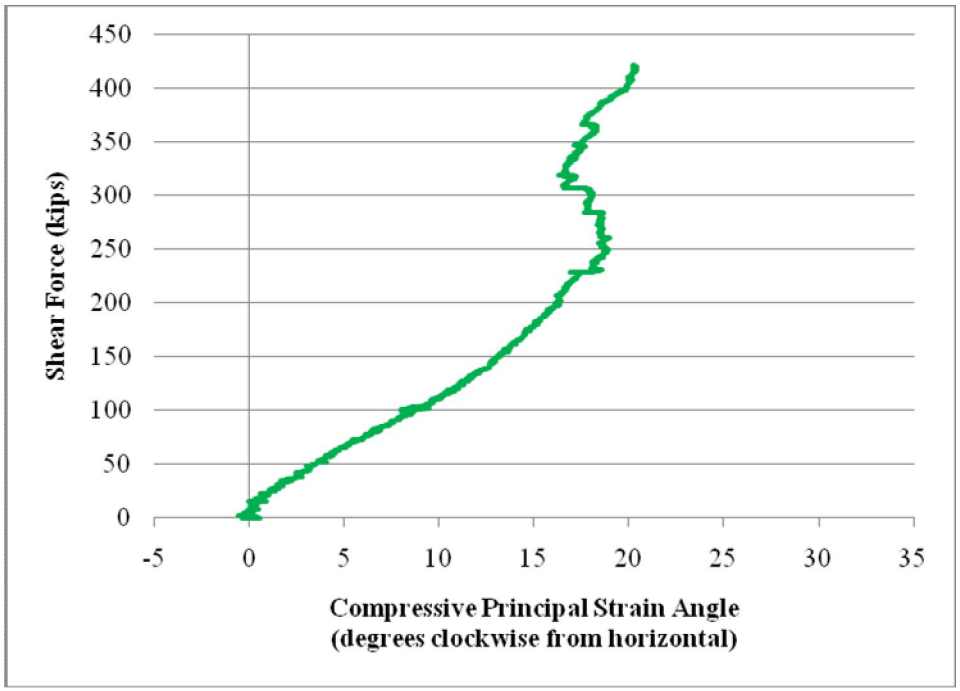

Figure 6-42: Adjusted principal compressive strain angle for shear test 3-1.

At a moment of 3,376 kip-ft (4577 kN-m), which was a load of 633 kips (2,820 kN), the top of the girder failed in flexural compression as seen in Figure 6-43. The same lamellar morphology seen in previous flexural compression failures was observed in shear test 3-1. The maximum shear force reached during this test was 422 kips (1,880 kN). At this shear force, the principal compressive strain angle reached a maximum of 20° as measured by the strain rosette. Figure 6-44 shows the fine shear cracking that occurred prior to flexural failure of the girder. The measured crack angle was approximately 25°. This was larger than the measured strain angle from the rosette, but this increase was attributed to differences in where the cracks were measured.

Figure 6-43: Flexural compression failure of shear test 3-1.

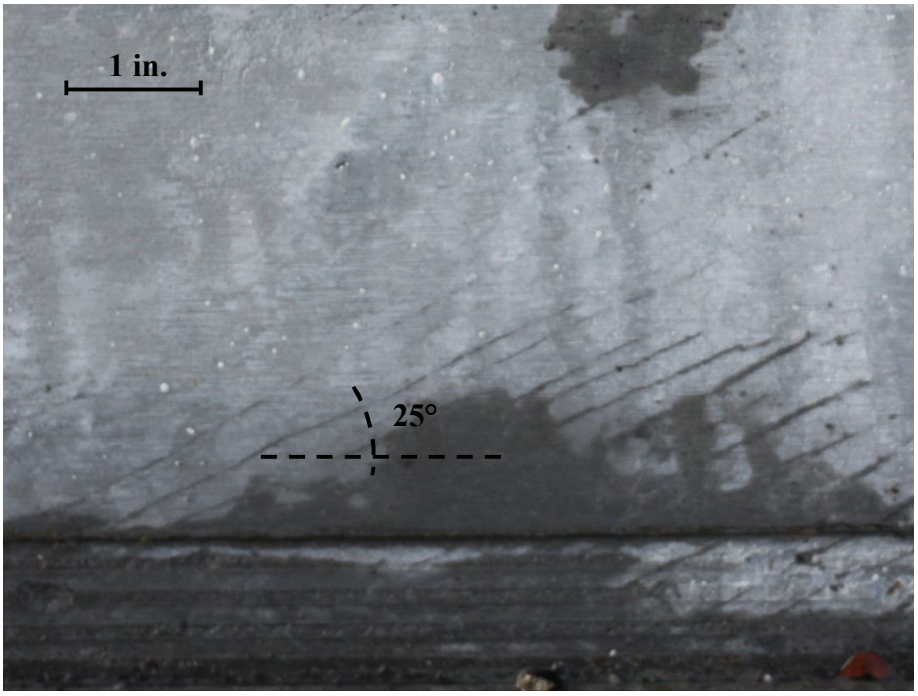

Figure 6-44: Shear cracking in test 3-1.

6.2.6 Shear Test 3-2 (reduced flange width, smooth interface with 2-#4 [M13] bars at 12-in [0.31m] spacing)

Shear test 3-2 was performed on the eastern end of girder 3. Setup and instrumentation for shear test 3-2 were identical to those of shear test 2-2 shown in Figure 6-31. Figure 6-45 shows the load deflection curve for shear test 3-2 along with the points at which interface slip initiated on either end of the girder. It is important to note that even after slip initiated on the east end, the stiffness was fairly high due to the high level of interface reinforcement present, 2-#4 bars at 12-in. spacing.

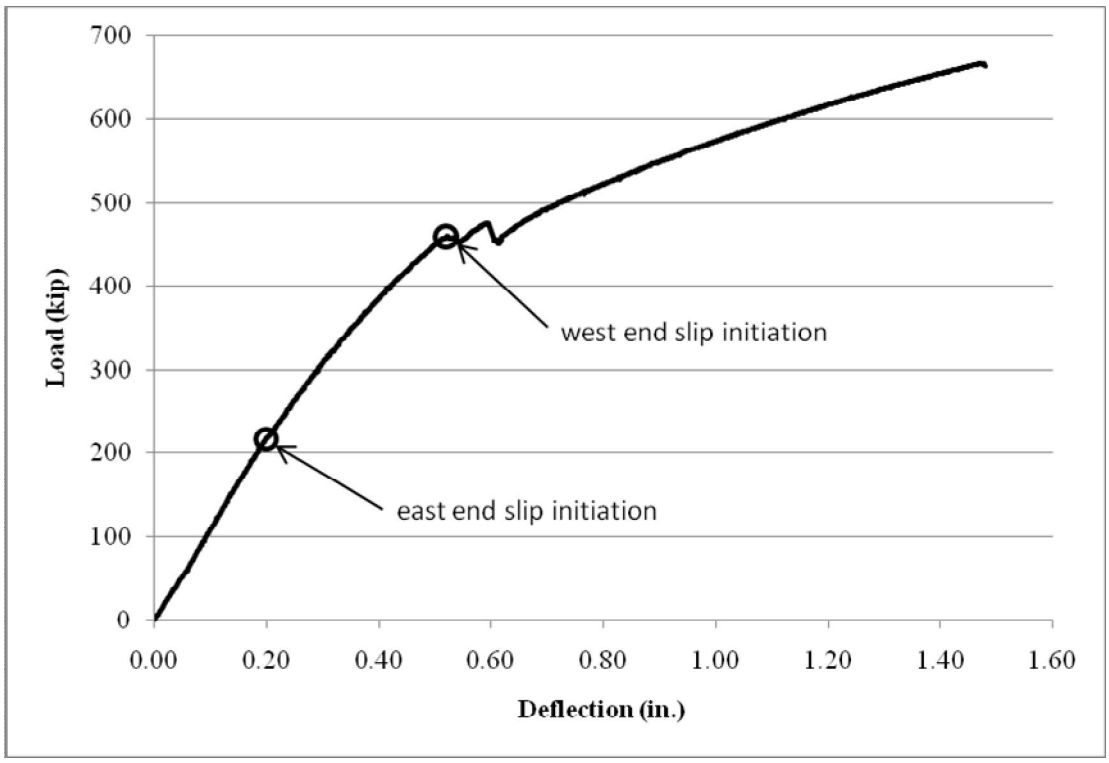

Figure 6-45: Load deflection curve for shear test 3-2. Initiation of slip on each end of the beam is marked with a circle.

Figure 6-46 and 6-47 show the principal strains and principal compression strain angle for test 3-2. These values were based on initial compressive strains of -0.000187, -0.000550, and -0.000184 in the top horizontal, bottom horizontal, and diagonal gauges, respectively, based on VWSG readings. The maximum diagonal tensile strain follows the same trend as previous tests with a noticeable change in slope at a load of 250 kips (1,110 kN) and with a strain of approximately 0.0003. The observed principal strain angle of 32° reached at 125 kips (556 kN) was much higher than that seen in previous tests. This was thought to be due to the much higher shear reinforcement ratio than had been used in previous tests. As the shear was increased beyond this load, the strain angle decreased slightly again until it was at a value of 34° at beam failure. Figure 6-48 shows the shear cracks in the area of the strain rosette. The angle measured from these cracks

was also 34°. The maximum shear carried by the girder was 444 kips (3,630 psi) [1,980 kN, 25.0 MPa].

Shear test 3-2 ultimately failed in flexural compression as shown in Figure 6-49 at a moment of 3,550 kip-ft (4,810 kN-m), which was a load of 666 kips (2,960 kN). This was not expected due to the fact that the interface shear steel was still intact. From a design perspective, this was very important because it showed that enough strain can be transferred to cause a flexural compression failure in the top of the girder prior to shearing of the interface steel. There appears to have been little or no composite behavior at failure. This behavior indicated that slip load values may be more appropriate than maximum loads for use in interface shear design.

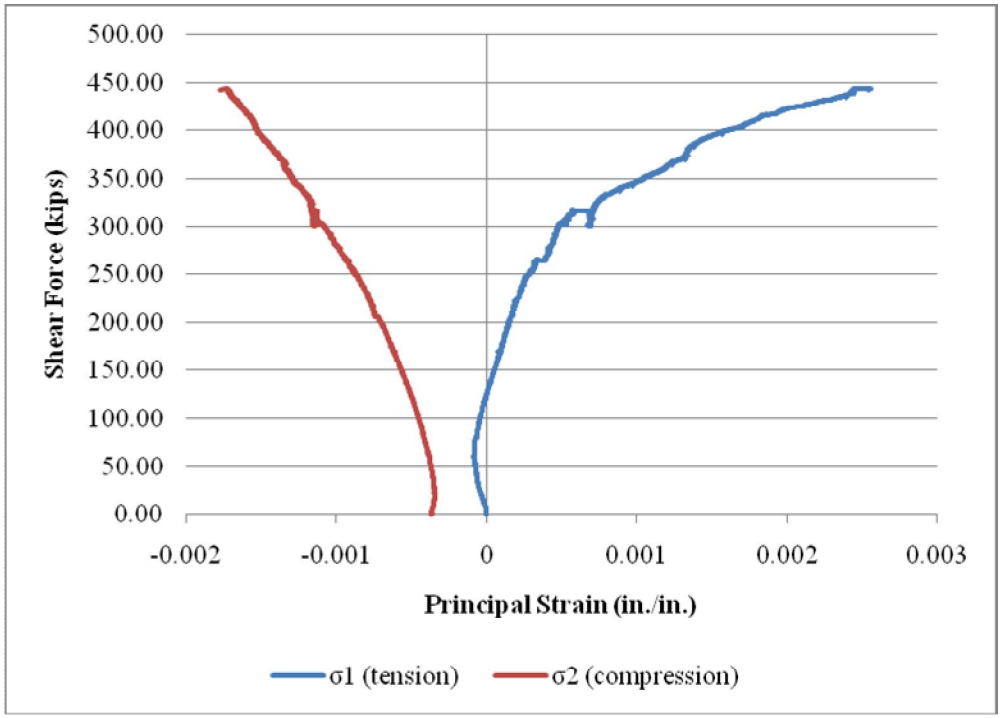

Figure 6-46: Principal strains for shear test 3-2.

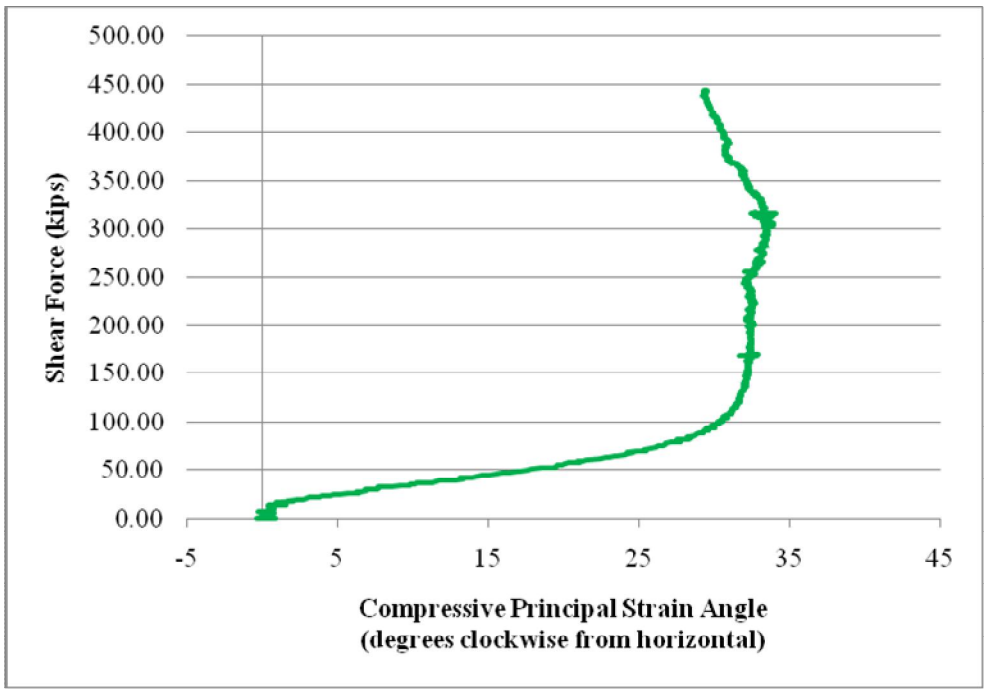

Figure 6-47: Principal compressive strain angle for shear test 3-2.

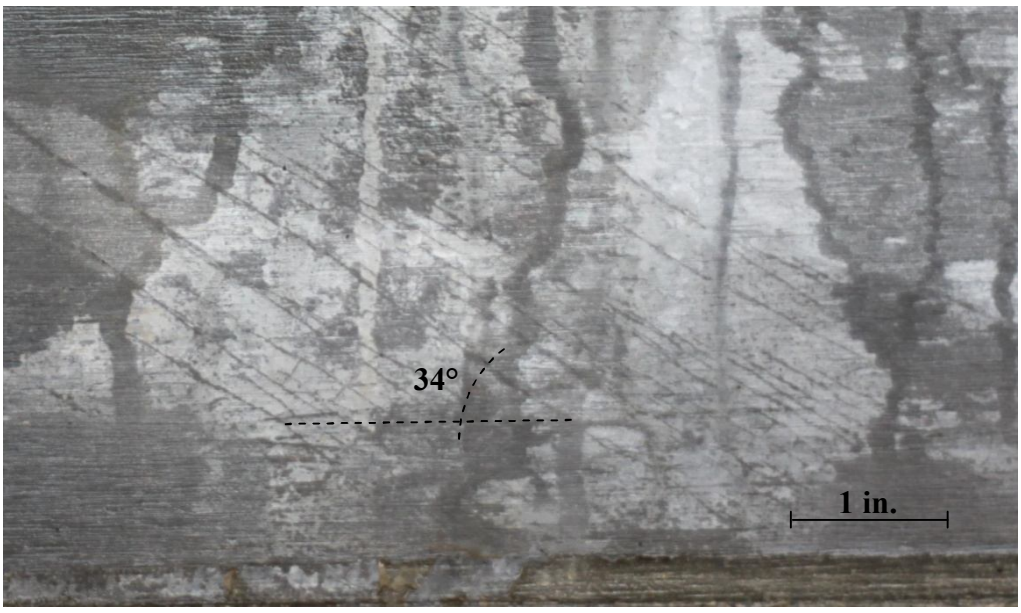

Figure 6-48: Shear cracking in test 3-2.

Figure 6-49: Flexural compression failure of shear test 3-2.

6.3 Analysis of Results

As was shown in section 6.2, existing AASHTO (2010) equations are not applicable for calculating shear performance of UHPC girders because they do not consider the shear carrying capacity of the steel fibers. In this section, experimental results are compared to two possible alternatives for analysis of UHPC shear capacity. The first is based on the direct tensile capacity of UHPC similar to the current calculation of V_{cw}. The second is based on including an additional term for fiber contribution, based on that used by the French code, in the Simplified Modified Compression Field Theory.

6.3.1 Shear Capacity Based on Direct Tension Capacity

From a direct Mohr's circle approach, the web shear capacity of a prestressed beam is given as (Hawkins et al., 2005):

$$V_{cw} = f_t \sqrt{1 + \frac{f_{pc}}{f_t}} b_w d_v + V_p , \tag{6-10}$$

where

f_t = the tensile strength of the concrete

f_{pc} = the compressive stress of the concrete at the centroid of the cross-section resisting external loads or at the junction of web and flange when the centroid lies within the flange.

V_p = portion of the prestressing force resisting shear.

Based on this equation, Table 6-4 gives the predicted shear capacities and compression strain angles for the tested girders. Due to the drastic difference in concrete properties between girder and deck, the effective shear depth, d_v, is based solely on the girder, rather than the composite section. A direct tension capacity f_t of 1,400 psi was used based on research by Garas (2009) on UHPC cured at 60°C for 72 hours at 100% R.H. This curing regimen most closely matched the field curing conditions experienced by the girders used in these tests.

Table 6-4 also includes the expected steel contribution to shear capacity based on the equations:

$$V_s = \frac{A_v f_y d_v}{s} \cot\theta , \tag{6-11}$$

and

$$\cot\theta = \sqrt{1 + \frac{f_{pc}}{f_t}} \tag{6-12}$$

where,

A_v = area of transverse reinforcement within distance s

f_y = minimum yield strength in reinforcing bars

s = spacing of reinforcing bars

θ = angle of inclination of diagonal compressive stresses.

The total nominal shear capacity, V_n, is taken as the sum of V_{cw} and V_s,.

The calculation of the angle, ϑ, was based on the assumption that the concrete matrix was isotropic. Chapter 7 shows that fiber distribution and compressive properties did not differ significantly between the X and Y directions, so this assumption was validated for calculation of shear in the plane of the web.

Table 6-4: Calculation of shear capacity by direct tension strength

Test	Direct Tension Shear Capacity (Eq. 6-10 and 6-11)					Experimental Values		$\frac{V_{exp} - V_n}{V_n}$
	f_{pc}, ksi (MPa)	θ	V_{cw}, kips (kN)	V_s, kips (kN)	V_n, kips (kN)	V_{exp}, kips (kN)	θ_{exp}	
1-1a	3.14 (21.7)	29°	235 (1,050)	43 (191)	279 (1,240)	452* (2010)	34°	63%
1-2	3.14 (21.7)	29°	235 (1,050)	0	235 (1,050)	431 (1920)	26°	83%
2-1	3.14 (21.7)	29°	235 (1,050)	0	235 (1,050)	466* (2070)	23°	98%
2-2	3.14 (21.7)	29°	235 (1,050)	43 (191)	279 (1,240)	480 (2140)	28°	72%
3-1	3.45 (23.8)	28°	243 (1,080)	0	243 (1,080)	422* (1880)	25°	74%
3-2	3.45 (23.8)	28°	243 (1,080)	90 (400)	333 (1,480)	444* (1980)	34°	33%

*These tests experience compression flexural failure. The values of V_u and θ presented for these cases are the maximum values prior to flexural failure.

6.3.2 Shear Capacity Based on Simplified Modified Compression Field Theory

The simplified version of the Modified Compression Field Theory (S-MCFT), uses an approximate linear fit to bypass the iterative process required by the Modified Compression Field Theory (Bentz et al., 2006). The shear capacity of the section is taken as the summation of the concrete contribution, the steel contribution and the portion of the prestressing force resisting shear. To this was added a new term for contribution of fiber reinforcement (V_f) to shear capacity:

$$V_n = V_c + V_s + V_p + V_f \quad (6\text{-}13)$$

Conceptually, the interaction of V_c and V_f is debatable. It is doubtful that the concrete is contributing directly to the shear capacity after cracking, and it is unknown how the fibers affect the shear capacity prior to cracking. For the purposes of this analysis, the combination of these terms is based on the same rationale that is used in combining V_s and V_c in high performance concretes were cracking occurs through the aggregate and no true aggregate interlock is expected to occur (Bentz et al., 2006). In these cases, smaller crack spacings are required to allow for any shear transfer across these cracks. Previous research (Graybeal, 2006; Graybeal, 2009) as well as shear cracks shown in this research clearly have clearly shown that UHPC with 2% steel fibers by volume has the ability to distribute cracks much better than normal concretes. Based on this fact, V_c can be thought of as the concrete contribution to shear via shear transfer across a crack when sufficient fibers are present to ensure tight crack spacing. V_f can be considered the direct contribution of fibers to the shear capacity of UHPC. This

treatment of the terms may not be totally precise, but it is consistent with the current treatment of similar HPC systems in the AASHTO (2010) provisions.

Based on S-MCFT, the concrete contribution is taken as:

$$V_c = 0.0316\beta\sqrt{f_c'}b_v d_v, \tag{6-14}$$

where

β = factor indicating ability of diagonally cracked concrete to transmit tension and shear.

Depending on whether the section contains at least minimum reinforcement, β is calculated by equation 5.8.3.4.2-1 or 5.8.3.4.2-2 (AASHTO, 2010). For the sake of this calculation, minimum reinforcement is used to ensure that strain is distributed between multiple cracks rather than localizing at one crack. Due to the very close crack spacing observed in these UHPC tests as discussed above, it was assumed that the fibers provided this level of minimum reinforcement. Therefore,

$$\beta = \frac{4.8}{(1+750\varepsilon_s)}. \tag{6-15}$$

where,

ε_s = the net longitudinal tensile strain in the section at the centroid of the tension reinforcement.

Details on calculation of ε_s can be found in the code (AASHTO, 2010). The reinforcing steel contribution to the shear capacity is defined by Equation 6-11, but with the compressive angle taken as:

$$\theta = 29 + 3500\varepsilon_s. \tag{6-16}$$

Based on the French code (AFGC, 2002), the fiber contribution was defined as:

$$V_f = b_v d_v f_{rr} \cot\theta \ . \tag{6-17}$$

where,

f_{rr} = the rupture residual stress, taken as the extreme fiber tensile stress carried between first cracking and a crack width of 0.3mm during a modulus of rupture test.

This number was taken to be 1 ksi (6.9 MPa) based on research by Graybeal (2005). Table 6-5 shows the predicted shear capacities based on the S-MCFT with fiber contribution. The values were calculated at a section d_v away from the support for the sake of comparison. Due to the very high amount of prestressing force in the girder, ε_s was less than the code-imposed minimum of -0.0004. This limit was ignored in the calculations.

Table 6-5: Calculation of shear capacity by simplified modified compression field theory

Test	Simplified Modified Compression Field Theory (Eq. 6-13 through 6-17)							Experimental Values		$\frac{V_{exp} - V_n}{V_n}$
	ε_s	β	θ	V_c, kips (kN)	V_s, kips (kN)	V_f, kips (kN)	V_n, kips (kN)	V_{exp}, kips (kN)	θ_{exp}	
1-1a	-0.000674	9.71	26.6	142 (632)	48 (214)	186 (827)	376 (1,670)	452* (2010)	34°	20%
1-2	-0.000458	7.31	27.4	107 (476)	0	180 (801)	287 (1,280)	431 (1920)	26°	50%
2-1	-0.000494	7.63	27.3	111 (494)	0	181 (805)	293 (1,300)	466* (2070)	23°	59%
2-2	-0.000432	7.10	27.5	104 (463)	46 (205)	179 (796)	330 (1,470)	480 (2140)	28°	45%
3-1	-0.000459	7.32	27.4	107 (476)	0	180 (801)	287 (1,280)	422* (1880)	25°	47%
3-2	-0.000406	6.90	27.6	101 (449)	92 (409)	179 (796)	372 (1,660)	444* (1980)	34°	19%

6.3.3 Comparison of Experimental and Theoretical Shear Capacities

Table 6-6 compares the experimental shear capacities from this study as well as from the tests by Graybeal (2005) and the pi-girder tests by Graybeal (2009) with the predicted capacities from direct tension and S-MCFT techniques. Each of cited tests by Graybeal failed in shear except the pi-girder test P4-57Ss, which failed in flexural tension. For this test, the shear value is the maximum shear carried prior to flexural failure. These results are also presented graphically in Figure 6-50. Direct tension was a conservative predictor for all of the tests. In some cases, direct tension under-predicted experimental behavior by up to 49%. On average, this equation predicted capacities 29% less than those observed in the experiments. The coefficient of variation of the predictor was 14%.

S-MCFT including the V_f addition was conservative in every case examined with the exception of test 28S performed by Graybeal (2005). Failure of girder 28S was observed to occur at the location of a large pre-existing crack, so its lower capacity was not considered an accurate indicator of girder performance. S-MCFT under-predicted the experimental shear capacity by a maximum of 37%. On average, S-MCFT predicted capacities 25% less than those observed. The coefficient of variation was 15%.

Table 6-6: Comparison of experimental shear capacities to prediction equations

Test	Experimental Shear at Failure, kip (kN)	Direct Tension Shear Capacity, kip (kN)	S-MCFT Shear Capacity, kip (kN)	$\frac{V_{exp}}{\text{Direct Tension}}$	$\frac{V_{exp}}{\text{S-MCFT}}$
1-1a*	452 (2,010)	279 (1,240)	376 (1,670)	1.62	1.20
1-2	431 (1,920)	235 (1,050)	287 (1,280)	1.83	1.50
2-1*	466 (2,070)	235 (1,050)	293 (1,300)	1.98	1.59
2-2	480 (2,140)	279 (1,240)	330 (1,470)	1.72	1.46
3-1*	422 (1,880)	243 (1,080)	287 (1,280)	1.73	1.47
3-2*	444 (1,980)	333 (1,480)	372 (1,660)	1.33	1.19
28S†	384 (1,710)	323 (1,440)	422 (1,880)	1.19	0.91
24S†	502 (2,230)	323 (1,440)	422 (1,880)	1.55	1.19
14S†	438 (1,950)	323 (1,440)	422 (1,880)	1.36	1.04
P2-21S‡	430 (1,930)	246 (1,090)	373 (1,660)	1.75	1.15
P4-57Sh‡	366 (1,630)	219 (974)	331 (1,470)	1.67	1.11
P4-57Ss‡	510 (2,270)	224 (996)	342 (1,520)	2.28	1.49
			Average††	1.71	1.31
			St. Dev. ††	0.27	0.19
			Coeff. Var. ††	16%	15%

*Test failed in flexural compression. Experimental shear is maximum value before failure.

† Tests performed by Graybeal (2005)

‡ Tests performed by Graybeal (2009)

†† Statistics exclude test 28S.

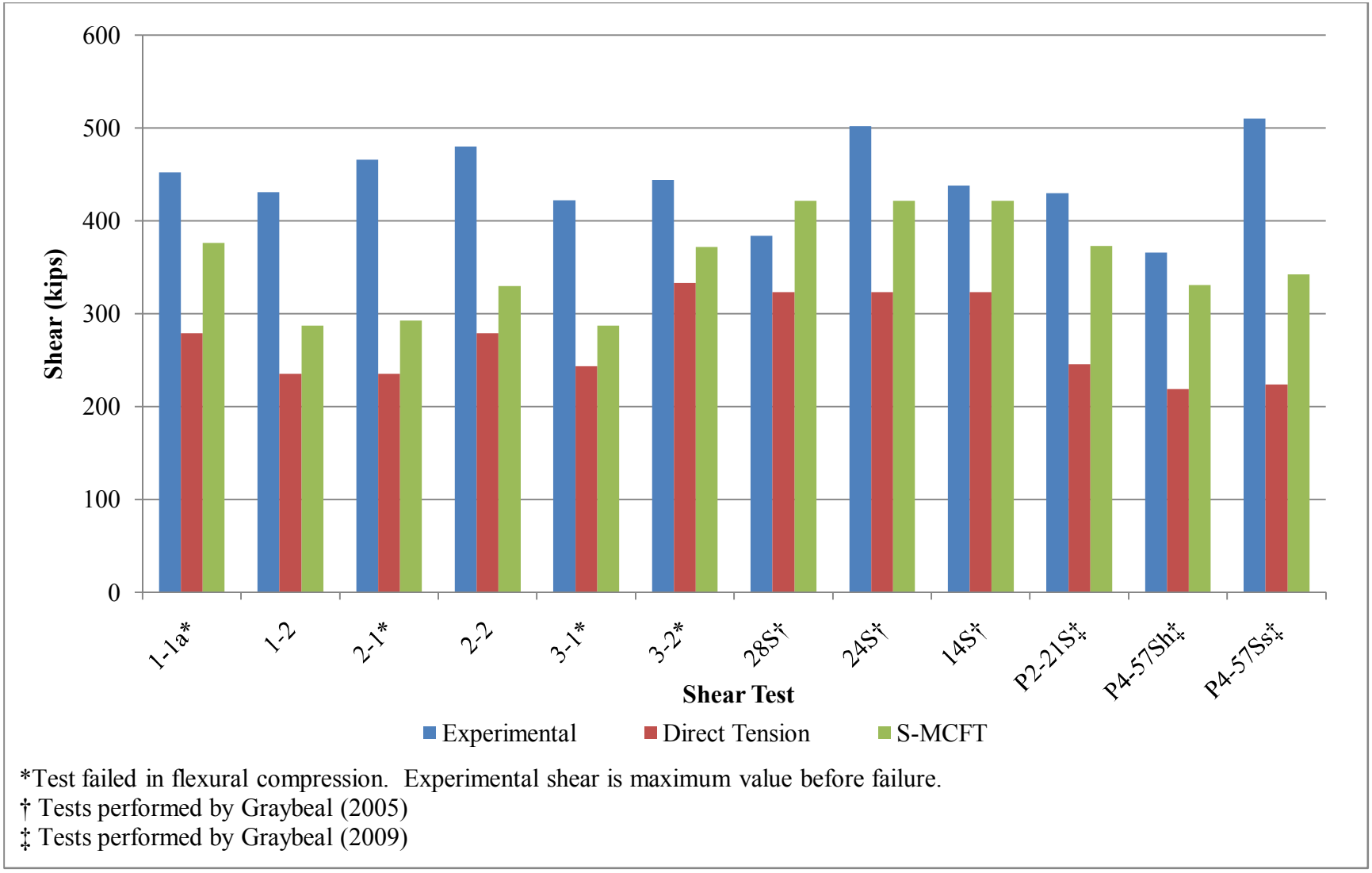

*Test failed in flexural compression. Experimental shear is maximum value before failure.
† Tests performed by Graybeal (2005)
‡ Tests performed by Graybeal (2009)

Figure 6-50: Observed shear stresses compared to Equation 6-10.

6.4 Conclusions

1. Lack of consideration of steel fiber reinforcement prevents AASHTO shear prediction equations from accurately assessing UHPC shear capacity in girders.
2. When steel fiber reinforcement is present at a level of 2% by volume, crack spacing is small enough that minimum shear reinforcement requirements can be considered to be met for the purposes of calculating V_c with the simplified MCFT based on AASHTO (2010).
3. Calculation of shear capacity based on direct tension capacity using Mohr's circle stress analysis yields a simple and conservative estimator of UHPC shear performance, but these values may be overly conservative. More work should be done in calibrating this method based on the use of different measures of UHPC tension capacity.
4. AASHTO (2010) equations based on Simplified Modified Compression Field Theory can be modified based on fiber capacity equations from French UHPC recommendations (AFGC, 2002). These proposed modifications gave predicted shear capacities which averaged 15% less than the average shear force at girder failure. More research must be done before these equations can be used in design, but they present a promising basis for future analyses.

6.5 References

AASHTO (2010). *AASHTO LRFD Bridge Design Specifications*. Washington, D.C., American Association of State Highway and Transportation Officials.

AFGC (2002). Interim recommendations for ultra high performance fibre-reinforced concretes. Association Française de Génie Civil, France.

AFGC (2003). Ultra High Performance Fibre-Reinforced Concretes: Additional Informations for Interim Recommendations. Association Française de Génie Civil, France.

Bentz, E. C., F. J. Vecchio, et al. (2006). "Simplified Modified Compression Field Theory for Calculating Shear Strength of Reinforced Concrete Elements." *ACI Structural Journal* 103(4): 614-623.

Garas, V. Y. (2009). Multi-Scale Investigation of Tensile Creep of Ultra-High Performance Concrete for Bridge Applications. *Civil and Environmental Engineering*. Ph.D. Thesis. Georgia Institute of Technology, Atlanta, GA.

Gowripalan, N. and R. I. Gilbert (2000). Design Guidelines for RPC Prestressed Concrete Beams. VSL (Aust) Pty Ltd, Sydney: 51.

Graybeal, B. A. (2005). Characterization of the Behavior of Ultra-High Performance Concrete. *Civil and Environmental Engineering*. Doctor of Philosophy Thesis. University of Maryland, College Park.

Graybeal, B. A. (2006). Structural Behavior of Ultra-high Performance Concrete Prestressed I-Girders. Federal Highway Administration. U.S. Department of Transportation, Mclean, VA.

Graybeal, B. A. (2009). Structural Behavior of a Prototype Ultra-High Performance Concrete Pi-Girder. Federal Highway Administration. U.S. Department of Transportation, McLean, VA.

Hawkins, N. M., D. A. Kuchma, et al. (2005). Simplified Shear Design of Structural Concrete Members. NCHRP, Transportation Research Board, National Research Council, Washington, D.C.: 54.

Hegger, J. and G. Bertram (2008). Shear Carrying Capacity of Steel Fiber Reinforced UHPC. *2nd International Symposium on Ultra High Performance Concrete*. E. Fehling, M. Schmidt and S. Stürwald. Kassel University Press, Kassel, Germany: 513-520.

Hegger, J., D. Tuchlinski, et al. (2004). Bond Anchorage Behavior and Shear Capacity of Ultra High Performance Concrete Beams. *International Symposium on Ultra High Performance Concrete*. M. Schmidt, E. Fehling and C. Geinsenhanslüke. Kassel University Press, Kassel, Germany: 351-360.

JSCE (2006). Recommendations for Design and Construction of Ultra High Strength Fiber Reinforced Concrete Structures (Draft). Japan Society of Civil Engineers, Tokyo: 106.

CHAPTER 7
FIBER ALIGNMENT IN UHPC GIRDERS

7.1 Introduction

During the flexural testing of girder 1 and during four out of six of the girder shear tests, flexural compression failures were observed in the UHPC girders. The morphology of the failure surface looked lamellar in nature, with plate-like sheets of UHPC peeling away from the web of the girder. This failure type suggested that the fibers were preferentially aligned in the vertical and longitudinal directions, with very few fibers in the transverse direction. The beam's preferential alignment of fibers was investigated by determining the fiber orientation and the UHPC compressive strength, strain, and elastic modulus, with respect to that orientation.

The objective of this part of the research was to quantify the preferential alignment of steel fibers in the web of the UHPC test girders and to draw a correlation between this alignment and the compressive strength of the concrete with respect to the longitudinal, vertical and transverse (width) axes of the girder.

7.2 Background

Current ACI and AASHTO design codes assume that concrete is isotropic with respect to compressive and tensile properties. The addition of steel fibers to concrete introduces a component with a large aspect ratio. Despite this potential issue of preferential fiber alignment, the recent Report on Physical Properties and Durability of

Fiber-Reinforced Concrete by ACI Committee 544 does not address the effect of fiber alignment/orientation on compressive or tensile properties.

Potential effect of fiber alignment is particularly important when considering UHPCs where these fibers are the largest particles in the concrete. Currently, UHPC design guidelines operate largely under the assumption that fiber alignment does not affect compressive behaviors, which allows for the material to be treated as isotropic with respect to compressive strength (AFGC, 2002). When fiber orientation is considered, it is usually primarily in conjunction with the tensile properties of the concrete (Lappa et al., 2004; Stiel et al., 2004; Fehling et al., 2004). Garas (2009) presented an extensive background and discussion of how fiber reinforcement affects tensile and shear properties of UHPC.

While little work has been done on the effect of fiber orientation in UHPC on its mechanical properties, extensive work has been done characterizing fiber orientation in UHPC and other concrete composites. Image analysis is the most basic method used for fiber orientation characterization and has been used by several researchers (Lappa et al., 2004; Stiel et al., 2004; Tue and Henze, 2008). Micro Computer Tomography (Micro-CT) has also been used to characterize fiber alignment, but is limited to very small samples (Schnell et al., 2008). Recently, researchers have also begun using non-destructive techniques for determining fiber alignment based on impedance spectroscopy (Ozyurt et al., 2006b).

Very limited research has been done trying to quantitatively link fiber alignment to material properties of fiber-reinforced concretes. Ozyurt et al. (2006a) performed a follow-up study to their initial work on impedance spectroscopy that focused on linking

tensile properties of fiber reinforced concrete to fiber alignment. This study was a forensic study performed on a section of a FRC beam that had previously been tested. The study showed a qualitative connection between fiber alignment and tensile performance of fiber reinforced concrete. Currently, there are no known studies that quantitatively link fiber alignment and compressive properties or fiber reinforced concrete, much less UHPC.

7.3 Experimental Methods

Beam 2 and beam 3 from the full-scale girder tests were chosen to study fiber alignment due to the relatively undamaged region of their webs at midspan – away from the tested shear spans (Figure 7-1). A 48-in. by 17-in. section of each web was cut from this undamaged region. Each of these specimens was further gridded and sectioned as shown in Figure 7-2. Each resulting piece of concrete was roughly 5-in. x 5-in. x 3.875-in. (127 mm x 127 mm x 98 mm). From each of these cubes, cores were cut in the X (longitudinal), Y (vertical), or Z (transverse) direction. Some of these cores were used for image analysis, while others were used for compressive strength testing.

In order to obtain the maximum number of samples in each direction and to keep the core's L/D ratio as close to 2 as possible, a 2-in. (51 mm) core diameter was chosen. Previous research by Graybeal and Davis (2008) has indicated that 2-in. (51 mm) cast cylinders of UHPC show greater scatter in compression than do 3 and 4-in. cast cylinders, but no work was done on comparison of cored cylinder strengths. The 2-in. (51 mm) diameter was considered adequate because the largest aggregate was only 0.012 in. (0.3

mm) and the fibers were only 0.5 in. (13 mm) long; therefore, the core diameter was greater than 3x the largest size constituent.

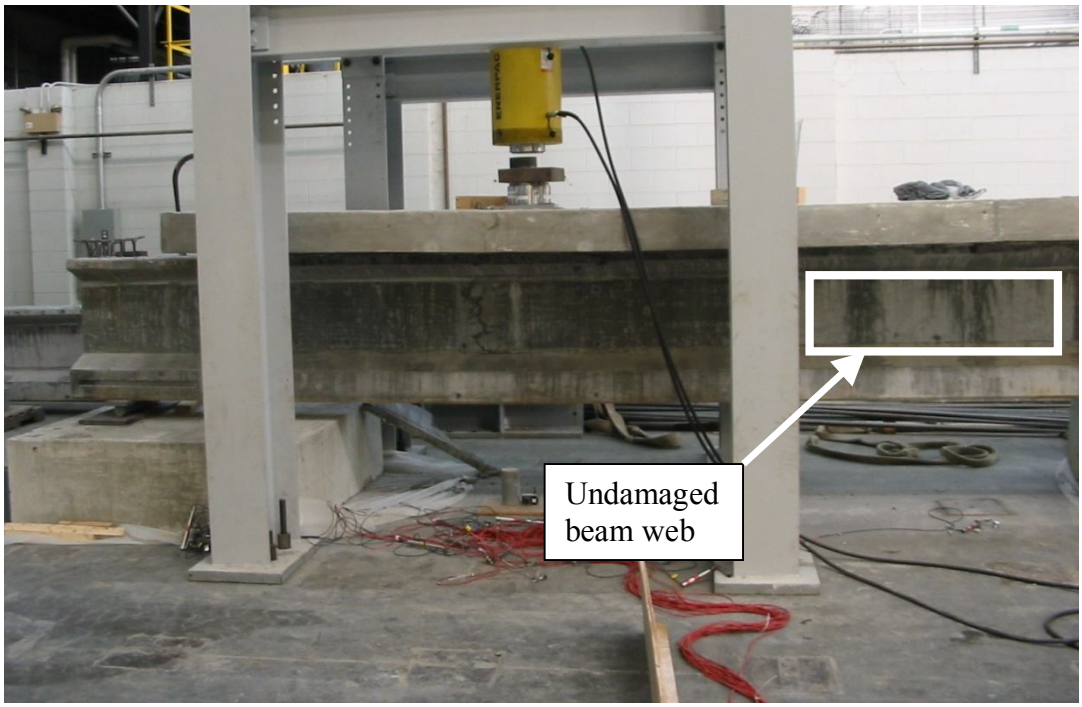

Figure 7-1: Girder 2 during shear testing. The undamaged portion at right was cut out for use in fiber alignment study.

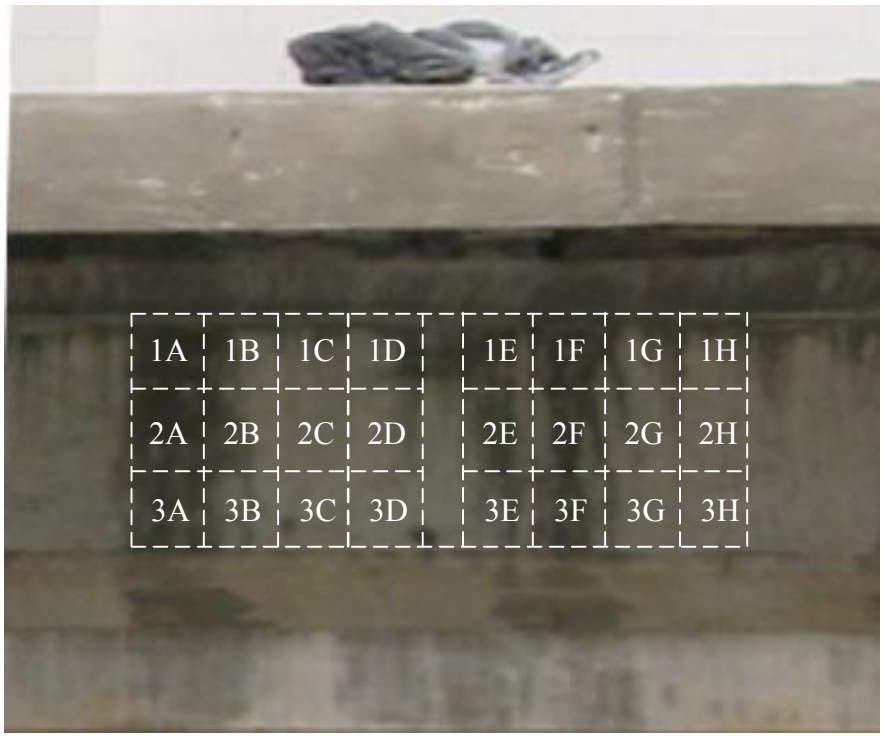

Figure 7-2: Cutting diagram and specimen numbering for fiber alignment study.

7.3.1 Image Analysis

In order to quantify the fiber alignment in the UHPC, image analysis was performed based on quantitative stereology. The UHPC 2-in. cores were cut into 1-in. lengths, and the flat surfaces were wet polished using a 60 grit paper on a Buehler EcoMet 4000 Grinder-Polisher as shown in Figure 7-3. After polishing, the diameter of each specimen was measured, and the specimens were photographed under lighting that maximized the reflectivity of the cut fibers on the surface as shown in Figure 7-4. The digital images were imported to ImageJ image analysis software (Rasband, 2010).

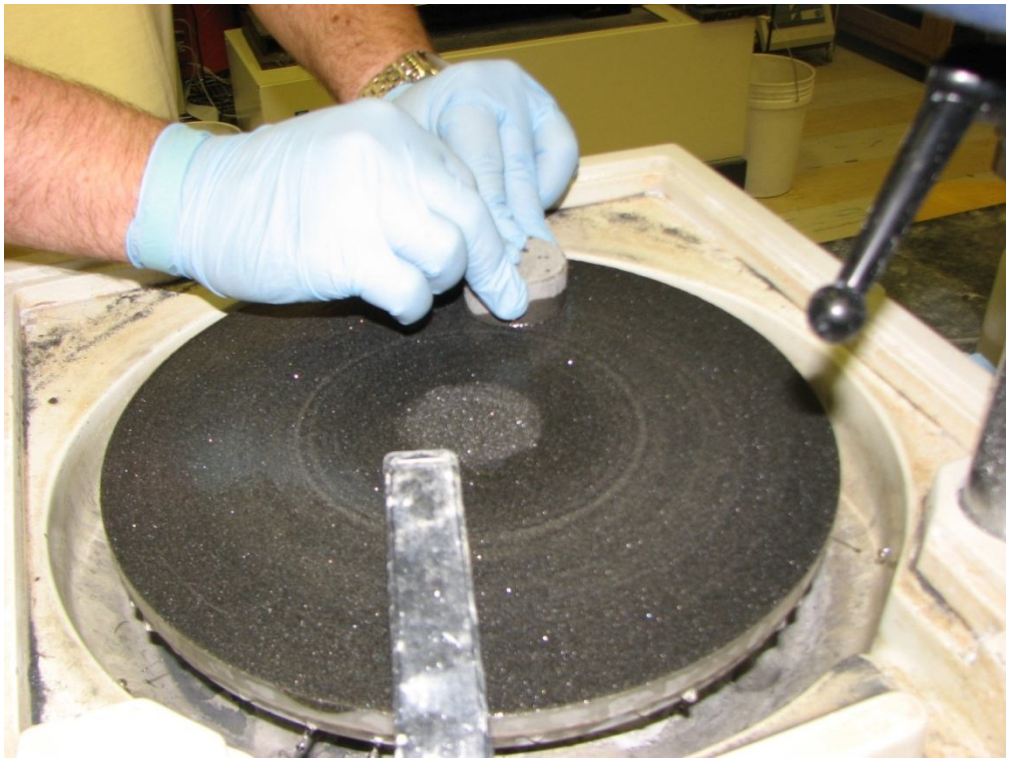

Figure 7-3: Grinder preparation of UHPC specimens for fiber alignment image analysis.

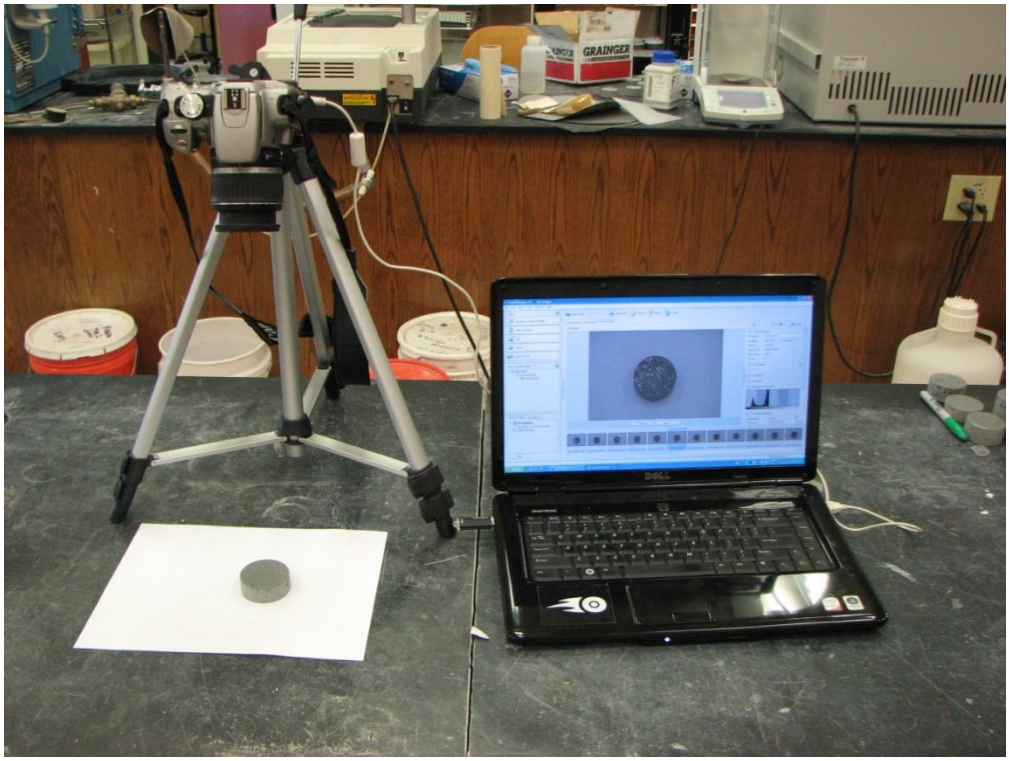

Figure 7-4: Image capture setup for fiber alignment analysis.

Inside ImageJ, the image was cropped and converted to 32-bit grayscale. A threshold was then applied to make the picture monochromatic and to show the fibers as black on a white background. The threshold was adjusted to make sure that all fibers were shown while comparing the black and white image to the original. Once the threshold was set, the particles were counted and numbered on the image. Particles along the edge and particles that were grouped were then counted manually and added, while any false positives were subtracted from the count. Figure 7-5 shows the steps in processing each image.

Using the fiber count obtained from the image analysis, the orientation coefficient, η_φ, was calculated as follows:

$$\eta_\varphi = \frac{N_f * A_f}{V_f}, \tag{7-1}$$

where N_f is the number of fibers per unit area (1/mm^2), A_f is the cross sectional area of an individual fiber (mm^2), and V_f is the fiber volume fraction (Ozyurt et al., 2006a). The orientation coefficient varies from 0 to 1 where "0" indicates that all fibers are parallel to the cut plane and "1" indicates that all fibers are perpendicular to the cut plane.

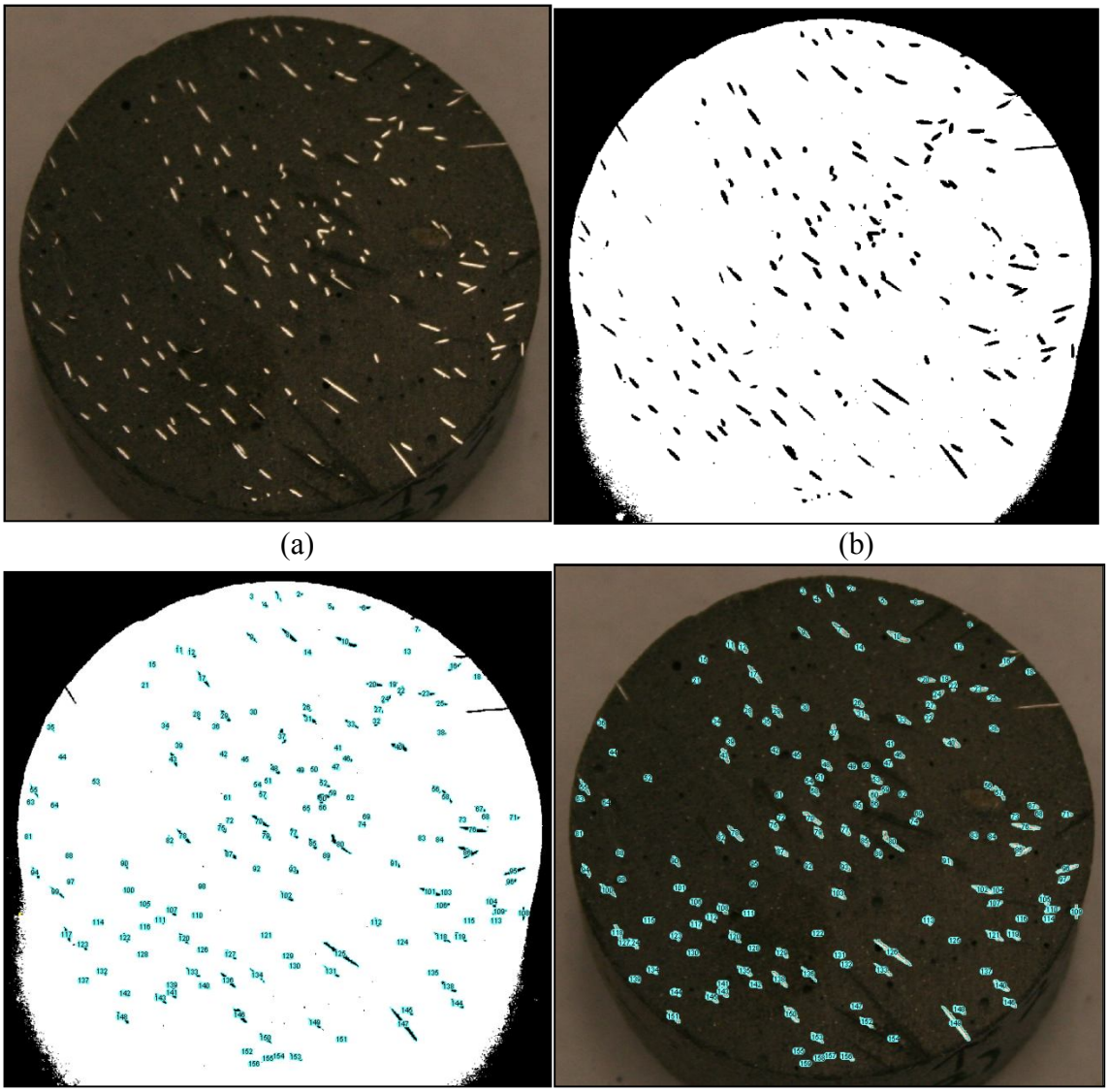

Figure 7-5: Steps of image analysis in ImageJ software. a) Image capture, b) application of threshold, c) fiber count, and d) analysis of uncounted fibers and combined fibers.

In the Z-direction, orientation numbers were calculated at ¼-in. intervals through the width of the web. This was done to evaluate if the fiber alignment varied based on Z-direction position in the web. Originally, three different cores were evaluated at each depth to establish an average and standard deviation at each position, but the standard deviation was particularly high at the 1.25 in., 1.5 in., and 1.75 in. positions, so additional

samples were taken at these depths. Figure 7-6 shows the variation in average orientation coefficient with depth along with a bar giving one standard deviation. Figure 7-7 shows the statistical analysis of these data with the mean being at the center of each diamond and the upper and lower vertices of the diamond representing the 95% confidence interval. The smaller lines near the peaks give a preliminary indication of significant difference. If these lines overlap, it is an indicator that data sets may not be significantly different. Even with the additional data points at the last three depths, there was still not a statistically significant difference between the orientation coefficients at the depths observed. A Tukey-Kramer Honestly Significant Difference (HSD) test was performed to determine statistical differences between orientation coefficients at varying depths. This test is similar to a traditional t-test, but is based on the studentized range distribution, q. Instead of comparing only two data sets, the Tukey test can compare multiple data sets without increasing the likelihood of false positives like multiple t-tests would. The results of the Tukey test are graphically represented by the circles along the right side of each figure. If the circles do not overlap or intersect such that the angle between them is acute, there is at least a 95% confidence that the data sets are significantly different. If the circles overlap in such a way that their intersection angle is greater than 90 degrees, there is not an indication of significant difference between data sets.

Based on the seven different depths evaluated, there were 28 pair-wise comparisons. With a 95% confidence, none of these pairs of means were statistically different. Because there was no statistical difference based on depth, an average value of the orientation coefficient in the Z-direction of 0.140 was used in comparison with X and

Y directions. This number was based on 29 separate measurements, but excluded three outlier measurements that were more than two standard deviations from the average.

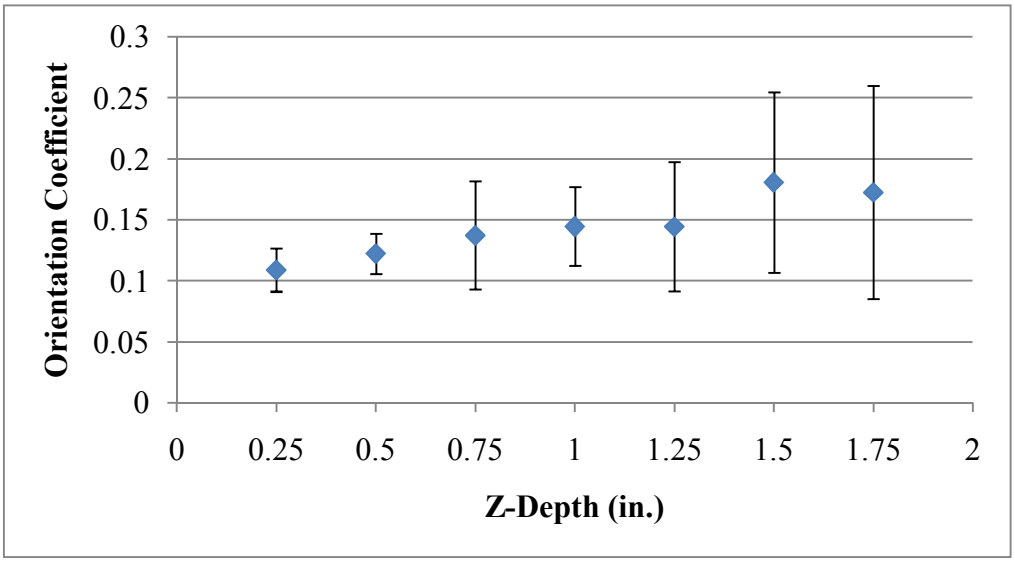

Figure 7-6: Variation of orientation coefficient with depth in the z-direction. For 0.25 in through 1 in depths, n=3; for 1.25 in, n=7; and for 1.5 and 1.75 in, n=6.

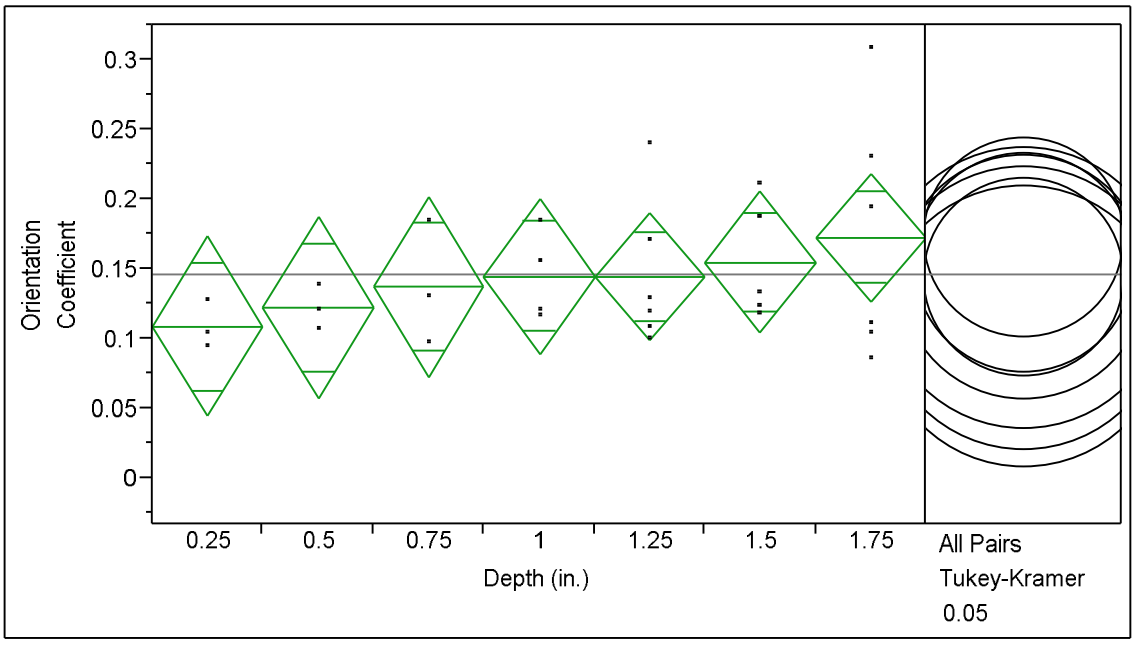

Figure 7-7: Statistical analysis of orientation number versus depth. No significant statistical difference exists based on available data.

In the X-direction and Y-direction, the fiber alignment was not expected to vary significantly based on position. Therefore, the cores were cut every inch to obtain multiple values of the orientation number for statistical analysis. Values of orientation number were taken equally from cylinders near the web face and through the center of the web. In the X-direction, the average orientation coefficient from 16 cores was 0.592 and excluded one outlier. In the Y-direction, the average orientation coefficient from 15 cores was 0.626, and no outliers were observed. Figure 7-8 compares the average values and standard deviations for the X, Y, and Z directions. Figure 7-9 shows the statistical analysis of these data. While there was a slight difference between the average orientation coefficients in the X and Y directions, it was statistically insignificant. Both of these values were at least 4 times greater than the Z direction orientation coefficient, showing that there was a clear preferential orientation of the steel fibers that favored the longitudinal and vertical axes of the beams over the transverse, Z axis.

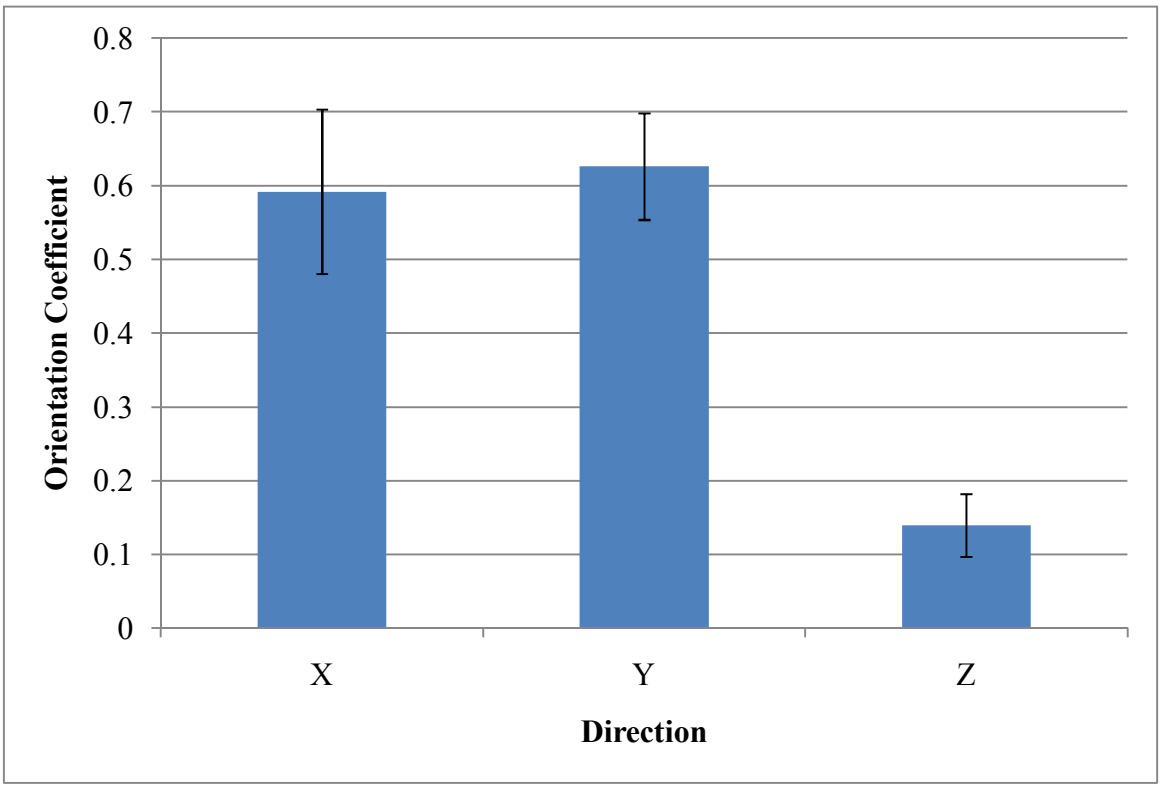

Figure 7-8: Orientation coefficients of fibers in UHPC beam web in three orthogonal axes. The X, Y, and Z direction averages and standard deviations are based on 16, 15, and 29 observations, respectively.

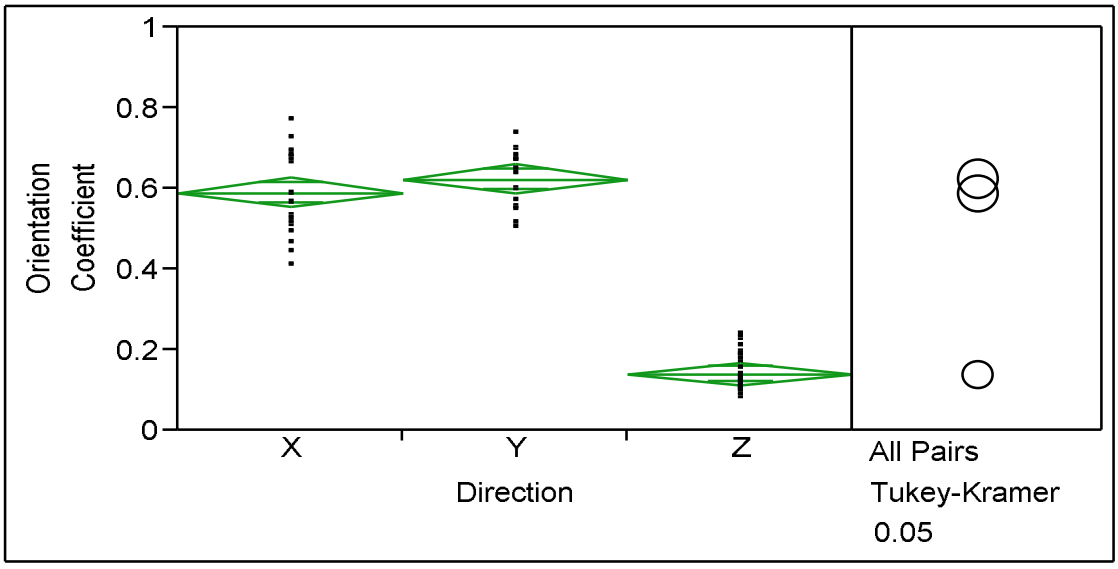

Figure 7-9: Statistical analysis of fiber orientation coefficient. Green diamonds represent 95% confidence intervals, that is, there is a 95% chance that the population mean lies in this range.

7.3.2 Compression Testing of Cores

7.3.2.1 Specimen Preparation

For compressive strength testing, the coring method specified by ASTM C 42 was generally followed for obtaining, storing, and testing the specimens (ASTM C 42, 2004). The exceptions to this standard were that due to the amount of time required to prepare each UHPC cylinder; more than 10 days elapsed between coring and final testing. During the time between coring and testing, the cores were also out of their sealed bags for periods which totaled greater than two hours, again due to the extensive preparation times. The core locations were chosen based upon crack mapping in the web. Cylinders were chosen to minimize the chance of their having pre-existing cracks.

The time requirements and sealed bags specified in the ASTM are due to potential creation of moisture gradients across the cylinder that could affect the compressive strength of the cylinders (Bartlett and MacGregor, 1994). The variations from ASTM were considered insignificant in the present tests due to the very low permeability of UHPC and low free water in the UHPC matrix. ASTM C 42 also does not normally allow for the use of 2-in cores in testing concrete because of the high variation in strength that can be experienced with that core size. In order to have a large enough sample size for statistical analysis, 2-in cores were the only option in this study. Due to the small MSA of UHPC and the homogeneity of the matrix, the potential negative effects of using small cylinders were considered to be small, though unknown.

After coring, the ends of the cores were ground using a surface grinder. The core was held in a 3-jaw chuck, while passed back and forth under a diamond grinding wheel. Each pass removed between .005 and .015 in. of material. Figure 7-10 shows the setup

for grinding of these cylinders. During grinding the cylinders were cooled by a water-soluble lubricant. After grinding, this lubricant was removed with brake cleaner, which served the dual purpose of double-checking for cracks in the cylinder. Any cylinder showing signs of pre-existing crack damage was discarded.

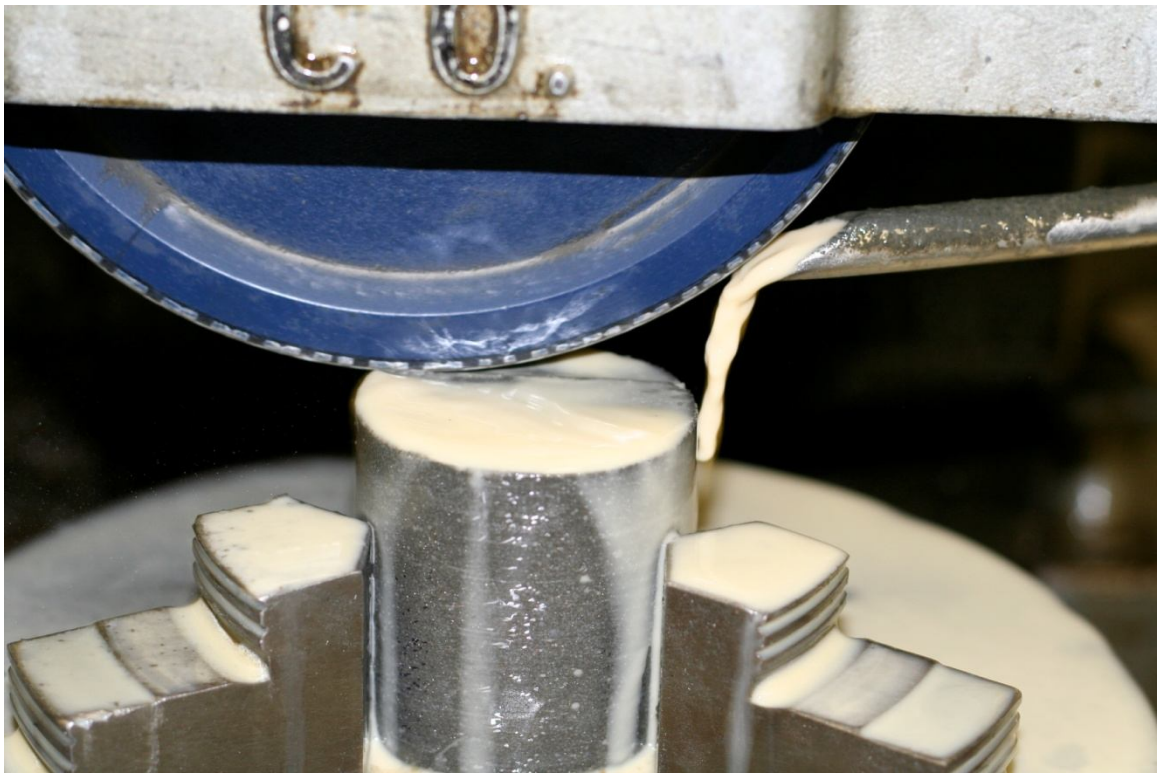

Figure 7-10: Cylinder end grinding for compression cylinders.

7.3.2.2 Specimen Testing

After specimen preparation was completed, specimen dimensions were recorded in order to calculate cross sectional area as well as L/D required by ASTM C 42 for adjustment of compressive strengths. Only three specimens required the use of this correction factor: 31AZ2, 31AZ3, and 31BZ3. Table 7-1 shows the specimen details for

each of the compression cylinders tested; ten cores were tested in the X-direction, twelve cores were tested in the Y-directions, and eleven cores were tested in the Z-direction

Table 7-1: Compression Core Details

Specimen	Direction	Length (in.)	Diameter 1 (in.)	Diameter 2 (in.)	L/D	Area (in^2)
21BX1	X	4.0	1.99	1.98	2.02	3.09
21BX2	X	4.0	1.99	1.99	2.01	3.11
21CX1	X	3.9	1.99	1.99	1.96	3.11
22BX1	X	4.0	1.98	1.99	2.02	3.09
22BX2	X	4.0	1.99	1.99	2.01	3.11
22DX2	X	4.2	2.01	2.01	2.06	3.17
31GX1	X	3.9	1.99	2.00	1.95	3.13
31GX2	X	3.9	1.99	1.99	1.96	3.11
31HX1	X	4.0	1.99	1.99	2.01	3.11
31HX2	X	4.0	1.99	2.00	2.01	3.13
33AX1	X	4.2	1.99	2.01	2.10	3.14
21AY1	Y	3.8	2.00	2.00	1.92	3.14
21AY2	Y	4.0	1.99	2.00	2.01	3.13
22CY1	Y	4.0	1.98	1.99	2.02	3.09
23DY2	Y	4.1	1.99	2.00	2.06	3.13
32AY1	Y	4.0	2.00	2.00	2.00	3.14
32AY2	Y	3.9	1.99	1.99	1.96	3.11
32BY1	Y	4.0	1.99	2.00	2.01	3.13
32BY2	Y	4.0	2.00	1.99	2.01	3.13
32HY1	Y	3.8	1.99	1.99	1.91	3.11
32HY2	Y	3.8	2.00	1.99	1.90	3.13
33BY1	Y	3.9	1.99	2.00	1.95	3.13
33BY2	Y	3.9	1.99	1.99	1.96	3.11
21EZ4	Z	3.9	1.99	1.99	1.94	3.11
21FZ2	Z	3.9	1.98	1.98	1.96	3.08
22EZ2	Z	3.6	1.98	1.98	1.82	3.08
22EZ3	Z	3.7	1.99	1.99	1.88	3.11
31AZ1	Z	3.7	1.99	1.99	1.86	3.11
31AZ2	Z	3.4	2.00	2.00	1.70*	3.14
31AZ3	Z	3.4	1.99	1.99	1.71*	3.11
31BZ1	Z	3.6	2.00	1.99	1.80	3.13
31BZ2	Z	3.5	1.99	1.99	1.76	3.11
31BZ3	Z	3.3	2.00	2.00	1.65*	3.14
31BZ4	Z	3.6	2.00	2.00	1.80	3.14

* denotes L/D less than 1.75 requiring strength correction factor

The compression testing was carried out on an 800-kip capacity SATEC compression testing machine. Each cylinder was tested at a load rate of 145 lbf/sec (1MPa/sec) as measured by the testing machine's instrumentation. An initial load of approximately 37,000 lbf (165 kN) was applied to each cylinder as a seating load. This load corresponds with 40% of the ultimate load as specified by ASTM C469 (2002). The load was then removed at the same rate. The data recorded were all from the second loading which was continued to failure for each specimen. Failure was considered to have occurred when a load drop of more than 40% of ultimate load occurred. This point was clearly defined in all cases by loud cracking and an instantaneous loss of almost all load capacity.

During loading, the load and strain were recorded every one second via a National Instruments data acquisition system coupled with Labview data collection software. To reduce noise, each recorded data point was an average of 50 consecutive data points taken at a rate of 5 kHz. The load was measured continuously via a 200-kip capacity Interface load cell. The strains were measured by three RDP DCTH500 linear variable displacement transducers (LVDTs) spaced around the cylinder at 120 degrees from each other. These LVDTs were secured to the cylinder as shown in Figure 7-11. The gauge length between the fixed rings was 2.25 in. (57mm) at the beginning of each test.

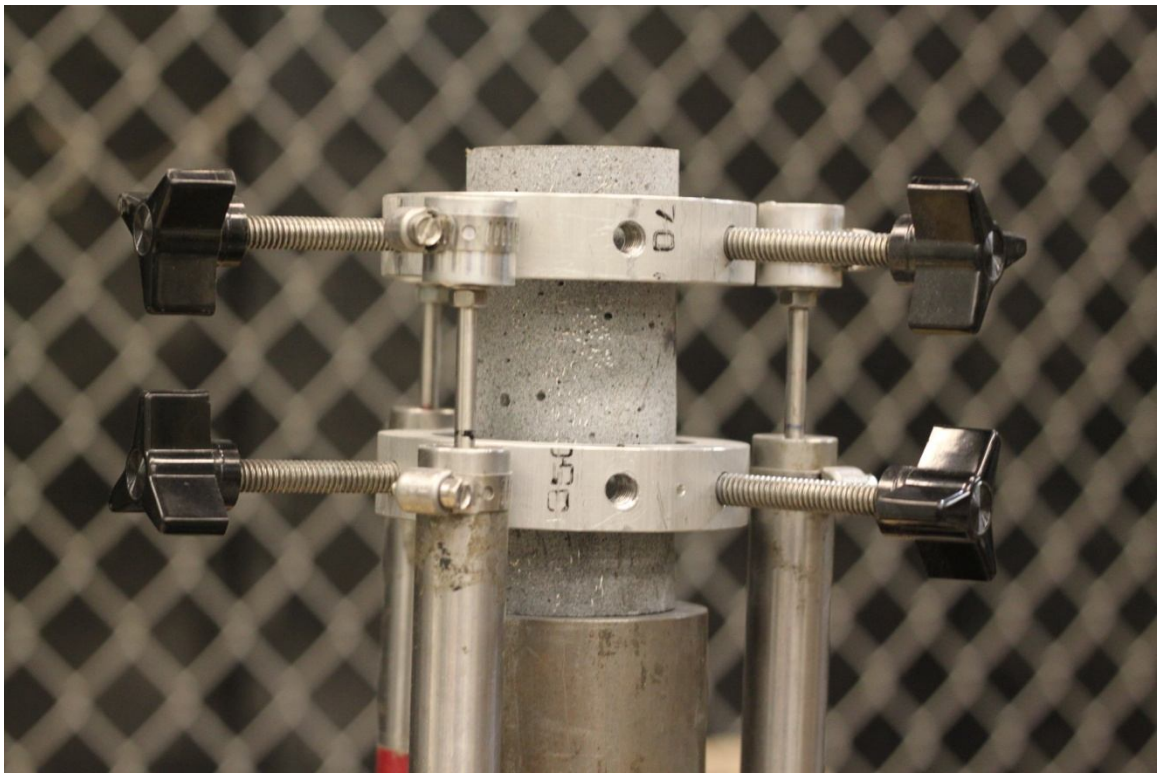

Figure 7-11: Compression and modulus of elasticity test setup.

Five values were recorded for each test when available: maximum stress as measured by the Interface load cell, maximum measured strain prior to failure, strain at peak load (from load cell), secant modulus of elasticity up to 40% load (E40), and secant modulus of elasticity up to 90% load (E90). The E40 modulus of elasticity was defined as per ASTM C469 (2002). The E90 modulus was measured in the same way as the E40 modulus except the chord modulus was taken up to 90% of the compressive failure stress of the cylinder. This metric was added to evaluate if fibers had a significant effect on the stiffness of UHPC at very high stresses. A sixth value was taken as the difference between the E40 and the E90 moduli. This can be thought of as a measure of how much fiber orientation affects change of stiffness in an individual specimen.

The correction factor specified in ASTM C39 (2009) was applied to both the strength and modulus observations. The correction factor ranged from 0.972 to 0.976; therefore the maximum adjustment on any data point was less than 3%. Table 7-2 gives the recorded results of the compression tests for each specimen. Some values were not available for some tests due to errors in the data acquisition setup. For these tests, stress values based on the SATEC's internal instrumentation were recorded in place of load cell measurements.

Based on the values reported in Table 7-2, the averages, standard deviations, coefficients of variation, and sample numbers of each set were calculated and recorded in Table 7-3. A Tukey-Kramer HSD test was performed to determine differences between the samples in the X, Y, and Z-directions. Table 7-4 presents the results of the Tukey pair wise comparisons. p-values less than 0.05 represent a significant difference between compared data sets. The comparisons with significant differences are highlighted in the table.

Table 7-2: Compression Test Results

Specimen	Peak Stress (psi)	Max Strain (in./in.)	Strain at Peak Stress (in./in.)	Modulus of Elasticity, 40% [E40] (ksi)	Modulus of Elasticity, 90% [E90] (ksi)	E40-E90 (ksi)
21BX1	30,761	0.00359	0.00359	9,892	8,634	1,257
21BX2	29,182	0.00383	0.00383	8,052	7,725	327
21CX1	32,087	–	–	8,387	–	–
22BX1	34,571	0.00499	0.00499	8,126	7,326	800
22BX2	29,654	0.00447	0.00407	8,090	7,526	564
22DX2	30,393‡	–	–	–	–	–
31GX1	29,983	0.00446	0.00398	8,348	7,684	663
31GX2	28,672	0.00464	0.00342	9,729	8,398	1,332
31HX1†	27,984	0.00352	0.00269	13,089	11,490	1,599
31HX2	31,918	0.00515	0.00393	11,113	8,501	2,612
33AX1	32,195	0.00476	0.00462	8,107	7,507	600
21AY1	25,700‡	–	–	–	–	–
21AY2	29,947	0.00452	0.00362	9,978	8,561	1,528
22CY1	28,893	0.00516	0.00361	8,905	8,911	-6
23DY2	29,133	0.00430	0.00373	8,497	7,967	529
32AY1	30,845	0.00386	0.00385	8,710	8,077	633
32AY2	31,460	0.00408	0.00408	8,313	7,809	505
32BY1	31,481	0.00414	0.00414	8,483	7,828	655
32BY2	32,192	0.00495	0.00440	8,048	7,649	399
32HY1	31,485	0.00403	0.00403	8,345	8,094	251
32HY2	31,393	0.00446	0.00395	8,445	8,061	384
33BY1	30,090‡	–	–	–	–	–
33BY2	34,986	0.00463	0.00453	8,362	7,778	584
21EZ4	30,615‡	–	–	–	–	–
21FZ2	32,289‡	–	–	–	–	–
22EZ2	35,787	0.00511	0.00511	8,797	7,323	1,475
22EZ3	32,335‡	–	–	–	–	–
31AZ1	33,188	0.00587	0.00506	8,158	7,380	778
31AZ2	35,877*	0.00714	0.00643	7,768	7,126	642
31AZ3	34,301*‡	–	–	–	–	–
31BZ1	37,046	0.00601	0.00511	9,839	8,424	1,415
31BZ2	34,576‡	–	–	–	–	–
31BZ3	37,727*	0.00769	0.00612	7,662	7,104	558
31BZ4	33,849‡	–	–	–	–	–

*corrected values based on ASTM C 42

†outlier not included in statistical analysis

‡load cell malfunction, stress taken from SATEC pressure gauge

Table 7-3: Summary of Compression Test Results

		Peak Stress [Load Cell] (psi)	Max Strain (in./in.)	Strain at Peak Stress (in./in.)	Modulus of Elasticity, 40% [E40] (ksi)	Modulus of Elasticity, 90% [E90] (ksi)	E40-E90 (ksi)
X	Avg.	30,673	0.00438	0.00390	9,293	7,912	1,019
	St. Dev.	1,900	0.00060	0.00067	1,691	514	730
	Coeff. Var.	6%	14%	17%	18%	6%	72%
	n	11	9	9	10	8	8
Y	Avg.	30,634	0.00442	0.00399	8,608	8,074	546
	St. Dev.	2,226	0.00042	0.00031	533	387	398
	Coeff. Var.	7%	9%	8%	6%	5%	73%
	n	12	10	10	10	10	10
Z	Avg.	34,326	0.00636	0.00556	8,445	7,471	974
	St. Dev.	2,167	0.00104	0.00066	817	545	438
	Coeff. Var.	6%	16%	12%	10%	7%	45%
	n	11	5	5	5	5	5

Table 7-4: Tukey-Kramer HSD Analysis of Compression Test Results

		Peak Stress [Load Cell] (psi)	Max Strain (in./in.)	Strain at Peak Stress (in./in.)	Modulus of Elasticity, 40% [E40] (ksi)	Modulus of Elasticity, 90% [E90] (ksi)	E40-E90 (ksi)
X-Y	DoF	32	22	22	23	22	22
	q stat	2.465	2.530	2.530	2.521	2.530	2.530
	p-value	0.9364	0.9683	0.9628	0.7853	0.7523	0.1845
Y-Z	DoF	32	22	22	23	22	22
	q stat	2.465	2.530	2.530	2.521	2.530	2.530
	p-value	0.0005	<0.0001	<0.0001	0.9359	0.0721	0.3431
X-Z	DoF	32	22	22	23	22	22
	q stat	2.465	2.530	2.530	2.521	2.530	2.530
	p-value	0.0023	0.0001	<0.0001	0.6524	0.2478	0.9881

Note: statistically significant comparisons highlighted.

Figures 7-12 through 7-17 present visual comparisons of the data sets and their analyses of variance (ANOVAs). As previously stated, the centerline of each green diamond represents the mean of the data set with the diamond peaks indicating the 95% confidence interval.

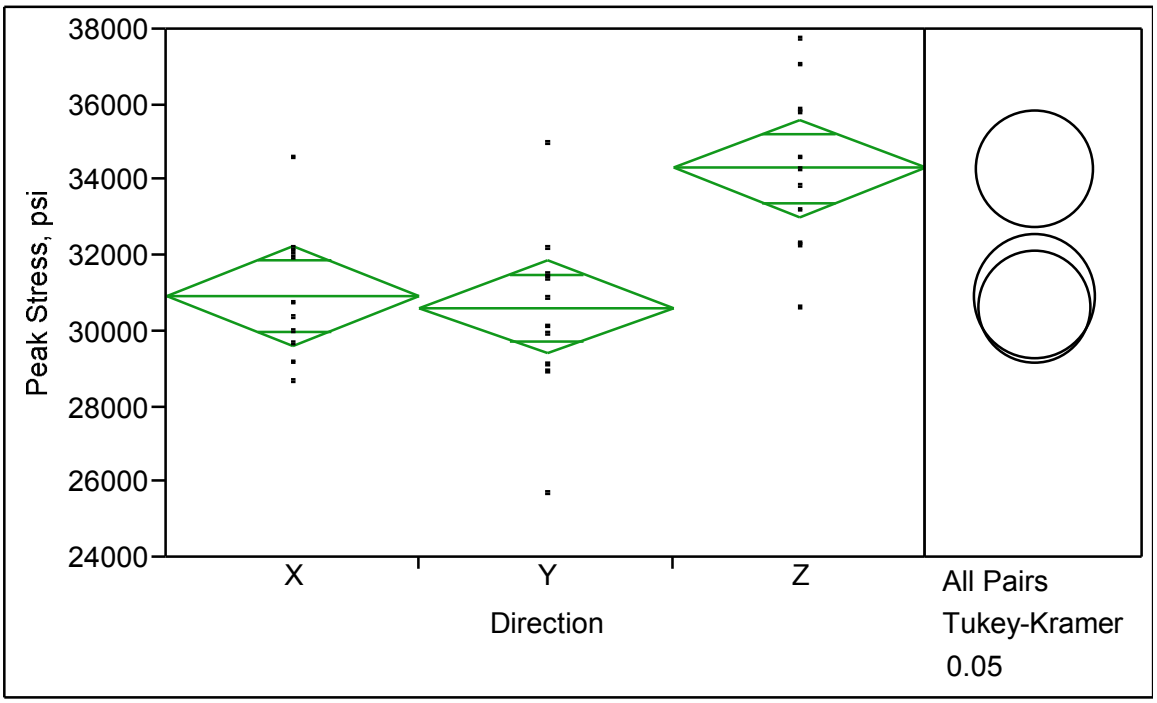

Figure 7-12: ANOVA and Tukey test for peak stress compared to direction.

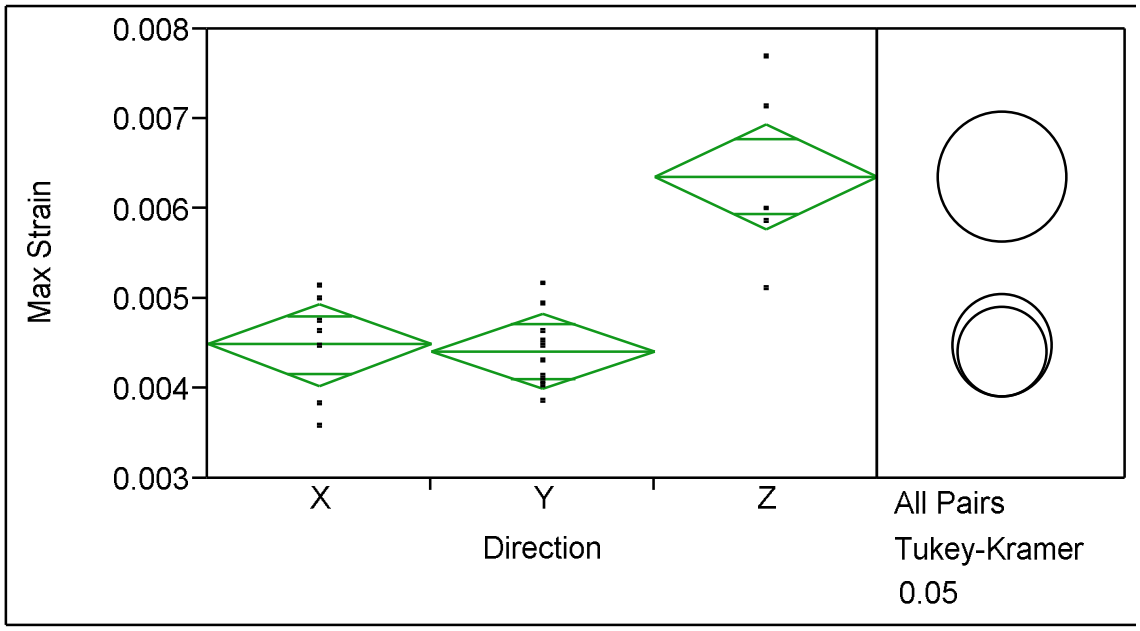

Figure 7-13: ANOVA and Tukey test for maximum strain compared to direction.

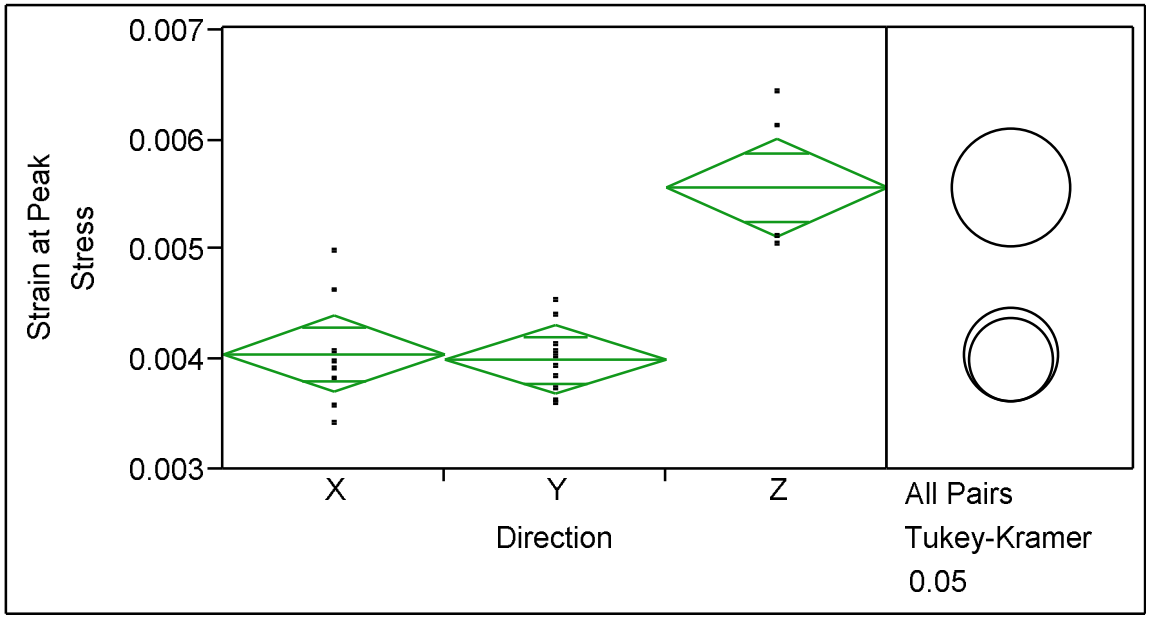

Figure 7-14: ANOVA and Tukey test for strain at peak stress compared to direction.

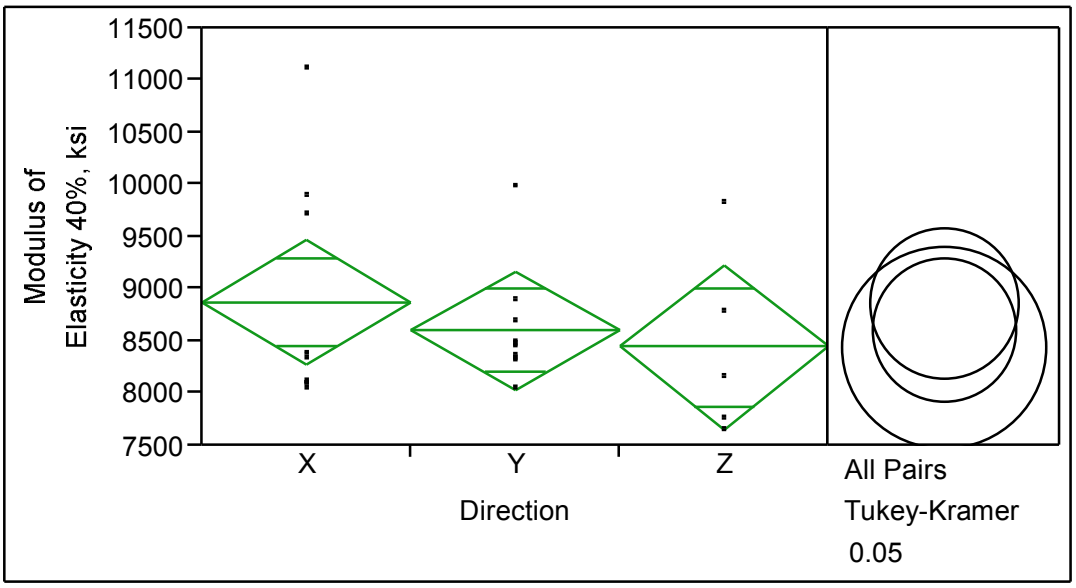

Figure 7-15: ANOVA and Tukey test for modulus of elasticity up to 40% of max stress [E40] compared to direction.

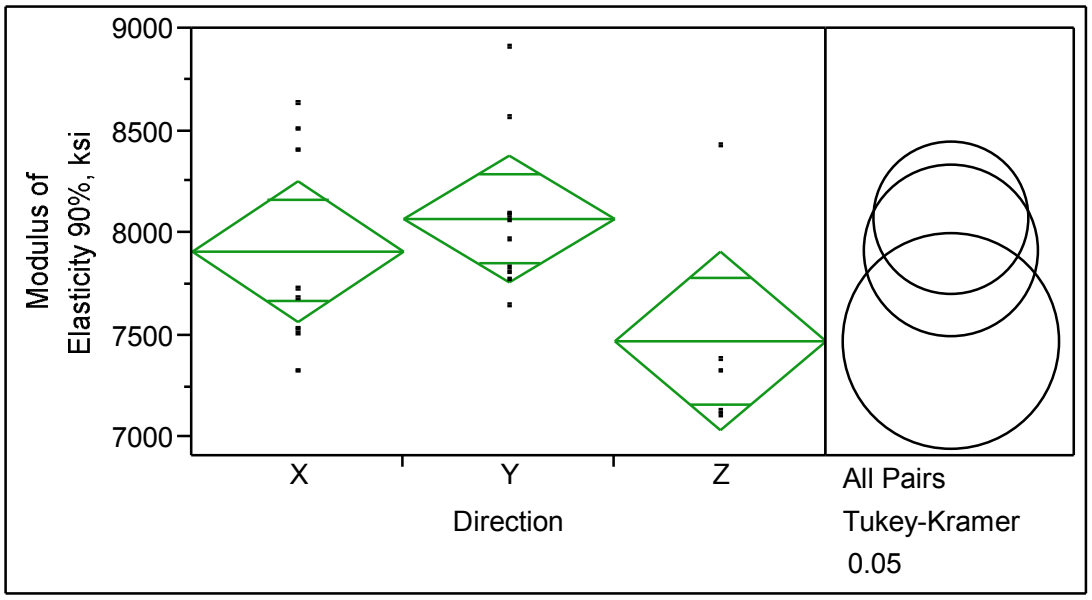

Figure 7-16: ANOVA and Tukey test for modulus of elasticity up to 90% of max stress [E90] compared to direction.

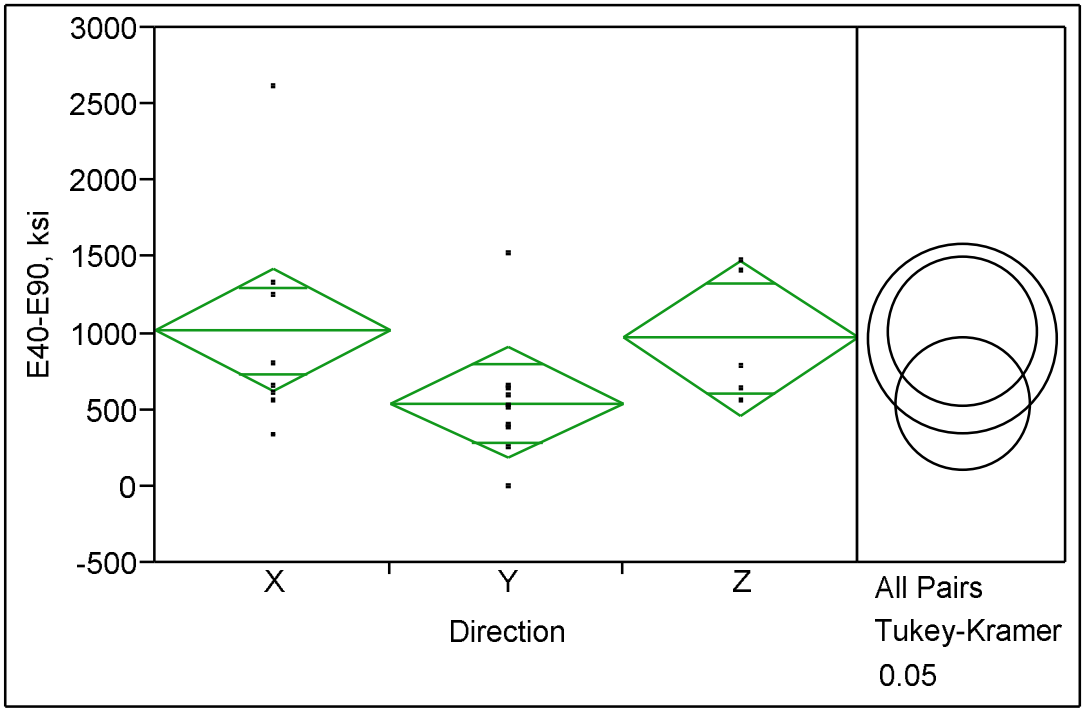

Figure 7-17: ANOVA and Tukey test for modulus of elasticity change [E40-E90] compared to direction.

The results did not show any statistically significant difference between the X and Y directions for any variable observed. For the maximum stress, the average capacity in the Z-direction was clearly different from those in either other direction. This difference was also true for the maximum strains and strains at maximum stress. The only observed behavior for which there was not a clear statistical difference in the Z direction was the modulus of elasticity.

7.4 Comparison of Results

The destructive nature of both the image analysis and the compressive tests created a problem with directly comparing orientation coefficient and compressive traits

of concrete cores. Since both types of data could not be taken on a single core, the data could not be collected as pairs. Since both orientation coefficients and compressive traits varied even between cores taken very close together, adjacent cores could not be assumed to be the same specimen for data collection purposes. This prevented traditional correlations such as regression analysis from being used.

While quantitative comparisons between orientation coefficients and compressive traits were not able to be made, qualitative correlations were readily apparent from the data. Figures 7-18 through 7-23 present the averages of the orientation coefficient tests versus the averages of the compressive traits as paired sets. The standard deviation of each variable is represented in its respective axis. In all but Figures 7-21, 7-22, and 7-23 (Modulus of Elasticity), it can be seen that the values obtained in the Z-direction lie significantly apart from those obtained in the X and Y direction for both variables plotted. This suggests that there is a link between fiber orientation and compressive behavior in UHPC.

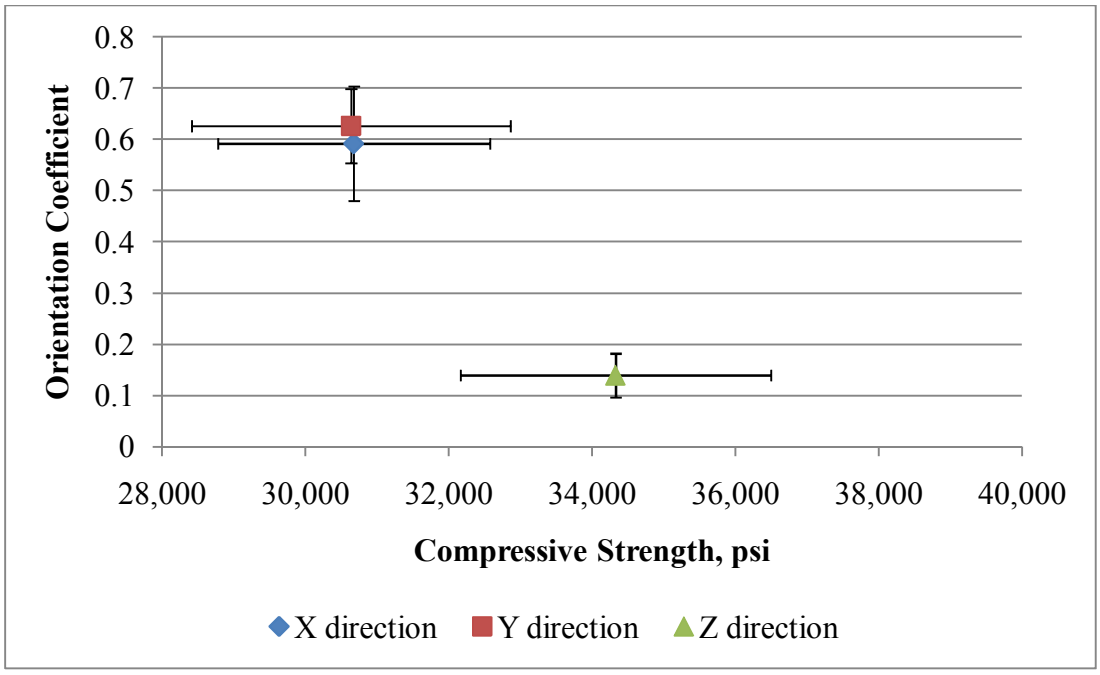

Figure 7-18: Average orientation coefficient versus average compressive strength (load cell) for X, Y, and Z directions.

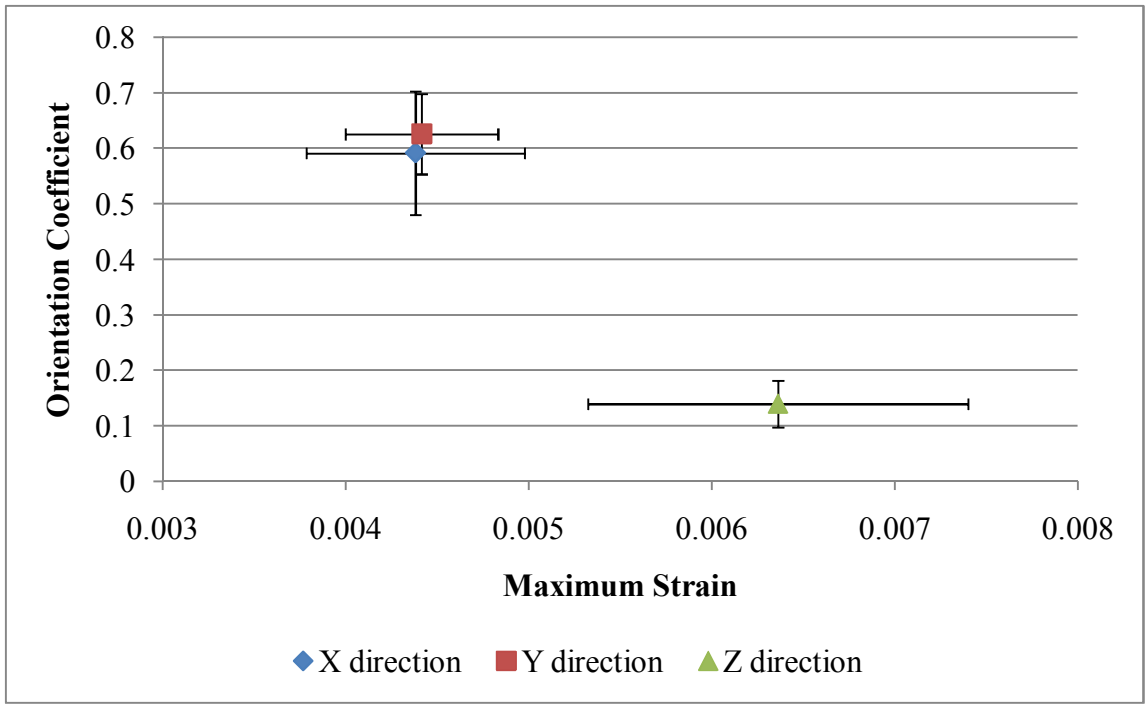

Figure 7-19: Average orientation coefficient versus average maximum strain for X, Y, and Z directions.

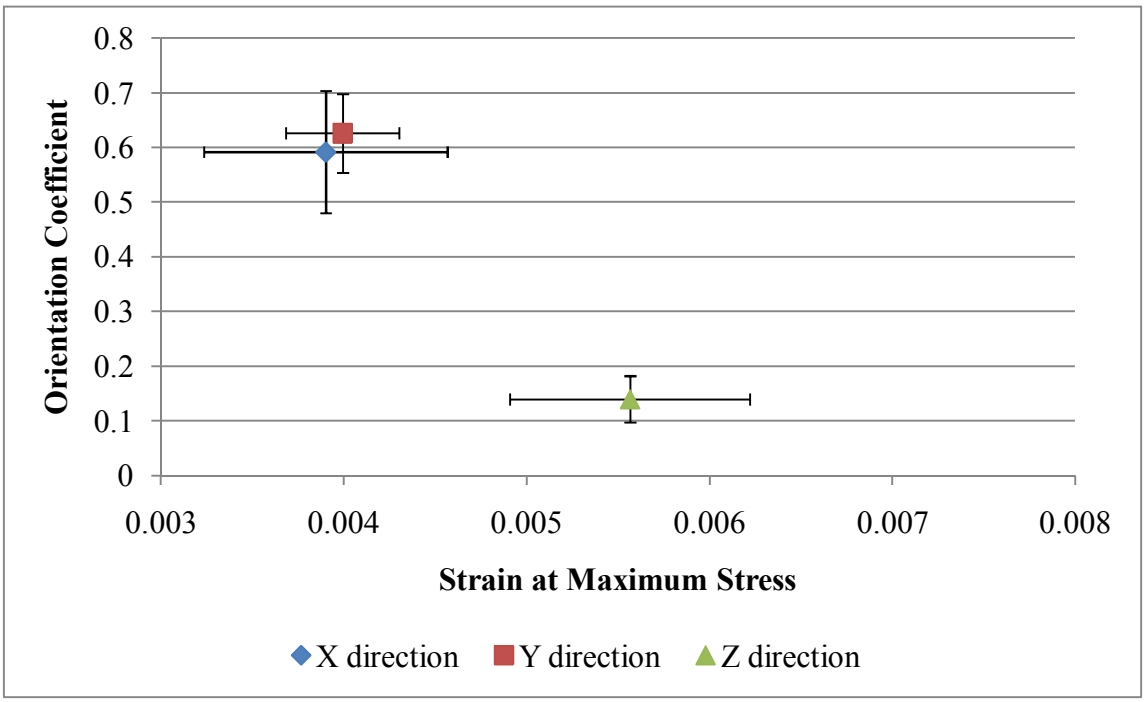

Figure 7-20: Average orientation coefficient versus average strain at maximum stress for X, Y, and Z directions.

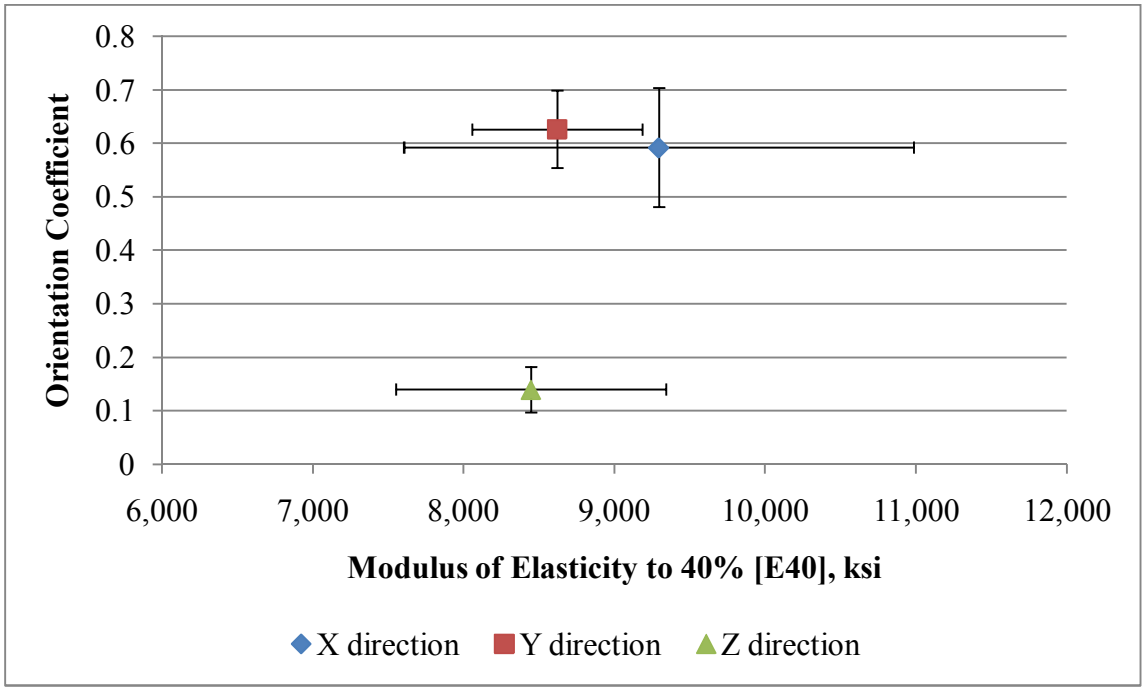

Figure 7-21: Average orientation coefficient versus average modulus of elasticity up to 40% of peak stress [E40] for X, Y, and Z directions.

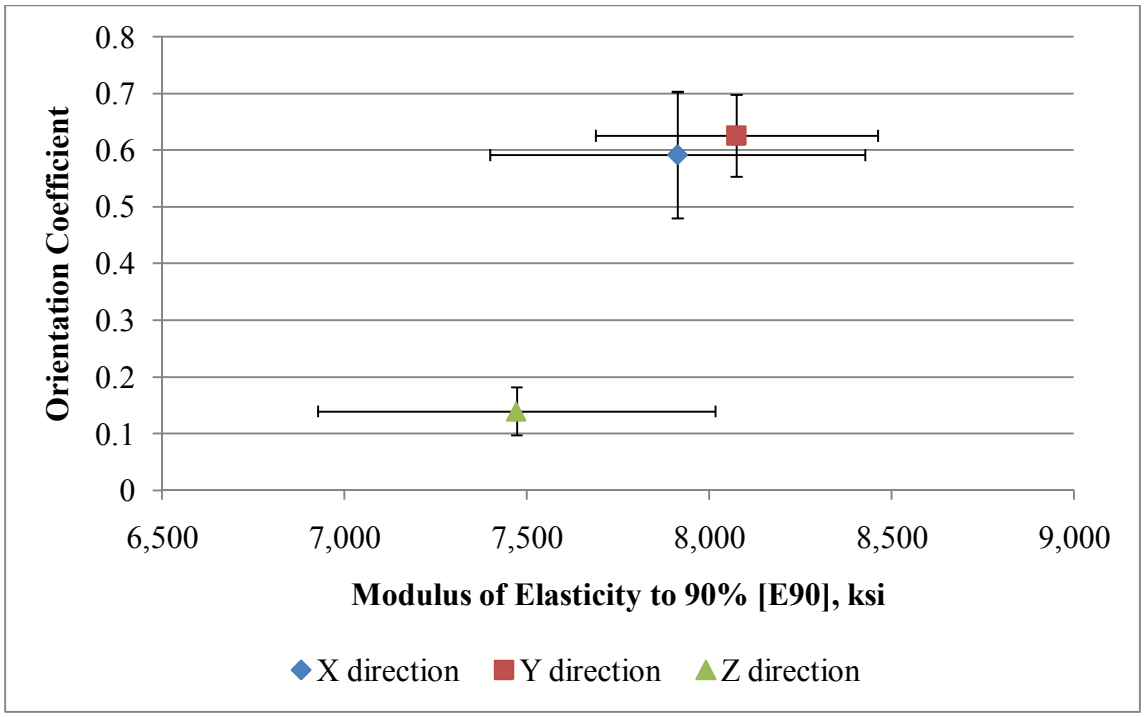

Figure 7-22: Average orientation coefficient versus average modulus of elasticity up to 90% of peak stress [E90] for X, Y, and Z directions.

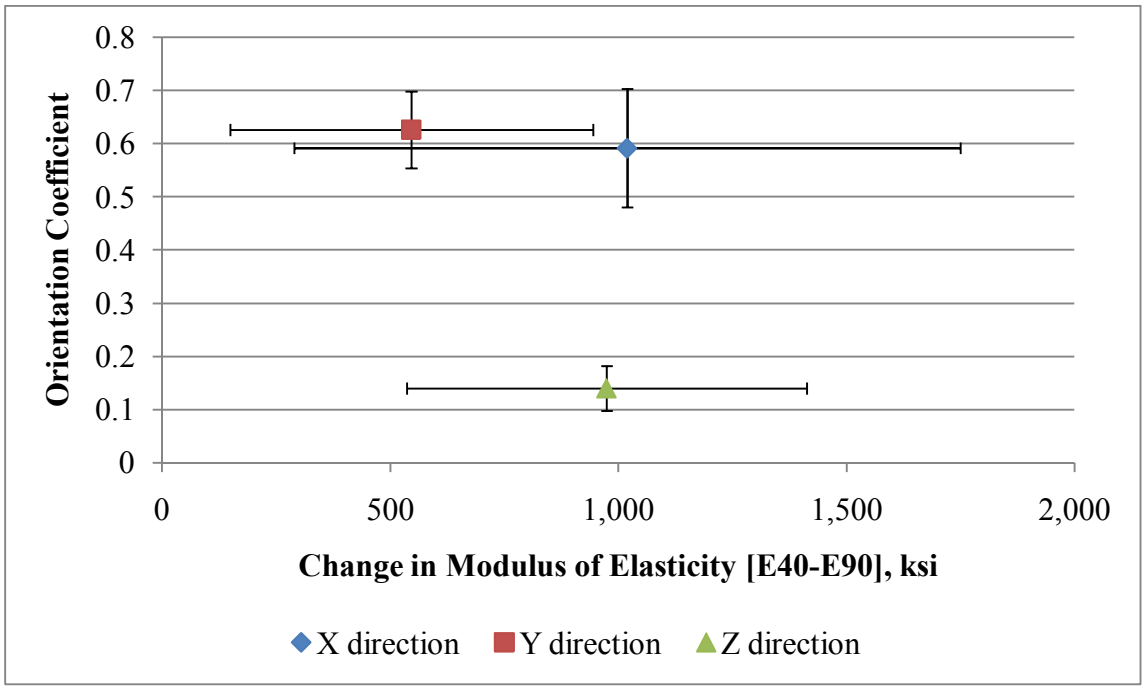

Figure 7-23: Average orientation coefficient versus average change in modulus of elasticity [E40-E90] for X, Y, and Z directions.

The higher compressive failure stress and strain values observed in the Z-direction were thought to be due to the high number of fibers oriented perpendicular to the compressive stress. These fibers would bridge any cracks caused by Poisson expansion of the cylinder. By slowing the growth of these cracks and making the failure mechanism more ductile, the concrete would be able to carry higher strains prior to failure. Similarly, higher stresses could be attained through the redistribution of stresses by the fibers. This mechanism was supported by the way in which the Z-direction cylinders failed. At ultimate load, Type 1 and Type 2 failures were observed as defined by ASTM C39 (2009).

When fibers were primarily oriented in a plane that was parallel to the direction of loading (i.e., the X and Y direction cylinders), the failure mechanism was largely columnar (Type 3). This indicated that failure occurred when tension parallel to direction of load application caused cracking that was not limited by fibers. In these cases, cracking was not mitigated by fibers bridging cracks so much less stress and strain redistribution was possible, leading to lower maximum stress and strain capacities.

In the case of modulus up to 40% of peak stress (E40), the lack of statistical difference was unexpected. It was thought that due to the very linear stress-strain behavior of UHPC, more difference might be observed if the chord modulus were taken up to a higher stress value where microcracking might influence stiffness more. A stress of 90% was chosen for this modulus, in order to capture behavior over a broad range while still staying below the range of extreme non-linearity immediately prior to failure.

The effect of cylinder direction on the modulus of elasticity up to 90% of peak stress (E90) was not statistically significant, though the p-values were much lower than

those observed in the E40 analysis. Specifically, the comparison of Z and Y direction cores gave a p-value of 0.072, which indicates that there may be a correlation. One primary reason for the lack of significance of these data was the very small sample size available in the Z direction.

Finally, the difference between the E40 and E90 modulus for each specimen was evaluated. This was done to see if the fiber alignment had an effect on how the secant modulus changed between low and high values of stress. No significant differences were found when these secant moduli were compared in the three directions.

It was unknown why no significant differences were seen in the moduli when significant differences had been observed in the stress and strain metrics. It appears that fibers oriented perpendicular to the stress direction increased capacity, but had no effect on stiffness properties. This would make sense if the concrete matrix was primarily responsible for modulus. Pairing of this type of testing with microstructural analysis is suggested for better understanding the relationship of stiffness to fiber alignment.

7.5 Conclusions

1. In the 32-in. deep BT-shaped beams with 4-in. (102 mm) wide webs cast by Georgia Tech, fiber alignment in the UHPC greatly favored the longitudinal and vertical, X and Y directions over the Z, transverse direction. The projection of the fibers' total length in the Z direction was 4 times less than the projections in the X and Y directions. Casting of full size UHPC girders did cause preferential alignment of fibers in the longitudinal and vertical axes of the girders which resulted in reduced compressive strength in the longitudinal direction.

2. The strength of compressive cores taken in the Z direction was between 4750 and 5220 psi (33 and 36 MPa) higher than the strengths of cores taken in the X and Y directions. The Z direction strength was up to 17% higher than the X and Y directions.
3. The maximum strain of compressive cores in the Z direction was almost 0.002 in./in. (44%) greater than that observed in the X and Y direction.
4. The strain at maximum compressive stress of cores in the Z direction was 0.0016 in./in. (41%) greater than in the X or Y directions.
5. A qualitative correlation can be drawn between fiber alignment and compressive behavior. When a majority of fibers are preferentially aligned perpendicular to the direction of applied compressive stress, the maximum stress and strain capacities are significantly increased. Conversely, when fibers align primarily in the direction of compressive loading, the stress and strain capacities decrease.

7.6 Further Research

This portion of the research was conducted as a forensic analysis of failures observed during flexural testing of full-scale prestressed UHPC girders. Because of this, the availability of samples and the ability to control variables were limited. While this research clearly showed that compressive behaviors of UHPC are affected by fiber alignment, the exact extent to which these behaviors are affected by varying degrees of fiber alignment could not be evaluated. More research is needed to fully quantify the effect of fiber alignment on compressive behaviors. The following research is suggested to begin this process:

1. Non-destructive methods for fiber alignment analysis would allow for compressive tests to be performed on the same specimens that had been analyzed for fiber alignment. This type of paired analysis would allow for regression analyses to be used in quantitative correlations.
2. Use of cubes with non-destructive testing would allow for fiber analysis in three orthogonal directions for each specimen. This would allow for the effect of off-axis fiber alignment on compressive properties to be studied.
3. Varied casting methods could be used to create fiber alignments other than those seen in this experimentation. For example, truly uniaxial fiber alignment may affect compressive properties differently than the biaxial alignment seen in the current study.
4. Microstructural investigation of UHPC could be paired with this type of fiber alignment, and mechanical properties could be tested in order to better understand the ways in which the matrix, fibers, and interfacial zone affect the mechanical properties.

7.7 References

AFGC (2002). Interim recommendations for ultra high performance fibre-reinforced concretes. Association Française de Génie Civil, France.

ASTM C 39 (2009). C39/C39M-09: Standard Test Method for Compressive Strength of Cylindrical Concrete Specimens. ASTM International, West Conshohocken, PA.

ASTM C 42 (2004). C 42-04 Standard Test Method for Obtaining and Testing Drilled Cores and Sawed Beams of Concrete. ASTM International, West Conshohocken, PA. C 42-04.

ASTM C 469 (2002). C 469-02 Standard Test Method for Static Modulus of Elasticity and Poisson's Ratio of Concrete in Compression. ASTM International, West Conshohocken, PA. C 469-02.

Bartlett, F. M. and J. G. MacGregor (1994). "Effect of Moisture Condition on Concrete Core Strength." *ACI Materials Journal* 91(3): 227-236.

Fehling, E., K. Bunje, et al. (2004). Design Relevant Properties of Hardened Ultra High Performance Concrete. *International Symposium on Ultra High Performance Concrete*. M. Schmidt, E. Fehling and C. Geinsenhanslüke. Kassel University Press, Kassel, Germany: 327-338.

Garas, V. Y. (2009). Multi-Scale Investigation of Tensile Creep of Ultra-High Performance Concrete for Bridge Applications. *Civil and Environmental Engineering*. Ph.D. Thesis. Georgia Institute of Technology, Atlanta, GA.

Graybeal, B. A. and M. Davis (2008). "Cylinder or Cube: Strength Testing of 80 to 200 MPa (11.6 to 29 ksi) Ultra-High-Performance Fiber-Reinforced Concrete." *Aci Materials Journal* 105(6): 603-609.

Lappa, E. S., C. R. Braam, et al. (2004). Static and Fatigue Bending Tests of UHPC. *International Symposium on Ultra High Performance Concrete*. M. Schmidt, E. Fehling and C. Geinsenhanslüke. Kassel University Press, Kassel, Germany: 449-458.

Ozyurt, N., T. O. Mason, et al. (2006a). "Non-destructive monitoring of fiber orientation using AC-IS: An industrial-scale application." *Cement and Concrete Research* 36(9): 1653-1660.

Ozyurt, N., L. Y. Woo, et al. (2006b). "Monitoring Fiber Dispersion in Fiber-Reinforced Cementitious Materials: Comparison of AC-Impedance Spectroscopy and Image Analysis." *Aci Materials Journal* 103(5): 340-347.

Rasband, W. (2010). ImageJ. National Institute of Mental Health, Bethesda, Maryland.

Schnell, J., F. P. Ackermann, et al. (2008). Statistical Analysis of Fibre Distribution in Ultra High Performance Concrete Using Computer Tomography. *2nd International Symposium on Ultra High Performance Concrete*. E. Fehling, M. Schmidt and S. Stürwald. Kassel University Press, Kassel, Germany: 145-152.

Stiel, T., B. L. Karihaloo, et al. (2004). Effect of Casting Direction on Mechanical Properties of CARDIFRC. *International Symposium on Ultra High Performance Concrete*. M. Schmidt, E. Fehling and C. Geinsenhanslüke. Kassel University Press, Kassel, Germany: 481-493.

Tue, N. V. and S. Henze (2008). Determination of the Distribution and Orientation of Fibres in Steel Fibre Reinforced UHPC by Photographic Method. *2nd International Symposium on Ultra High Performance Concrete*. E. Fehling, M. Schmidt and S. Stürwald. Kassel University Press, Kassel, Germany: 505-512.

CHAPTER 8
CONCLUSIONS, RECOMMENDATIONS, AND FUTURE RESEARCH

8.1 Conclusions

Based on the current study, the following conclusions were drawn about the use of UHPC in precast prestressed bridge girders:

1. Precast prestressed UHPC bridge girders with concrete compressive strengths above 24 ksi and tensile strengths above 1.2 ksi can be successfully cast and cured at Georgia precast plants.
2. Fluted deformations can be created in the top surface of UHPC girders by depressing 1/4-in. (6 mm) fluted formliner into the surface of the plastic concrete. These deformations satisfy the requirement for 1/4-in. (6 mm) surface roughness in ACI and AASHTO codes, and the fluted surface provides an excellent interface to develop composite behavior of UHPC bridge girders and cast-in-place deck.
3. Smooth UHPC cold joints have very low interface shear capacity even when combined with relatively large amounts of transverse reinforcement. If shear friction is used for smooth surfaces, a friction factor, μ, of 0.6 with a cohesion factor, c, of 0 was found to be satisfactory.
4. Monolithic UHPC with 2% fibers by volume has very high shear friction capacity, approximately 1500 psi, even when no additional reinforcement is used and a when crack exists along a high shear plane. Fiber reinforcement continues to transfer shear after the concrete matrix has cracked.

5. UHPC shear friction push-off specimens can be used to accurately predict the interface capacity of small and large composite beams made with UHPC girders and conventional concrete deck slabs. Small composite beams can be used as a conservative indicator of full-scale girder interface shear performance.
6. Fiber reinforcement greatly increases the shear capacity of UHPC girders, but current AASHTO codes do not consider this additional fiber capacity, V_f. Shear equations based on direct tension capacity of UHPC (a Mohr's circle analysis) can be used to take advantage of fiber contribution. Existing code equations based on the simplified modified compression field theory (S-MCFT) can also be adapted to take into account fiber contribution to shear capacity by the addition of a V_f term.
7. Placing the very flowable UHPC in girder forms causes preferential orientation of fibers. This fiber orientation can be quantitatively identified and is statistically significant. In the girders tested, the fibers were preferentially oriented along the longitudinal and vertical X and Y axes, which resulted in the longitudinal and vertical axial compressive strength being 11% less than the compressive strength in the transverse direction.
8. In the webs of UHPC girders, compressive properties of the UHPC are dependent on fiber direction. These variations are quantifiable and statistically significant.
9. A qualitative connection can be drawn between fiber alignment and compressive properties of UHPC. This finding indicates that ordinary assumptions of material isotropy are not necessarily correct.

8.2 Recommendations

UHPC exhibits many unique properties that could be beneficial to bridge construction. In order for the material to gain broad acceptance, codes must be written or modified to incorporate its use. Toward that end, the following design recommendations are made:

1. Smooth cold-joint interfaces should be avoided in design and construction with UHPC where shear forces must be transferred across the interface. Instead, cold-joint interfaces between precast UHPC and cast-in-place concretes should be fluted (roughened) which may be accomplished by depressing a formliner into the plastic concrete or by use of an equivalent roughening technique.
2. For interfaces roughened as recommended in (1), AASHTO shear friction guidelines may be used for design of interface shear transfer.
3. Diagonal tension shear capacity of UHPC girders similar to those in this study with 2% fibers by volume may be calculated using AASHTO S-MCFT equations with an additional V_f term accounting for fiber reinforcement based on the French UHPC recommendations (AFGC, 2002). The web shear capacity, V_{cw}, based on Mohr's circle analysis may be conservatively calculated using the direct tensile capacity of UHPC.

8.3 Future Research

Based on the current research, the following areas of continued research are suggested:

1. Existing studies on shear capacity of UHPC girders should be collected and results should be compared to the proposed prediction equations. Much of the existing research has taken place in France, Germany and Japan, and translation is required.
2. A full parametric study should be performed on the effect of fiber alignment on compressive and tensile properties of UHPC. The current study was forensic in nature, so variables could not be adjusted at will. The results of small-scale tests should be correlated to full-scale structures so design equations can take the anisotropic nature of UHPC into consideration.

8.4 References

AFGC (2002). Interim recommendations for ultra high performance fibre-reinforced concretes. France, Association Française de Génie Civil.

APPENDIX A
PUSH-OFF TEST LOAD-SLIP CURVES AND FAILURE PICTURES

This appendix presents the load-slip curves and failure images for all of the push-off tests performed. Detailed analysis of the push-off data is presented in Chapter 3.

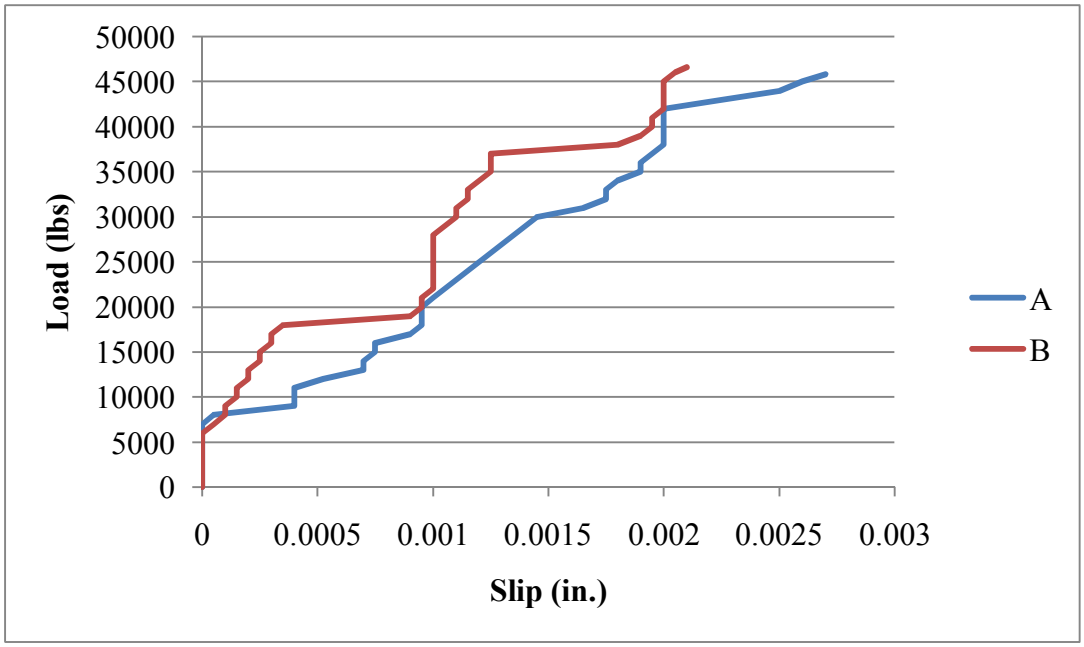

Figure A-1: Load-slip curves for U-H-F-0 specimens

Figure A-2: U-H-F-0-A after failure.


Figure A-3: UHPC side of failure interface for specimen U-H-F-0-A. Note shear failure through HPC "shear keys" created by fluted interface.

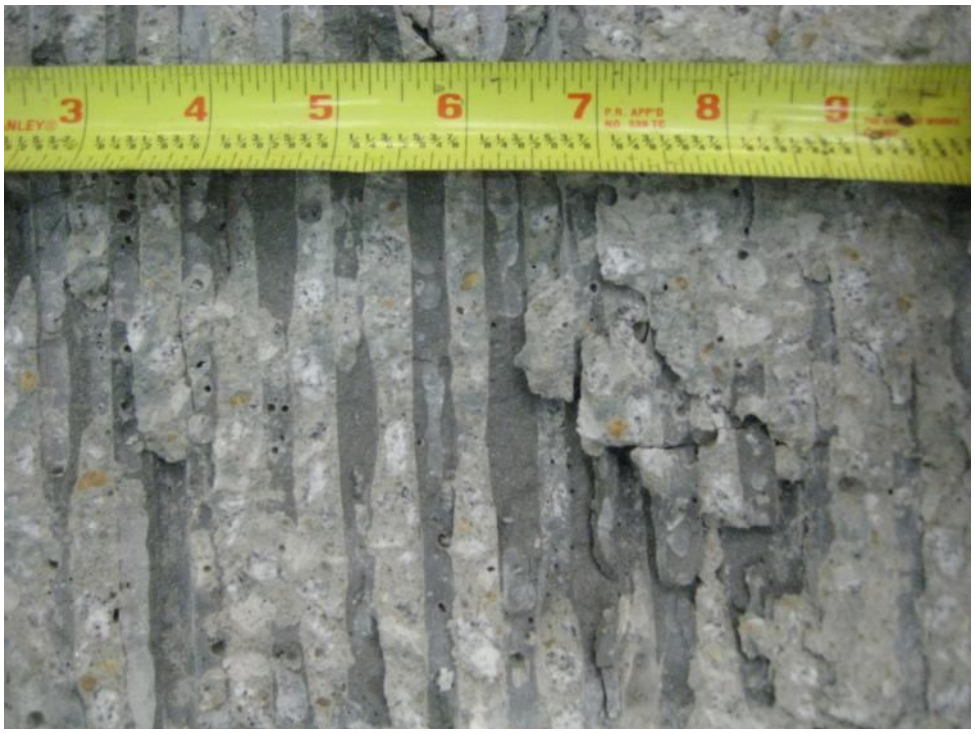

Figure A-4: Close-up of interface failure of specimen U-H-F-0-A.

Figure A-5: U-H-F-0-B after failure.

Figure A-6: HPC side of interface failure surface of specimen U-H-F-0-B. Notice the failure occurred almost totally through the HPC rather than the UHPC.

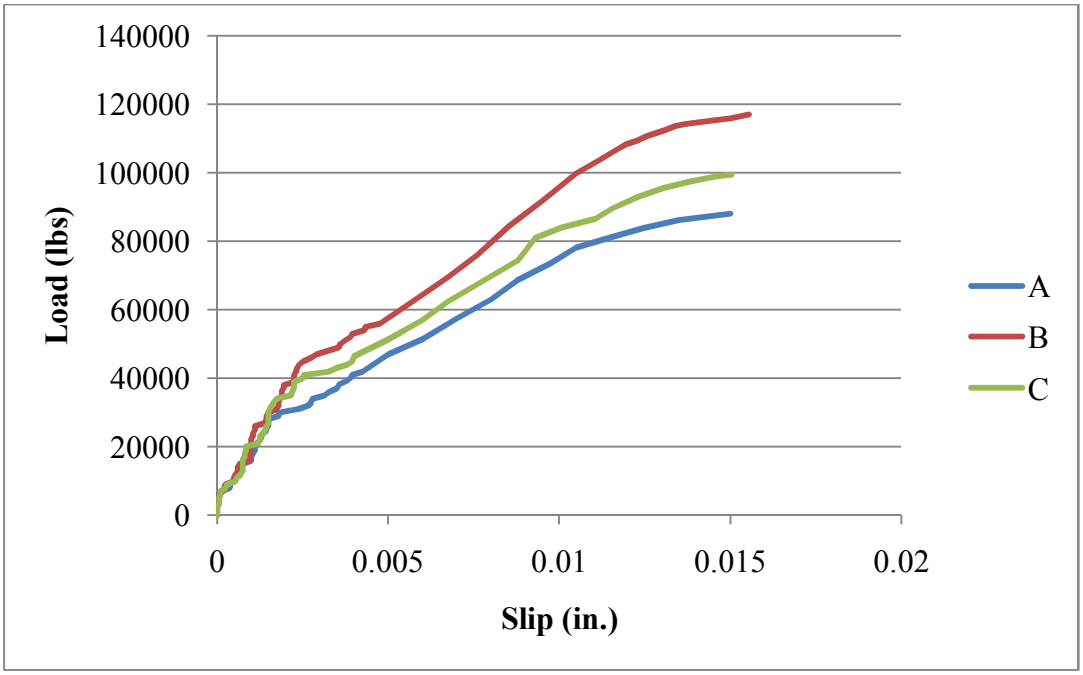

Figure A-7: Load-slip curves for U-H-F-2 specimens

Figure A-8: U-H-F-2-A after failure.

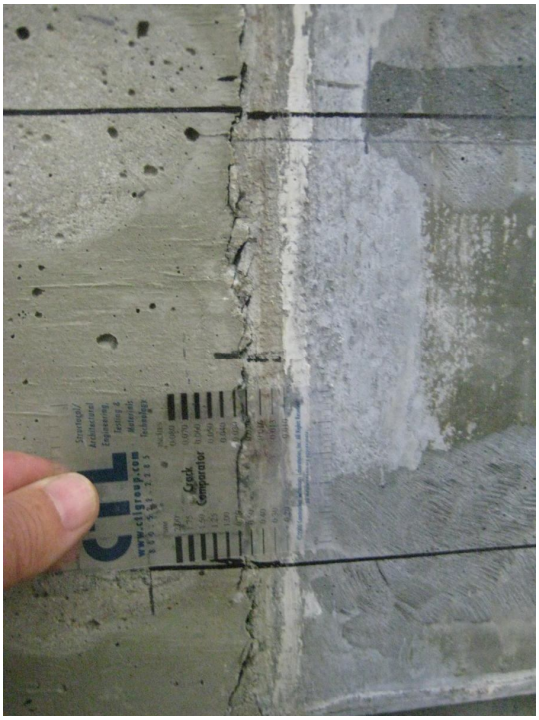
Figure A-9: Interface crack in specimen U-H-F-2-A. Notice differential slip between halves at rebar indicator line.

Figure A-10: U-H-F-2-B after failure. This specimen was taken past maximum load to emphasize the crack and to show the post-peak behavior.

Figure A-11: Reverse side of specimen U-H-F-2-B. Spalling was observed in the HPC above the stirrup locations.

Figure A-12: Close-up of spalling cracks in specimen U-H-F-2-B.

Figure A-13: U-H-F-2-C after failure.

Figure A-14: Close-up of interface crack in specimen U-H-F-2-C.

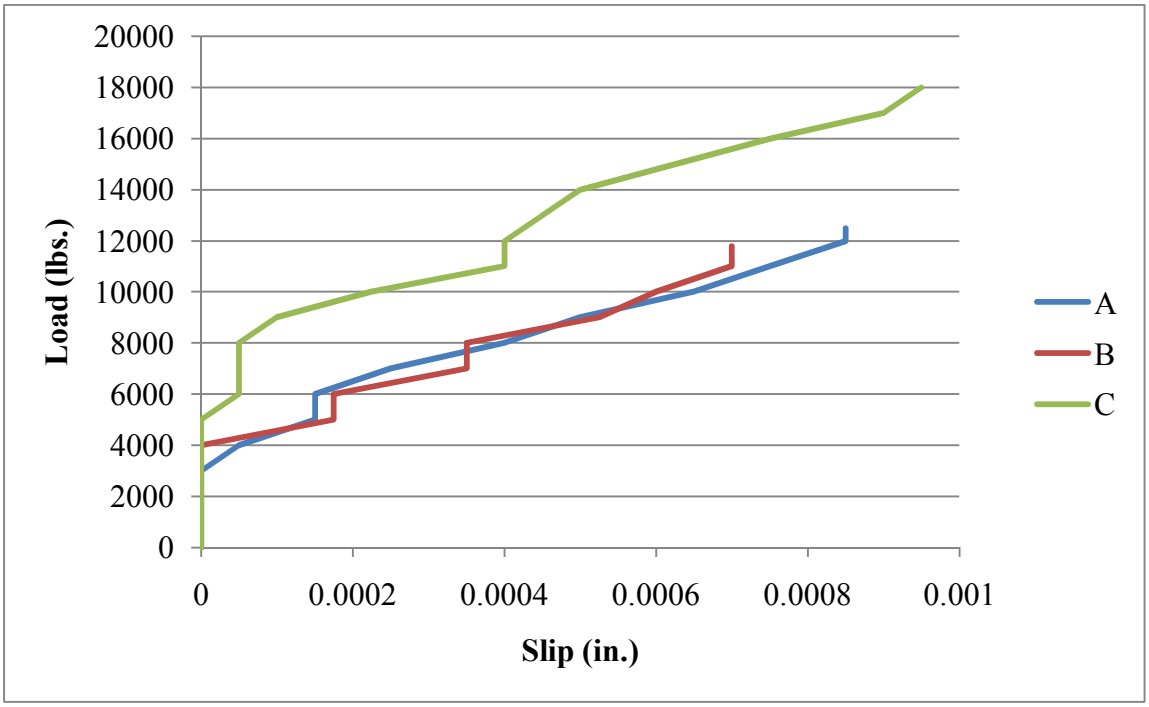

Figure A-15: Load-slip curves for U-H-S-0 specimens

Figure A-16: U-H-S-0-A after failure.


Figure A-17: Smooth UHPC surface of specimen U-H-S-0-A after interface failure.

Figure A-18: U-H-S-0-B after failure.

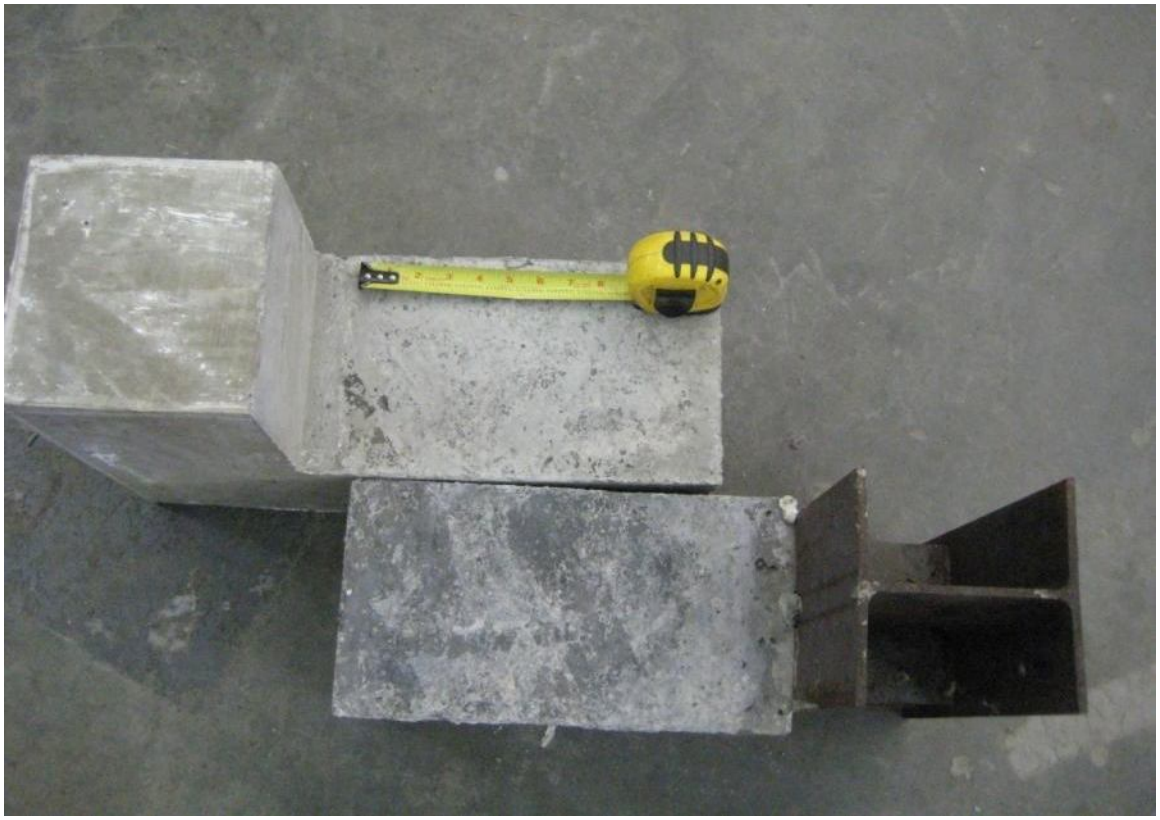
Figure A-19: Interface surfaces of specimen U-H-S-0-B.

Figure A-20: U-H-S-0-C after failure.


Figure A-21: UHPC failure surface of specimen U-H-S-0-C. Minor cracking of the surface UHPC can be seen at the left.

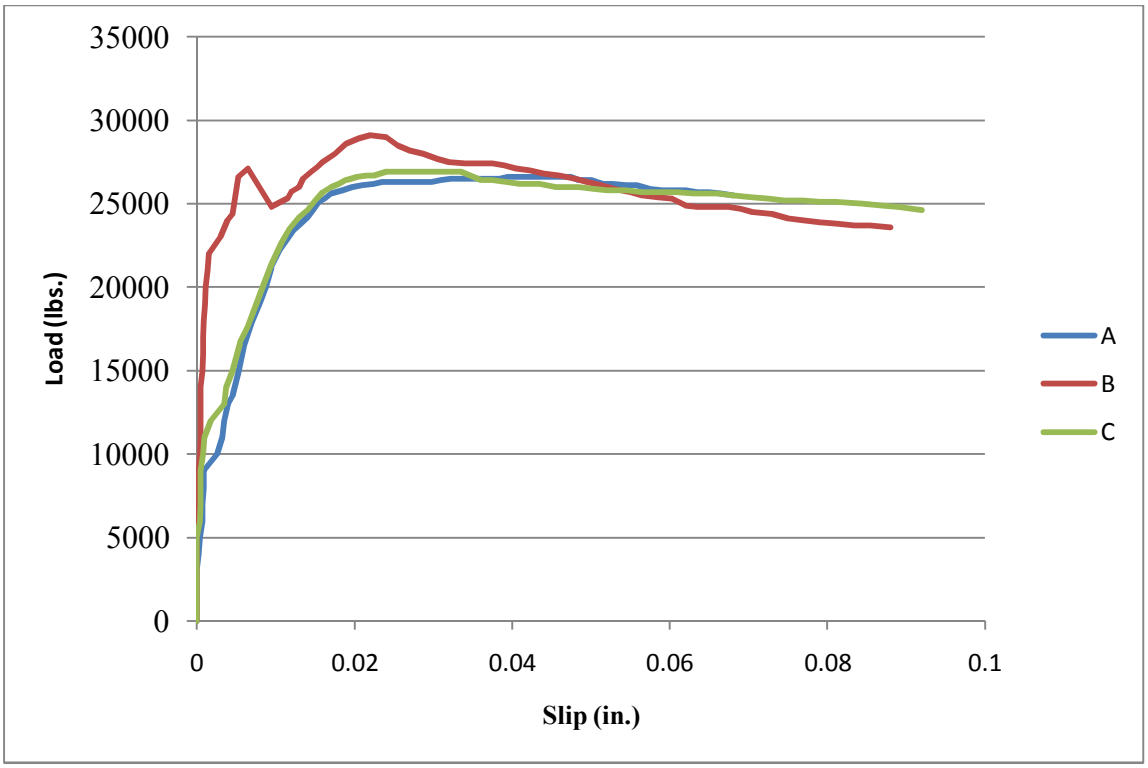

Figure A-22: Load-slip curves for U-H-S-1 specimens

Figure A-23: U-H-S-1-A after failure.

Figure A-24: Close-up of interface crack in specimen U-H-S-1-A.

Figure A-25: U-H-S-1-B after failure.

Figure A-26: Interface crack in specimen U-H-S-1-B.

Figure A-27: U-H-S-1-C after failure.

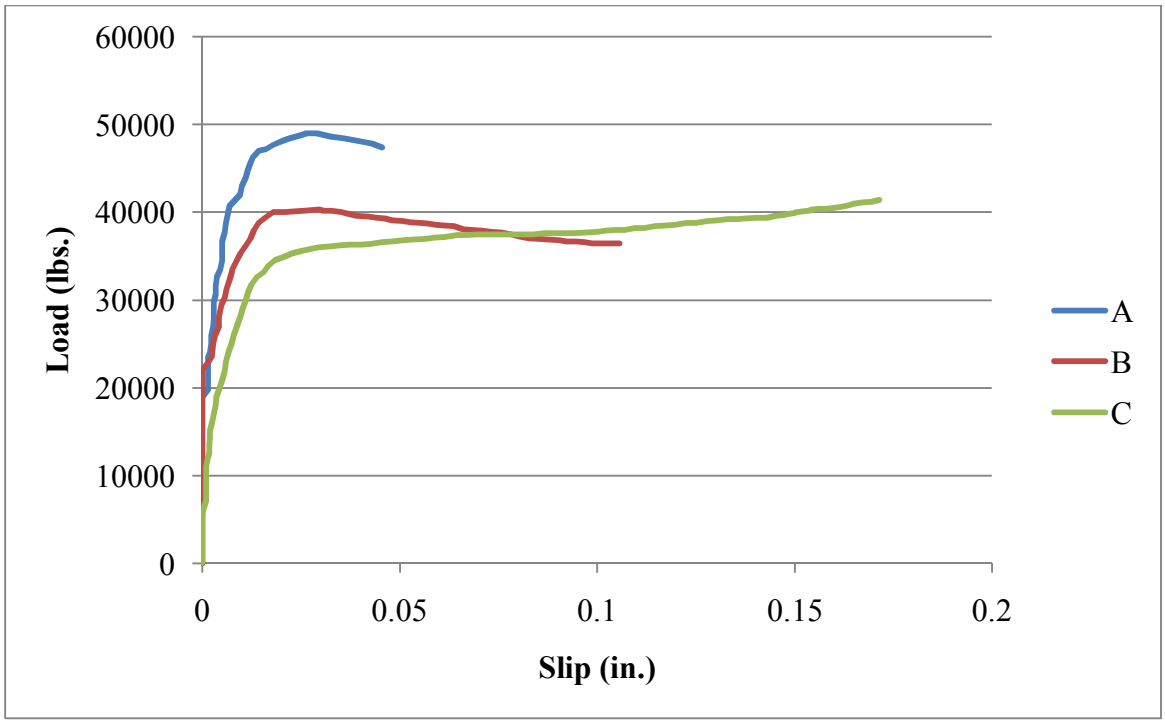

Figure A-28: Load-slip curves for U-H-S-2 specimens

Figure A-29: U-H-S-2-A after failure.

Figure A-30: Interface crack in specimen U-H-S-2-A.

Figure A-31: Spalling of HPC over rebar locations in specimen U-H-S-2-A.

Figure A-32: U-H-S-2-B after failure.


Figure A-33: Spalling of HPC over rebar locations in specimen U-H-S-2-B.

Figure A-34: Interface surfaces of specimen U-H-S-2-B after failure.

Figure A-35: U-H-S-2-C after failure.

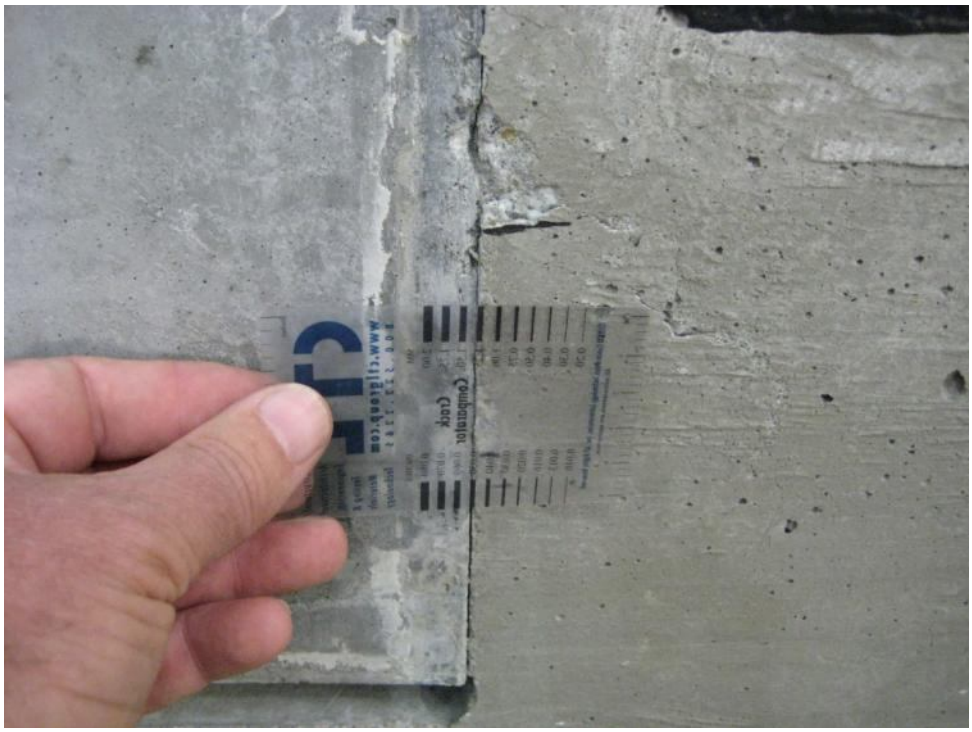

Figure A-36: Interface crack in specimen U-H-S-2-C.

Figure A-37: Spalling of HPC over stirrup in specimen U-H-S-2-C.

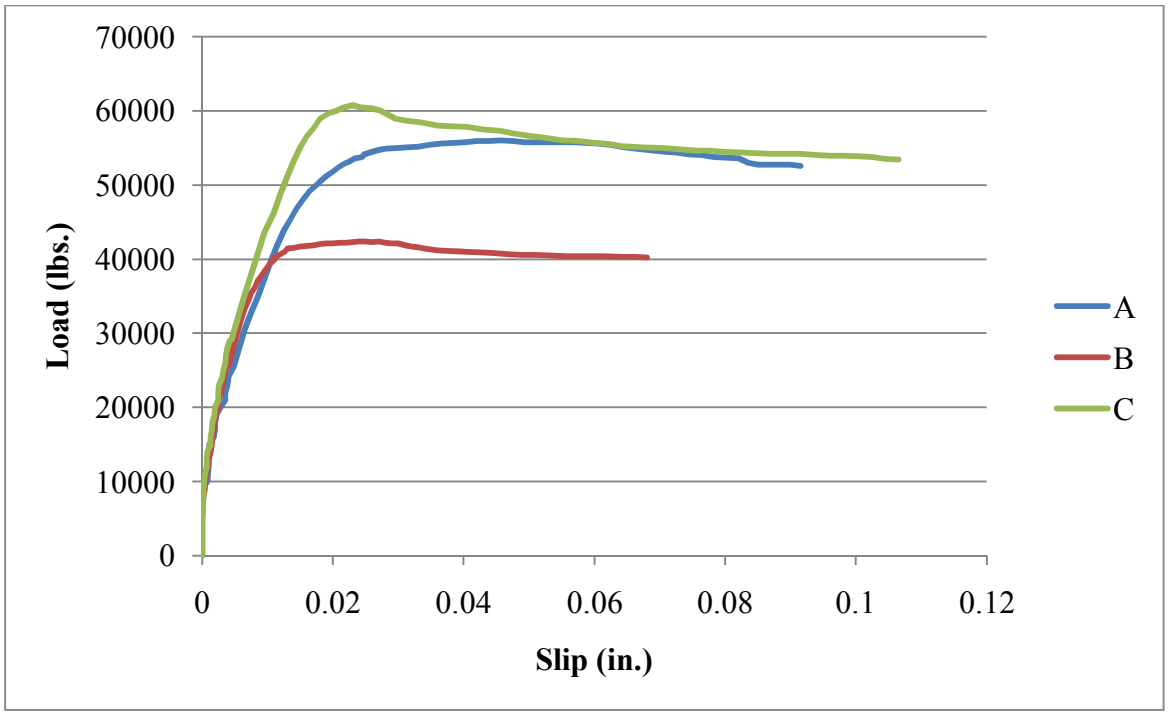

Figure A-38: Load-slip curves for U-H-S-3 specimens

Figure A-39: U-H-S-3-A after failure.

Figure A-40: Interface crack in specimen U-H-S-3-A.

Figure A-41: U-H-S-3-B after failure.

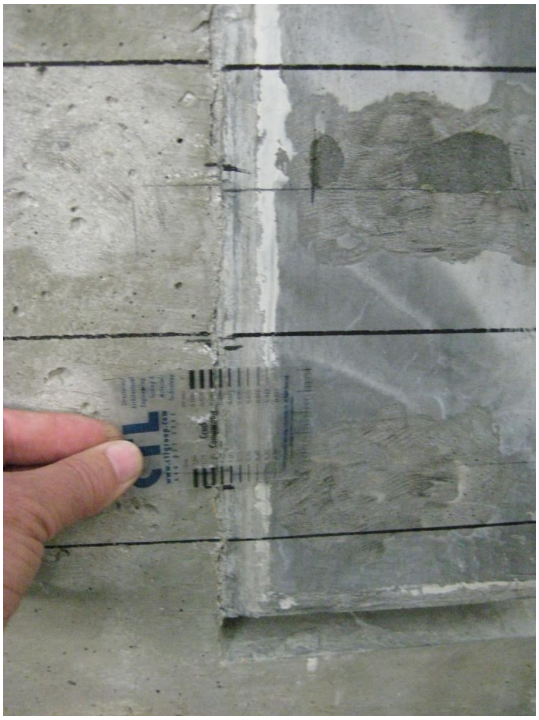

Figure A-42: Interface crack in specimen U-H-S-3-B.

Figure A-43: U-H-S-3-C after failure.

Figure A-44: Interface crack in specimen U-H-S-3-C.

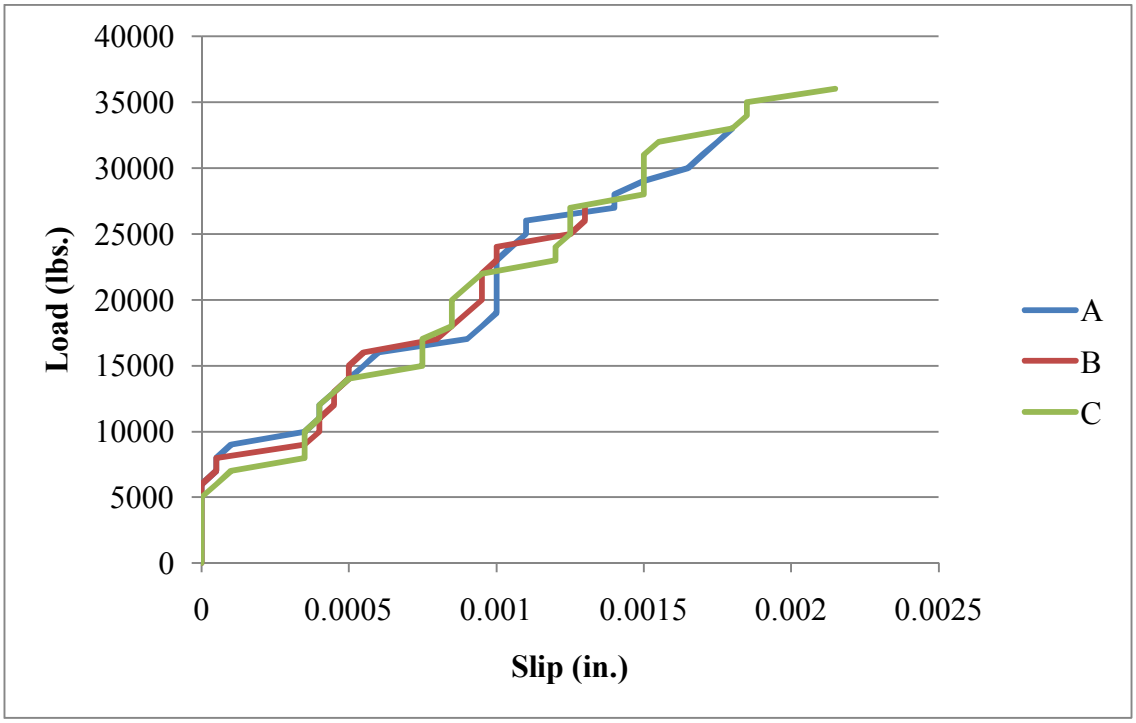

Figure A-45: Load-slip curves for U-H-B-0 specimens

Figure A-46: U-H-B-0-A after failure.


Figure A-47: Interface surfaces of specimen U-H-B-0-A.

Figure A-48: U-H-B-0-B after failure.


Figure A-49: Interface surfaces of specimen U-H-B-0-B.

Figure A-50: U-H-B-0-C after failure.


Figure A-51: Interface surfaces of specimen U-H-B-0-C.

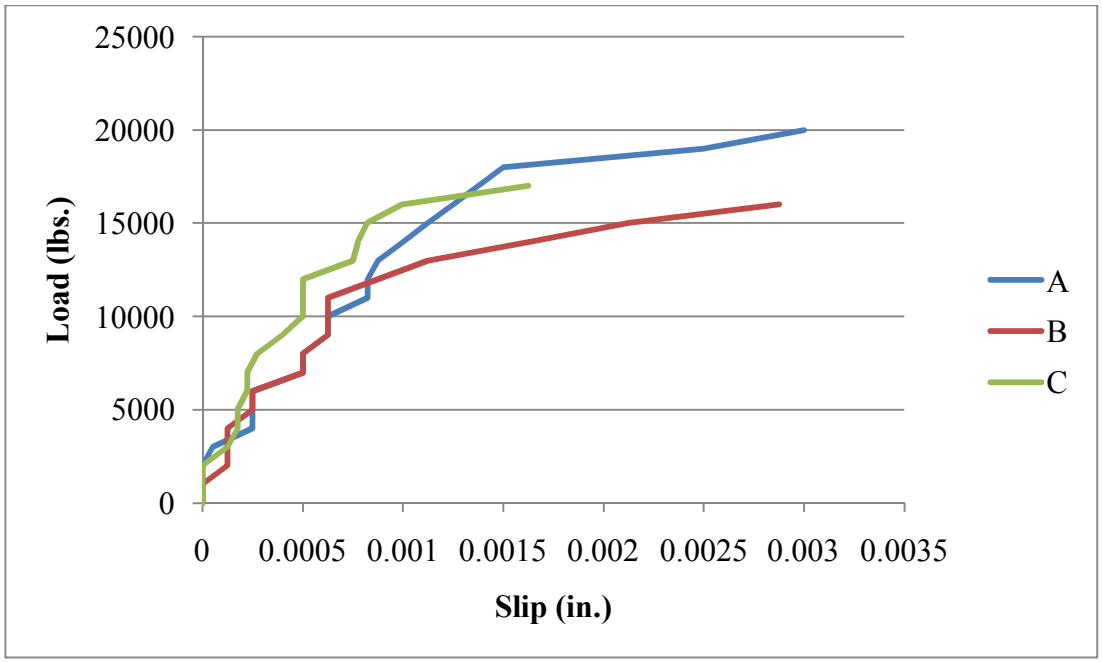

Figure A-52: Load-slip curves for U-U-S-0 specimens

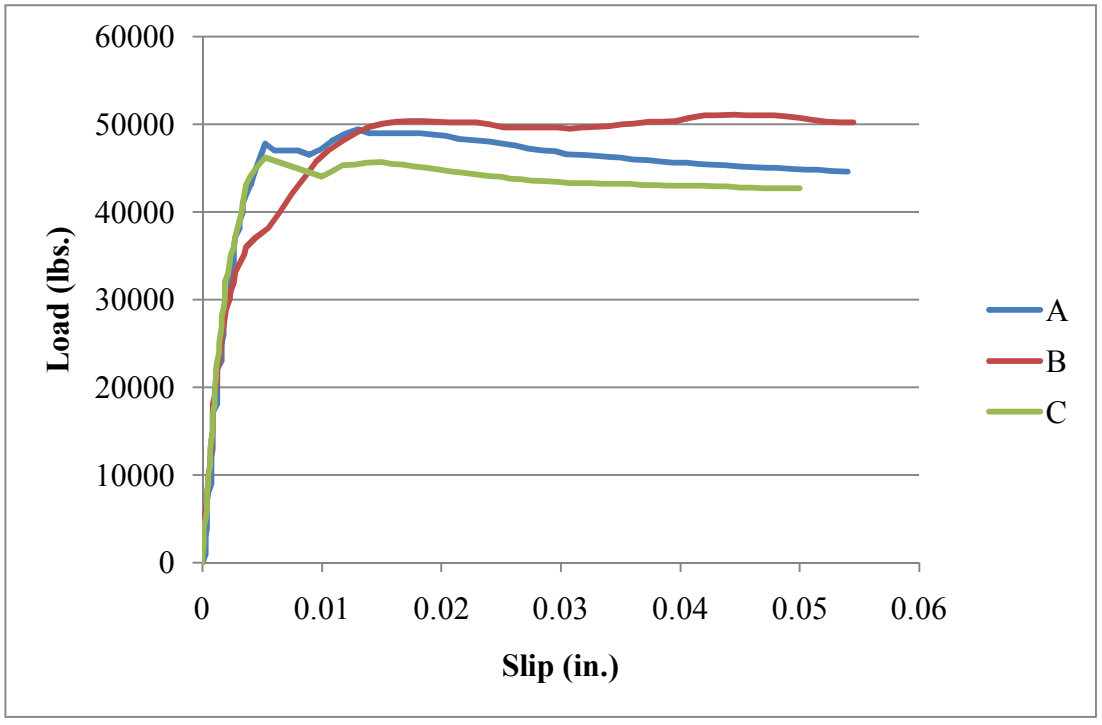

Figure A-53: Load-slip curves for U-U-S-2 specimens

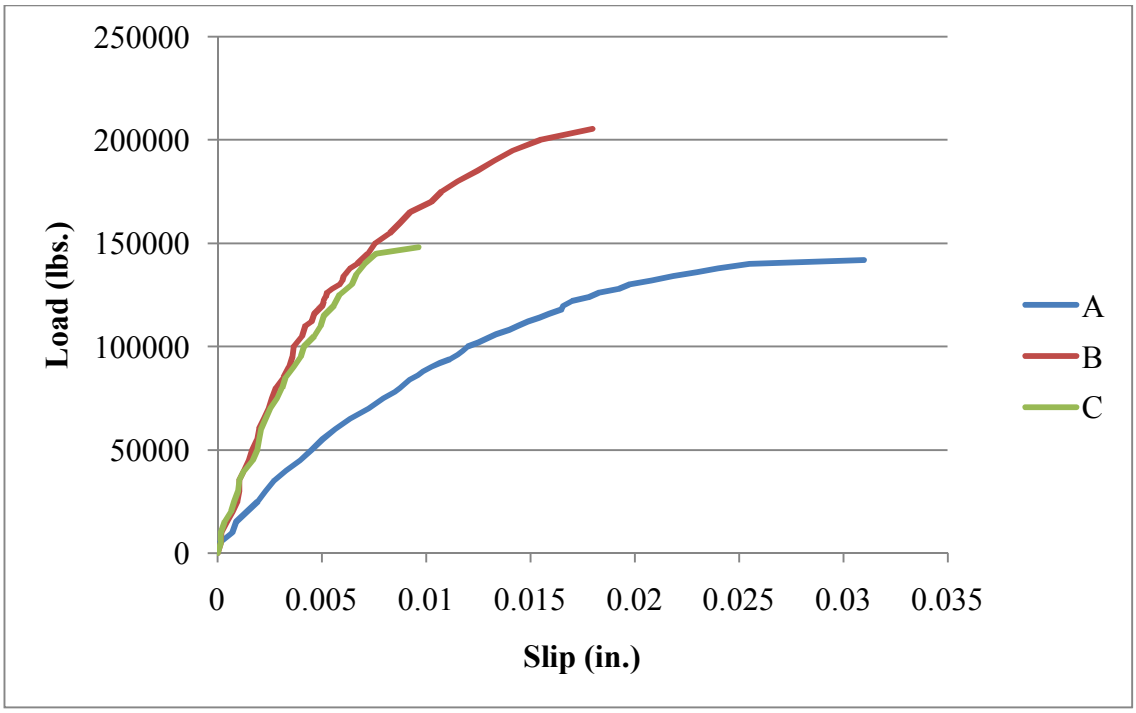

Figure A-54: Load-slip curves for U-U-MC-0 specimens

Figure A-55: U-U-MC-0-A after failure.

Figure A-56: Failure crack in specimen U-U-MC-0-A.

Figure A-57: U-U-MC-0-B after failure.

Figure A-58: Failure crack in specimen U-U-MC-0-B.

Figure A-59: U-U-MC-0-C after failure.

Figure A-60: Failure crack in specimen U-U-MC-0-C.

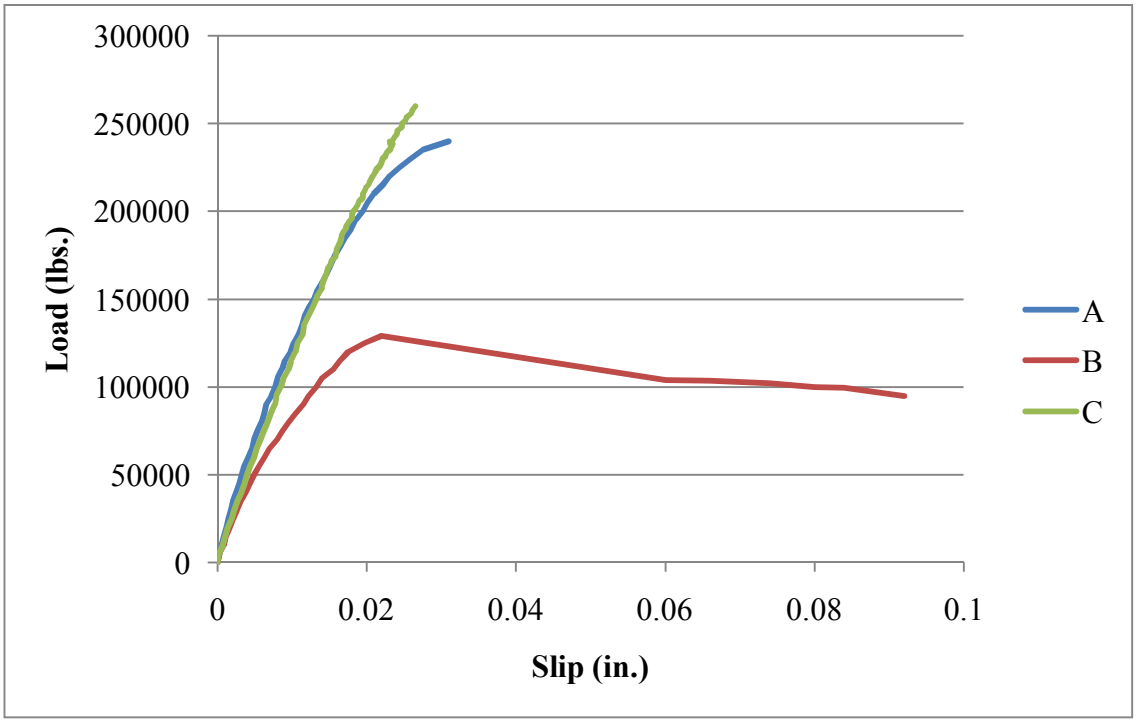

Figure A-61: Load-slip curves for U-U-MC-2 specimens

Figure A-62: U-U-MC-2-A after failure.


Figure A-63: Interface crack slip in specimen U-U-MC-2-A

Figure A-64: U-U-MC-2-B after failure.

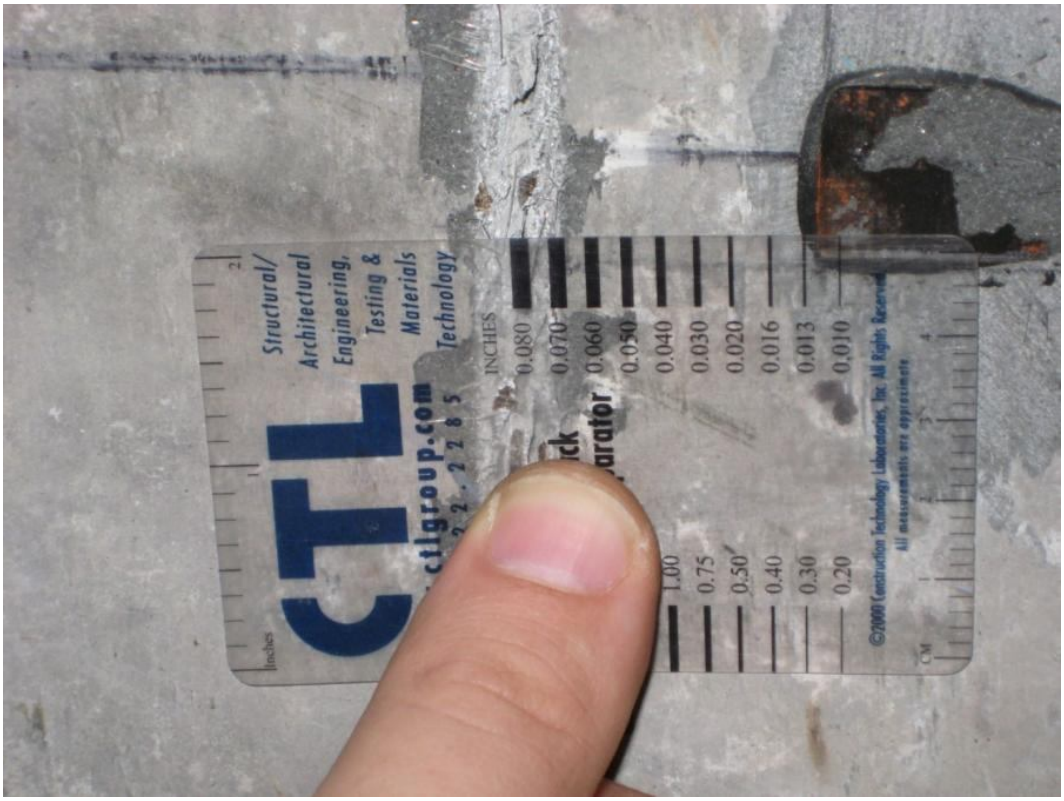

Figure A-65: Slip along pre-induced crack in specimen U-U-MC-2-B

Figure A-66: U-U-MC-2-C after failure.


Figure A-67: Separation across pre-existing interface crack in specimen U-U-MC-2-C.

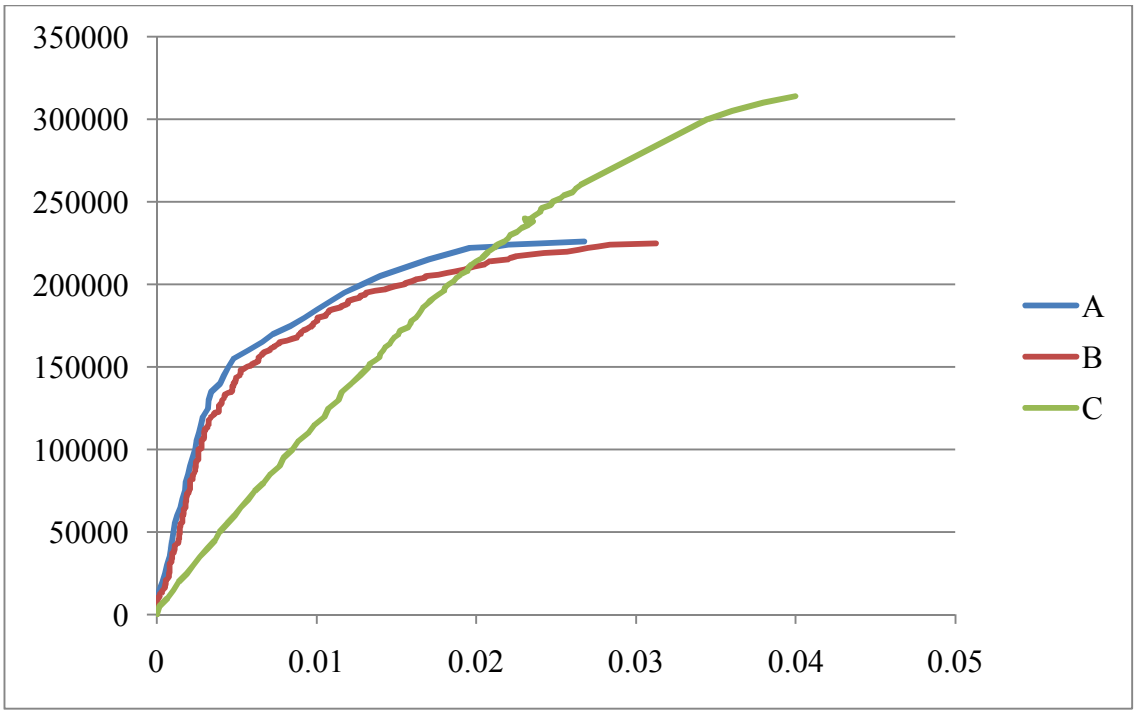

Figure A-68: Load-slip curves for U-U-MU-0 specimens. Specimen C had to be loaded twice.

Figure A-69: U-U-UC-0-A after failure.

Figure A-70: Reverse side of U-U-UC-0-A after failure.

Figure A-71: Halves of specimen U-U-UC-0-A.

Figure A-72: Close-up of failure surface of specimen U-U-UC-0-A.

Figure A-73: U-U-UC-0-B after failure.

Figure A-74: Reverse side of specimen U-U-UC-0-B after failure.

Figure A-75: Halves of specimen U-U-UC-0-B. Note failure along rebar interface.

Figure A-76: U-U-UC-0-C after failure.


Figure A-77: Reverse side of specimen U-U-UC-0-C after failure. Note two failure cracks.

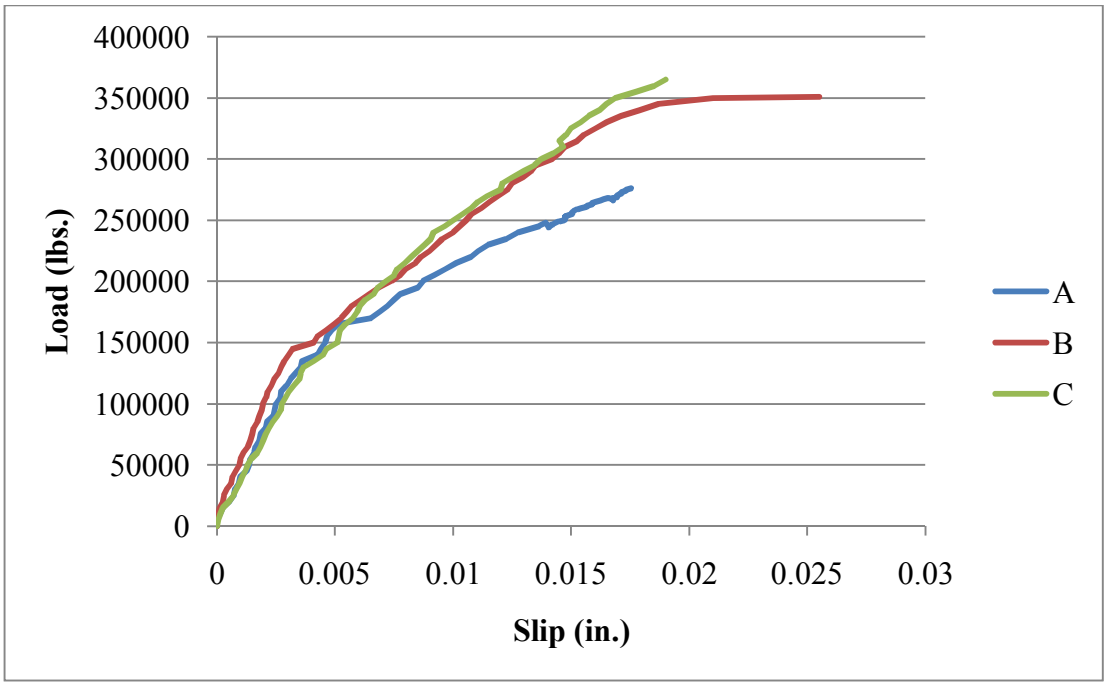

Figure A-78: Load-slip curves for U-U-MU-2 specimens.

Figure A-79: U-U-UC-2-A after failure.

Figure A-80: Reverse side of specimen U-U-UC-2-A after failure.

Figure A-81: Close-up of failure surface of specimen U-U-UC-2-A.

Figure A-82: U-U-UC-2-B after failure.


Figure A-83: Failure surfaces of specimen U-U-UC-2-B.

Figure A-84: U-U-UC-2-C after failure.


Figure A-85: Separation of steel wide flange from specimen U-U-UC-2-C. Note weld failures.

APPENDIX B
SHEAR ROSETTE STRAINS

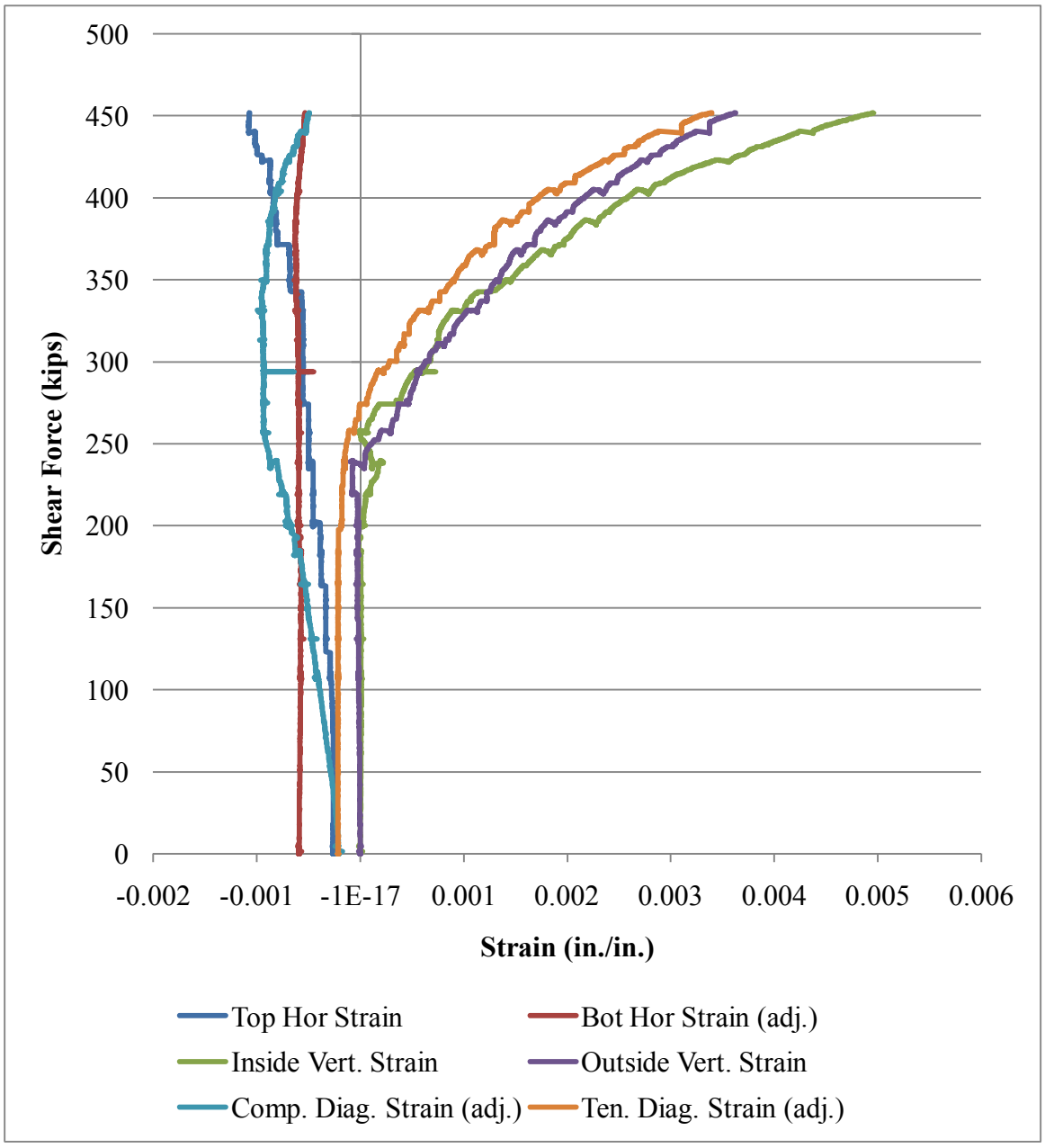

Figure B-1: Shear test 1-1a rosette strains.

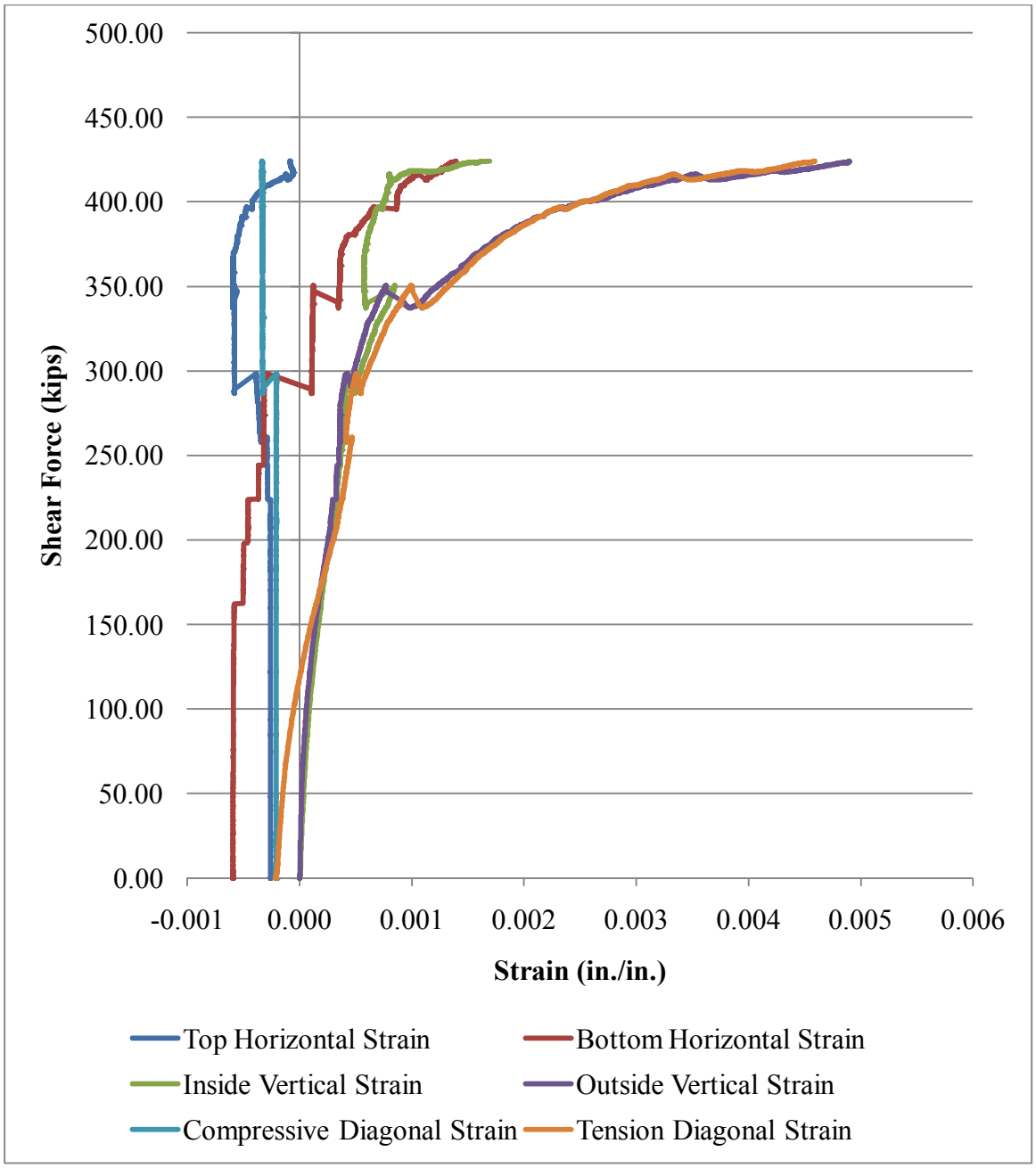

Figure B-2: Shear test 1-2 rosette strains.

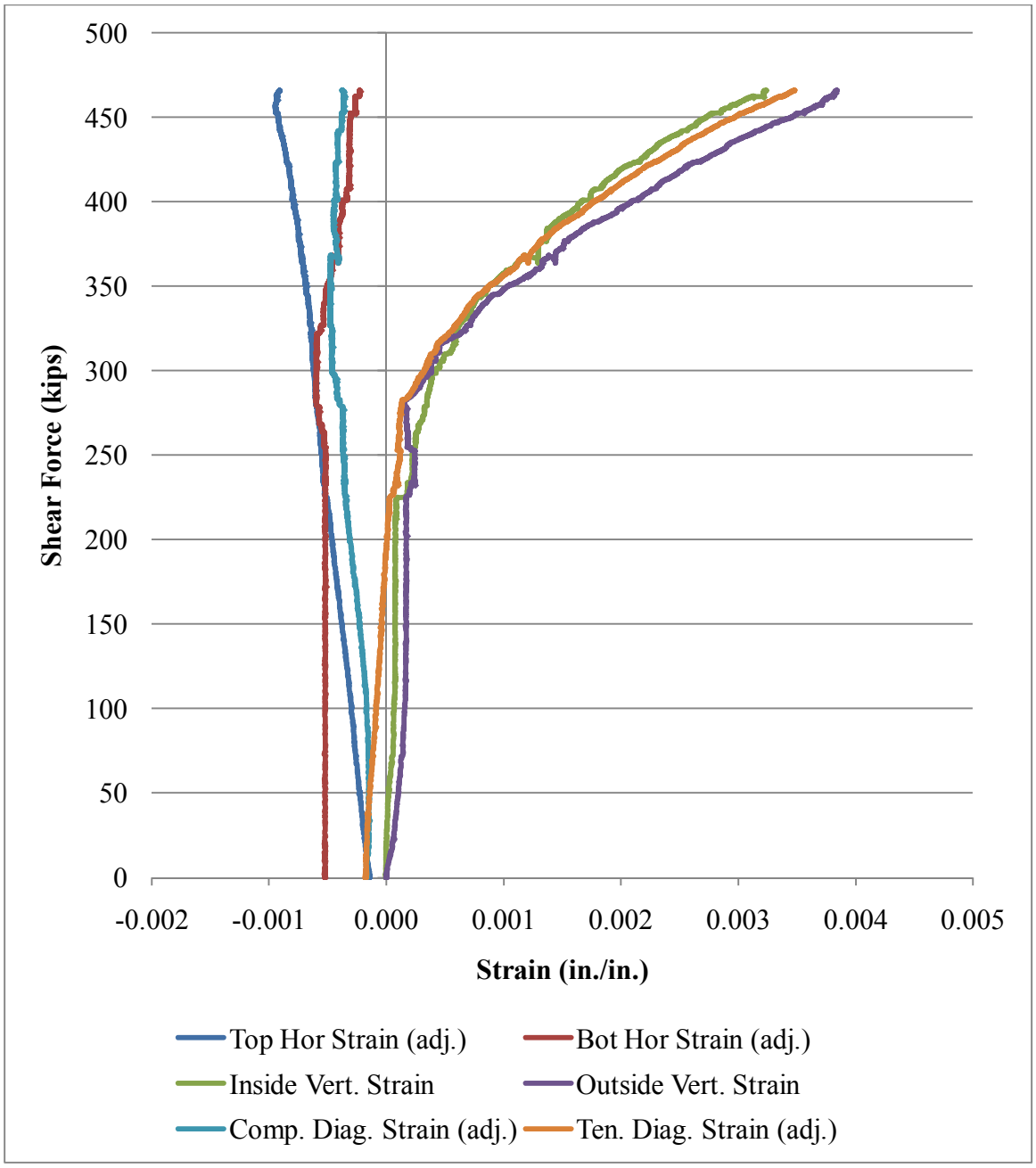

Figure B-3: Shear test 2-1 rosette strains.

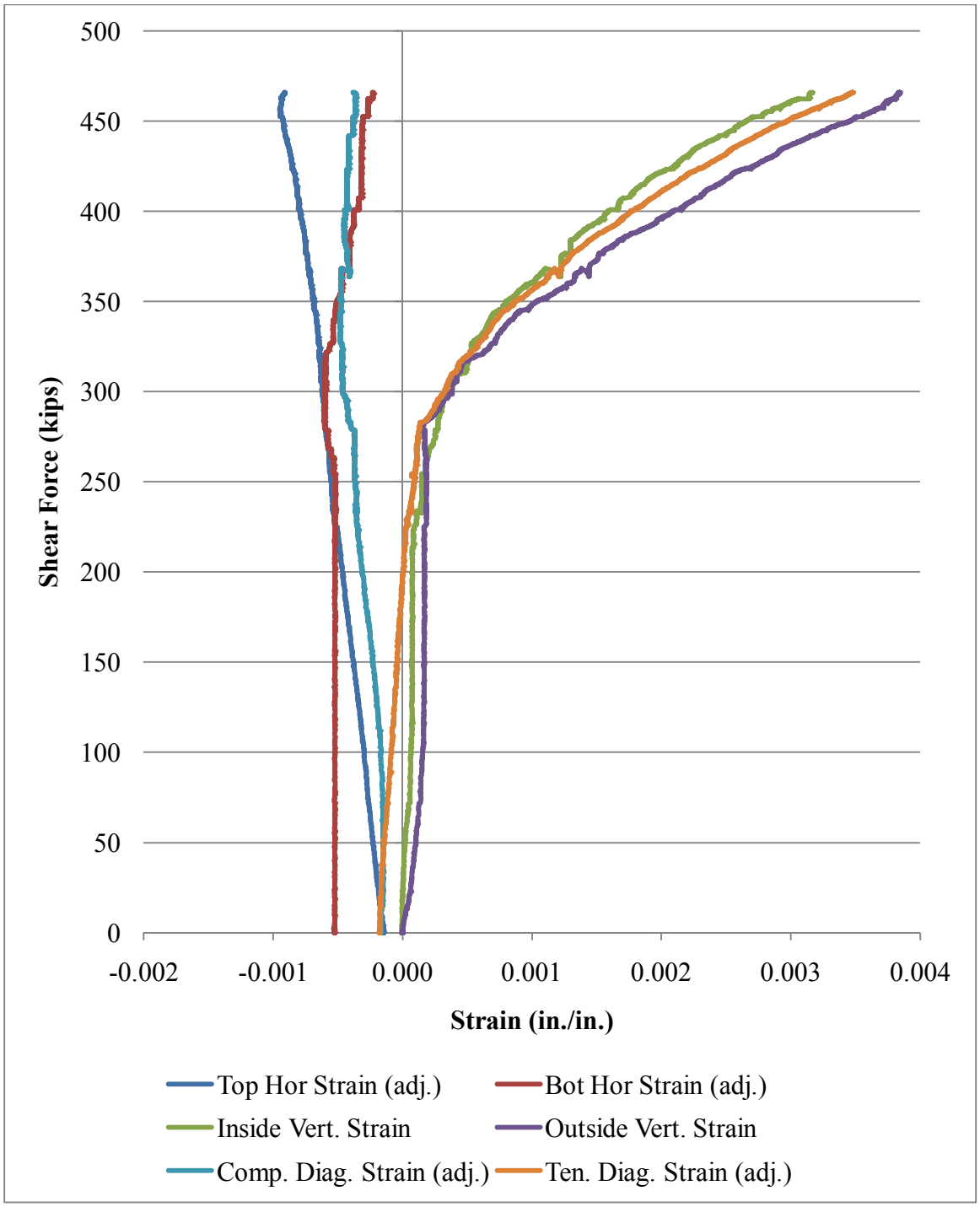

Figure B-4: Shear test 2-1 adjusted rosette strains.

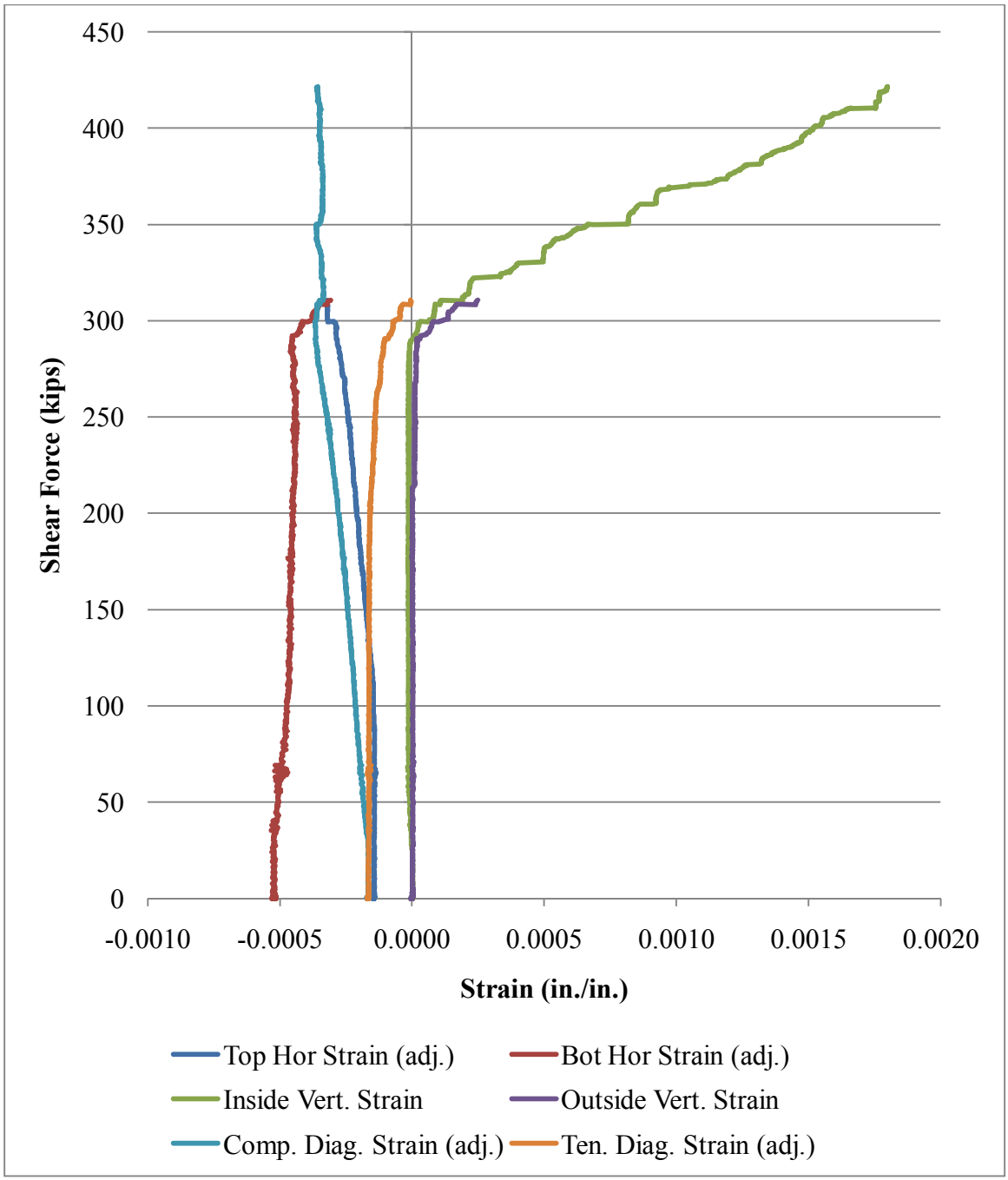

Figure B-5: Shear test 2-2 rosette strains.

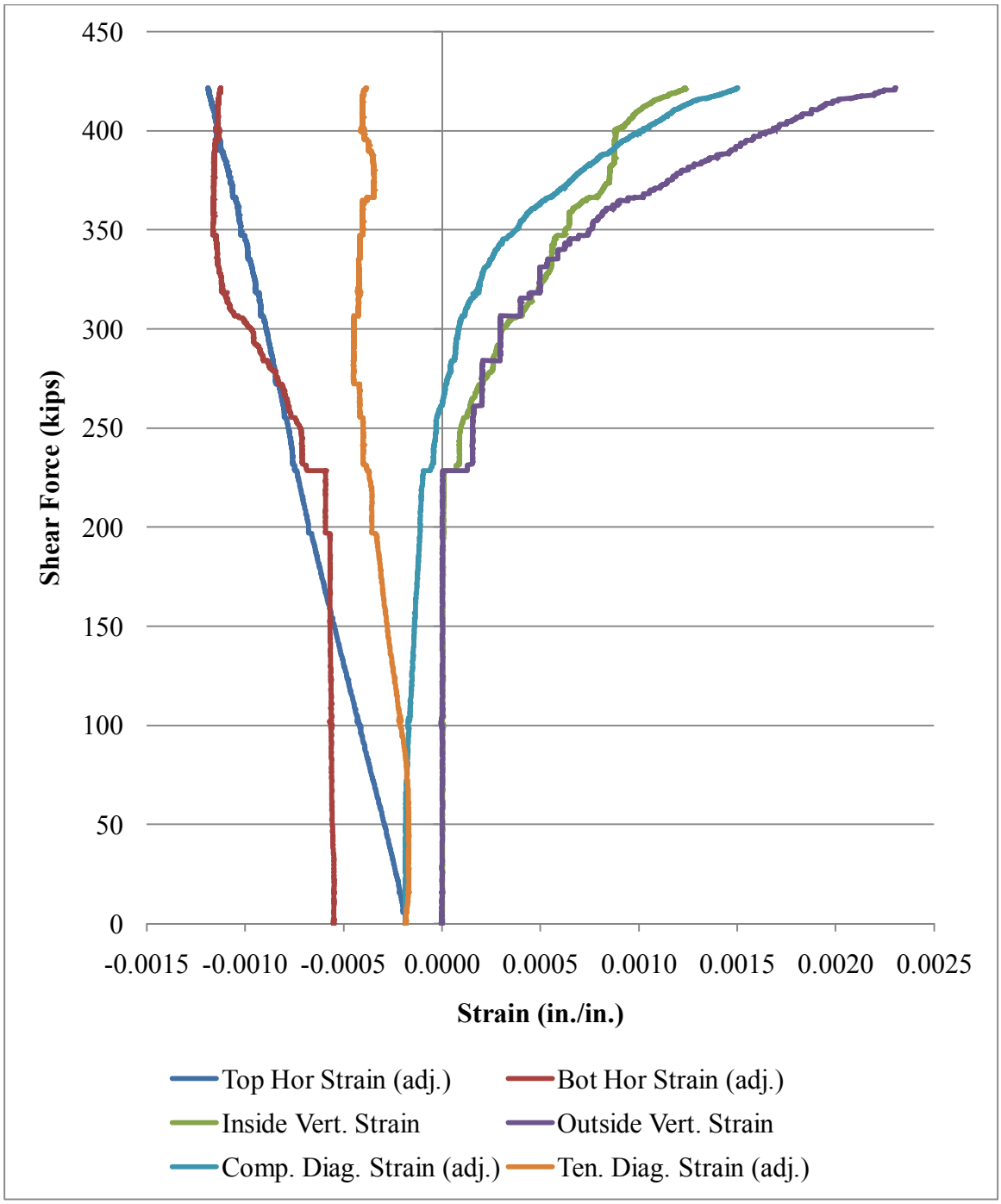

Figure B-6: Shear test 3-1 rosette strains.

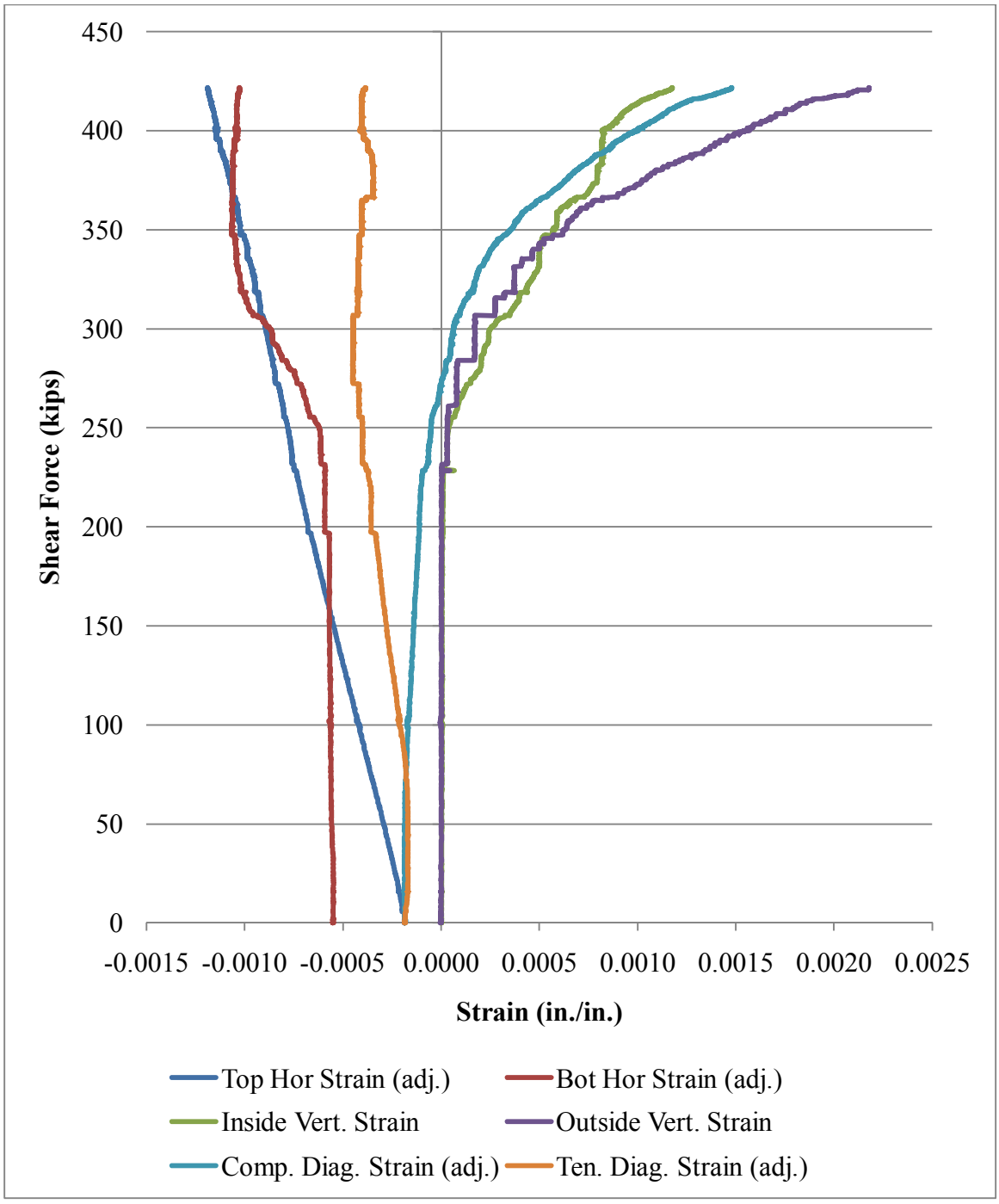

Figure B-7: Shear test 3-1 adjusted rosette strains.

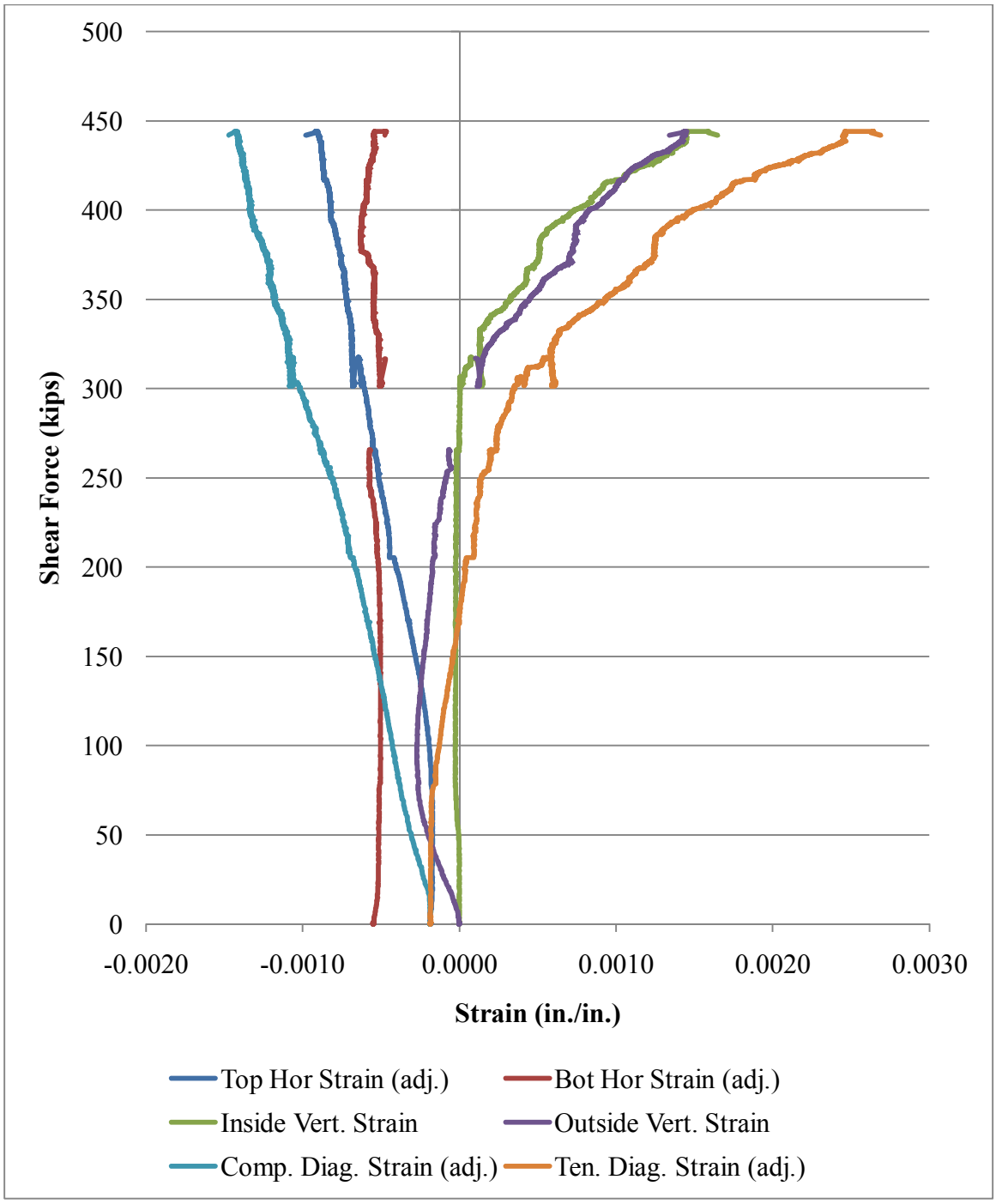

Figure B-8: Shear test 3-2 rosette strains.

APPENDIX C
SMALL COMPOSITE BEAM DATA

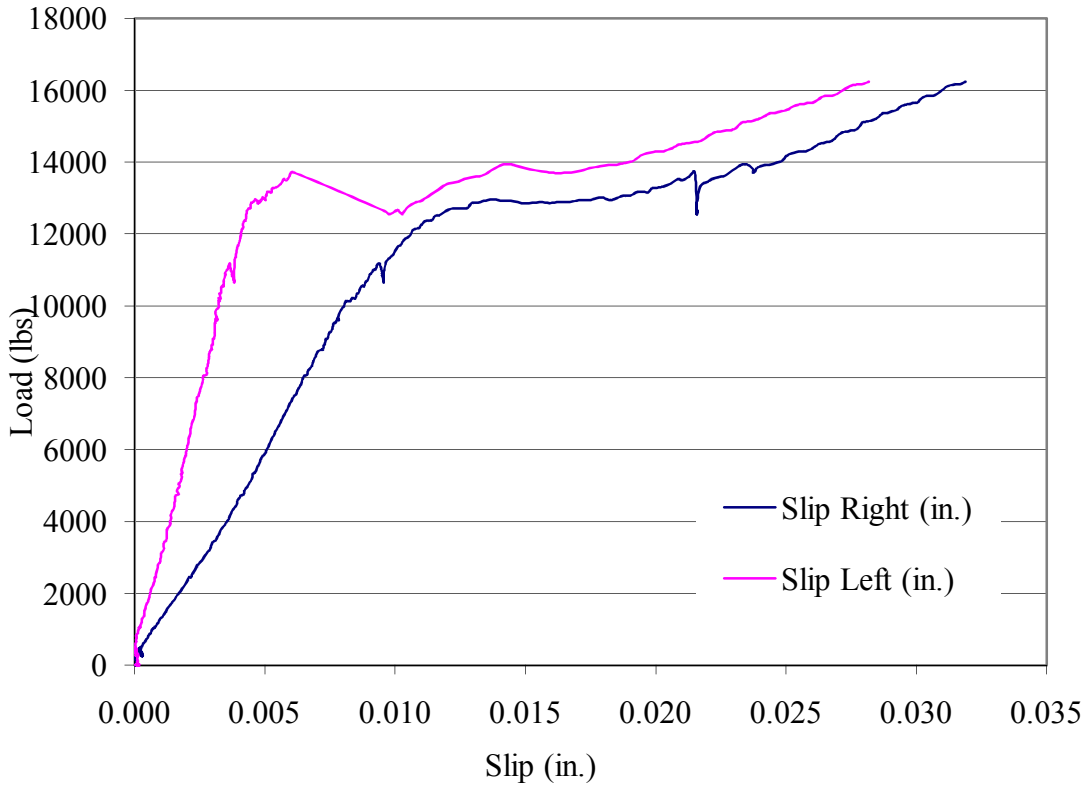

Figure C-1: Load-slip curves for left and right sides of beam 0-B.

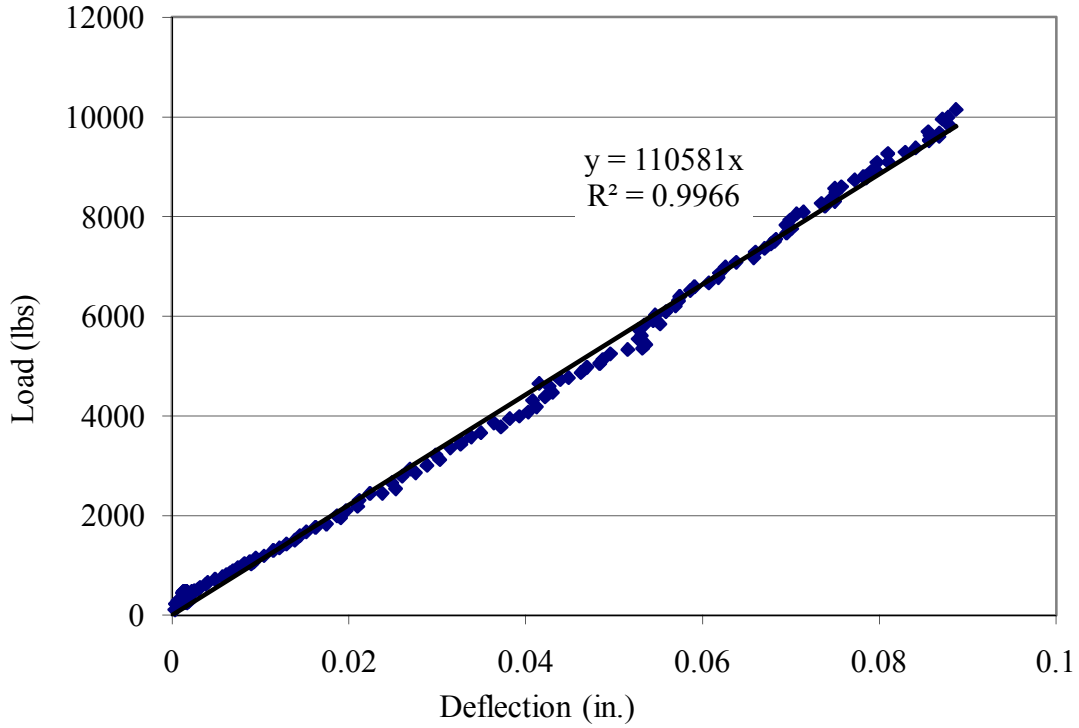

Figure C-2: Linear curve fit of initial portion of load-deflection curve for beam 0-B.

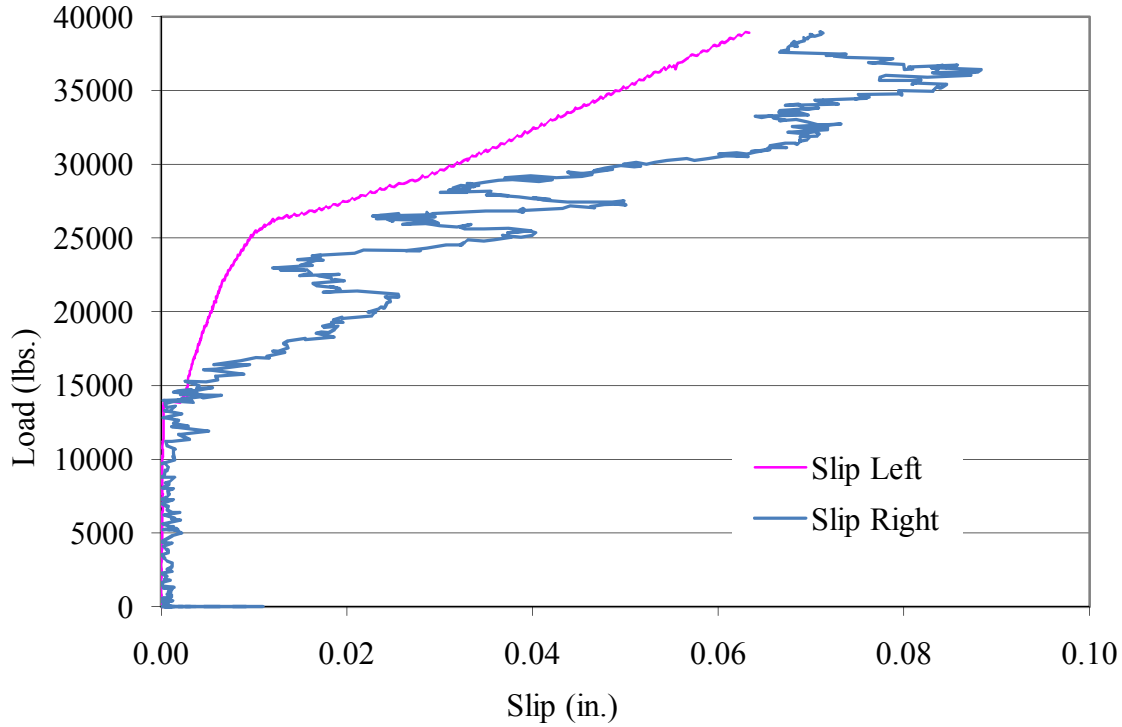

Figure C-3: Load-slip curves for left and right sides of beam 4-S. Right slip gauge experienced very high amounts of noise.

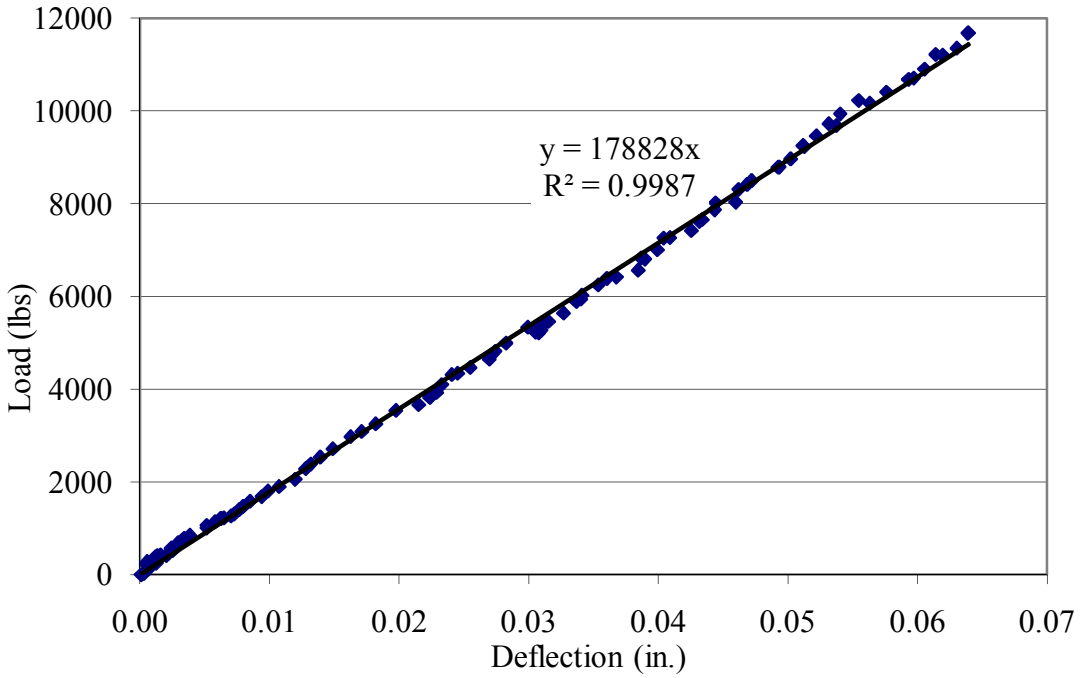

Figure C-4: Linear curve fit of initial portion of load-deflection curve for beam 4-S.

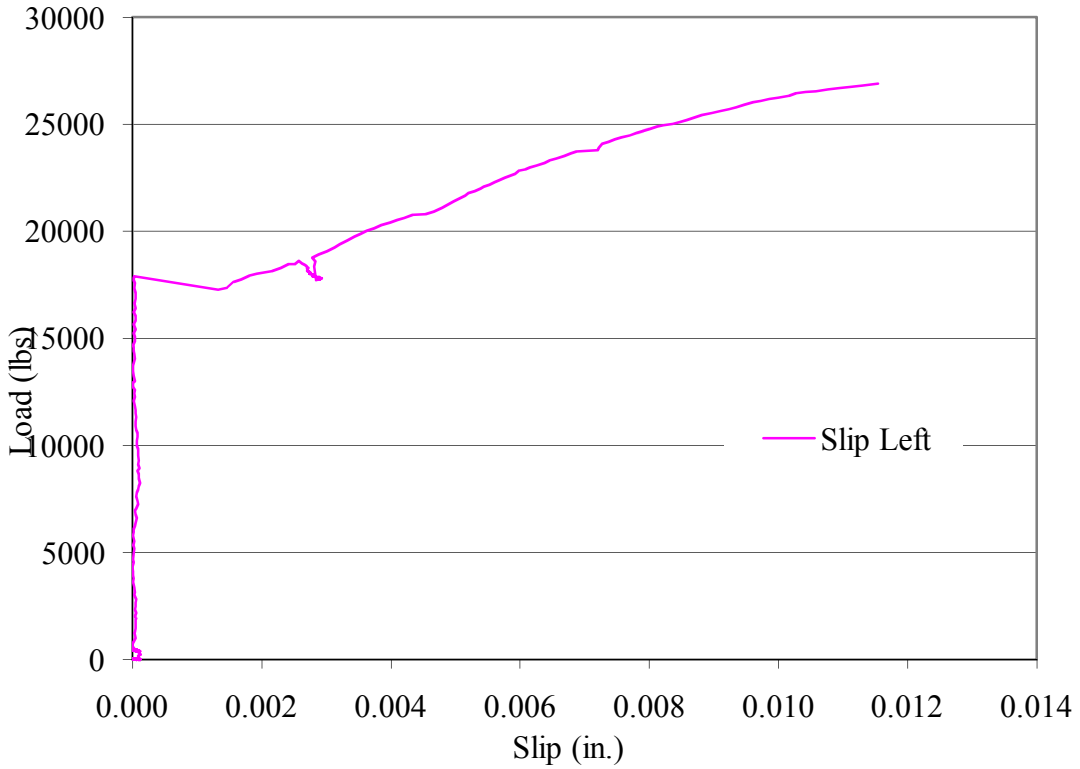

Figure C-5: Load-slip curves for left side of beam 7-S. Right slip gauge data was not useable.

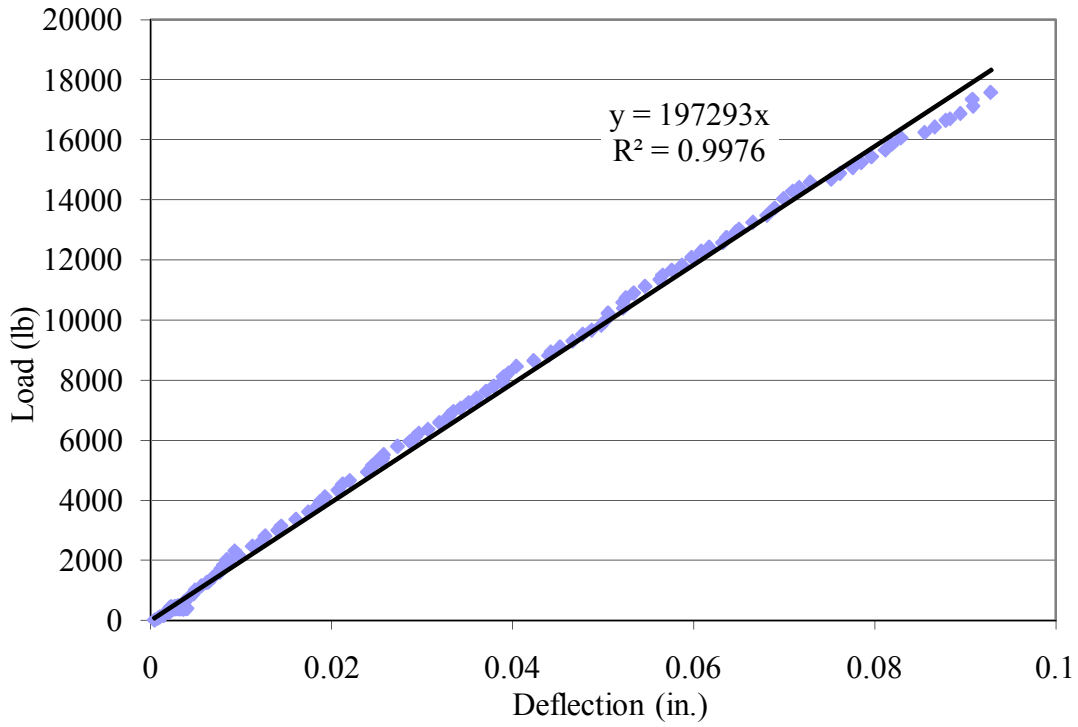

Figure C-6: Linear curve fit of initial portion of load-deflection curve for beam 7-S.

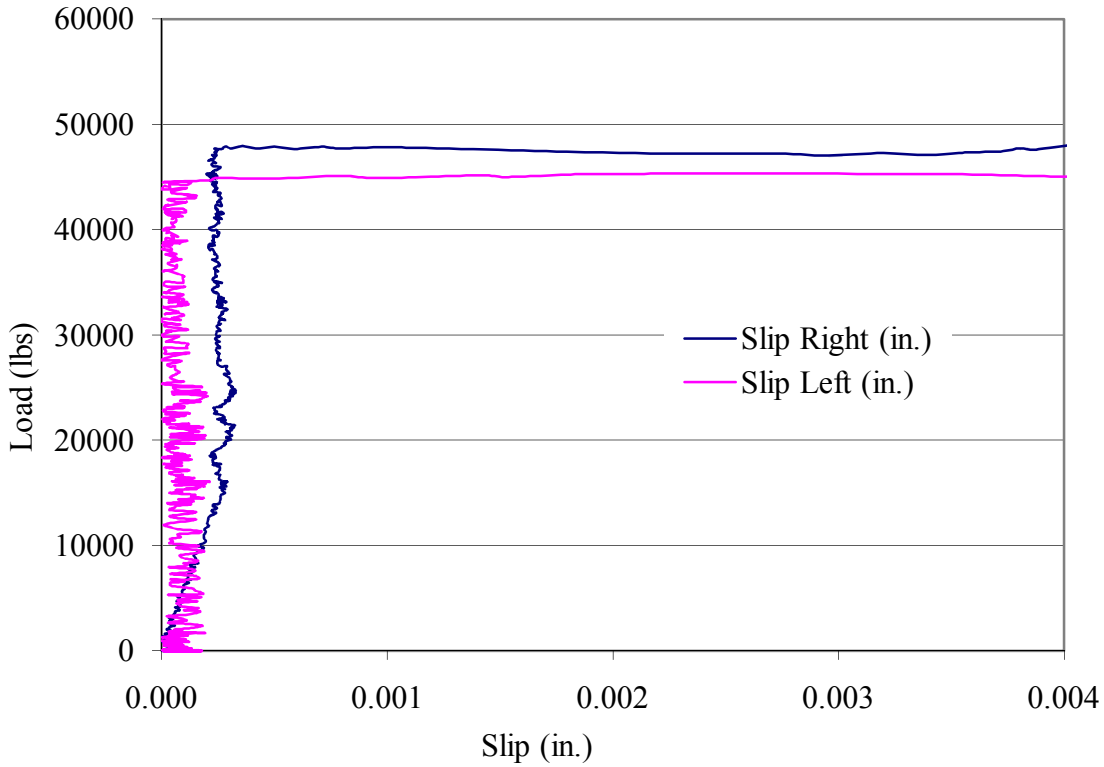

Figure C-7: Load-slip curves for left and right sides of beam 0-FL

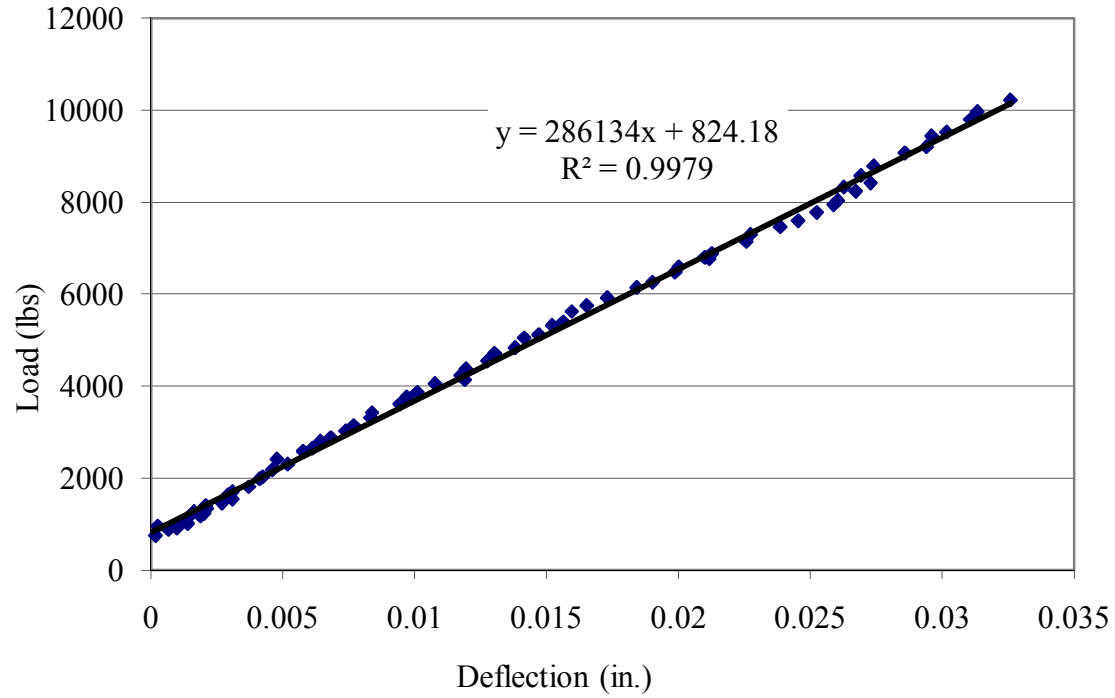

Figure C-8: Linear curve fit of initial portion of load-deflection curve for beam 0-FL.

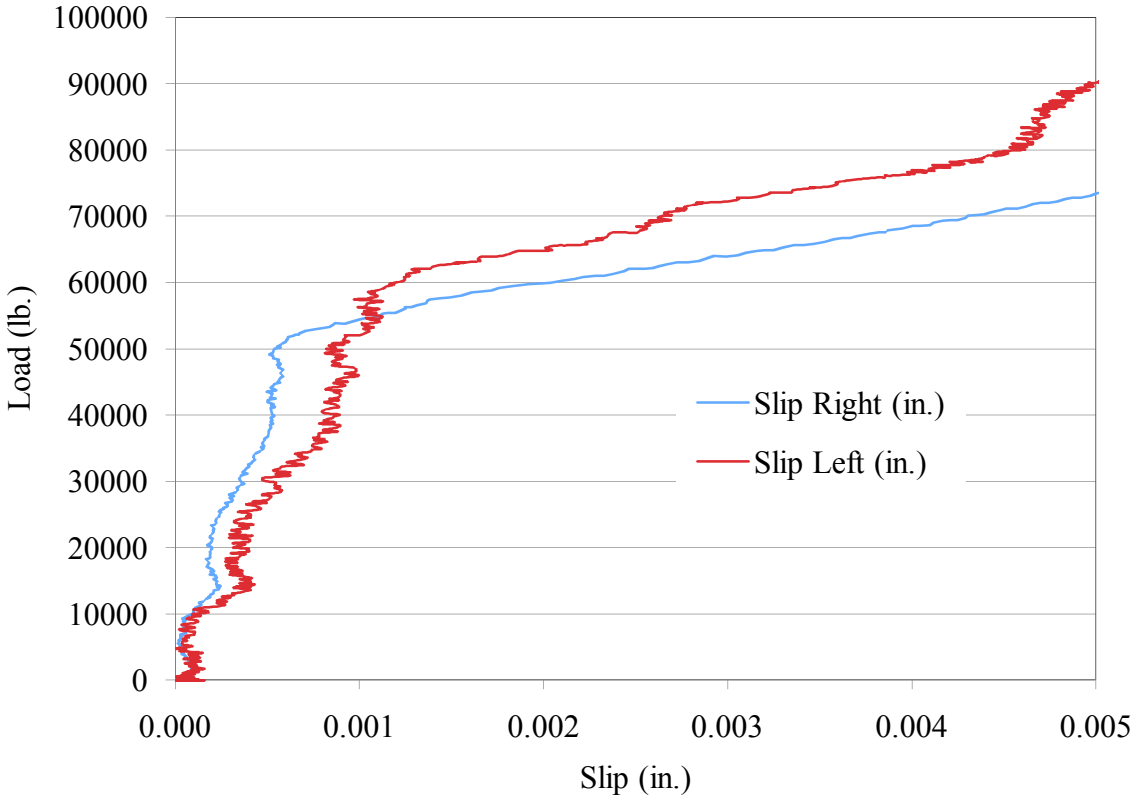

Figure C-9: Load-slip curves for left and right sides of beam 7-FL.

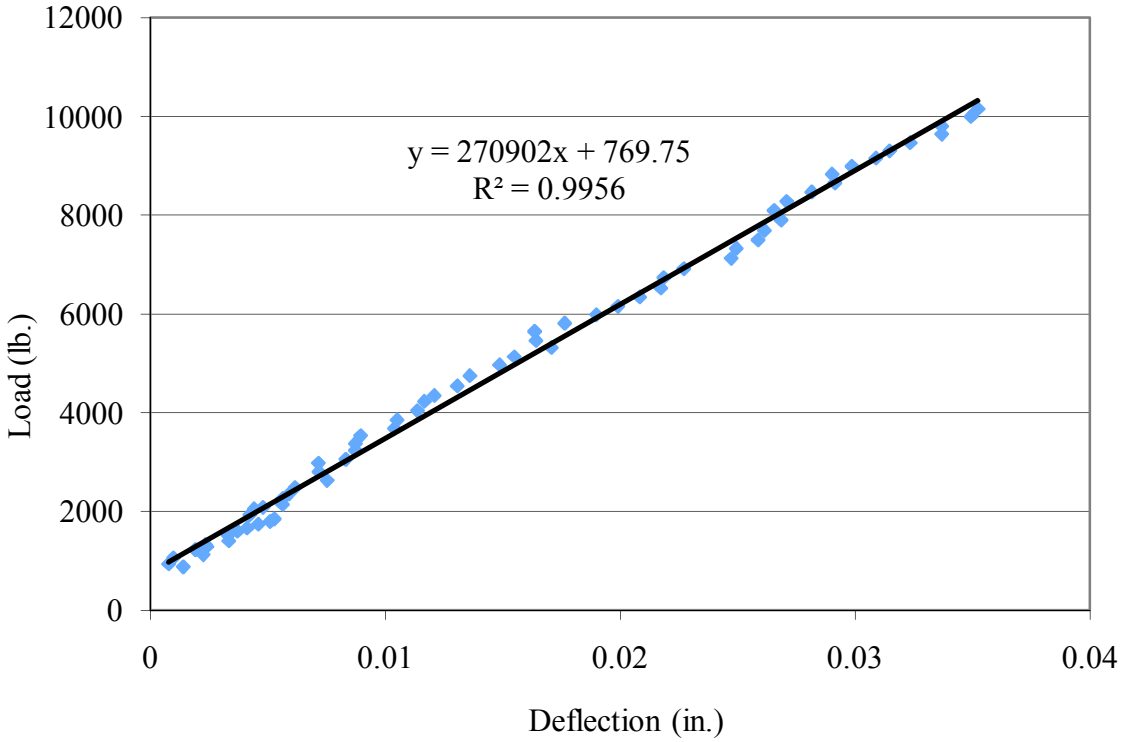

Figure C-10: Linear curve fit of initial portion of load-deflection curve for beam 7-FL.

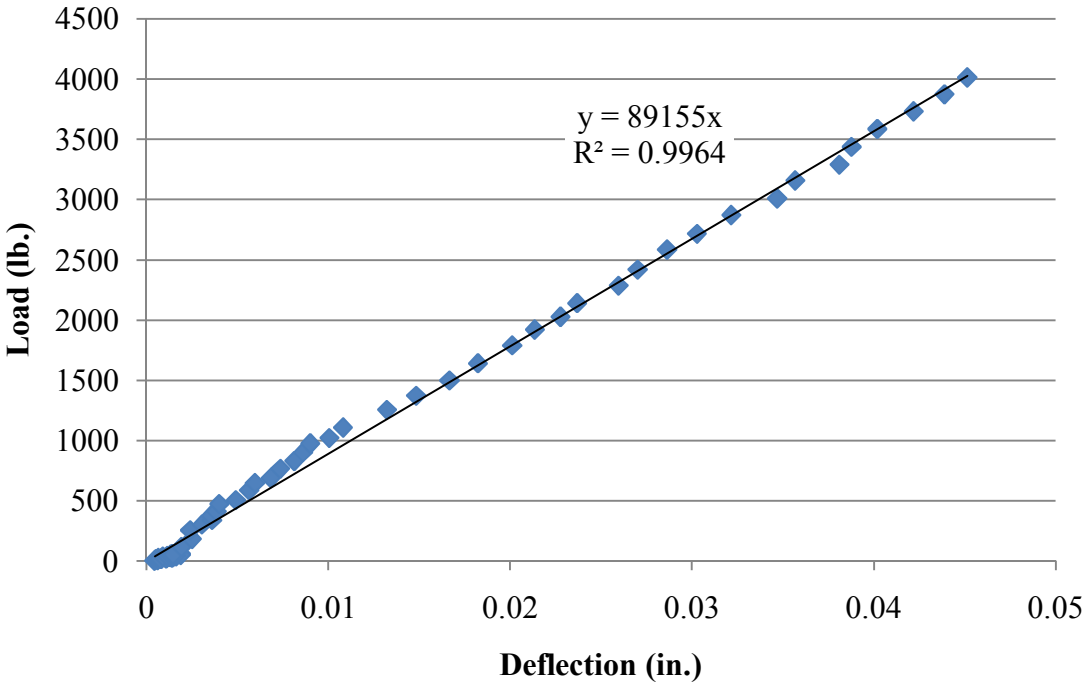

Figure C-11: Linear curve fit of initial portion of load-deflection curve for plain beam.

APPENDIX D
FULL-SCALE COMPOSITE PRESTRESSED UHPC GIRDER DATA

D.1 Instrumentation of Full-Scale Composite UHPC Bridge Girders

Several different types of instrumentation were used to capture different behaviors prior to and during testing of the full-scale UHPC girders. This section provides an explanation of why each type of gauge was chosen and details of their usage.

D.1.1 Embedded Gauges

In order to capture the early-age strain (elastic deformations after strand cut, as well as time-dependent strains), vibrating wire strain gauges (VWSGs) were embedded in each of the UHPC girders at midspan prior to casting. Thermocouples were also embedded at midspan of girders 1 and 3 in order to measure the internal girder temperatures during curing of the concrete. Figure D-1 shows the locations of each of the embedded gauges. Figure D-2 shows these gauges as placed in the girder prior to casting of the UHPC. Figure D-3 shows a closer view of the embedded thermocouples and Figure D-4 shows the VWSG mounted between the two bottom rows of strands in the UHPC girder prior to casting.

On the exterior of the bottom flange of each girder, gauge points were embedded every 2 in (51mm) for a distance of approximately 2.5 ft (760mm). The distance between these gauge points was measured with a detachable mechanical (DEMEC) gauge. Figure D-5 shows the DEMEC gauge points embedded in the UHPC girder and the DEMEC gauge used to measure the distance between these points.

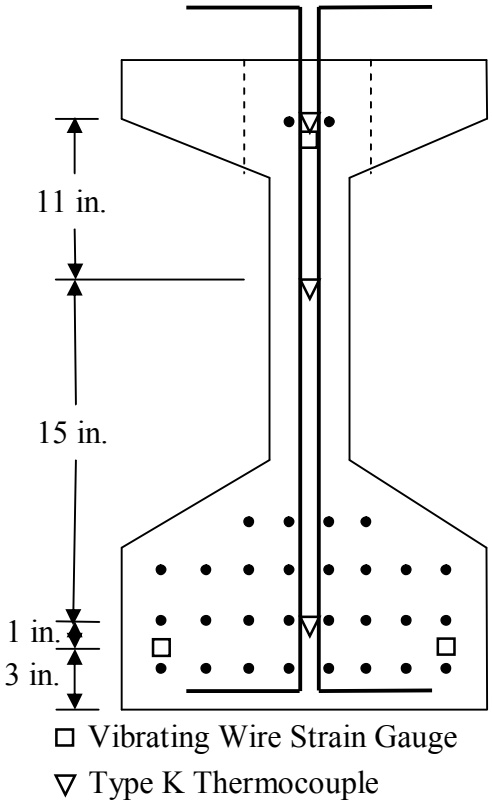

Figure D-1: Internal gauge locations in UHPC girders.

Figure D-2: Placement of internal gauges in UHPC girders.

Figure D-3: Thermocouple placement prior to casting of UHPC girders.

Figure D-4: Close-up of VWSG placement at bottom of UHPC girder.

Figure D-5: DEMEC gauge and gauge points in bottom flange of UHPC girder.

D.1.2 Longitudinal Strain Measurement

In order to capture strain profiles at the location of the maximum moment in the beam, an array of longitudinal linearly variable displacement transducers (LVDTs) was placed on the side of the girder and deck at varying depths. Figure D-6 shows the gauges on the side of the beam during shear test 2-1. The gauge length for the LVDTs was 30 in (760mm). This length was chosen to get an average strain behavior across the gauge length and to improve the probability of capturing any flexural cracks that formed during testing. The disadvantage of using such a long gauge length was that local behaviors could not be captured and that the moment varied over the gauge length. The bottom LVDT was placed 2 in (51mm) from the bottom of the girder at the same depth as the bottom-most layer of prestressing strands. The next LVDT was placed 12 in (305mm) from the bottom. This location was near the bottom of the web. The third LVDT was

placed at 24 in (610mm) from the bottom of the girder, which was near the top of the web. The final longitudinal LVDT on the girder was placed as close to the top of the girder as possible, 30.9 in (785mm) from the bottom of the girder. With these four LVDTs, the strain profile of the UHPC girder could be captured at any given point.

Two more longitudinal LVDTs were used on the sides of the deck. They were 1 in. (25 mm) and 7.25 in (184mm) from the bottom of the deck. These longitudinal deck LVDTs were used to measure the strain profile through the deck. Comparing the strain in the top-most girder LVDT and the bottom-most deck LVDT also allowed for an indication of whether there was composite action. While composite action was maintained, all six LVDTs showed the one linear strain profile. As soon as slip began to occur between the deck and girder, the strain profile changed to two separate profiles – one in the girder and one in the deck.

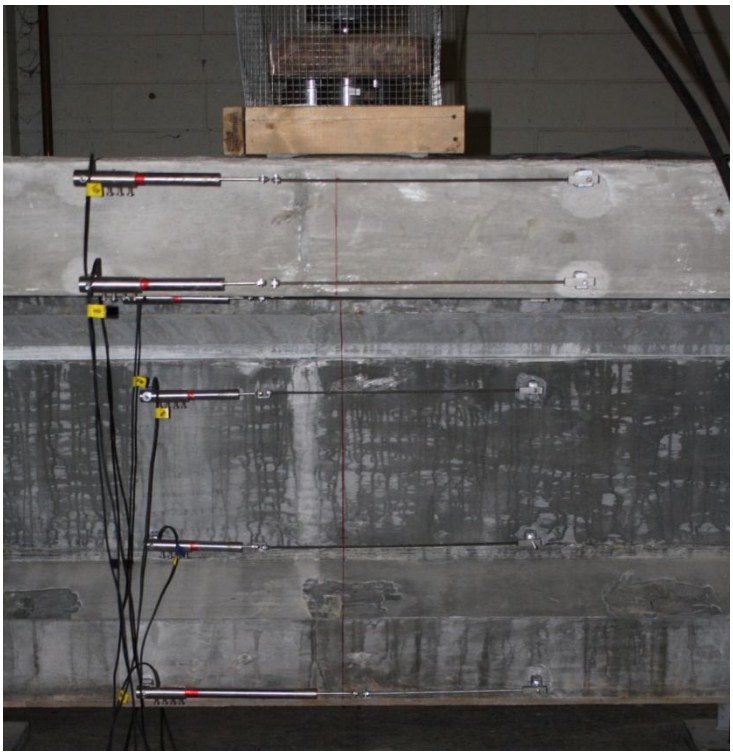

Figure D-6: Longitudinal LVDTs used for measuring strain profiles in full-scale girders during flexural and shear testing.

D.1.3 Deck Slip Measurement

In order to measure the differential motion between the girder and the deck during testing of the full-scale UHPC girders with cast-in-place conventional concrete decks, LVDTs were attached in the center of each shear span. The body of the LVDT was attached to the top flange of the girder, approximately 1 in (25mm) from the top of the girder. The other end of the LVDT was attached to the underside of the deck. Figure D-7 shows the setup of a slip LVDT during testing of a full-scale girder.

Figure D-7: Slip LVDT during full-scale girder testing.

D.1.4 Shear Strain Measurement

The setup for the strain rosettes that were used to measure shear is discussed in Chapter 6. In choosing the size and placement of these gauges, there was a trade-off between the precision and size of the array. As the array got larger, the assumption that

the strains could just be averaged at the center-point of the gauge array became less accurate. However, decreasing the size of the array was problematic for two reasons. First, the size of the physical LVDTs limited the minimum size of the array. Second, as the array size decreased, the chances of not capturing the shear failure crack increased. A 12 in x 12 in (305mm x 305mm) array size was chosen to try to capture the majority of the depth of the web. In order to try to minimize the effect of the large size on accuracy of the shear strain calculations, the compression diagonal LVDT was used in calculation of the principal shear strains and strain angles. This was done because both attachment locations of the compression diagonal LVDT were much closer to the center of the theoretical shear strut than were the ends of the tension diagonal LVDT.

D.1.5 Deflection Measurement

Deflection measurements were taken via string potentiometers attached to the underside of the girders. The body of the potentiometer was attached to a piece of plywood and held in place by concrete cylinders. The end of the potentiometer was attached to the girder using a picture hanging loop epoxied to the center of the underside of the girder. Figure D-8 shows the potentiometer and the attachment loop.

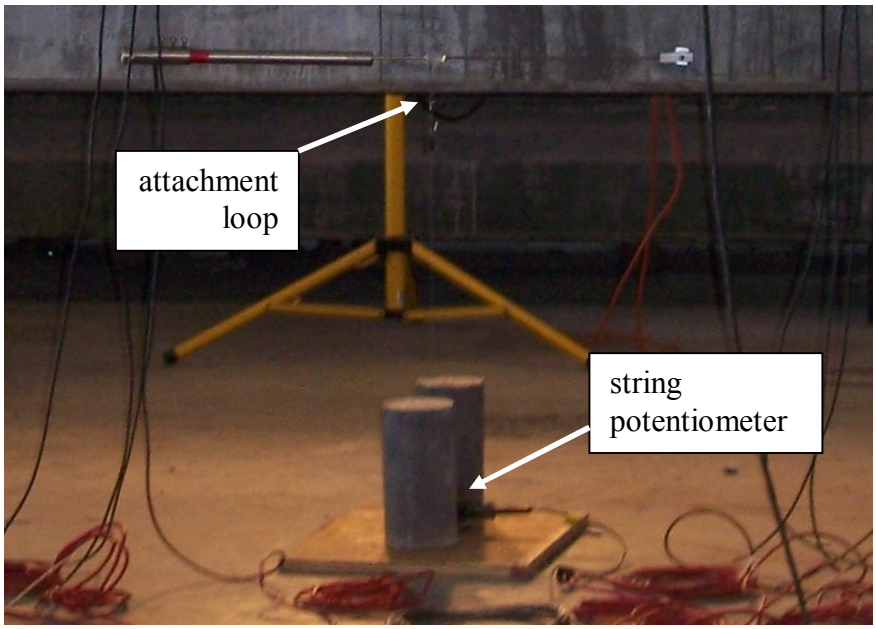

Figure D-8: String potentiometer for measuring deflection during full-scale girder testing.

D.1.6 Force Measurement

For the flexural test (1-1) and the first shear test (1-1a), a single 700-kip (3,100 kN) capacity Interface load cell was placed between the loading actuator and the load-distribution plate. This load cell was difficult to calibrate, which was thought to be due to either a low-level voltage leak or an extreme sensitivity to the orthogonality of the load application. The load cell setup for these tests is shown in Figure D-9.

For the remaining full-scale tests, a group of three 300-kip (1,300 kN) Interface load cells arranged in a triangle was used. A 3-in (76mm) thick steel plate was used to distribute the load from the actuator to the load cells as evenly as possible. The load was applied to the plate via a 2-in (51mm) steel ball centered over the geometric center of the triangle of load cells. A socket in the plates above and below the ball prevented the ball

from slipping. The load cell setup for these tests is shown in Figure D-10. A wire mesh cage was used as a safety precaution in case of a sudden beam failure.

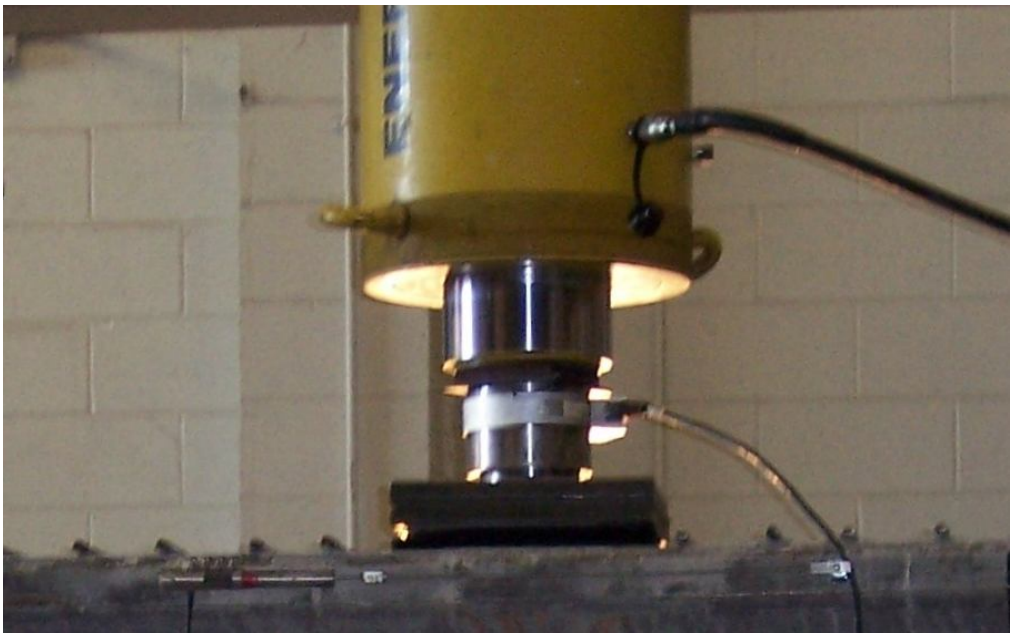

Figure D-9: Load cell setup for tests 1-1 and 1-1a.

Figure D-10: Load cell setup for tests 1-2, 2-1, 2-2, 3-1, and 3-2.

D.2 Thermal Curing Data for UHPC Girders

Seventy-six hours after the completion of casting, the girders began thermal curing. The objective was to maintain a temperature of 95°C (203°F) at 95% R.H for 48 hours. Figure D-11 shows the actual average internal temperatures attained in girders 1 and 3. Since the desired temperature was not reached, the thermal curing time was increased to try to achieve concrete maturity and mechanical properties equivalent to the specified thermal curing. Figure D-12 shows the increase of compressive strength with time before and during thermal curing.

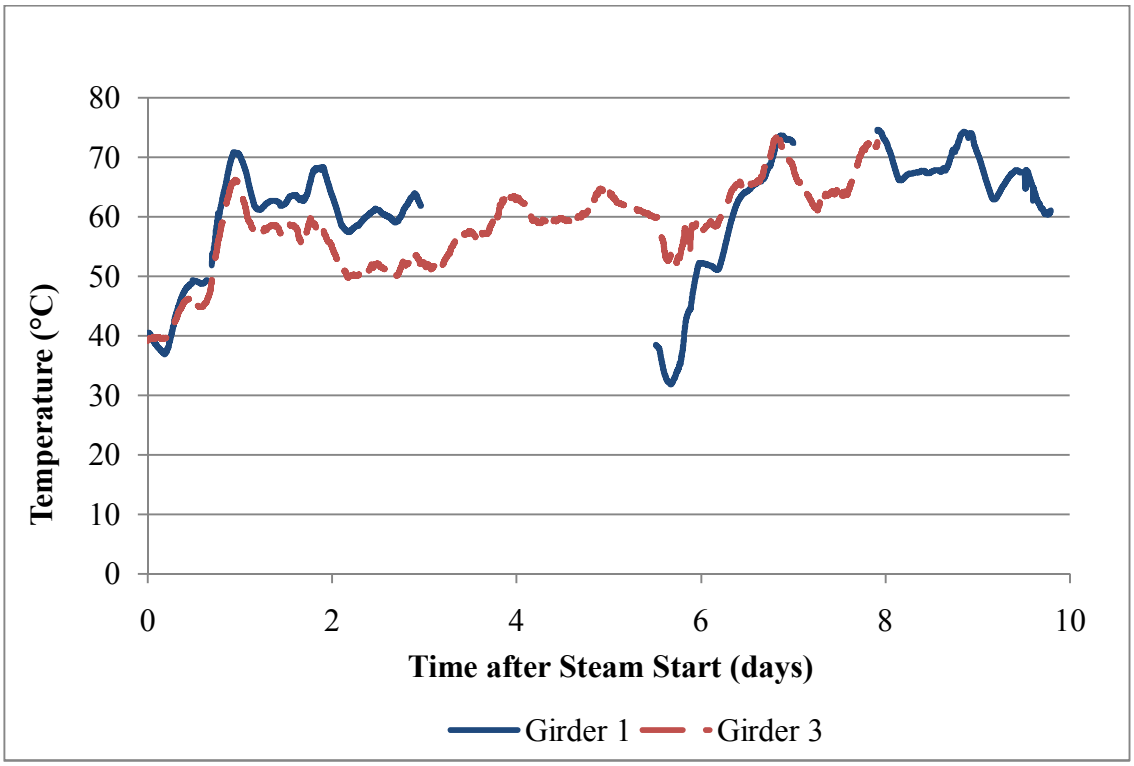

Figure D-11: Temperature variations during thermal curing of UHPC girders.

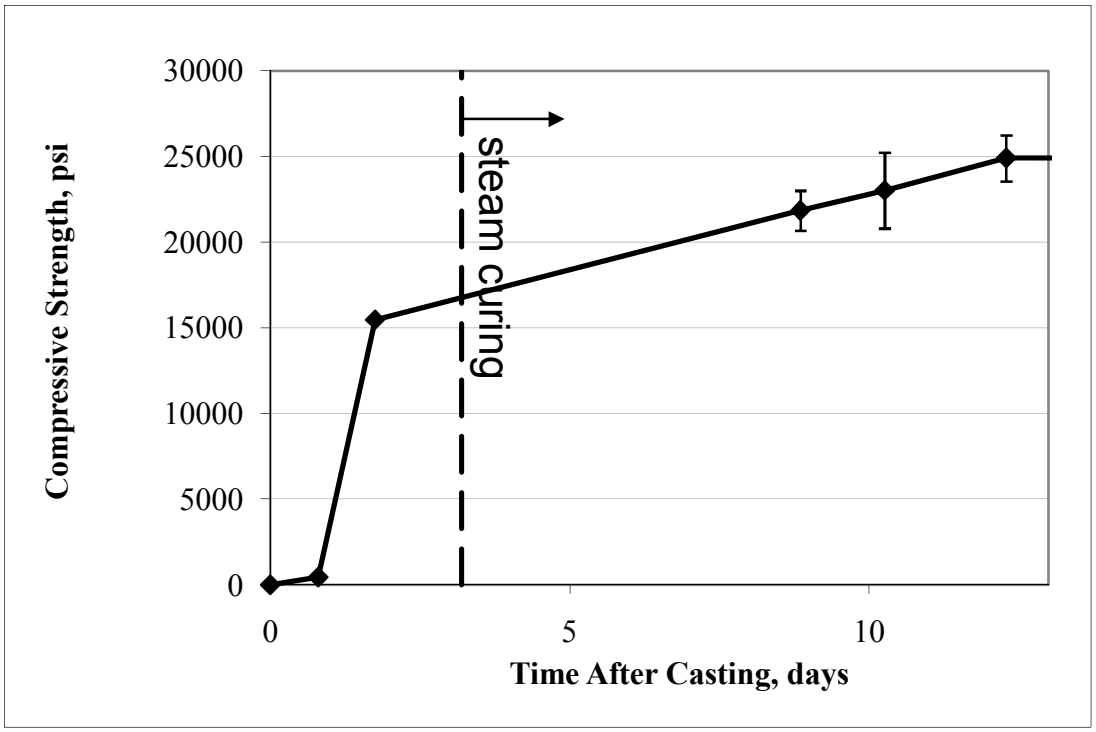

Figure D-12: UHPC compressive strength gain.

D.3 Losses at Strand Release

Table D-1 gives the VWSG readings two hours before and three hours after strand release. Due to the three hour time lapse following strand release, the measured elastic shortening may include some time-dependent deformations, but these were considered negligible in comparison to the elastic deformation. The average elastic deformation at the level of the top strands was calculated to be -188 με. The average elastic deformation between the two bottom layers of strands was calculated to be -815 με. These values had standard deviations of 85 and 42 με, respectively. The strain profile from this data was extrapolated to the top and bottom of the girders and was used for calculation of initial elastic deformation in any longitudinal gauges (including those in the shear strain rosettes).

Table D-1: VWSG readings before and after strand release.

Girder	Gauge Position	Strain before Strand Release (με)	Strain after Strand Release (με)	Measured Elastic Shortening (με)
1	1 - Top	115	-164	-279
	2 - N Bot.	-30	-873	-843
	3 - S Bot.	125	-617	-742
2	1 - Top	64	-48	-112
	2 - N Bot.	4	-802	-806
	3 - S Bot.	147	-695	-842
3	1 - Top	69	-103	-172
	2 - N Bot.	-5	-862	-856
	3 - S Bot.	137	-665	-802

Time dependent deformations were calculated by taking periodic VWSG readings. These measurements were averaged for each beam and are presented in Figure D-13. Since the first two data points after cutdown were taken 3 hours and 8 hours after cutdown, the creep data was linearly extrapolated back to the time of cutdown. The assumption of linear creep behavior was not exact, but was closer than simply taking some later point as time "zero". The observed time-dependent strains at one year were around 900 με, which was consistent with data from the literature.

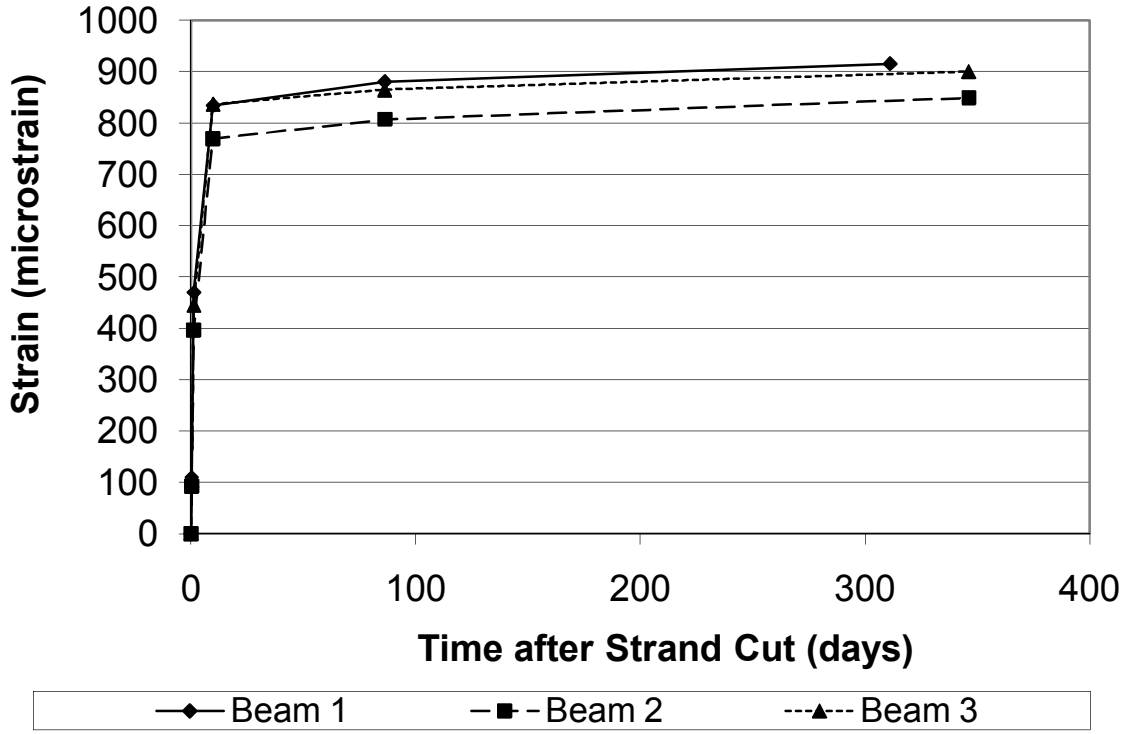

Figure D-13: Creep and Shrinkage Strain of UHPC Beams (extrapolated linearly to time=0 from time=0.32).

D.4 Transfer Length of Strands in UHPC Girders

DEMEC gauge readings were taken prior to strand release as well as after the beams had been cut down and one end of each beam had been lifted off the casting bed and set back down to release friction. The difference of these two sets of readings was used to calculate the point at which the strain in the strand was fully transferred into the surrounding concrete. The method recommended by Russell (1992) was used to create transfer length diagrams similar to that shown in Figure D-14. Based on this data, an average plateau value was calculated. The transfer length was taken as the point at which the smoothed data points crossed 95% of the plateau value. The average transfer length

calculated from the twelve different DEMEC point groups on the three girders was 15.2 in (390 mm) with a standard deviation of 1.9 in (48 mm). This value is 53% lower than the AASHTO LRFD (2010) value of $50d_b$.

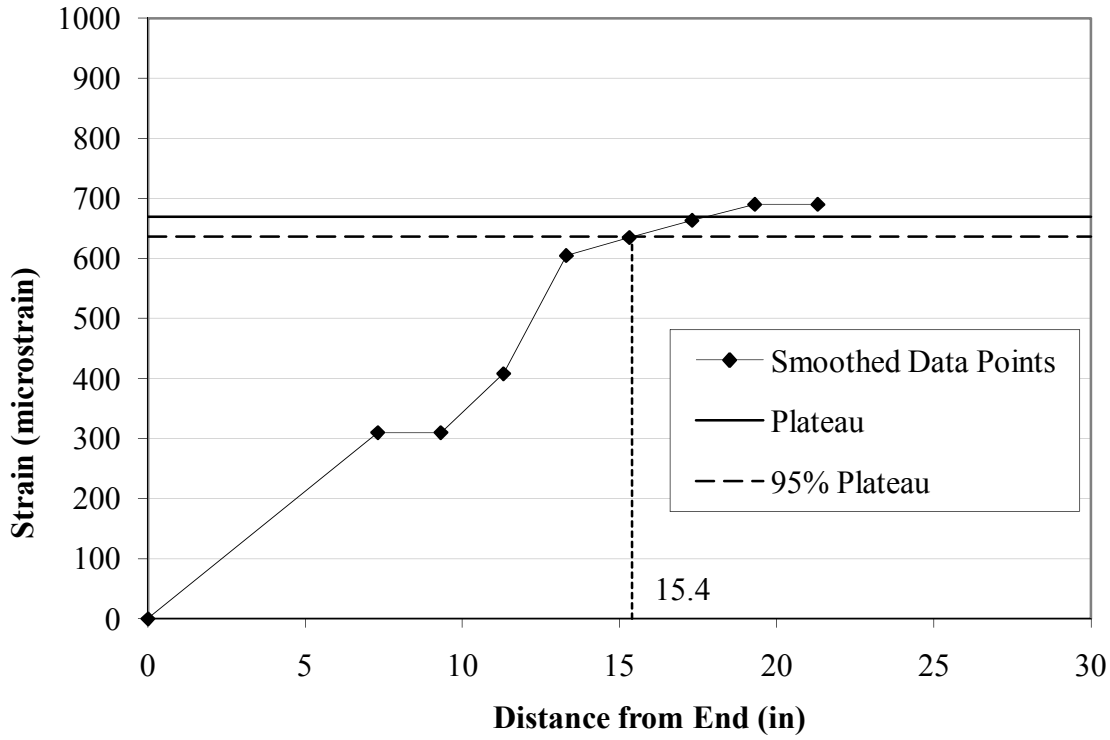

Figure D-14: Typical transfer length plot. Transfer length was determined to be the point at which the smoothed data line crossed 95% of the plateau value.

D.5 Longitudinal Strain Gauge Test Data

Figures D-15 through D-21 give the load-strain curves for the longitudinal LVDTs that were located beneath the load application point in each full-scale girder test.

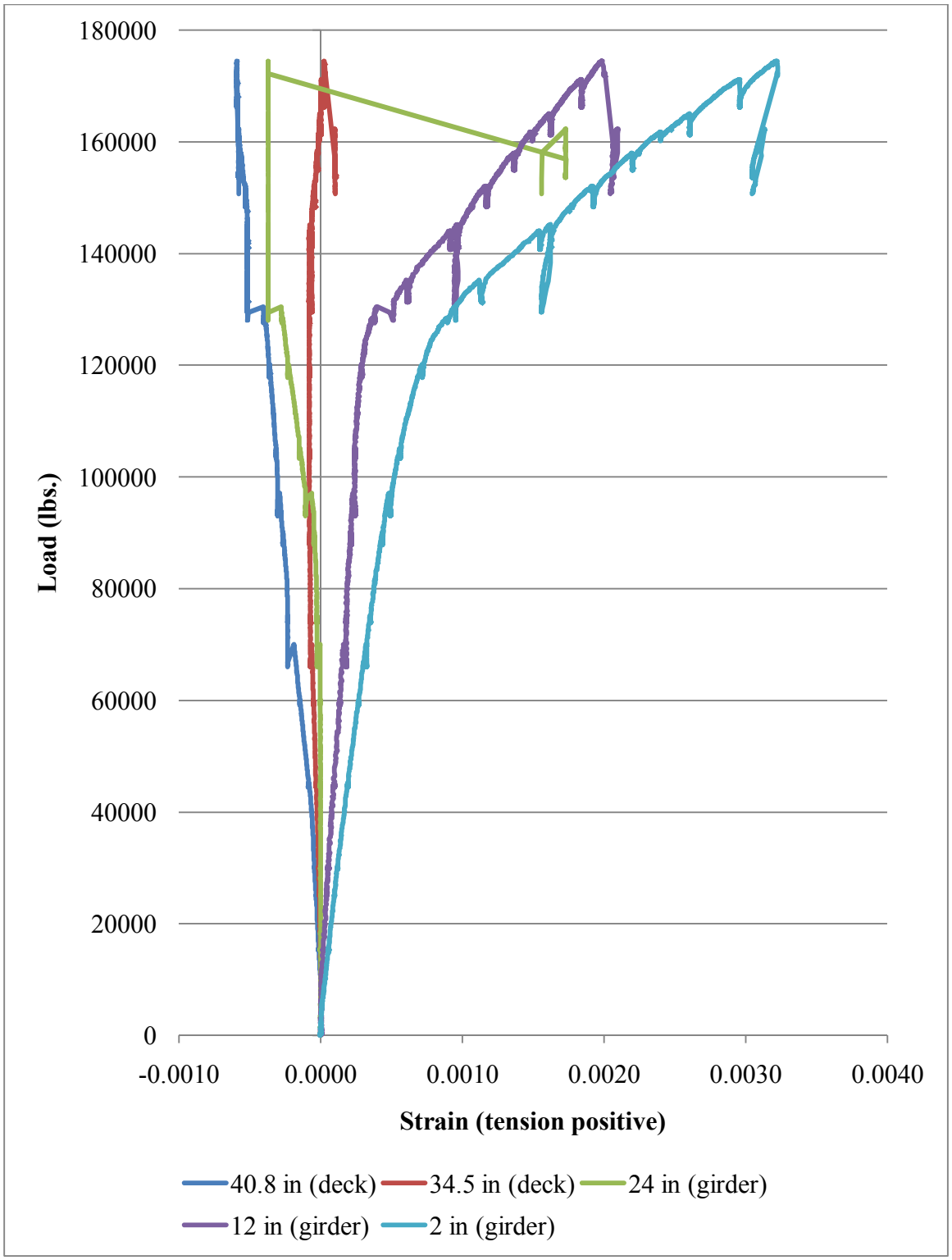

Figure D-15: Longitudinal strains at center span in test 1-1. All gauge locations are measured from the bottom of the girder.

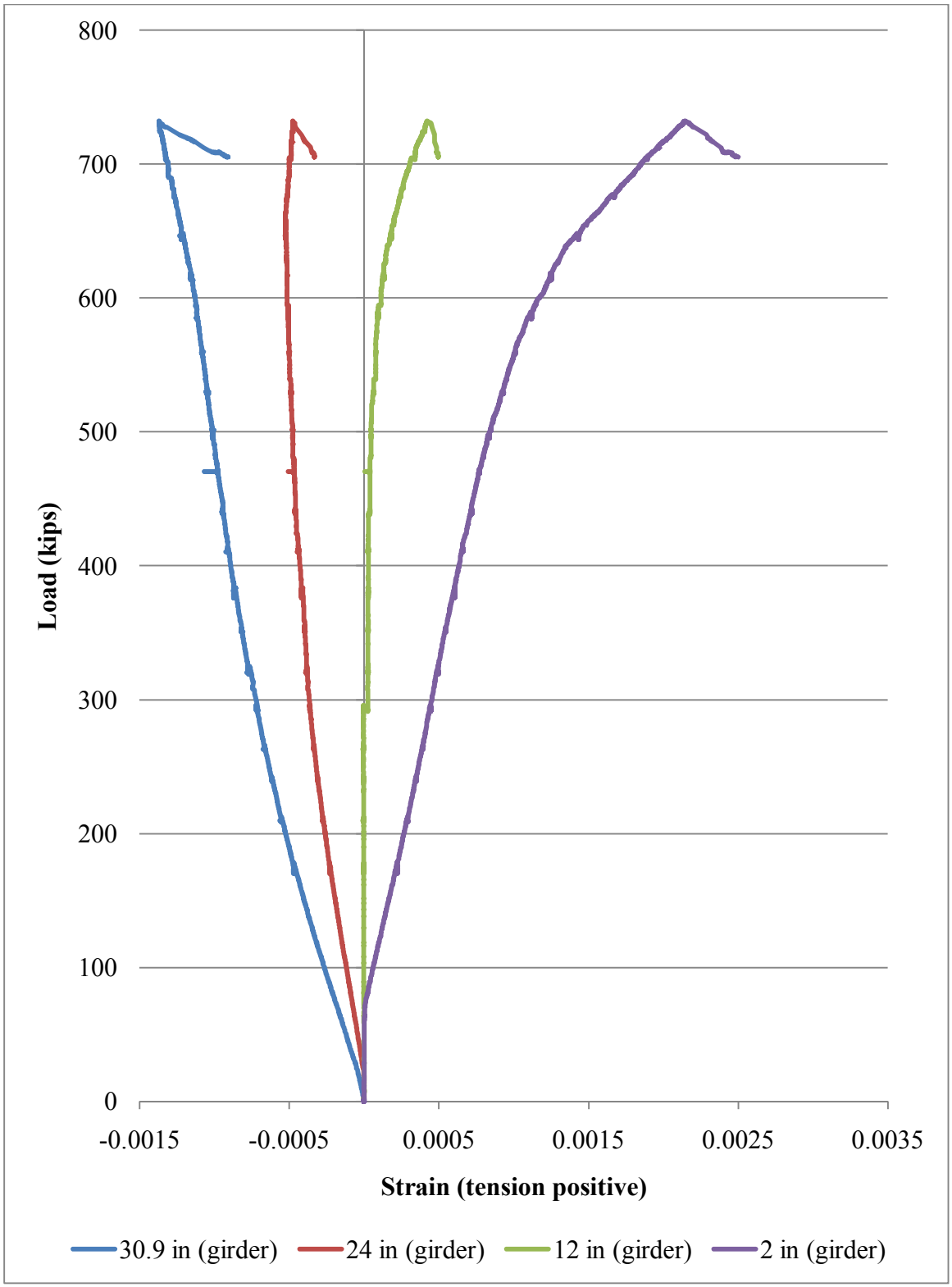

Figure D-16: Longitudinal strains at load location in test 1-1a. All gauge locations are measured from the bottom of the girder.

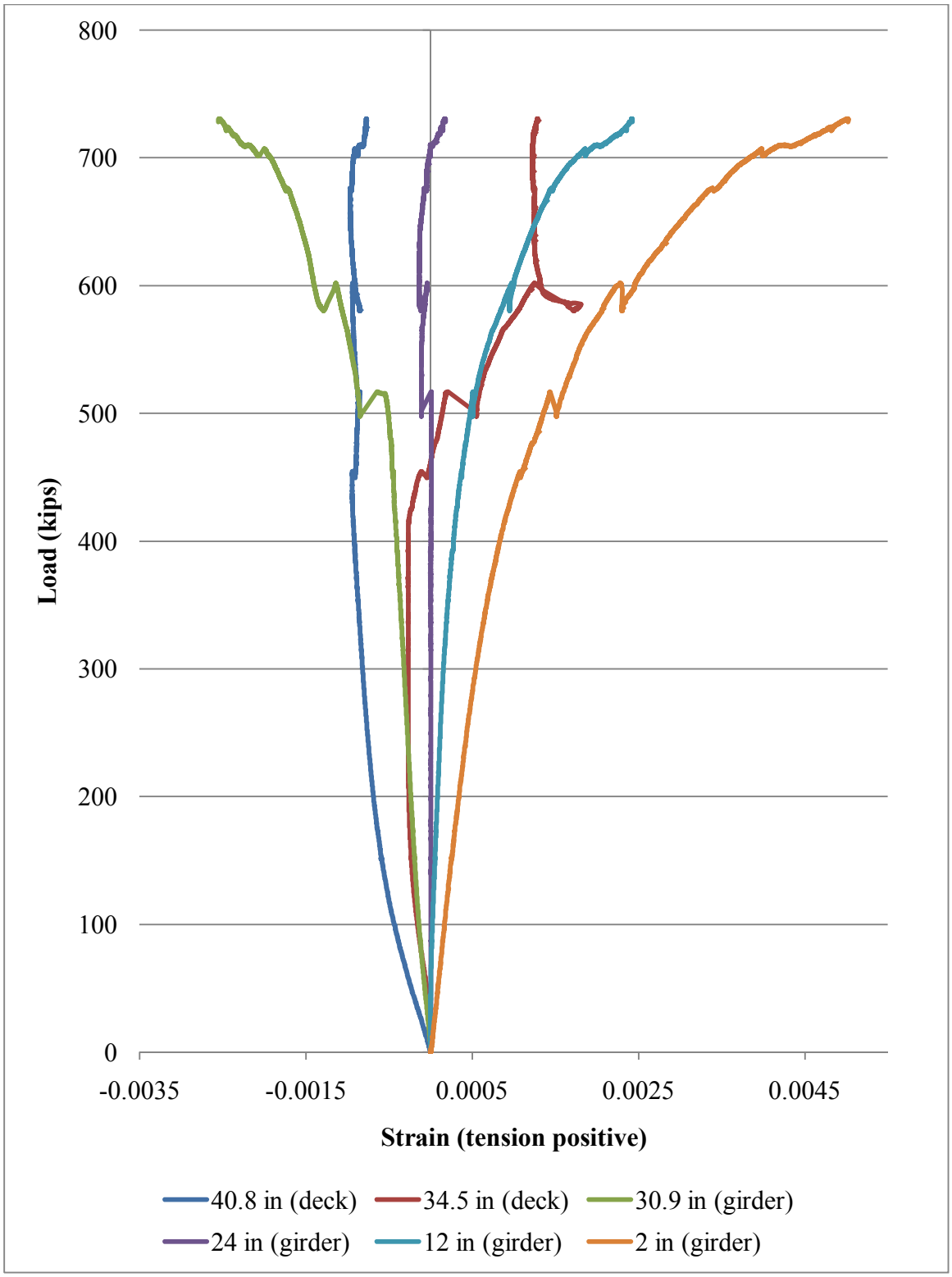

Figure D-17: Longitudinal strains at load location in test 1-2. All gauge locations are measured from the bottom of the girder.

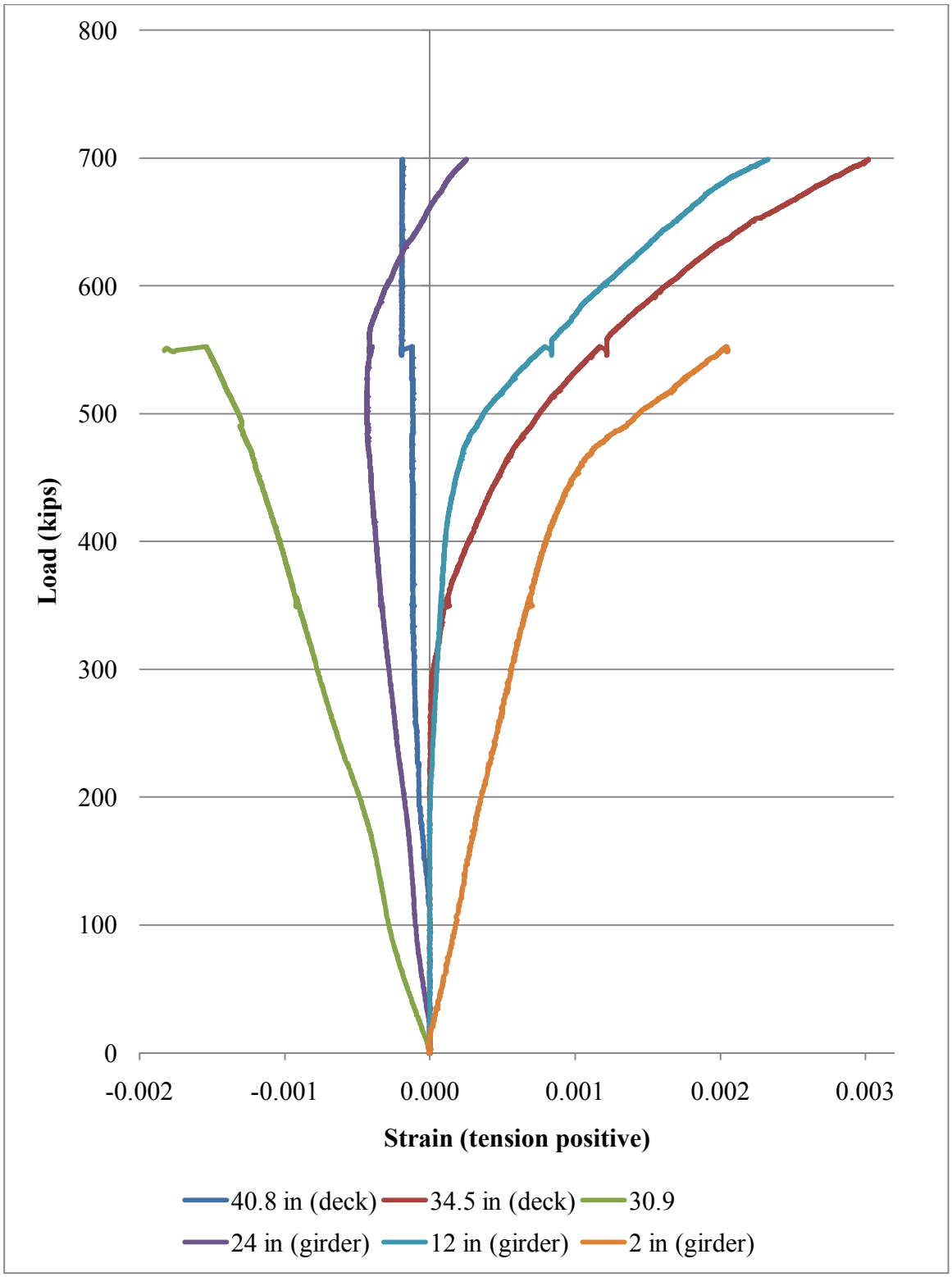

Figure D-18: Longitudinal strains at load location in test 2-1. All gauge locations are measured from the bottom of the girder.

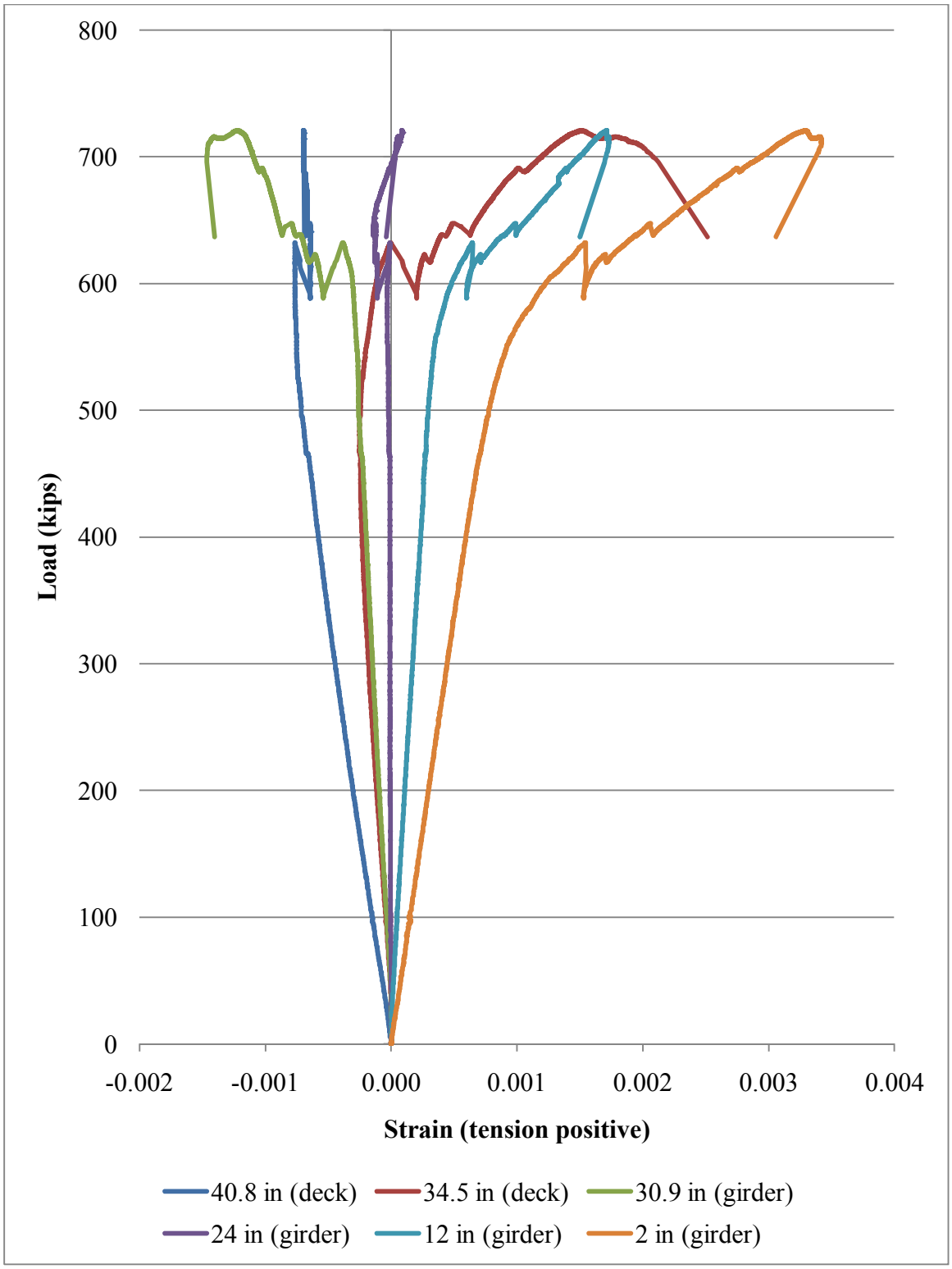

Figure D-19: Longitudinal strains at load location in test 2-2. All gauge locations are measured from the bottom of the girder.

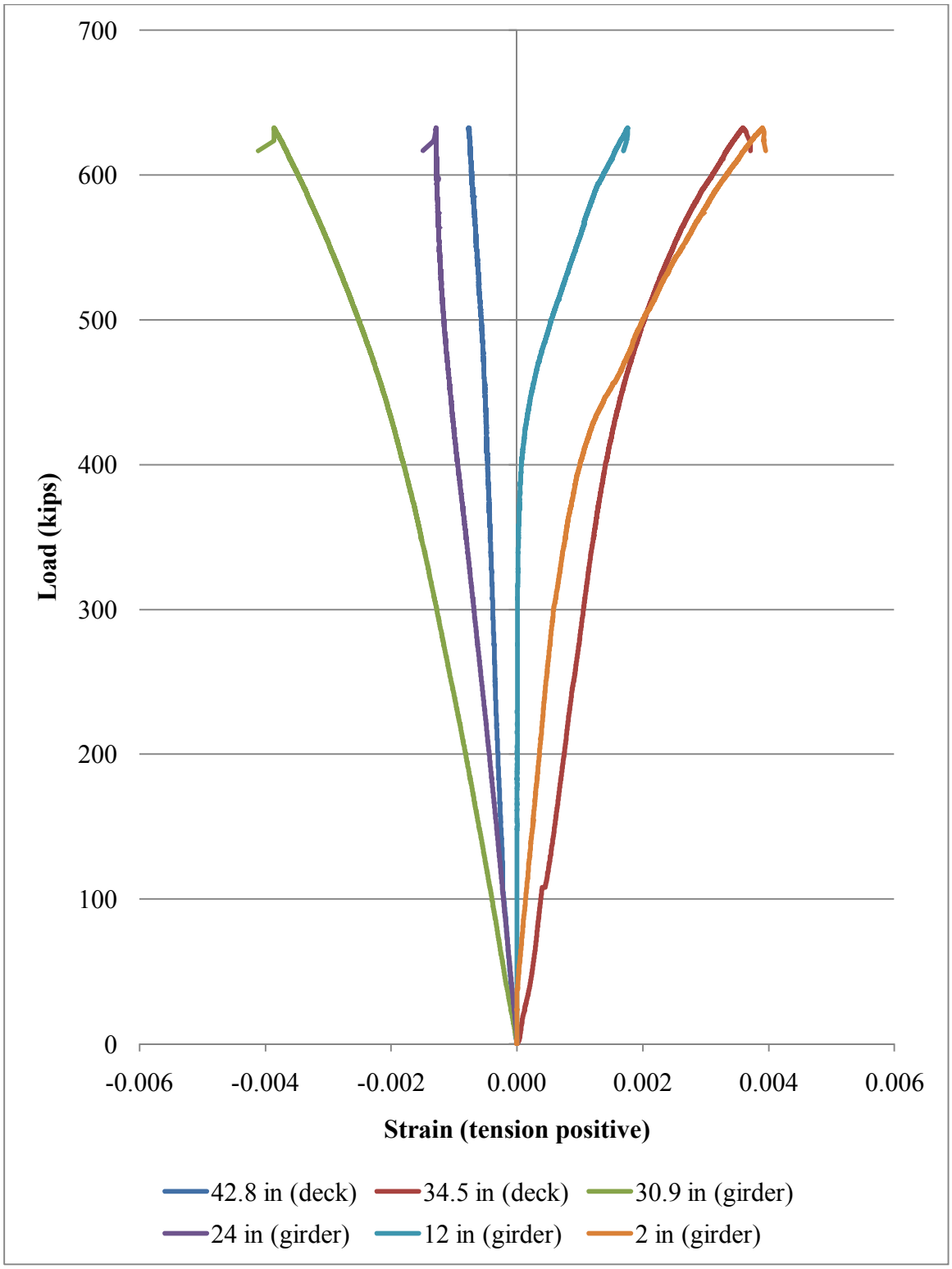

Figure D-20: Longitudinal strains at load location in test 3-1. All gauge locations are measured from the bottom of the girder.

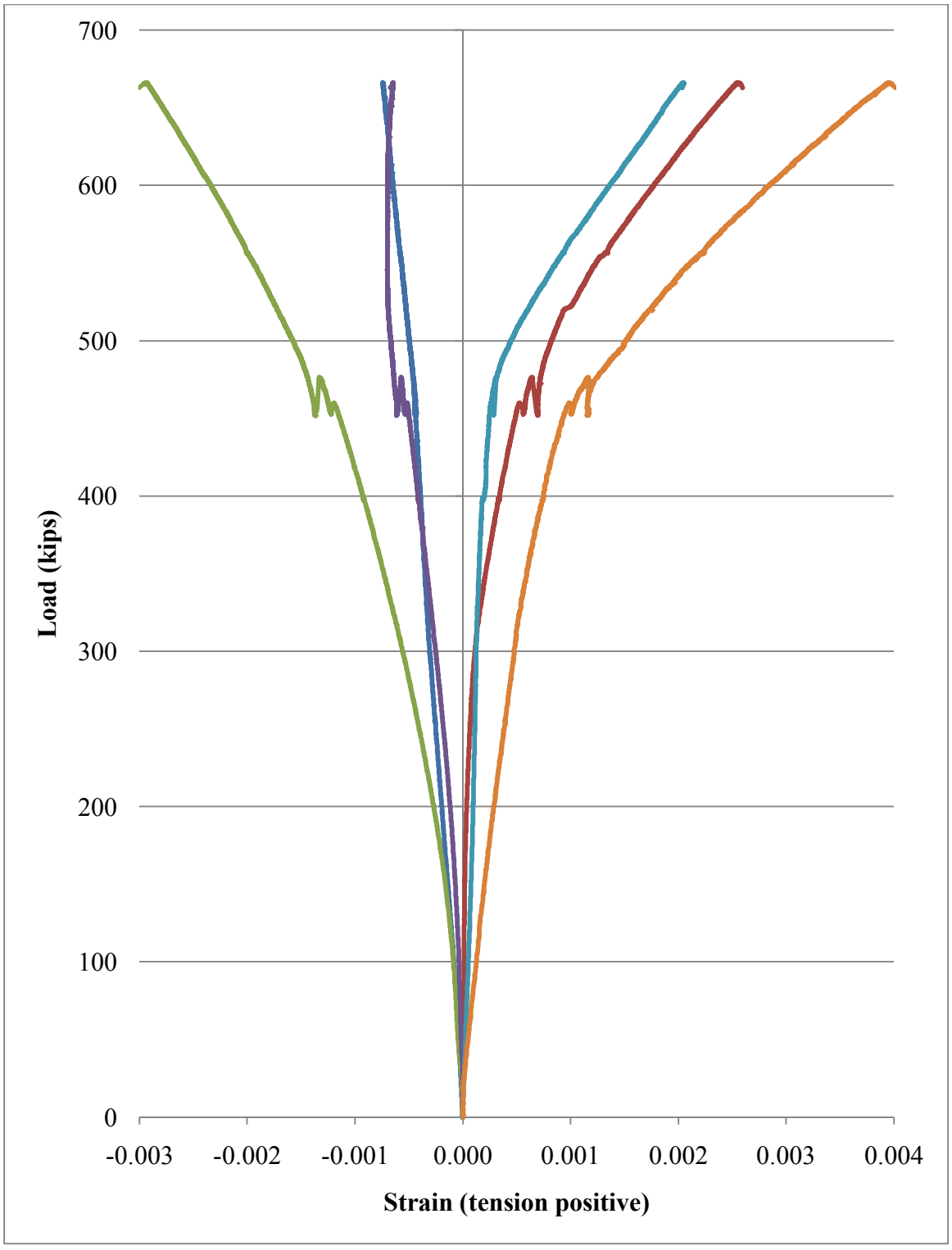

Figure D-21: Longitudinal strains at load location in test 3-2. All gauge locations are measured from the bottom of the girder.

D.6 References

AASHTO (2010). *AASHTO LRFD Bridge Design Specifications*. Washington, D.C., American Association of State Highway and Transportation Officials.

Russell, B. W. (1992). Design Guidelines for Transfer, Development and Debonding of Large Diameter Seven Wire Strands in Pretensioned Concrete Girders. *Civil Engineering*. Ph.D. Thesis. University of Texas at Austin, Austin.